DTU Library

Influence of Microstructure and Processing on the Corrosion Resistance of Medical Device

Henriksen, Nikolaj Gersager

Publication date:
2023

Document Version
Publisher's PDF, also known as Version of record

Link back to DTU Orbit

Citation (APA):
Henriksen, N. G. (2023). *Influence of Microstructure and Processing on the Corrosion Resistance of Medical Device*. Technical University of Denmark.

Department of Civil and Mechanical Engineering
PhD Thesis

Influence of Microstructure and Processing on the Corrosion Resistance of Medical Device

Nikolaj Gersager Henriksen

Influence of Microstructure and Processing on the Corrosion Resistance of Medical Device

Thesis Submitted to the Technical University of Denmark for the Degree of Doctor of Philosophy in the Department of Civil and Mechanical Engineering

By

Nikolaj Gersager Henriksen

May 2023

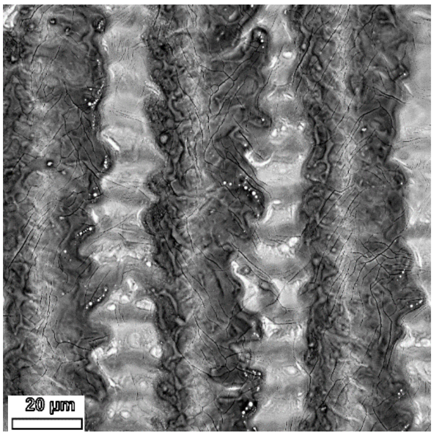

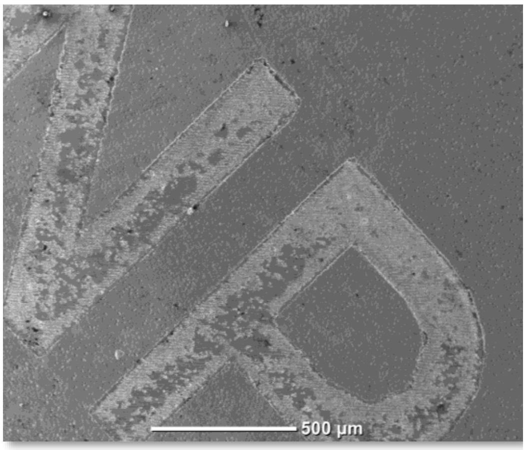

Elos Medtech

Gørløse, Denmark

Technical University of Denmark

Department of Civil and Mechanical Engineering

Section of Materials and Surface Engineering

A Doctoral Thesis by
Nikolaj Gersager Henriksen
Email: nigehe@dtu.dk
Nikolaj.henriksen@elosmedtech.com
Elos Medtech
Engvej 33, 3330 Gørløse, Denmark

Principal University Supervisor
Marcel A.J. Somers
Email: majs@dtu.dk
Technical University of Denmark
Department of Civil and Mechanical Engineering
Section of Materials and Surface Engineering
Building 425, room 120

University Co-Supervisor
Thomas L. Christiansen
Email: thoch@dtu.dk
Technical University of Denmark
Department of Civil and Mechanical Engineering
Section of Materials and Surface Engineering
Building 425, room 110

Principal Company Supervisor
Frederik Bojsen-Møller
Email: Frederik.bojsen-moller@elosmedtech.com
Elos Medtech
Engvej 33, 3330 Gørløse, Denmark

Company Co-Supervisor
Henrik Andersen
Email: Henrik.Andersen@Elosmedtech.com
Elos Medtech
Engvej 33, 3330 Gørløse, Denmark

A collaboration between the Technical University of Denmark and Elos Medtech

Published by: Department of Civil and Mechanical Engineering, Section of Materials and Surface Engineering, Produktionstorvet, Building 425, DK-2800 Kgs. Lyngby

Preface

This document is a doctoral thesis and part of the requirements to receive a degree of Doctor of Philosophy (Ph.D.) given by the Technical University of Denmark (DTU). The project was co-funded by Elos Medtech and Innovation Foundation Denmark under the grant number 9065-00210B. The Ph.D.-student was enrolled at DTU during the project at the Department of Civil and Mechanical Engineering in the section of Materials and Surface Engineering. The project lasted from February 2020 until May 2023 with a hiatus of 3 months as a consequence of Covid-19 lock down of the company.

At the university, Professor Marcel A. J. Somers acted as principal supervisor. Co-supervision was provided by lector Thomas L. Christiansen. The principal industrial supervisor from Elos Medtech was initially research manager Ole Z. Andersen and later his successor Frederik Bojsen-Møller. Head of Engineering Henrik Andersen acted as the industrial co-supervisor.

Nikolaj Gersager Henriksen

May 10th, 2023

Kongens Lyngby, Denmark

Abstract

The research work in this thesis revolved around the laser marking of materials used in metallic medical devices, specifically on how the laser marking affects the microstructure and associated properties such as corrosion and fatigue performance. The project was motivated by the increasing demand for traceability in the form of oxidative laser marking applied directly onto medical devices. Medical device manufacturers experienced issues with delamination and corrosion in the laser markings. If the laser marking delaminates or corrodes, it will be considered unreadable and will therefore no longer be fit for application or sale. Laser marking is relatively well-studied regarding the production of high color strength markings, however there is little knowledge regarding the impact on mechanical properties or corrosion resistance. The industry has moved significantly faster than research on the subject.

The impact of laser marking on corrosion resistance of free-machining martensitic stainless steel was investigated to address the current issues in industry. Several sets of laser parameters were investigated regarding the microstructure and the corrosion resistance. It was found that a sub-µm oxide layer forms on the laser marked surface and that the color strength depends largely on the thickness of this oxide layer. The oxide layer was identified to be either Fe_3O_4 and/or $FeCr_2O_4$ and contained chromium. The thickness of the oxide layer depends largely on the heat input (J/area) of the laser treatment. The heat input is also the deciding factor for retention of corrosion resistance, as it was demonstrated that high heat input results in a darker color but also poorer corrosion resistance. This was attributed to chromium depletion in the sub-surface zone and corrosion underneath the oxide layer was identified. It was additionally found that the presence of abundant MnS jeopardizes the corrosion resistance after laser marking. The rod-like MnS inclusions, aligned perpendicular to the surface where laser marking was performed, thermally degraded leaving crater-like features. These craters are thought to act effectively as pits for corrosion initiation.

Abstract

Large tensile residual stresses were found in martensitic stainless steel after laser marking and were the result of a complicated thermal history and altering of the chemical composition during laser marking. The residual stresses on the surface were found to depend on the degree of melting and the hatch spacing of the laser tracks. The chemical composition was severely altered in the HAZ, and a significant chromium depletion could be measured as well as uptake of hydrogen and oxygen. It was discussed that as laser marking alters the chemical composition, resulting in state of tensile residual stress.

The influence of laser marking was also investigated on commercially pure titanium and Ti6Al4V. It was found that laser marking resulted in severe crack-development, such that the cracks develop perpendicular to the surface. Close to the surface the alloys had reached the liquid state during laser marking and distinct microstructural zones were discerned in the depth direction. High oxygen ingress in the melted zone suppressed the liquid → BCC transformation and, instead, the material solidified directly as HCP. The cracks were found to jeopardize the fatigue strength of both types of titanium alloys by up to 80 % relative to unmarked specimen. As cracks are developed before loading of the material, the crack initiation stage is essentially by-passed on subsequent loading.

Resumé

Forskningsarbejdet i denne afhandling omhandler lasermarkering af metalliske medicinske materialer, specifikt om hvordan lasermarkering påvirker mikrostrukturen og andre egenskaber såsom korrosionsresistens og udmattelsesegenskaber. Projektet er motiveret af stigende krav til sporbarhed i form af oxiderende lasermarkering placeret direkte på medicinsk udstyr. Producenter af medicinsk udstyr oplever problemer med delaminering og korrosion i lasermarkeringen. Hvis lasermarkeringen de-laminerer eller korroderer, betragtes den som ulæselig og er derfor ikke længere egnet til brug eller salg. Lasermarkering er relativt velstuderet med hensyn til at producere markeringer med høj farvestyrke, men der findes kun lidt forskning omkring konsekvenserne på mekaniske egenskaber eller korrosionsresistens. Industrien har bevæget sig bemærkelsesværdigt hurtigere end forskningen af emnet.

Indvirkningen af lasermarkering på korrosionsbestandigheden af martensitiske rustfrie automatstål blev undersøgt for at adressere nuværende problemer i industrien. Flere laserparametersæt blev undersøgt vedrørende mikrostrukturen og korrosionsbestandigheden. Der fandtes, at et sub-µm oxidlag dannes på den lasermarkerede overflade og at farvestyrken var meget afhængig af tykkelsen på oxidlaget. Oxidlaget blev identificeret til at være enten Fe_3O_4 og/eller $FeCr_2O_4$ og indeholdt en øget mængde krom. Tykkelsen af oxidlaget afhang kraftigt af varmeinputtet (J/areal) af laserbehandlingen. Varmeinputtet var også den bestemmende faktor for bibeholdelse af korrosionsbestandighed, da det blev demonstreret at højt varmeinput resulterede i en mørkere farve men også en lavere korrosionsbestandighed. Dette blev tilskrevet kromforarmning i underoverfladen, og der blev demonstreret korrosion under oxidlaget. Herudover fandtes, at tilstedeværelsen af rigelig MnS gjorde materialet mere følsomt overfor reduceret korrosionsbestandighed fra lasermarkering. De stangagtige MnS inklusioner var justeret i trækretningen, og da lasermarkering blev udført på trækretningen, degraderede MnS inklusionerne termisk og dannede krateragtige træk. Disse kratere tænkes at opføre sig som pits produceret allerede i lasermarkeringen.

Store rest-trækspændinger blev fundet i martensitisk rustfrit stål efter lasermarkering og var resultatet af en kompliceret termisk historik og ændring af den kemiske sammensætning under lasermarkering. Restspændingerne på den yderste overflade blev bestemt til at afhænge af smeltegraden og afstanden mellem lasersporene. Den kemiske sammensætning blev kraftigt ændret i den varmepåvirkede zone og en betydelig kromforarmning kunne måles samt et optag af hydrogen og oxygen. Åbenbart ændrer lasermarkering den kemiske sammensætning således at der dannes høje trækspændinger.

Indflydelsen af lasermarkering blev undersøgt på kommercielt rent titan og Ti6Al4V. Der blev fundet at lasermarkering resulterede i kraftig revnedannelse vinkelret på overfladen. Der var tegn på at materialet var smeltet tæt ved overfladen og flere tydeligt forskellige mikrostrukturelle zoner var dannet. Højt oxygenoptag i den smeltede zone undertrykte transformationen fra flydende → BCC og materialet størknede i stedet direkte som HCP. Revnerne viste sig at reducere udmattelsesstyrken af begge typer titanlegeringer med op til 80 % relativt til umarkerede prøver. Da revnerne udviklede sig før belastning af materialet, blev revnedannelsesstadiet af et udmattelsesbrud essentielt sprunget over.

Acknowledgements

First, I would like to express my appreciation for my principal and co-supervisor Marcel Somers and Thomas Christiansen for their support and availability. Their knowledge and expertise have been invaluable, not only during engaging scientific discussions, but also for guidance in my professional life. You have been a source of inspiration and I have felt a dedication to the well-being of both myself and the project. Thank you for your support.

I would also like to thank my industrial supervisors. Ole Andersen for initiating the project and providing a good start at the company. Thank you for your advice and understanding, and I wish you well in your new position. My co-supervisor and leader Henrik Andersen, I thank you for your support during my time at Elos Medtech and I have greatly benefitted from your almost inexhaustible knowledge of the dental industry. I would also like to acknowledge Frederik Bojsen-Møller for taking over the role of supervisor after Ole and for your enthusiasm.

Gratitude goes towards Innovation Fund Denmark for kindly providing funding for the project and direction during COVID. It has allowed me to conduct my Ph.D. studies and to experience both the academic and industrial world.

My other colleagues at Elos Medtech have been a great support. My greatest appreciation for my office mates Arvan, Danilo, Nise, Tobias, Søren, Brian, Andreas, Mette, and Nichlas among others for the amazing work environment. I would also like to individually thank Michel Lunde for his expertise on the laser equipment and for always being available and optimistic about the experiments. Additionally, I want to express my gratitude towards Brian Jensen for his flexibility and technical knowledge about fatigue testing of dental equipment.

I want to thank the staff at ‘Materials and Surface Engineering’ section at DTU. The technical staff, Niklas Gammeltoft-Hansen and Flemming Grumsen, for providing me with the technical know-how and for helping me overcoming the challenges of the different analyses. I cannot express my appreciation enough for my fellow Ph.D. students and the fellowship we built. Magnus, Felix, Sajjad, Cecilie, Emilie, Konstantin, Basit, Andreas, Daniel, Bjarke, Kleanny and many others, the social aspect and support you provided has been invaluable.

Finally, I must extend my sincerest thanks and gratitude towards my family for being understanding and supporting me through everything. My girlfriend Andrea, I would like to thank you for your unconditional support through both good and bad times and for being ever patient.

Publications

Articles included in thesis:

- Nikolaj G. Henriksen, O. Z. Andersen, Morten S. Jellesen, Thomas L. Christiansen, Marcel A. J. Somers; Influence of Laser Marking on Microstructure and Corrosion Performance of Martensitic Stainless Steel Surfaces for Biomedical Applications; **Published** in Heat Treatment and Materials.
- Nikolaj G. Henriksen, Thomas L. Christiansen, Morten S. Jellesen, Marcel A. J. Somers; Effect of Manganese Sulfides and Nitriding on the Corrosion Resistance of Laser Marked Medical Martensitic Stainless Steel; **Published** as a conference paper and presentation at ESSC Stainless Steel and Duplex 2022.
- Nikolaj G. Henriksen, Konstantinos Poulios, Marcel A. J. Somers, Thomas L. Christiansen; Impact of Laser Marking on Microstructure and Fatigue Life of Medical Grade Titanium; **Published** in Materials Science and Engineering A.
- Nikolaj G. Henriksen, Thomas L. Christiansen, Frederik Bojsen-møller, Sebastién Jegou, Laurent Barralier, Marcel A. J. Somers; Residual Stress Generation in Laser Marked Martensitic Stainless Steel and Dependence on Laser Parameters; **In preparation**.

Articles not included in thesis:

- T. Dahmen, N. G. Henriksen, K. V. Dahl, A. Lapina, D. B. Pedersen, J. H. Hattel, T. L. Christiansen, M. A. J. Somers; Densification Microstructure and Mechanical Properties of Heat-Treated MAR-M247 Fabricated by Binder Jetting; **Published** in Additive Manufacturing.

Conference contributions:

- Oral presentation and written contribution, ESSC Stainless steel and Duplex, Bardolino, Italy, 15th-17th June 2022.
- Oral presentation, Dansk Metallurgisk Selskabs Vintermøde, Roskilde, Denmark, 25th- 27th January 2023.

Table of Contents

Units, Symbols and Abbreviations

Units

%	Percent
°	Degree
°C	Degrees celsius
µm	Micrometer
cm	Centimeter
dec.	Decade
HV	Hardness Vickers
Hz	Hertz
J	Joule
kHz	Kilohertz
kV	Kilovolt
m	Meter
mA	Milliampere
mbar	Millibar
min	Minute
mm	Millimeter
MPa	Megapascal
mV	Millivolt
N	Newton
nm	Nanometer
ns	Nanosecond
s	seconds
W	Watt
w%	Weight percent
Å	Angstrom

Symbols

A	Area
E_{corr}	Corrosion potential
E_p	Single laser pulse energy
Es	Heat input
f	Frequency
F	Force
I	Moment of intertia
I_{corr}	Corrosion Current
L	Moment arm
l_s	Hatch spacing
Ms	Martensite start temperature
P	Average Power
P_p	Power density
R	Load ratio
r	Radius
t_p	Pulse time
v	Scan speed
α	BCC ferrite (steel) HCP (titanium)
α'	Martensite – BCC/tetragonal (steel) Martensite – HCP (titanium)
β	BCC (titanium)
β_a	Anodic Tafel slope
β_c	Cathodic Tafel slope
γ	FCC Austenite (steel)
θ	Scattering angle
σ	Stress
d	Lattice parameter
ψ	Polar angle
φ	Azimuth angle

Abbreviations

BCC	Body centered cubic
BSE	Backscatter electron
CP	Commercially pure
DTU	Technical university of denmark
EDS	Energy dispersive x-ray spectroscopy
EU	European union
FCC	Face centered cubic
FDA	Food and drug administration
GDOES	Glow discharge optical emission spectrocopy
GIXRD	Grazing incidence X-ray diffraction
HAZ	Heat affected zone
HCP	Hexagonal close packed
MDR	Medical device regulative
Nd:YAG	Neodymium-doped Yttrium aluminium garnet
YAG	Yttrium aluminium garnet
OCP	Open current potential
PREN	Pitting resistance equivalence number
QR	Quick response
SE	Secondary electron
SEM	Scanning electron microscopy
SHE	Standard hydrogen electrode
UDI	Unique device identification
UM	Unmarked
USA	United states of america
XRD	X-ray diffraction
GD-OES	Glow discharge optical emission spectroscopy

1. Introduction

1.1. Project Background and Motivation

The entire life science industry, including the medical device industry, is soon required to uphold the current Medical Device Regulative (MDR), imposed by the European Union as of April 2017 [1]. It outlines and defines requirements and practices that medical device manufacturers are required to comply with if their products are sold and used within the European Union. Contained in the MDR is the requirement of ‘unique device identifiers’ (UDI) on all medical devices, as it was proposed in the European Union before the introduction of MDR [2]. Device identification as part of medical directives and regulations has been a part of the industry for many years and has been present on both a national and European level [3]–[5]. An initiative which has been transferred to the MDR is the concept of Materials Vigilance [5], where a device identification database will enable swift reactions in the event of product recalls. This is still an essential requirement of the industry. The responsibility of materials vigilance and application of UDI lies with the original manufacturer of any medical device.

Currently, manufacturers are required to apply UDI on all medical devices, but for different levels of packaging. There is a general preference for UDI on the lowest level of packaging, which would be direct product marking. This is not a requirement for all types of products, but there is a tendency towards this in case more restrictive requirements are formulated. Medical devices for single use where the user is generally aware of how to use it, such as staples, sutures, etc., must have UDI on the bulk packaging level and not on the individual device. An example would be UDI on a box containing many medical staples. Devices for multiple use should have UDI applied directly on the product but can be exempt if there is no space for a meaningful application of UDI, or if the application of UDI endangers the functionality of the product and thereby the patient. The UDI must then be applied to the next level of packaging, which usually entails the packaging of a single device. Implantable devices can be exempt from UDI, but there is, as mentioned, a general trend in the industry to warrant traceability on all products and UDI markings have historically been applied on implantable devices in orthopedics. The UDI has in relation been determined as the cause of failures. Due to the flexibility, speed, and the perception of permanence and immunity to tampering, laser marking has become the industry standard for applying UDI directly on products [6]. Interaction of a laser with a metallic substrate can be used to (locally) provide a dark surface layer for contrast. Unfortunately, demands for laser marked UDI on medical devices have moved significantly faster than research on the subject, and only little known about the consequences of laser marking and the risk for premature product failure.

Medical device manufacturing company Elos Medtech is one of the manufacturers with the responsibility of applying UDI on both packaging and directly on the products. They produce both surgical tools and implantable devices, mainly for dental applications. They have experienced challenges regarding corrosion resistance and retaining the color strength of the laser marking on certain stainless-steel grades. Laser marking is the last step of the manufacturing process, just before cleaning/sterilization and packaging. Manufacturing typically consists of a process chain including several machining steps and surface/heat treatment. As such, when the laser marking fails, and the manufactured devices are discarded it is expensive and time consuming. Therefore, there has been a general need for knowledge and understanding of the laser process and its influence on corrosion resistance and other properties, as well as the interplay with the other processes involved. There was a need to develop competences within the subject regarding the most common metallic materials for medical devices, titanium alloys and stainless steel. This led to Elos Medtech pursuing collaboration with the Technical University of Denmark with the support of Innovation Fund Denmark, to define a research project for an industrial Ph.D.

1.2. Stakeholders and Objectives

This project was established as a collaboration between the Technical University of Denmark, Elos Medtech and funding was provided by Innovation Fund Denmark. It was established via the industrial Ph.D. program managed by Innovation Fund Denmark under the case number 9065-

00210B, where it is co-financed by both Innovation Fund Denmark and Elos Medtech. It is in the nature of such a collaboration that the research output should be both industrially and academically relevant. In this case, industrially relevant entails the formulation of solutions and directly applicable knowledge, while academically relevant output entails high quality research which expands knowledge on the subject and can potentially be published in the scientific journal literature.

The work in this project is mainly be related to the laser marking process. The goal was to explore known issues related to the laser marking process and to provide solutions or mitigation strategies based on the results of a scientific investigation. This was specifically directed at instances of corrosion on laser marked stainless steel. It was also expected that there would be a general investigation of laser marking and its influence on other materials and properties. This would reveal additional challenges to which mitigation strategies were also required. The research entail types of metallic materials already utilized for manufacturing within Elos Medtech. The anticipated results are of scientific relevance and provide a basis for Elos Medtech to improve the quality of their products and ensure the ability to deliver safe products with quality UDI.

1.3. Outline

The work performed throughout the Ph.D. studies is presented in manuscripts which are either published in scientific journals or ready for submission. Some work is presented as a supplementary chapter and contains sections presenting methods, results, interpretation, and a discussion section.

Chapter 1 provides an initial introduction chapter, that documents the background and motivation behind the project, as well as a description of stakeholders and following those, the objectives, purpose, and anticipated outcomes of the project. A state-of-the-art and literature review is presented in chapter 2, providing the theoretical background to the results and methods presented in the manuscripts. Chapter 3 to 7 contains the experimental results and interpretations which makes up the bulk of the thesis. Laser marking guidelines for industrial purposes are presented in chapter 8. Finally, a summary of the most important results and conclusions is presented in chapter 9. An illustration of the outline is given in Figure 1.1.

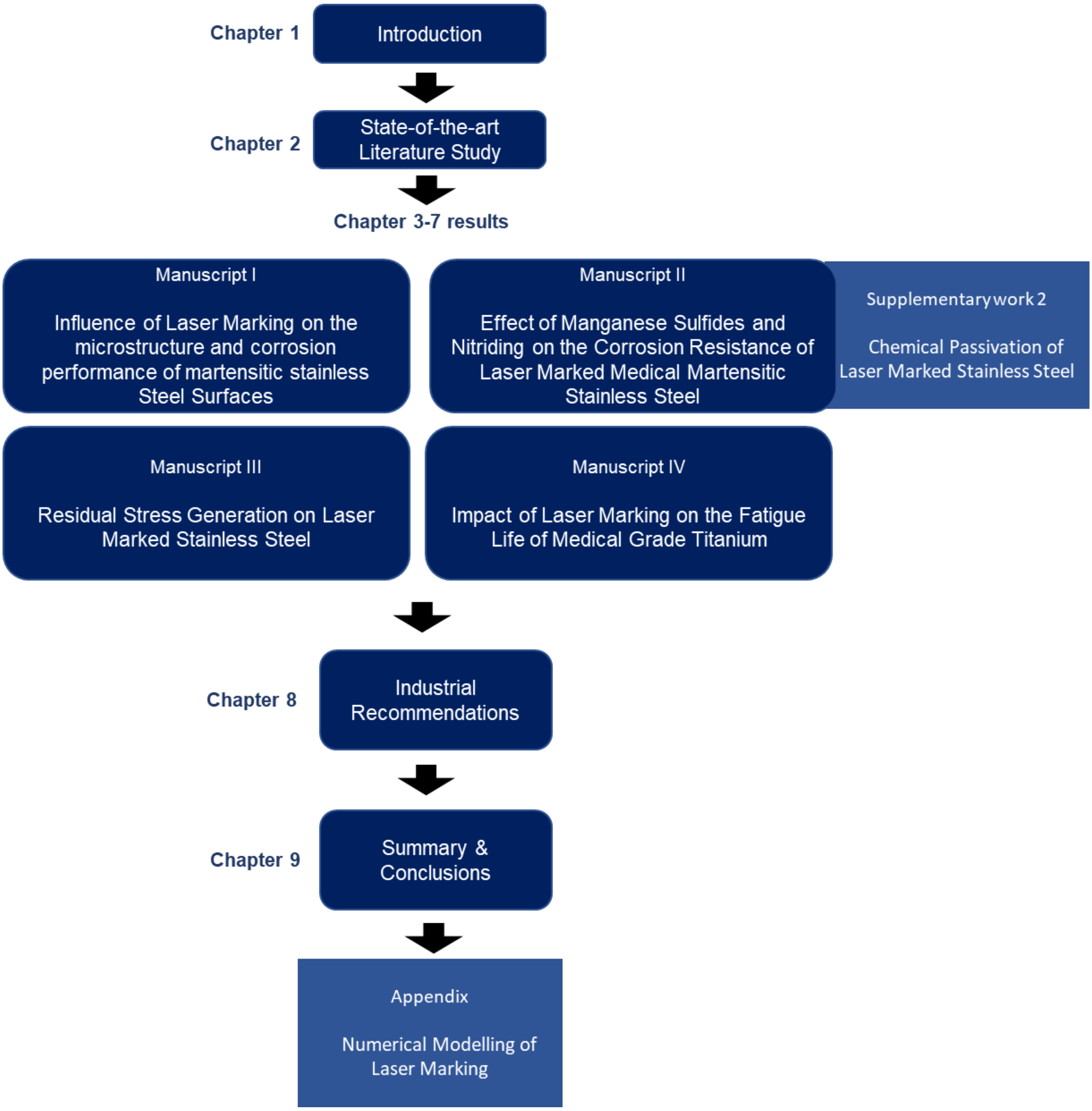

Figure 1.1: A diagram showing an overview of the structure and content of the thesis.

1.4. References

[1] European Union, Regulation (EU) 2017/745 of the European Parliament and of the Council on Medical Devices, amending Directive 2001/83/EC. 2017.

[2] European Union, “The European Commision, Commision recommendation of 5 April 2013 on a common framework for a unique device identification system of medical devices in the Union,” *Official Journal of the European Union*, Apr. 2015.

[3] European Union, “Regulation of the European Parliament and of the Council on Medical Devices, and Amending Directive 2001/83/EC, Regulation (EC) No 178/2002 and Regulation (EC) No 1223/2009”.

[4] European Union, “Market surveillance and vigilance,” https://health.ec.europa.eu/medical-devices-sector/directives/market-surveillance-and-vigilance_en, Nov. 21, 2022.

[5] P. Tracol, “Materials vigilance and traceability,” *Orthopaedics & Traumatology: Surgery & Research*, vol. 102, no. 1, pp. S95–S103, Feb. 2016, doi: 10.1016/j.otsr.2015.05.013.

[6] R. Hack, “State of the art in fiber laser making,” L. N. Durvasula, Ed., Jul. 2003, p. 202. doi: 10.1117/12.484175.

2. Literature Study and State of the Art

2.1. Medical Device, UDI, and Traceability

2.1.1. Medical Device

Medical device is an umbrella term describing everything from medical staples and syringes, to implants and surgical tools. At Elos Medtech in Denmark, the main production consists of dental implantable medical devices and surgical tools for dental applications. Surgical tools are manufactured in both titanium and stainless steel and for dental applications this would include tools such as torque wrenches for implantation of dental prostheses, and bone mills for drilling bone. Tools requiring high strength and good wear properties such as the bone mills are manufactured primarily in stainless steel. Dental implants are manufactured exclusively in titanium to utilize its corrosion resistance, biocompatibility, and high potential for successful osseointegration [1], [2]. A typical fixed implant consists of one or more screws/abutments inserted into the jawbone, which will provide a fixture for a porcelain crown or a bridge containing several crowns. The medical device industry is already a large market, but it is expected to grow due to the increase in life-expectancy of the world's population [3], [4].

There is a distinction between reusable and single-use medical devices. Staples and such are single use only, while a torque wrench for dental surgery is considered multiuse. Multiuse devices must of course be sterilized and/or disinfected between uses, whereas single-use instruments are sterilized before packaging if needed. These sterilization/disinfecting techniques have historically consisted of immersion in saline solutions, moist autoclavation and chemical sterilization [5], [6]. Modern methods utilizing radiation and ozone gas are also emerging [7]. Other distinct types of medical device could be long time invasive devices, which are different from permanent implants. These are still considered single use.

In Figure 2.1 a few examples of metallic dental medical devices are presented. Figure 2.1a illustrates a typical titanium-based implant system, with a screw inserted into the jawbone and an abutment with a porcelain crown on top, resembling a tooth. Figure 2.1b shows a similar type of implant with a fractured screw, while Figure 2.1c shows an Elos Medtech torque wrench of the type used to mount a dental implant. The head of the torque wrench is manufactured from stainless-steel while the body is made of either steel or titanium.

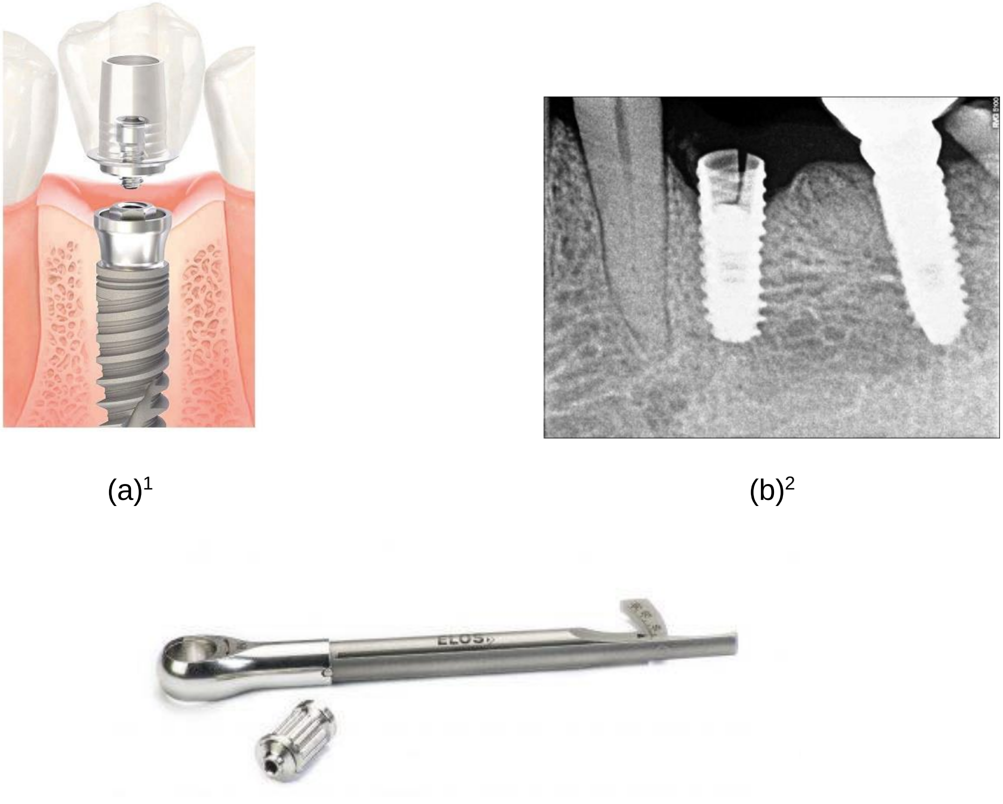

(a)[1]

(b)[2]

(c)[3]

Figure 2.1: Examples of metallic dental products illustrating (a) A typical dental implant system, (b) a failed dental implant, and (c) an Elos Medtech torque wrench for dental application.

---

[1] Credit to F. Soares et. al. (Soares et al., 2021)
[2] Credit to A. Tunkiwala and U. Kher (Tunkiwala & Kher, 2019)
[3] https://elosmedtech.com/products/instruments/ visited 09.12.2022

2.1.2. Traceability in Medical Device

The advantages of applying full traceability on medical devices are clear, especially regarding recalls and ensuring high quality products which do not jeopardize the health or safety of patients. It is mandatory to report any failed medical device, whereas health authorities could demand recalls or investigations of certain batches or products. Traceability is also utilized before surgery for information about compatible instruments for removal of implant as well as suitable replacements [8]–[10]. This is the concept of materials vigilance, and it requires full traceability of the product [11], [12]. Wilson et. al. projected that significant man hours and extensive money will be spent on identifying failed implants, constituted partly from the increase in implants [9]. This is based on data from the United States, which indicates that failed implants for knee and hip arthroplasty that cannot be identified may exceed 25.000 in the USA alone. In parallel, it has been projected by Elani et. al. that there will be a significant increase in dental implants, with an average increase of 14 % per year until 2026 [13]. Accordingly, there is a large economic incentive to implement full traceability along with the arguably more important incentive from patient health.

Traceability on medication has statistically been proven to reduce the risk for errors substantially. The implementation of barcodes during administration of medication reduced the relative risk errors by 41 % [14]. Some medical fields may benefit more than others. Plastic surgery was significantly behind in traceability of implants, so information about the implants would not necessarily be retrievable after implantation [8]. Statistics is a powerful tool in medical science, to which post market surveillance included in full traceability and materials vigilance would contribute greatly [15].

By keeping careful databases and ensuring registration of medical devices with serial numbers or barcodes, full traceability can be fulfilled. Traceability has even been used in situations where implants have been the determining factor to identify otherwise unidentifiable bodies in forensics science [16]. The potential of the UDI database is huge. For statistical purposes, the materials and their composition of implantable devices could be included (chromium, cobalt, titanium) and for other types of devices, known allergenics could also be included. This is currently not the case [17], but the industry is moving in the right direction, motivated by medical regulations.

2.1.3. Unique Device Identification

For some years now, the medical device industry has been moving towards a harmonized traceability system on an international scale. The system consists of unique device identification markings (UDI) and databases with device information. In another study by Wilson [18], this framework has been shown to be the best practice in orthopedics where implants had to be identified. The average time spent on identification was 20 minutes, where in 10% of the cases, identification had to be done intraoperatively. However, just applying UDI is not enough to ensure traceability, the codes must also regularly be scanned (or typed manually) and stored electronically, which represents a challenge for effective implementation [19], [20]. It is largely the case that legislations moved faster than what manufacturers could adapt [21]. This is also the case for research around the subject of applying UDI.

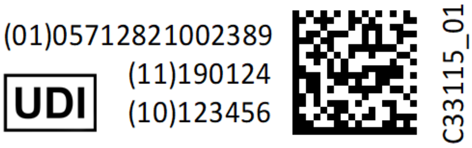

Figure 2.2: An example of a UDI label applied in Elos Medtech.

An example of a UDI label is given in Figure 2.2, showing the unique code (01) for the device, manufacturing date (11), and the manufacturer code (10). A QR code is attached for quick scanning of the information. There are two major regulatory bodies demanding traceability in Europe and the United states, which are respectively the European Union and the FDA [22]–[25]. The purpose of implementing UDI was to provide a common framework for traceability, initially for the European Union and later globally. At the time of writing, MDR dictates that UDI must be applied on the lowest level of packaging as well as all higher levels if applicable. The lowest level of packaging for implantable devices would be in unit packs, but it is both allowed, and not uncommon to mark implants directly. For reusable devices, the direct marking is mandatory if it is technologically feasible and does not endanger the patient.

2.2. Materials in Medical Devices

The medical device industry utilizes many different materials for biomedical applications, such as the more conventional steel, cobalt-chromium alloys, and titanium alloys, as well as polymers [26]. Stainless steels are routinely applied as temporary implants [27] but rarely as permanent implants due to the lower corrosion resistance than titanium and cobalt-chromium alloys. Cobalt-chromium alloys are the most common material for total joint replacement [27]. This is motivated by the good corrosion and wear performance of cobalt-chromium alloys, whereas wear performance is the Achilles heel of titanium alloys [28], [29]. Titanium is utilized for most other permanent implants [30]–[32], since it boasts full biocompatibility and good corrosion resistance, as well as great properties for osteointegration [2]. Additionally advanced biomedical materials and nanostructures/surface treatments are utilized in the field of dental implants. This is the main topic of advancements in dental implant materials, as it can potentially improve osteointegration and increase the overall quality of the implant-bone interface [33]–[36]. The two main materials in this project, titanium alloys and stainless steel, are described in further detail below.

2.2.1. Stainless Steel

Stainless steel is commonly used as the material for surgical tools. This is due to the fact that it does have decent biocompatibility and high strength, which is required for some surgical applications. It also boasts high resistance to oxidation, meaning it can usually withstand the different sterilization techniques utilized in the medical and dental fields [37]. It is commonly agreed upon that steel becomes stainless by addition of chromium of more than about 11 wt% of the total chemical composition. Other alloying elements are common such as the austenite-stabilizing element nickel as well as nitrogen and molybdenum for enhanced corrosion resistance [38], [39].

The crystal structure of stainless steel is usually either face centered cubic (FCC) referred to as austenite, see Figure 2.3a. or body centered cubic (BCC) referred to as ferrite, see Figure 2.3b. For most steels, there is a phase transition from BCC to FCC at higher temperatures. The addition of nickel, or elements with an equivalent effect, can lower this temperature and, in some cases, stabilize FCC at room temperature. Alloying elements of stainless steel can be divided into two categories, substitutional and interstitial. Substitutional alloying elements are typically chromium, nickel or other atoms of comparative size to iron and substitute iron atoms in the lattice. Interstitials on the other hand, are typically the smaller elements such as oxygen, carbon and nitrogen and are positioned in the empty spaces in-between the atoms in the crystal lattice [40].

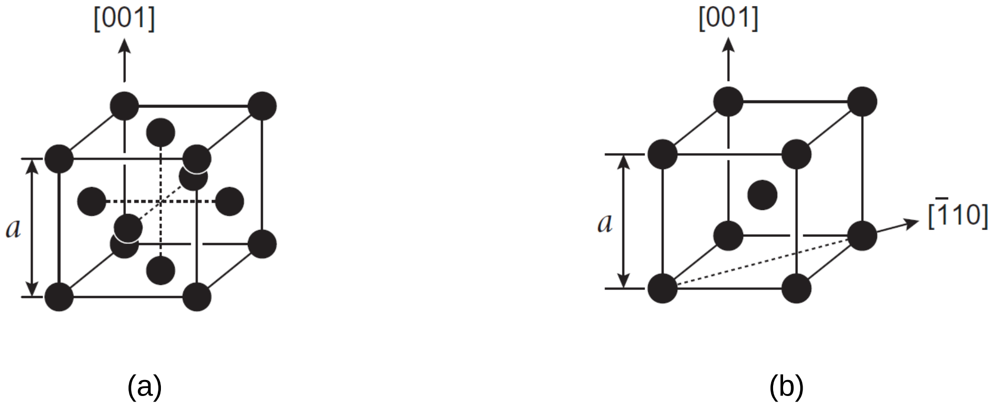

(a) (b)

Figure 2.3: Illustrations of the crystal structure of (a) FCC and (b) BCC [41].

The crystal structure and thereby type of stainless steel can be predicted based on the alloying elements, by utilizing Schaeffler diagrams. An example of a Schaeffler diagram is found in Figure 2.4, illustrating the effects of alloying elements on the resulting crystal structure at room temperature [42]. Elements are divided into two categories: FCC stabilizing Ni-equivalents, and BCC stabilizing Cr-equivalents. The Schaeffler diagram nicely outlines typical compositions austenitic and martensitic stainless steels, which are the most commonly used steels for biomedical applications [43].

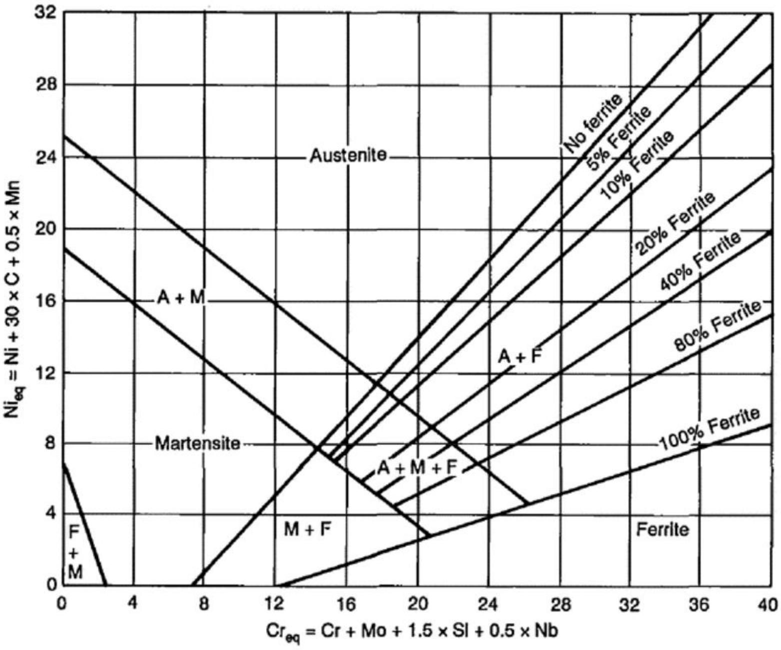

Figure 2.4: Schaeffler diagram for stainless steel [42].

There are several sub-categories of stainless steel, largely depending on alloying elements and hardening mechanisms [44]. Most common in the medical device industry are the austenitic stainless steels, which would include the common AISI 304L and 316L. These steels contain a high amount of chromium (16-20 wt%) and nickel (8-10 wt%), to ensure stainless properties and a metastable austenite phase. Due to the allergic reactions that nickel can provoke [45]–[47], there is some concern regarding applying these steels where metal ions might be released in the body. Because of this there is currently a trend to develop high nitrogen steels for the medical device industry, as nitrogen will also stabilize austenite but does not possess the toxicity associated with nickel [48], [49].

When high hardness and strength are required, martensitic stainless steels as well as precipitation hardening or maraging steels are also utilized for medical device. The advantages of such materials compared to their austenitic counterparts is that they can and should be hardened [50], meaning parts can be manufactured in an annealed state where the material is relatively soft. The machined parts can then be heat treated to increase the strength significantly. Martensitic stainless steels are hardened by inducing a martensitic transformation from austenite to ferrite, typically via a quenching from an austenitization temperature and a subsequent tempering treatment. At lower cooling rates, the phase transformation from FCC to BCC takes place via diffusion of interstitials (mainly carbon) [51]. The martensitic transformation takes place within such short timeframes, that diffusion does not occur, rendering the transformation diffusionless. This results in a metastable BCC (or tetragonal) crystal structure which is supersaturated with substitutional and/or interstitial elements. During tempering the elements in supersaturated condition precipitate. If these are interstitials, carbides or nitridies form, sacrificing some strength for a more ductile material. If the precipitating elements are essentially substitutionals, the martensite was soft and gains its hardness/strength from precipitation hardening. Typical heat treatments for stainless steels are illustrated in Figure 2.5.

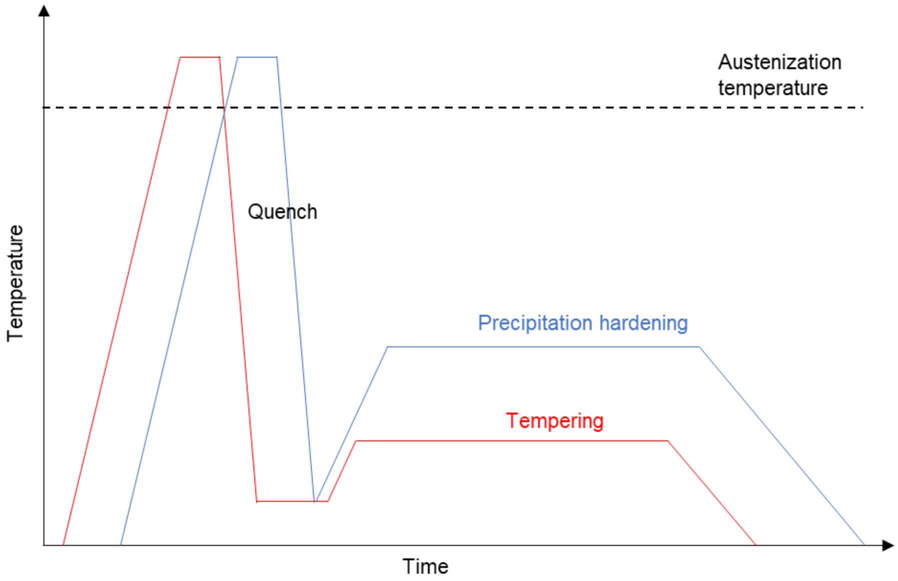

Figure 2.5: An illustration of typical heat treatments for a martensitic stainless steel (red) and a precipitation hardening steel (blue).

The stainless properties of stainless steel rely on the high chromium content, and corrosion resistance generally scales with higher contents of chromium. Other elements, such as nitrogen and molybdenum, also have a positive effect on corrosion, as reflected by the pitting resistance equivalent number (PREN) [52]. Chromium is a self-passivating metal, just like aluminum and titanium. This behavior results from the high reactivity with oxygen to form a passive layer of Cr_2O_3, which retards further ingress of oxygen or outdiffusion of Cr. This passive layer is so effective that at room temperature it will grow to only 5-25 nm of thickness for most stainless steels [53].

2.2.2. Titanium Alloys

Titanium is the choice material for implants due to its full biocompatibility, meaning that it is not toxic upon contact with human cells. Further, it has a low elastic modulus, and depending on the alloy, a modulus close to that of bone [54], [55]. In the biomedical field, in particular the titanium alloys designated as commercially pure (CP) are utilized, as well as the titanium alloy of Ti6Al4 for higher strength. In addition, certain alloys with zirconium and niobium have found their way into orthopedics [56]. Analogous to steel, metallic titanium exists mainly in two allotropic forms: α-titanium with a hexagonal close packed (HCP) crystal structure and at higher temperatures (>882°C for unalloyed titanium), it will form β-titanium with a BCC structure [57], [58]. Illustrations of the crystal structures can be seen in Figure 2.6. CP-titanium belongs to the so-called α-alloys based on their predominant HCP crystal structure. Similar to stainless steel, the crystal structure at room temperature can be predicted based on alloying elements. A Schaeffler diagram can be constructed from the HCP stabilizing Al-equivalent and BCC stabilizing Mo-equivalent [59]. Alloys containing large amounts of β-stabilizers such as Niobium and Vanadium, have a predominant BCC crystal structure, referred to as β-alloys[56], [58]. The Ti6Al4 which is an α-β-alloy, contains some amount of β-phase in an α-matrix, enhancing the mechanical properties [60], [61], placing it as the most utilized titanium alloy for high strength applications [56]. The development of this α-β-alloys enabled the use of titanium in applications where the CP-alloys failed. Titanium gained attention, when the biocompatibility was demonstrated in animal testing in the 40’s and 50’s [62], [63], but due to the lower strength than steel and its poor wear qualities, applications were limited to implantable devices with little to no mechanical demands, until the development of Ti6Al4V [64]. However, in the last decade there has been a trend of development in titanium alloys, to produce high strength CP-alloys, to avoid potentially toxic alloying elements, such as Al and V. This is done by modifying the microstructure to form ultrafine grains so CP-alloys can be used in applications were Ti6Al4V is traditionally used [65].

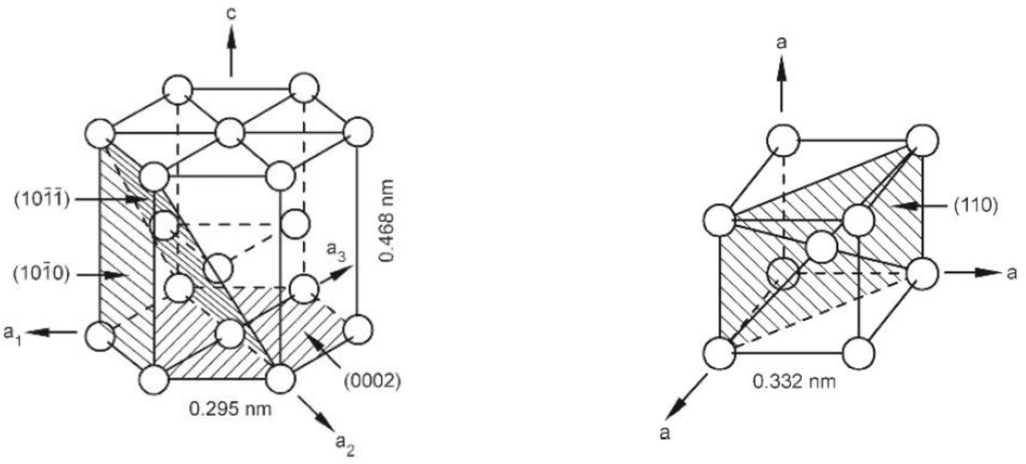

(a) (b)

Figure 2.6: Illustrations of crystal structures of (a) HCP α-titanium and (b) BCC β-titanium [58].

In many industries, titanium is utilized because of its high strength-to-weight ratio, such as the aerospace industry [66], but in biomedical applications, it is the high corrosion resistance and biocompatibility that motivates the choice for titanium [1], [2], [64], [67]–[70]. Titanium is like stainless steel and aluminum, a self-passivating material, due to its high reactivity [58]. Titanium reacts very strongly with oxygen, forming TiO_2, the corrosion resistance is excellent in most environments where oxygen is present [71], including environments which would in many cases be considered as aggressive, such as oxidizing acids [72]. To cause uniform corrosion in environments where TiO_2 is no longer stable, the environment must be strongly reducing, e.g., strongly acidic like HF [73]. Even if there is a general high corrosion resistance among titanium alloys, there is an important effect of alloying elements. The wear resistance of titanium is lacking as compared to steel, as has been known since the metals commercial debut [74]. CP-titanium and Ti6Al4V exhibit poor wear resistance in most sliding wear tests and are susceptible to fretting, crack formation and peeling during wear situations. Of course the tendency to form a passive layer rather quickly, renders the alloys vulnerable to tribo-corrosion which can accelerate the material loss rate substantially [75]–[77], meaning it is not the choice material for implant applications where wear is expected, such as joint replacement implants.

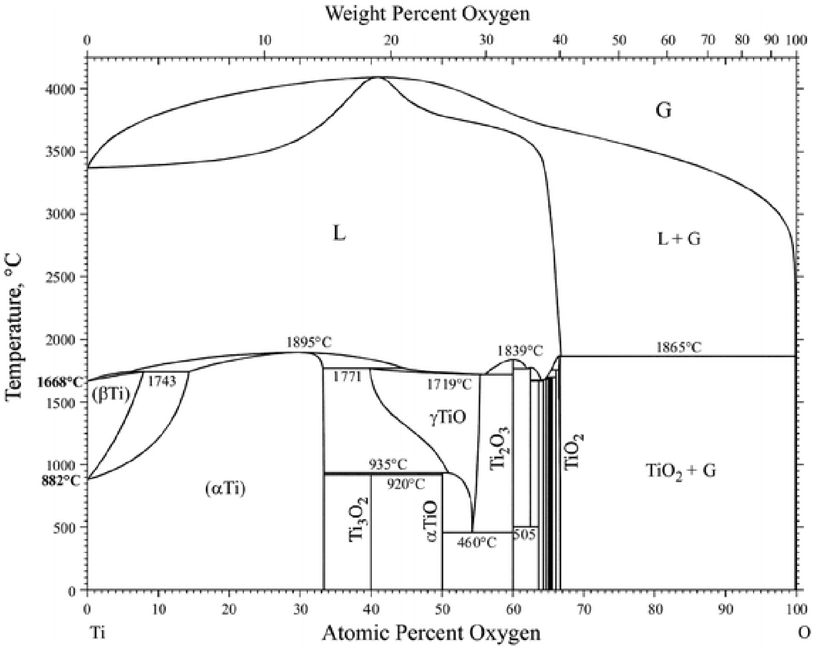

Figure 2.7: A binary phase diagram of titanium and oxygen [57].

The high reactivity of titanium with oxygen is further expressed as a high solubility and an abundance of oxides, as illustrated on the phase diagram in Figure 2.7. A large quantity of oxygen can be dissolved, up to 34 wt%, before oxide formation takes place. An abundance of oxides is stabilized between 63-67 wt% oxygen, commonly referred to as Magnéli phases, before the formation of TiO_2 [58]. TiO_2 is the most common and stable oxide which is the compound that the passive layer will consist of.

2.3. State of the Art in Laser Marking

The first fiber lasers were showcased in 1973 at AT&T Bells Labs but had little commercial success due to the expensive production of the necessary crystal fibers and inefficient technology [78]. Today, the technology of laser marking has developed substantially and is a competitive choice among other product marking methods, such as dot peening, ink-jet printing, and electrochemical etching [79]. The success is a consequence of the high degree of flexibility, automation and reliability. The technology has also been marketed as a greener alternative to marking with ink-jet printers, as no waste is produced during marking [80]. Modern fiber lasers operate at 5-25 W and can do so for >10,000 hours with little to no maintenance [79]. While there are different laser technologies, fiber lasers are the preferred type [81], and specifically for metals the neodymium-doped yttrium aluminum garnet (Nd:YAG) pulsed fiber lasers are preferred [82] for the high absorptivity of the generated wavelength. These types of fiber lasers utilize a wavelength of 1064 nm, while the next most common laser, the CO_2 laser, emits a wavelength of 10600 nm. Pulsed lasers are further categorized by their pulse length, with the most common categories in descending pulse length nanosecond-, picosecond- and femtosecond pulsed lasers. Traditionally, nanosecond pulsed lasers have been used in industry, but in the past few years, substantial progress has been achieved in laser marking with shorter pulses [83]. An overview of the marking applications of fiber lasers in modern industry after Lazov et. al. is given in Table 2.1.

Table 2.1: An overview of modern marking applications of fiber lasers. Adapted from [79].

Purpose	**Result**
Oxidation/Diffusion	Color change
Bonding	Relief image generation
Melting	Relief image generation
Evaporation/ablation	Channel formation or layer removal
Heating	Thermo- or photo structures

As the purpose of laser marking in relation to UDI can be reduced to the formation of contrast, there are obviously several ways of achieving this. In the medical industry, mainly three of the methods listed in Table 2.1 are utilized for metallic substrates: Ablative laser marking, oxidative laser marking, and evaporation of a surface layer. By far the least utilized method is the ablation of a surface layer, where a surface of a different color than the substrate is locally removed via laser to form contrast. This layer could be black diamond-like carbon or golden Titanium Nitride. Ablative laser marking generates contrast without forming an oxide layer by locally melting and evaporating the substrate, thereby generating a surface roughness contrast, usually appearing white on a metallic surface. Oxidative laser marking is the method of choice in this thesis, as it is the most widely used method. The dark markings generate high contrast and are perceived as permanent. They are applied by heating the material locally to promote reaction and diffusion of oxygen, most commonly in atmospheric air [78], [79]. It is a widely used technology on metallic components to produce traceability in the form of permanent markings. This is not only applied on ferrous and titanium alloys but has also been successfully implemented for other metals such as magnesium, lead, nickel and tin [84].

As the laser marking process can be adjusted via many different parameters, such as scan speed, laser power, pulse frequency, pulse length and the marking pattern, Švantner et. al. and Chen et. al. had success investigating the effects of laser marking using two main dependable parameters; peak power density, P_p, (W/area) and heat input, E_s, (J/area) [85], [86]. They propose the following equations:

$$P_p = \frac{E_p}{A \cdot t_p} \tag{2.1}$$

$$E_s = \frac{P}{v \cdot l_s} \tag{2.2}$$

For both martensitic and austenitic stainless steel it has been shown that the generated oxide layer consists of chromium containing oxide, either Cr_2O_3 or $[Fe,Cr]_3O_4$ spinel [87]–[89], however several authors reported the identification of Fe_3O_4 and/or Fe_2O_3 [87], [90]. It should be noted that the majority of research on laser marking has been performed for the most common austenitic stainless steels AISI 304 and 316. It was found that the laser process could be switched between ablative and oxidative marking by changing the power density of the laser, while the heat input has been related to the color strength, thereby the oxide layer thickness, of oxidative marking [86], [90]. Some authors relate the resulting oxide layer thickness on various substrates to more fundamental parameters which directly affects the heat input, most commonly the scan speed and pulse frequency [91]–[93]. By varying the heat input the mentioned authors created different morphologies and thicknesses of the oxide layer on stainless steel, making the point that the visual appearance of the oxide layer depends strongly on the parameters.

Brihmat-Hamadi et al. investigated the oxide layer on titanium laser marked with a nanosecond pulsed YAG fiber laser, and identified the formation of the oxides TiO, Ti_2O_3, and TiO_2 [94]. Adams et. al. performed oxidative laser marking and characterized thin oxide layers of 10-120 nm, showing the presence of TiO_2, TiO and an inhomogeneous layer of TiO_xN_{1-x}, confirming nitrogen uptake when laser marking in atmospheric air [95]. With the high degree of control, which is inherent to laser marking, the oxide layer thickness can be controlled to a very high degree, opening up the possibility of applying interference colors on the substrate. It has been successfully performed by several authors on both titanium and stainless steel substrates [81], [94], [96]–[100]. Chen et. al. color marked both stainless steel and titanium by carefully controlling the heat input of the laser, while limiting the power density to avoid melting. They found that nitrides were formed in both materials in addition to the oxides [96].

The interaction between substrate and the laser can also complicate the laser marking process in both modes of operation. The actual power of the laser depends strongly on the absorption of the substrate, known as laser fluence, at the applied wavelength, which in turn depends on the substrate surface. The fluence will not be constant during the course of marking and will change both with temperature and when oxides form on the surface [87], [101], [102].

Although nanosecond pulsed lasers are currently the most commonly applied technology, in recent years lasers utilizing shorter pulses have gained traction, namely the pico- and femtosecond lasers [103], [104]. A review study of laser ablation processes to form nano features was performed by Lei et. al. [103]. They found that for nano-sized features, the ultra-short pulse lengths (femto- and picosecond) produced smoother features than for the conventional nanosecond lasers. They attribute the better results to the focused beam and the small interaction lengths, which limit the thermal diffusion to the surrounding material even in metals [104]. Femtosecond lasers have also been shown to produce black laser markings on metallic substrates, however not by oxidative laser marking. Without forming a color-giving oxide layer, light trapping nanostructures are formed, resulting in absorption of light in the visible spectrum, comparable to- or larger than what is achievable for oxidative laser-marking [105]. The authors of the mentioned papers mention the picosecond laser as an alternative to nanosecond laser, as the resulting black markings are more corrosion resistant. Rusu et. al. investigated the effect of femtosecond laser marking relative to conventional nanosecond laser marking on titanium alloys [106]. They found that for the lower interaction time, there was little to no change in microstructure and only superficial oxidation. No difference between marked and unmarked specimens were found via X-ray diffraction, further supporting the hypothesis that the effects are purely superficial.

For information on the thermal fields and melt pools generated by pulsed nanosecond laser marking in stainless steel, please see appendix, where a simulation of the laser marking process is presented and validated experimentally for stainless steel.

Oxidative laser marking is essentially a local thermochemical surface treatment and is far from the only surface treatment where lasers are utilized. Historically, lasers have been utilized to perform surface hardening by melting the surface of iron-based alloys. The dissolution of carbides at high temperatures and the inherently high cooling rates lead to the formation of new martensite in the surface region [107], [108]. This martensite will have a high hardness and improves the wear resistance [109]. Lasers have been utilized for laser nitriding as well to improve material properties or to form surface layers. Especially relevant is the formation of TiN on titanium substrates, as it has been shown to have a positive effect on biocompatibility and tribological properties in orthopedics [110]. Höche et. al. outlines the nanosecond pulsed lasers as an option for laser nitriding, but highlights that the short interaction times do not allow long-range diffusion and therefore the nitrided layer will be relatively shallow [111]. Laser nitriding is also relevant for steels and other iron-based alloys. Schaaf has shown that a hardness and wear resistance increase, as well as an increase in corrosion resistance can be achieved via laser nitriding on several ferrous alloys [112]. Höche et. al. also outlines the process of laser carburizing of steel, as carbon is one of the most important alloying elements in steel [111]. Lasers have even been used to form layers of hard cementite on iron-based alloys [113]. As such, lasers are commonly used for surface treatments of metallic materials, however nitriding and carburizing are far more researched topics than laser oxidizing which will usually occur in a much less controlled atmosphere and is performed for the purpose of changing the appearance.

2.4. Corrosion in Laser Marked Medical Device

It is well-known in the industry that the markings produced via oxidative laser marking are not as permanent as initially thought. It is often seen that the markings fade after repeated autoclavation [104] or other cleaning processes. This is due to corrosion in stainless steel and there is a consensus of a general reduction in corrosion resistance in the marking. A reduction in corrosion resistance is almost always observed, but the severity depends on the chosen parameters [114]. Investigations on ablative laser marking on AISI 316L stainless steel, also indicated a reduction in corrosion resistance, but to a lesser degree than for oxidative laser marking [115]. There is however an indication that the effect on chemical composition, and in extension the corrosion resistance, can be minimized for ablative laser marking, yielding a generally better corrosion resistance than for oxidative laser marking [116]. P. Steyer also found that the surface was transformed into a favorable layer of austenite when performing ablative laser marking [116].

Several authors have identified chromium depletion in the material immediately underneath the formed oxide layer, identified to be caused by the formation of either Cr_2O_3 or $FeCr_2O_4$ [86], [89], [116], [117]. There is general consensus that during the formation of the black oxide, the sub-surface is depleted in chromium, resulting in a loss of the passivating ability which jeopardizes the character of stainless steels. It is consistent with regular thermochemical heat treatment of stainless steel, where one would expect the first formed oxide to be based on the element with the highest oxygen affinity (Si, Cr), followed by outer layers of oxides with lesser thermodynamic stability, i.e. higher Gibbs energy of formation than Cr_2O_3 [118]–[120]. The same has been found for laser color oxidizing, which is usually a longer process allowing a better comparison to conventional oxidation [121]. Li et. al. identified an inner layer of Cr-oxide and an outer layer of Fe-oxide, after color oxidizing AISI 304 stainless steel [122]. This presents a paradox regarding the generation of thick high contrast oxide, which must be both corrosion resistant and readable by certain automatic equipment. This paradox suggests that in the oxidative regime of laser marking, the determining parameter for both corrosion resistance and color strength is the heat input, shown in equation (2.1) [83], [86], [88], [90], [116].

2.5. Chemical Passivation

Chemical passivation in the medical device industry is widely used, to enhance the inherent corrosion resistance of stainless steel. The concept is to ensure a coherent passive layer, with no initiation points for pitting corrosion, which is known to occur in points where there is a weak point such as a gap or particle interrupting the oxide layer [123]. The process of chemical passivation has been applied to dissolve free iron particles embedded in the surface of machined components, or selectively remove iron oxide instead of chromium oxide, which would be pitting initiation sites [124]. For many years, chemical passivation has been performed with nitric acid, which would dissolve impurities and enable oxidation to form the passive layer of Cr_2O_3 [125]–[128], but principally any oxidizing acid could be utilized. The effect of different acids was investigated by Laoire et. al. and showed that the ratio of Cr:Fe increased in the surface for chemical passivation performed with both nitric and citric acid [129]. Li et. al. has recently shown that both the general corrosion resistance and the pitting corrosion resistance are enhanced [127], [130]

For some time now, the industry has been moving towards citric acid passivation instead of the conventional nitric acid passivation [131]. The motivation behind this is the clear environmental advantages of citric acid and the reduced health/accident risks when handling the chemicals [132]–[134]. Citric acid is a much weaker acid and can be freely added to food without health risks, while nitric acid is a strong acid which can be a serious health risk upon contact with liquid or vapor and has stricter requirements for waste handling [132].

Comparing nitric- and citric acid passivation, most authors observe similar or even improved corrosion resistance after citric acid passivation, via electrochemical measurements [135]–[139]. Da Costa et. al. investigated the composition of the passive layer on AISI 316L stainless steel, after citric acid passivation at different levels of citric acid concentrations [138]. They found an increase of Cr_2O_3, which translates to a higher corrosion resistance, by increasing the acid content at concentrations from 10-20 wt%. At higher acid concentrations, they instead found a decrease of Cr_2O_3, indicating that high acid contents are instead harmful to corrosion resistance, as the passive layer is dissolved.

Even if titanium is perceived as the pinnacle of biomedical materials with excellent corrosion resistance, it is still commonly cleaned and passivated in HCl. Citric acid passivation has also been investigated as an alternative on titanium-based alloys. Verdeguer et. al. showed that citric acid improved the corrosion resistance and acted as a bactericide compared to HCl and is a viable chemical to treat titanium-based products before application [140].

2.6. Fatigue Strength

Fatigue in metals is the concept of progressive weakening after cyclic loading of the material. The applied load can result in either tensile or compressive stresses. In relation to fatigue strength, it is the tensile stresses which are of particular importance [141]. This progressive degradation takes place in the form of a crack which will develop and be responsible for a final fracture. There are three stages to fatigue damage: Crack initiation, crack propagation, and fracture. Crack initiation is by far the longest stage and will happen earlier in geometries where a stress concentration is present during loading [142]. In bending fatigue testing, a notch is sometimes created in the material to simulate such a geometry. However, the sensitivity of a material to notches is also largely affected by the direction of the applied load [143]. After crack initiation, the crack will grow a little with each load cycle, as the crack itself acts as a site for stress concentration, causing plastic deformation at the tip for each load cycle. [141], [142]. The factor of stress concentration depends strongly on the crack length, and eventually a critical stress level is reached, causing the crack to grow fast, resulting in a fast (brittle) fracture.

Several factors influence the fatigue strength of materials and has been the subject of research for many years [144]. The general strength of the materials is important as it resists the crack propagation and increases the critical stress, while notches increase the likelihood for crack initiation. Other more subtle factors such as the microstructure are also of importance. Titanium alloys can be optimized for fatigue performance by ensuring a bi-modal microstructure to inhibit the deformation and crack growth, meaning features on the grain-level are of importance [145]. In a review performed of J. A. Hall on the fatigue crack initiation of α-β-titanium alloys it is estimated that 80-90 % of the fatigue life is the development of crack-like features to a size where they can be observed [146]. The author gives several recommendations on how to improve the fatigue life other than creating defect free components [145]. The α/β ratio can be optimized, and a finer microstructure with no macroscopic texture should increase the resistance to crack nucleation [146]. Ti6Al4V is generally performing better than the CP-titanium alloys regarding fatigue, however the performance of this strongly influenced by microstructure. The bi-lamellar microstructure of Ti6Al4V is reportedly performing worse than globularized microstructures [147].

For dental implants, certification of the fatigue strength and reliability is measured according to ISO 14801 [148]. It is the standard method for dental implants, as it describes the worst-case scenario, where force is applied on the implant during chewing, and where the implant is angled. Figure 2.8 shows a sketch of a generalized fatigue testing setup according to ISO 14801, where the specimen in placed in an angle of 30° to a piston which will apply pressure to simulate the patient chewing.

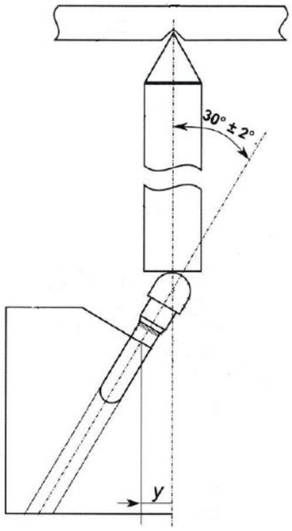

Figure 2.8: An illustration of a generalized setup of dental implant fatigue testing according to ISO 14801.[4]

The test can be performed either in air or in isotonic salt water. Many factors affect the performance of a dental implant such as mechanical properties, stress concentration factors as well as the geometry and dimensions of the implant system. Léon et. al. has via ISO 14801 shown that increasing the height of the crown lowers the measured endurance limit [149]. This is equivalent to increasing the arm length. The method is commonly used as a comparison between commercially established products and new developed technologies. It has been used to compare conventional titanium-based implants to biocompatible ceramics, showing insufficient fatigue strength in the otherwise promising ceramics [150]. It is also used in combination with numerical simulation to evaluate changes in implant system geometry [151].

---

[4] Adapted from [148].

2.7. References

[1] M. McCracken, “Dental Implant Materials: Commercially Pure Titanium and Titanium Alloys,” *Journal of Prosthodontics*, vol. 8, no. 1, pp. 40–43, Mar. 1999, doi: 10.1111/j.1532-849X.1999.tb00006.x.

[2] J. W. Nicholson, “Titanium Alloys for Dental Implants: A Review,” *Prosthesis*, vol. 2, no. 2, pp. 100–116, Jun. 2020, doi: 10.3390/prosthesis2020011.

[3] A. Festas, A. Ramos, and J. Davim, “Medical devices biomaterials <scp>– A</scp> review,” *Proceedings of the Institution of Mechanical Engineers, Part L: Journal of Materials: Design and Applications*, vol. 234, no. 1, pp. 218–228, Jan. 2020, doi: 10.1177/1464420719882458.

[4] A. Pandey and S. Sahoo, “Progress on Medical Implant: A Review and Prospects,” *J Bionic Eng*, Oct. 2022, doi: 10.1007/s42235-022-00284-z.

[5] I. Gurevich, R. Dubin, and B. A. Cunha, “Dental instrument and device sterilization and disinfection practices ,” *Journal of Hospital Infection*, vol. 32, pp. 295–304, 1996.

[6] S. Sreekumar, K. Varghese, J. Abraham, and J. Jaysa, “An in vitro evaluation of the efficiency of various disinfection and sterilization methods to decontaminate dental handpieces,” *Journal of Dental Research and Review*, vol. 5, no. 2, p. 50, 2018, doi: 10.4103/jdrr.jdrr_19_18.

[7] R. Mensudar and D. Amudha, “Newer Sterilization Methods,” *Biosci Biotechnol Res Asia*, vol. 11, no. 1, pp. 189–191, Apr. 2014, doi: 10.13005/bbra/1252.

[8] J. W. Aston, A. L. Howarth, N. A. Wilson, and R. C. Mahabir, “The Value of Unique Device Identifiers in Plastic Surgery,” *Aesthet Surg J*, vol. 38, no. 11, pp. 1264–1266, Oct. 2018, doi: 10.1093/asj/sjy210.

[9] N. Wilson, J. Broatch, M. Jehn, and C. Davis, “National projections of time, cost and failure in implantable device identification: Consideration of unique device identification use,” *Healthcare*, vol. 3, no. 4, pp. 196–201, Dec. 2015, doi: 10.1016/J.HJDSI.2015.04.003.

[10] N. A. Wilson, A. J. Reich, J. Graham, D. L. Bhatt, L. L. Nguyen, and J. S. Weissman, “Patient perspectives on the need for implanted device information: Implications for a post-procedural communication framework,” *Health Expectations*, vol. 24, no. 4, pp. 1391–1402, Aug. 2021, doi: 10.1111/hex.13273.

[11] European Union, “Market surveillance and vigilance,” *https://health.ec.europa.eu/medical-devices-sector/directives/market-surveillance-and-vigilance_en*, Nov. 21, 2022.

[12] P. Tracol, “Materials vigilance and traceability,” *Orthopaedics & Traumatology: Surgery & Research*, vol. 102, no. 1, pp. S95–S103, Feb. 2016, doi: 10.1016/j.otsr.2015.05.013.

[13] H. W. Elani, J. R. Starr, J. D. da Silva, and G. O. Gallucci, “Trends in Dental Implant Use in the U.S., 1999–2016, and Projections to 2026,” *J Dent Res*, vol. 97, no. 13, pp. 1424–1430, Dec. 2018, doi: 10.1177/0022034518792567.

[14] E. G. Poon *et al.*, “Effect of Bar-Code Technology on the Safety of Medication Administration,” *New England Journal of Medicine*, vol. 362, no. 18, pp. 1698–1707, May 2010, doi: 10.1056/NEJMsa0907115.

[15] Kathleen Blake, “Postmarket surveillance of medical devices: current capabilities and future opportunities,” *Springer Science+Business Media New York*, Mar. 2013.

[16] M. M. Blessing and P. T. Lin, “Identification of Bodies by Unique Serial Numbers on Implanted Medical Devices,” *J Forensic Sci*, vol. 63, no. 3, pp. 740–744, May 2018, doi: 10.1111/1556-4029.13598.

[17] M. Kinard and L. McGiffert, “Medical Device Tracking—How It Is and How It Should Be,” *JAMA Intern Med*, vol. 181, no. 3, p. 305, Mar. 2021, doi: 10.1001/jamainternmed.2020.7797.

[18] N. A. Wilson, M. Jehn, S. York, and C. M. Davis, “Revision Total Hip and Knee Arthroplasty Implant Identification: Implications for Use of Unique Device Identification 2012 AAHKS Member Survey Results,” *J Arthroplasty*, vol. 29, no. 2, pp. 251–255, Feb. 2014, doi: 10.1016/j.arth.2013.06.027.

[19] N. A. Wilson, J. E. Tcheng, J. Graham, and J. P. Drozda Jr, “Advancing Patient Safety Surrounding Medical Devices: A Health System Roadmap to Implement Unique Device Identification at the Point of Care,” *Medical Devices: Evidence and Research*, vol. Volume 14, pp. 411–421, Nov. 2021, doi: 10.2147/MDER.S339232.

[20] Elisabetta Bianchini, Martina Francesconi, Marisa Testa, Maya Tanase, and Vincenzo Gemignani, “Unique device identification and traceability for medical software: A major challenge for manufacturers in an ever-evolving marketplace,” *J Bioinform*, vol. 93, May 2019.

[21] T. Bayrak and F. Özdiler Çopur, “Evaluation of the unique device identification system and an approach for medical device tracking,” *Health Policy Technol*, vol. 6, no. 2, pp. 234–241, Jun. 2017, doi: 10.1016/j.hlpt.2017.04.003.

[22] Center for Devices and Radiological Health/U.S. Food and Drug Administration, “Medical device tracking guidance for industry and food and drug administration staff,” *Silver Spring, MD: Center for Devices and Radiological Health/U.S. Food and Drug Administration*, pp. 1–12, 2014.

[23] European Union, “Regulation of the European Parliament and of the Council on Medical Devices, and Amending Directive 2001/83/EC, Regulation (EC) No 178/2002 and Regulation (EC) No 1223/2009”.

[24] European Union, *Regulation (EU) 2017/745 of the European Parliament and of the Council on Medical Devices, amending Directive 2001/83/EC*. 2017.

[25] European Union, “The European Commision, Commision recommendation of 5 April 2013 on a common framework for a unique device identification system of medical devices in the Union,” *Official Journal of the European Union*, Apr. 2015.

[26] G. Radenković and D. Petković, “Metallic Biomaterials,” in *Biomaterials in Clinical Practice*, Cham: Springer International Publishing, 2018, pp. 183–224. doi: 10.1007/978-3-319-68025-5_8.

[27] H. A. Zaman, S. Sharif, M. H. Idris, and A. Kamarudin, “Metallic Biomaterials for Medical Implant Applications: A Review,” *Applied Mechanics and Materials*, vol. 735, pp. 19–25, Feb. 2015, doi: 10.4028/www.scientific.net/AMM.735.19.

[28] Md. O. Alam and A. S. M. A. Haseeb, “Response of Ti–6Al–4V and Ti–24Al–11Nb alloys to dry sliding wear against hardened steel,” *Tribol Int*, vol. 35, no. 6, pp. 357–362, Jun. 2002, doi: 10.1016/S0301-679X(02)00015-4.

[29] M. Hussein, A. Mohammed, and N. Al-Aqeeli, “Wear Characteristics of Metallic Biomaterials: A Review,” *Materials*, vol. 8, no. 5, pp. 2749–2768, May 2015, doi: 10.3390/ma8052749.

[30] Q. Chen and G. A. Thouas, “Metallic implant biomaterials,” *Materials Science and Engineering: R: Reports*, vol. 87, pp. 1–57, Jan. 2015, doi: 10.1016/j.mser.2014.10.001.

[31] M. Geetha, A. K. Singh, R. Asokamani, and A. K. Gogia, “Ti based biomaterials, the ultimate choice for orthopaedic implants – A review,” *Prog Mater Sci*, vol. 54, no. 3, pp. 397–425, May 2009, doi: 10.1016/j.pmatsci.2008.06.004.

[32] David H Kohn, “Metals in medical applications,” *Curr Opin Solid State Mater Sci*, vol. 3, pp. 309–316, 1998.

[33] S. R. Kandavalli *et al.*, “A Brief Review on the Evolution of Metallic Dental Implants: History, Design, and Application,” *Front Mater*, vol. 8, May 2021, doi: 10.3389/fmats.2021.646383.

[34] E. Pellicer, M. Lorenzetti, J. Fornell, M. D. Baró, S. Novak, and J. Sort, “Progress Beyond the State-of-the-Art in the Field of Metallic Materials for Bioimplant Applications,” in *Biomaterials in Clinical Practice*, Cham: Springer International Publishing, 2018, pp. 25–46. doi: 10.1007/978-3-319-68025-5_2.

[35] Y. Xu, Y. Qiao, P. Q. Guo, and Y. Li, “The Surface Topography in Machining of Medical Metallic Materials: A Review,” *Materials Science Forum*, vol. 861, pp. 127–132, Jul. 2016, doi: 10.4028/www.scientific.net/MSF.861.127.

[36] D. Vojtěch, J. Kubásek, J. Čapek, and I. Pospíšilová, “Novel Trends in the Development of Metallic Materials for Medical Implants,” *Key Eng Mater*, vol. 647, pp. 59–65, May 2015, doi: 10.4028/www.scientific.net/KEM.647.59.

[37] U. R. Khairy, S. J. Hamandi, and A. S. A. Ali, “Mechanical analysis of four different stainless-steel alloys used for knee replacement surgical tool,” 2022, p. 020079. doi: 10.1063/5.0109386.

[38] Outokumpu, “Handbook of Stainless Steel,” pp. 1–89, 2013.

[39] G. L. Winters and M. J. Nutt, “Stainless steels for medical and surgical applications,” vol. 1438, 2002.

[40] D. A. Porter, K. E. Easterling, and M. Y. Sherif, “Thermodynamics and Phase Diagrams,” in *Phase Transformations in Metals and Alloys*, 3rd ed.2009, pp. 11–59.

[41] D. Hull and D. J. Bacon, “Defects in Crystals,” in *Introduction to Dislocations*, 5th ed.Elsevier, 2011, pp. 5–6.

[42] S. Lampman, “Properties of Stainless Steel Welds,” in *Weld Integrety and Performance: a Source Book adapted from ASM International Handbooks, Conference Proceedings, and Technical Books*, ASM International, 1997, pp. 250–250.

[43] V. Geanta, I. Voiculescu, R. Stefanoiu, and E. R. Rusu, “Stainless Steels with Biocompatible Properties for Medical Devices,” *Key Eng Mater*, vol. 583, pp. 9–15, Sep. 2013, doi: 10.4028/www.scientific.net/KEM.583.9.

[44] K. H. Lo, C. H. Shek, and J. K. L. Lai, “Recent developments in stainless steels,” *Materials Science and Engineering: R: Reports*, vol. 65, no. 4–6, pp. 39–104, May 2009, doi: 10.1016/j.mser.2009.03.001.

[45] A. Pillai, N. Kumar, A. Gangadharan, and J. Gangadharan, “Cytotoxic effects of the nickel release from the stainless steel brackets: An *in vitro* study,” *J Pharm Bioallied Sci*, vol. 5, no. 5, p. 1, 2013, doi: 10.4103/0975-7406.113279.

[46] M. H. Zarei, S. F. Hosseini Shirazi, M. Aghvami, A. Salimi, and J. Pourahmad, “Analysis of cytotoxic effects of nickel on human blood lymphocytes,” *Toxicol Mech Methods*, vol. 28, no. 2, pp. 79–86, Feb. 2018, doi: 10.1080/15376516.2017.1364314.

[47] L. P. Felix, J. E. Perez, M. F. Contreras, T. Ravasi, and J. Kosel, “Cytotoxic effects of nickel nanowires in human fibroblasts,” *Toxicol Rep*, vol. 3, pp. 373–380, 2016, doi: 10.1016/j.toxrep.2016.03.004.

[48] K. Yang, Y. Ren, and P. Wan, “High nitrogen nickel-free austenitic stainless steel: A promising coronary stent material,” *Sci China Technol Sci*, vol. 55, no. 2, pp. 329–340, Feb. 2012, doi: 10.1007/s11431-011-4679-3.

[49] X. Z. Zou *et al.*, “The Biocompatibility on Medical High Nitrogen Nickel-Free Stainless Steel <i>In Vitro</i>,” *Adv Mat Res*, vol. 1053, pp. 473–481, Oct. 2014, doi: 10.4028/www.scientific.net/AMR.1053.473.

[50] ASTM International, “ASTM F899-20 Standard Specification for Wrought Stainless Steels for Surgical Instruments.” 2020.

[51] D. A. Porter and K. E. Easterling, “Diffusionless Transformations,” in *Phase Transformations in Metals and Alloys*, 3rd ed.CRC Press, 2009, pp. 383–408.

[52] H. Feng *et al.*, “Influence of nitrogen on corrosion behaviour of high nitrogen martensitic stainless steels manufactured by pressurized metallurgy,” *Corros Sci*, vol. 144, pp. 288–300, Nov. 2018, doi: 10.1016/j.corsci.2018.09.002.

[53] Claus Qvist Jensen, “Passivity,” in *Stainless Steel and Corrosion*, C. Q. Jensen and Damstahl a/s, Eds., 1st ed.Skanderborg, Denmark: Damstahl, 2011, pp. 66–70.

[54] R. Davis *et al.*, “A comprehensive review on metallic implant biomaterials and their subtractive manufacturing,” *The International Journal of Advanced Manufacturing Technology*, vol. 120, no. 3–4, pp. 1473–1530, May 2022, doi: 10.1007/s00170-022-08770-8.

[55] L. Zhang and L. Chen, “A Review on Biomedical Titanium Alloys: Recent Progress and Prospect,” *Adv Eng Mater*, vol. 21, no. 4, p. 1801215, Apr. 2019, doi: 10.1002/adem.201801215.

[56] G. Lütjering and J. C. Williams, “Titanium Industry Status,” in *Titanium*, B. Derby, Ed., 2nd ed.Springer, 2007, pp. 4–8.

[57] H. Okamoto, “O-Ti (Oxygen-Titanium),” *J Phase Equilibria Diffus*, vol. 32, no. 5, pp. 473–474, Oct. 2011, doi: 10.1007/s11669-011-9935-5.

[58] G. Lütjering and J. C. Williams, “Fundamental Aspects,” in *Titanium*, B. Derby, Ed., 2nd ed.Springer, 2007, pp. 15–50.

[59] K. Ishida, “Schaeffler-Type Phase Diagram of Ti-Based Alloys,” *Metallurgical and Materials Transactions A*, vol. 48, no. 10, pp. 4990–4998, Oct. 2017, doi: 10.1007/s11661-017-4218-3.

[60] ASTM International, “Standard Specification for Titanium and Titanium Alloy Bars and Billets,” *ASTM B348-13*, 2019.

[61] ASTM International, “Standard Specification for Wrought Titanium-6Aluminum-4Vanadium ELI (Extra Low Interstitial) Alloy for Surgical Implant Applications (UNS R56401),” *ASTM F136-13(2021)e1*, 2021.

[62] G. S. LEVENTHAL, “Titanium, a metal for surgery.,” *J Bone Joint Surg Am*, vol. 33-A, no. 2, pp. 473–4, Apr. 1951.

[63] R. T. Bothe, L. E. Beaton, and H. A. Davenport, “Reaction of bone to multiple metallic implants,” *Gynecology and Obstetrics*, vol. 71, pp. 598–602, 1940.

[64] K. Wang, “The use of titanium for medical applications in the USA,” *Materials Science and Engineering: A*, vol. 213, no. 1–2, pp. 134–137, Aug. 1996, doi: 10.1016/0921-5093(96)10243-4.

[65] C. N. Elias, M. A. Meyers, R. Z. Valiev, and S. N. Monteiro, “Ultrafine grained titanium for biomedical applications: An overview of performance,” *Journal of Materials Research and Technology*, vol. 2, no. 4, pp. 340–350, Oct. 2013, doi: 10.1016/j.jmrt.2013.07.003.

[66] R. R. Boyer, “Titanium for aerospace: Rationale and applications,” *Advanced Performance Materials*, vol. 2, no. 4, pp. 349–368, Oct. 1995, doi: 10.1007/BF00705316.

[67] M. Niinomi and C. J. Boehlert, “Titanium Alloys for Biomedical Applications,” 2015, pp. 179–213. doi: 10.1007/978-3-662-46836-4_8.

[68] H. J. Rack and J. I. Qazi, “Titanium alloys for biomedical applications,” *Materials Science and Engineering: C*, vol. 26, no. 8, pp. 1269–1277, Sep. 2006, doi: 10.1016/j.msec.2005.08.032.

[69] H.-D. Jung, “Titanium and Its Alloys for Biomedical Applications,” *Metals (Basel)*, vol. 11, no. 12, p. 1945, Dec. 2021, doi: 10.3390/met11121945.

[70] S. Hussain Din, “BIOMEDICAL APPLICATIONS OF TITANIUM AND ITS ALLOYS,” *Proceedings on Engineering Sciences*, vol. 3, no. 1, pp. 41–52, Mar. 2021, doi: 10.24874/PES03.01.005.

[71] M. Aziz-Kerrzo, K. G. Conroy, A. M. Fenelon, S. T. Farrell, and C. B. Breslin, “Electrochemical studies on the stability and corrosion resistance of titanium-based implant materials,” *Biomaterials*, vol. 22, no. 12, pp. 1531–1539, Jun. 2001, doi: 10.1016/S0142-9612(00)00309-4.

[72] J. Vaughan and A. Alfantazi, “Corrosion of Titanium and Its Alloys in Sulfuric Acid in the Presence of Chlorides,” *J Electrochem Soc*, vol. 153, no. 1, p. B6, 2006, doi: 10.1149/1.2126580.

[73] L. Casanova, M. Gruarin, M. Pedeferri, and M. Ormellese, “A comparison between corrosion performances of titanium grade 2 and 7 in strong reducing acids,” *Materials and Corrosion*, vol. 72, no. 9, pp. 1506–1517, Sep. 2021, doi: 10.1002/maco.202112392.

[74] P. D. Miller and J. W. Holladay, “Friction and wear properties of titanium,” *Wear*, vol. 2, no. 2, pp. 133–140, Nov. 1958, doi: 10.1016/0043-1648(58)90428-9.

[75] J. Komotori, N. Hisamori, and Y. Ohmori, “The corrosion/wear mechanisms of Ti–6Al–4V alloy for different scratching rates,” *Wear*, vol. 263, no. 1–6, pp. 412–418, Sep. 2007, doi: 10.1016/j.wear.2006.11.025.

[76] H. Attar *et al.*, “Comparison of wear properties of commercially pure titanium prepared by selective laser melting and casting processes,” *Mater Lett*, vol. 142, pp. 38–41, Mar. 2015, doi: 10.1016/j.matlet.2014.11.156.

[77] R. B. Sreesha, D. Kumar, S. Chandraker, and A. Agrawal, “Room temperature sliding wear behavior of Ti6Al4V: A review,” 2021, p. 040041. doi: 10.1063/5.0049962.

[78] R. Hack, “State of the art in fiber laser making,” L. N. Durvasula, Ed., Jul. 2003, p. 202. doi: 10.1117/12.484175.

[79] L. Lazov, H. Deneva, and P. Narica, “Laser Marking Methods,” 2016.

[80] L. Sobotova and M. Badida, “Laser marking as environment technology,” *Open Engineering*, vol. 7, no. 1, pp. 303–316, Nov. 2017, doi: 10.1515/eng-2017-0030.

[81] H. Roozbahani, M. Alizadeh, H. Handroos, and A. Salminen, “Color Laser Marking: Repeatability, Stability and Resistance Against Mechanical, Chemical and Environmental Effects,” *IEEE Access*, vol. 8, pp. 214196–214208, 2020, doi: 10.1109/ACCESS.2020.3040744.

[82] J. Gabzdyl, “Fibre lasers make their mark,” *Nat Photonics*, vol. 2, no. 1, pp. 21–23, Jan. 2008, doi: 10.1038/nphoton.2007.268.

[83] C. Neugebauer, S. Quaranta, S. Ehrenmann, C. Rest, and J. Sadowitz, “Latest advances in medical black marking: technology and techniques,” in *Laser-based Micro- and Nanoprocessing*

XIII, U. Klotzbach, R. Kling, and A. Watanabe, Eds., SPIE, Mar. 2019, p. 3. doi: 10.1117/12.2508408.

[84] A. Fraser, J. Maltais, and X. P. Godmaire, “Analysis of Laser Marking Performance on Various Non-ferrous Metals,” 2018, pp. 937–941. doi: 10.1007/978-3-319-72284-9_122.

[85] H. Chen, G. Shannon, and M. Brodsky, “Permanent marking on stainless steels for corrosion resistance through control of oxide growth,” in *29th International Congress on Applications of Lasers and Electro-optics*, Icaleo: Laser Institute of America, 2010, pp. 884–889.

[86] M. Švantner, M. Kučera, E. Smazalová, Š. Houdková, and R. Čerstvý, “Thermal effects of laser marking on microstructure and corrosion properties of stainless steel,” *Appl Opt*, vol. 55, no. 34, p. D35, Dec. 2016, doi: 10.1364/AO.55.000D35.

[87] D. P. Adams, V. C. Hodges, D. A. Hirschfeld, M. A. Rodriguez, J. P. McDonald, and P. G. Kotula, “Nanosecond pulsed laser irradiation of stainless steel 304L: Oxide growth and effects on underlying metal,” *Surf Coat Technol*, vol. 222, pp. 1–8, May 2013, doi: 10.1016/J.SURFCOAT.2012.12.044.

[88] S. K. Lawrence, D. P. Adams, D. F. Bahr, and N. R. Moody, “Environmental resistance of oxide tags fabricated on 304L stainless steel via nanosecond pulsed laser irradiation,” *Surf Coat Technol*, vol. 285, pp. 87–97, Jan. 2016, doi: 10.1016/j.surfcoat.2015.11.021.

[89] C. Y. Cui, X. G. Cui, X. D. Ren, M. J. Qi, J. D. Hu, and Y. M. Wang, “Surface oxidation phenomenon and mechanism of AISI 304 stainless steel induced by Nd:YAG pulsed laser,” *Appl Surf Sci*, vol. 305, pp. 817–824, Jun. 2014, doi: 10.1016/j.apsusc.2014.04.025.

[90] M. Kučera, M. Švantner, and E. Smazalová, “Influence of laser marking on stainless steel surface and corrosion resistance,” in *Metal 2014 - 23rd International Conference on Metallurgy and Materials, Conference Proceedings*, 2014, pp. 890–895.

[91] S. Izumi, M. Yamasaki, M. Otsu, and Y. Kawamura, “Use of Laser Irradiation to Form Anti-Corrosive Surface Oxide Layer on Mg Metal,” *Mater Trans*, vol. 48, no. 7, pp. 1965–1968, 2007, doi: 10.2320/matertrans.L-MRP2007859.

[92] J. Qi, K. L. Wang, and Y. M. Zhu, “A study on the laser marking process of stainless steel,” *J Mater Process Technol*, vol. 139, no. 1–3, pp. 273–276, Aug. 2003, doi: 10.1016/S0924-0136(03)00234-6.

[93] V. Hristov, L. Lazov, E. Yankov, T. Karadzhov, R. Minev, and N. Angelov, “Surface Analysis Study of Laser Marking Process of Stainless Steel X5CrNi18-10,” in *2021 Sixth Junior Conference on Lighting (Lighting)*, IEEE, Sep. 2021, pp. 1–5. doi: 10.1109/Lighting49406.2021.9598992.

[94] F. Brihmat-Hamadi, E. H. Amara, and H. Kellou, “Characterization of Titanium Oxide Layers Formation Produced by Nanosecond Laser Coloration,” *Metallurgical and Materials Transactions B*, vol. 48, no. 3, pp. 1439–1449, Jun. 2017, doi: 10.1007/s11663-017-0952-6.

[95] D. P. Adams *et al.*, “Nanosecond pulsed laser irradiation of titanium: Oxide growth and effects on underlying metal,” *Surf Coat Technol*, vol. 248, pp. 38–45, Jun. 2014, doi: 10.1016/j.surfcoat.2013.12.052.

[96] J. Chen, J. Shao, and H. Zhao, “Investigation on the mechanism of laser colorful marking,” D. Fan, H. Weber, X. Zhu, D. Jiang, X. Xiao, W. Dong, and D. Xu, Eds., Aug. 2009, p. 75150E. doi: 10.1117/12.843424.

[97] V. Veiko *et al.*, “Development of complete color palette based on spectrophotometric measurements of steel oxidation results for enhancement of color laser marking technology,” *Mater Des*, vol. 89, pp. 684–688, Jan. 2016, doi: 10.1016/j.matdes.2015.10.030.

[98] E. H. Amara, F. Haïd, and A. Noukaz, “Experimental investigations on fiber laser color marking of steels,” *Appl Surf Sci*, vol. 351, pp. 1–12, Oct. 2015, doi: 10.1016/j.apsusc.2015.05.095.

[99] S. M. Gorbatyuk, I. G. Morozova, M. G. Naumova, and N. A. Chichenev, “Effect of laser treatment modes on metal surface marking color,” *CIS Iron and Steel Review*, pp. 37–40, Dec. 2020, doi: 10.17580/cisisr.2020.02.09.

[100] V. Veiko *et al.*, “Controlled oxide films formation by nanosecond laser pulses for color marking,” *Opt Express*, vol. 22, no. 20, p. 24342, Oct. 2014, doi: 10.1364/OE.22.024342.

[101] Hipp, Mahrle, and Beyer, “Energy Coupling of Laser Radiation on AISI 304 Stainless Steel: Effect of High Temperatures and Surface Oxidation,” *Materials*, vol. 12, no. 17, p. 2802, Aug. 2019, doi: 10.3390/ma12172802.

[102] P. Gregorčič, M. Conradi, L. Hribar, and M. Hočevar, “Long-Term Influence of Laser-Processing Parameters on (Super)hydrophobicity Development and Stability of Stainless-Steel Surfaces,” *Materials*, vol. 11, no. 11, p. 2240, Nov. 2018, doi: 10.3390/ma11112240.

[103] S. Lei *et al.*, “Ultrafast Laser Applications in Manufacturing Processes: A State-of-the-Art Review,” *J Manuf Sci Eng*, vol. 142, no. 3, Mar. 2020, doi: 10.1115/1.4045969.

[104] T. Ferbach and F. Gaebler, “Picosecond lasers perform subsurface marking of stainless steel medical devices,” *Laser Focus World*, vol. 54, no. 2, pp. 29–32, 2018.

[105] H. Huang, L.-M. Yang, S. Bai, and J. Liu, “Blackening of metals using femtosecond fiber laser,” *Appl Opt*, vol. 54, no. 2, p. 324, Jan. 2015, doi: 10.1364/AO.54.000324.

[106] S. Rusu, A. Buzaianu, L. Ionel, D. Ursescu, and D. G. Galusca, “Titanium alloy nanosecond vs. femtosecond laser marking,” *Appl Surf Sci*, vol. 259, pp. 311–319, Oct. 2012, doi: 10.1016/j.apsusc.2012.07.039.

[107] F. Frerichs, Y. Lu, T. Lübben, and T. Radel, “Process Signature for Laser Hardening,” *Metals (Basel)*, vol. 11, no. 3, p. 465, Mar. 2021, doi: 10.3390/met11030465.

[108] S. Bonß, “Laser transformation hardening of steel,” in *Advances in Laser Materials Processing*, Elsevier, 2010, pp. 291–326. doi: 10.1533/9781845699819.4.291.

[109] C. Papaphilippou and M. Jeandin, “Spot laser hardening,” *J Mater Sci Lett*, vol. 15, no. 12, pp. 1064–1066, 1996, doi: 10.1007/BF00274908.

[110] R. P. van Hove, I. N. Sierevelt, B. J. van Royen, and P. A. Nolte, “Titanium-Nitride Coating of Orthopaedic Implants: A Review of the Literature,” *Biomed Res Int*, vol. 2015, pp. 1–9, 2015, doi: 10.1155/2015/485975.

[111] D. Höche, J. Kaspar, and P. Schaaf, “Laser nitriding and carburization of materials,” in *Laser Surface Engineering*, Elsevier, 2015, pp. 33–58. doi: 10.1016/B978-1-78242-074-3.00002-7.

[112] P. Schaaf, “Laser nitriding of metals,” *Prog Mater Sci*, vol. 47, no. 1, pp. 1–161, Jan. 2002, doi: 10.1016/S0079-6425(00)00003-7.

[113] E. Carpene and P. Schaaf, “Formation of Fe3C surface layers by laser plasma cementation,” *Appl Phys Lett*, vol. 80, no. 5, pp. 891–893, Feb. 2002, doi: 10.1063/1.1447009.

[114] E. F. Pieretti, E. J. Pessine, O. V. Correa, W. de Rossi, and M. D. M. das Neves, “Effect of Laser Parameters on the Corrosion Resistance of the ASTM F139 Stainless Steel,” *International Journal of Electrochemical Science*, vol. 10, no. 2, pp. 1221–1232, 2015.

[115] B. Krawczyk and D. L. Engelberg, “Effect of Aqua Blasting, Sandblasting and Laser Engraving on the Corrosion Resistance of Type 316 Stainless Steel,” *BHM Berg- und Hüttenmännische Monatshefte*, vol. 161, no. 1, pp. 50–55, Jan. 2016, doi: 10.1007/s00501-016-0446-x.

[116] P. Steyer, S. Valette, B. Forest, J. P. Millet, C. Donnet, and E. Audouard, “Surface modification of martensitic stainless steels by laser marking and its consequences regarding corrosion resistance,” *Surface Engineering*, vol. 22, no. 3, pp. 167–172, Jun. 2006, doi: 10.1179/174329406X108861.

[117] E. F. Pieretti and I. Costa, “Surface characterisation of ASTM F139 stainless steel marked by laser and mechanical techniques,” *Electrochim Acta*, vol. 114, pp. 838–843, Dec. 2013, doi: 10.1016/j.electacta.2013.05.101.

[118] T. Zheng and J. T. Han, “High Temperature Oxidation Behavior of SUS310S Austenitic Stainless Steel,” *Adv Mat Res*, vol. 941–944, pp. 212–215, Jun. 2014, doi: 10.4028/www.scientific.net/AMR.941-944.212.

[119] S. Chandra-ambhorn, S. Hayashi, L. Latu-Romain, and P. Wongpromrat, “CHAPTER 4 High Temperature Oxidation of Stainless Steels,” *Solid State Phenomena*, vol. 300, pp. 81–106, Feb. 2020, doi: 10.4028/www.scientific.net/SSP.300.81.

[120] R. K. Wild, “HIGH TEMPERATURE OXIDATION OF AUSTENITIC STAINLESS STEEL IN LOW OXYGEN PRESSURE,” *Corros Sci*, vol. 17, no. 2, pp. 87–104, 1977.

[121] H. Y. Zheng, G. C. Lim, X. C. Wang, J. L. Tan, and J. Hilfiker, “Process study for laser-induced surface coloration,” *J Laser Appl*, vol. 14, no. 4, pp. 215–220, Nov. 2002, doi: 10.2351/1.1514222.

[122] Z. L. Li *et al.*, “Analysis of oxide formation induced by UV laser coloration of stainless steel,” *Appl Surf Sci*, vol. 256, no. 5, pp. 1582–1588, Dec. 2009, doi: 10.1016/j.apsusc.2009.09.025.

[123] J. R. GALVELE, “Pitting Corrosion,” 1983, pp. 1–57. doi: 10.1016/B978-0-12-633670-2.50006-1.

[124] R. R. Maller, “Passivation of stainless steel,” *Trends Food Sci Technol*, vol. 9, no. 1, pp. 28–32, Jan. 1998, doi: 10.1016/S0924-2244(97)00004-6.

[125] M. A. Barbosa, “PITTING RESISTANCE OF AISI 316 STAINLESS STEEL PASSIVATED IN DILUTED NITRIC ACID,” *Corros Sci*, vol. 23, no. 12, pp. 1293–1305, 1983.

[126] J. S. Noh, N. J. Laycock, W. Gao, and D. B. Wells, “Effects of nitric acid passivation on the pitting resistance of 316 stainless steel,” *Corros Sci*, vol. 42, no. 12, pp. 2069–2084, Dec. 2000, doi: 10.1016/S0010-938X(00)00052-4.

[127] J. Li *et al.*, “Enhancing Pitting Corrosion Resistance of Severely Cold-Worked High Nitrogen Austenitic Stainless Steel by Nitric Acid Passivation,” *J Electrochem Soc*, vol. 166, no. 13, pp. C365–C374, Aug. 2019, doi: 10.1149/2.0211913jes.

[128] B. Laurent, N. Gruet, B. Gwinner, F. Miserque, K. Rousseau, and K. Ogle, “Dissolution and Passivation of a Silicon-Rich Austenitic Stainless Steel during Active-Passive Cycles in Sulfuric and Nitric Acid,” *J Electrochem Soc*, vol. 164, no. 13, pp. C892–C900, Nov. 2017, doi: 10.1149/2.1531713jes.

[129] C. O’Laoire, B. Timmins, L. Kremer, J. D. Holmes, and M. A. Morris, “Analysis of the Acid Passivation of Stainless Steel,” *Anal Lett*, vol. 39, no. 11, pp. 2255–2271, Aug. 2006, doi: 10.1080/00032710600755363.

[130] Y. Yang, Q. Wang, J. Li, L. Tan, and K. Yang, “Enhancing General Corrosion Resistance of Biomedical High Nitrogen Nickel-Free Stainless Steel by Nitric Acid Passivation,” *Acta Metallurgica Sinica (English Letters)*, vol. 33, no. 2, pp. 307–312, Feb. 2020, doi: 10.1007/s40195-019-00952-w.

[131] L. v. Kremer, “Improvements in Passivation Using Citric Acid Formulations,” in *Medical Device Materials I - Proceedings from the 2003 Materials & Processes for Medical Device Conference*, ASTM international, 2003, pp. 87–90.

[132] S. Parsons, O. Poyntz-Wright, A. Kent, and M. C. McManus, “Green chemistry for stainless steel corrosion resistance: life cycle assessment of citric acid versus nitric acid passivation,” *Materials Today Sustainability*, vol. 3–4, p. 100005, Mar. 2019, doi: 10.1016/j.mtsust.2019.01.001.

[133] Inc. ITB, “Test Protocol for Validation of Citric Acid as an Alternative to Nitric Acid for Passivation of Stainless Steels at Kennedy Space Center,” Dayton, OH 45459, 2012.

[134] M. Kolody and J. Curran, “Alternative to Nitric Acid Passivation of Stainless Steel Alloys,” *NASA Technology Evaluation for Environmental Risk Mitigation Principal Center*, 2019.

[135] M. del R. Lara Banda, D. Y. Pérez Ortíz, C. Gaona Tiburcio, P. Zambrano-Robledo, J. A. Cabral Miramontes, and F. Almeraya Calderon, “Citric Acid Passivation of 15-5PH and 17-4PH Stainless Steel Used in the Aeronautical Industry,” in *Proceedings of the Symposium of Aeronautical and Aerospace Processes, Materials and Industrial Applications*, Cham: Springer International Publishing, 2018, pp. 95–104. doi: 10.1007/978-3-319-65611-3_9.

[136] F. Almeraya *et al.*, “Electrochemical Corrosion of the Stainless Steel 15-5PH and 17-4PH Passivation in Citric Acid,” *ECS Meeting Abstracts*, vol. MA2018-02, no. 13, pp. 665–665, Jul. 2018, doi: 10.1149/MA2018-02/13/665.

[137] Y. Sugawara, T. Mohri, I. Muto, and N. Hara, “Improvement of Corrosion Resistance of Stainless Steel by Chemical Passivation Treatment in Citric Acid Systems,” *ECS Meeting Abstracts*, vol. MA2011-02, no. 22, pp. 1700–1700, Aug. 2011, doi: 10.1149/MA2011-02/22/1700.

[138] A. T. Costa, M. C. L. Oliveira, and R. A. Antunes, “Interplay between the composition of the passive film and the corrosion resistance of citric acid-passivated AISI 316L stainless steel,” *Surface and Interface Analysis*, vol. 53, no. 3, pp. 374–384, Mar. 2021, doi: 10.1002/sia.6927.

[139] B. Martinez, C. Gaona Tiburcio, D. Bastidas, M. Lara-Banda, O. Samaniego, and F. Almeraya Calderon, “Electrochemical Evaluation of 15-5PH Stainless Steel Passivated in Citric Acid.,” *ECS Trans*, vol. 106, no. 1, pp. 223–228, Jan. 2022, doi: 10.1149/10601.0223ecst.

[140] P. Verdeguer *et al.*, “Citric Acid in the Passivation of Titanium Dental Implants: Corrosion Resistance and Bactericide Behavior,” *Materials*, vol. 15, no. 2, p. 545, Jan. 2022, doi: 10.3390/ma15020545.

[141] M. S. K. Chong, Y. E. Teo, and S. H. Teoh, “Fatigue Failure of Materials for Medical Devices,” in *Degradation of Implant Materials*, New York, NY: Springer New York, 2012, pp. 303–328. doi: 10.1007/978-1-4614-3942-4_11.

[142] T. L. Anderson and T. L. Anderson, *Fracture Mechanics*. CRC Press, 2005. doi: 10.1201/9781420058215.

[143] F. Berto, A. Campagnolo, T. Welo, S. Vantadori, and A. Carpinteri, “Multiaxial fatigue strength of titanium alloys,” *Frattura ed Integrità Strutturale*, vol. 11, no. 41, pp. 79–89, Jun. 2017, doi: 10.3221/IGF-ESIS.41.12.

[144] V. I. Tseitlin, G. A. Gromov, and A. N. Kryuchkova, “Low-cycle fatigue of titanium alloys,” *Metal Science and Heat Treatment*, vol. 14, no. 4, pp. 343–344, Apr. 1972, doi: 10.1007/BF00657027.

[145] M. BACHE, “Processing titanium alloys for optimum fatigue performance,” *Int J Fatigue*, vol. 21, pp. 105–111, Sep. 1999, doi: 10.1016/S0142-1123(99)00061-4.

[146] J. A. Hall, “Fatigue crack initiation in alpha-beta titanium alloys,” *Int J Fatigue*, vol. 19, no. 93, pp. 23–37, Jun. 1997, doi: 10.1016/S0142-1123(97)00047-9.

[147] C. Fleck and D. Eifler, “Corrosion, fatigue and corrosion fatigue behaviour of metal implant materials, especially titanium alloys,” *Int J Fatigue*, vol. 32, no. 6, pp. 929–935, Jun. 2010, doi: 10.1016/j.ijfatigue.2009.09.009.

[148] “CSN EN ISO 14801 Dentistry - Implants - Dynamic loading test for endosseous dental implants.” 2016.

[149] P. Pérez León, J. F. Bartolomé, C. Lombardía, and G. Pradíes, “Mechanical fatigue behaviour of different lengths screw-retained restorations connected to two designs prosthetic connection level,” *J Oral Rehabil*, p. joor.12809, May 2019, doi: 10.1111/joor.12809.

[150] P. Sevilla, C. Sandino, M. Arciniegas, J. Martínez-Gomis, M. Peraire, and F. J. Gil, “Evaluating mechanical properties and degradation of YTZP dental implants,” *Materials Science and Engineering: C*, vol. 30, no. 1, pp. 14–19, Jan. 2010, doi: 10.1016/j.msec.2009.08.002.

[151] Y. Duan, J. A. Gonzalez, P. A. Kulkarni, W. W. Nagy, and J. A. Griggs, “Fatigue lifetime prediction of a reduced-diameter dental implant system: Numerical and experimental study,” *Dental Materials*, vol. 34, no. 9, pp. 1299–1309, Sep. 2018, doi: 10.1016/j.dental.2018.06.002.

[152] F. M. S. Soares, C. N. Elias, E. S. Monteiro, M. E. R. Coimbra, and A. I. C. Santana, “Galvanic Corrosion of Ti Dental Implants Coupled to CoCrMo Prosthetic Component,” *Int J Biomater*, vol. 2021, pp. 1–11, Oct. 2021, doi: 10.1155/2021/1313343.

[153] A. Tunkiwala and U. Kher, “Implant prosthodontics: Challenges, complications, and solutions,” *Journal of Dental Implants*, vol. 9, no. 2, p. 66, 2019, doi: 10.4103/jdi.jdi_14_19.

3. Manuscript I: Influence of Laser Marking on Microstructure and Corrosion Performance of Martensitic Stainless Steel Surfaces for Biomedical Applications[5]

Nikolaj G. Henriksen[a,b], O. Z. Andersen[a,c], Morten S. Jellesen[b], Thomas L. Christiansen[b], Marcel A.J. Somers[b]

[a] Elos MedTech Pinol Gørløse, Engvej 33, 3330 Gørløse, Denmark

[b] Technical University of Denmark, Department of Civil and Mechnical Engineering, Produktionstorvet b. 425, 2800 Kgs. Lyngby, Denmark

[c] Now with Straumann and University of Bern, Department of Periodontology, School of Dental Medicine, CH-3210 Bern, Switzerland

The medical device industry demands unique device identification (UDI) tags on metallic components applied via laser marking. A common issue is that the visual appearance of the marking becomes poorly legible over time due to loss of contrast. Nanosecond pulsed laser irradiation was used to grow an oxide layer on two different martensitic stainless steels AISI 420F mod and 420B to compare the influences of the chemical composition of the steel (with and without S), power density, and energy input. The corrosion behavior was found to depend strongly on laser energy input. The presence of sulfur negatively affected the corrosion resistance and narrowed the applicable window for the laser processing parameters significantly. For the sulfur-containing AISI 420F steel, 3–5 µm wide craters formed on the surface after laser marking, which is interpreted as thermal degradation of protruding MnS inclusions resulting from the laser marking process. Also,

---

[5] Published work: Henriksen, N. G., Andersen, O. Z., Jellesen, M. S., Christiansen, T. L., & Somers, M. A. J. (2022). *Influence of Laser Marking on Microstructure and Corrosion Performance of Martensitic Stainless Steel Surfaces for Biomedical Applications*. HTM Journal of Heat Treatment and Materials, 77(3), 177–196. https://doi.org/10.1515/htm-2022-1010. The format has been adapted to the format of this Ph.D. thesis.

substantial cracking in the oxide layer was observed. The marked specimens suffered from corrosion in a thin zone below the formed oxide layer. This behavior is attributed to Cr-depletion in the zone adjacent to the oxide layer, resulting from providing Cr to the growing oxide layer.

***Keywords**: Laser marking, martensitic stainless steel, corrosion, surface treatment, heat affected zone, manganese sulfide*

3.1. Introduction

In recent years, the focus on product traceability has increased steadily. The medical device industry is required to provide full traceability for all medical devices in the form of unique device identification (UDI) systems [1, 2]. This requirement infers that items are marked with a permanent identification marking applied directly onto the product. It is recommended that the marking should appear in a ‘human-readable format’; QR- (quick response) code and barcodes are also common. A prerequisite for a ‘human-readable format’ is significant contrast or color difference between the marking and the component, so it is readable without aids. The benefits of full traceability by UDI systems are particularly evident for medical implants. Wilson et al. projected a significant increase in cost and man-hours spent on failed implants that cannot be identified [3]. UDI was proposed as a standard method for part identification to document treatment of patients with a history log describing the specific equipment used [4]. An increasingly popular technology for producing permanent, direct UDI product marking is the laser marking method, also referred to as laser annealing [5, 6]. This method is established as the industry standard marking method for medical devices. Depending on the laser parameters, the interaction of a laser with a substrate surface causes heating, resulting in oxidation, melting and/ or ablation [7]. For metallic components sufficient color strength or contrast relative to the substrate is commonly achieved through the growth of an oxide layer or, if the device is coated, by ablation of a darker surface layer [6]. For pulsed lasers, irrespective of whether oxidation or ablation is practiced, the outcome is strongly affected by the peak power density, P_p *(W/m2)*. This parameter depends on the energy of a single pulse E_p, the projected spot size of the laser A, and the pulse length t_p [8]:

$$P_p = \frac{E_p}{A \cdot t_p} \tag{3.1}$$

The energy of a single pulse can be calculated from the average power *P*, and the pulse frequency *f*, $E_p = \frac{P}{f}$.

The peak power density is adjusted to achieve laser marking in the oxidative or in the ablative regime. Lower P_p, as applicable for this investigation, is chosen so that laser marking occurs in the oxidative regime where no ablation and limited melting occurs. A local increase in temperature enables the reaction of atmospheric oxygen and oxide-forming elements (chromium) from the steel to form an oxide layer. This oxide layer appears black on the metallic surface. The high temperature alters the composition and microstructure in the surface-near region, not only by reaction with the atmosphere, but potentially also by evaporation of more volatile species from the steel. For relatively high P_p, laser marking occurs in the ablative regime where oxides are no longer stable. In this mode of operation material melts and evaporates, leaving engravings in the metal surface. Ablative laser marking provides contrast by local surface roughness, and generally appears white on the substrate. Another important parameter is the energy input, E_s *(J/m2)*, which describes the energy per unit area transferred to the surface and influences oxide layer growth [8]:

$$E_s = \frac{P}{v \cdot l_s} \tag{3.2}$$

here *v* is the scanning speed and ls is the hatch spacing. In this work, oxidative laser marking is considered; ablation is avoided. Laser marking with nanosecond pulsed YAG fiber lasers, operating at a near-infrared wavelength of 1064 nm and up to 25 W of power, is widely used in the medical device industry. The economical alternative to fiber lasers is CO2 lasers, which operate at significantly higher power of up to 200 W for laser marking. The wavelength of CO2 lasers is 10-600 nm [6]. The effect of laser markings on the corrosion performance has been investigated for the austenitic stainless steels AISI 304L and 316L, which are widely applied in the medical industry [8–11]. It was found that laser marking locally alters the microstructure and chemical composition, and that corrosion resistance is generally deteriorated after laser marking. Švantner et al. identified, via saline mist corrosion tests, that corrosion resistance is most sensitive to the laser energy input [10]. Lawrence et al. [9] explained a lower corrosion resistance by chromium depletion from the substrate, after growth of a chromium containing oxide layer.

Limited research attention has been given to laser-marked martensitic stainless steels. This class of steels has generally lower inherent corrosion resistance, as compared to their austenitic (or ferritic) counterparts, due to the generally lower chromium (and nickel) content and the tendency to form chromium-containing carbides. Steyer et al. evaluated the corrosion resistance of martensitic stainless steel after laser marking in both the oxidation and the ablation regime [12]. They identified chromium depletion in the substrate adjacent to the oxide layer as the cause of loss of passivity after oxidative laser marking. For laser ablation, only a slight modification of the chemical composition was observed and, consequently, the corrosion resistance was only modestly reduced.

In the present study, the response of two martensitic stainless steel types after oxidative laser marking is investigated. One of the investigated martensitic stainless steel types contains a relatively high amount of sulfur and manganese. For some steel grades, manganese sulfide (MnS) is added intentionally to improve machinability [13]. Manganese sulfide inclusions in stainless steel are notorious pit initiation sites that accelerate corrosion attacks. The exact mechanism is debated to be either chromium depletion around MnS, the effect of MnS oxidation products or combined effects [14–17]. The effect of MnS inclusions on laser marking performance is presently unknown. This study investigates the effect of various laser marking treatments on the microstructure and associated corrosion performance of martensitic stainless steels.

3.2. Experimental: Materials and Methods

3.2.1. Materials

Two martensitic stainless steels, AISI 420Fmod and 420B, were provided by Klein Metals in the form of drawn rods. These steels are commonly utilized in the manufacturing of medical devices in the dental sector for surgical tools (not for implants) and are also listed in the ASTM F899 standard for wrought stainless steels for surgical instruments. The chemical compositions of the investigated steels are listed in Table 3.1. The main difference in chemical composition is the presence of more sulfur, manganese, and molybdenum in 420Fmod. From the chemical composition [13] and supplier information, abundant manganese sulfides are expected in 420Fmod. This phase is known to improve machinability and prolong cutting tool life during milling and lathe-turning [18]. The carbon content is higher in 420B and will promote the formation of chromium carbides.

Table 3.1: Chemical composition of the investigated stainless steels AISI 420Fmod and 420B, carbon and sulfur are measured via infrared spectroscopy on the LECO CS230 combustion analyzer and other elements are measured via energy dispersive X-ray spectroscopy.

Element (w%)	C	Si	Mn	S	Cr	Ni	Mo	Fe
AISI 420Fmod EN 1.4197 X20CrNiMoS13-1	0.21	0.4	1.5	0.27	12.7	0.8	1.1	bal.
AISI 420B EN 1.4028 X30Cr13	0.27	0.4	0.6	0.03	12.0	0.2	-	bal.

Samples were in the form of lathe-turned discs with a diameter of 18 mm (420Fmod) and 12 mm (420B), both with a thickness of 3 mm. Before laser marking, heat treatment was performed in an industrial vacuum furnace. The heat treatment consisted of annealing at 1050 °C in 2 mbar H2 gas followed by gas quenching in 3 bar N2. Tempering occurred at 300 °C for 2 hours. Subsequently, approximately 300 µm of the surface was removed by grinding on metallographic preparation equipment; the last grinding step was mesh 4000 SiC abrasive paper.

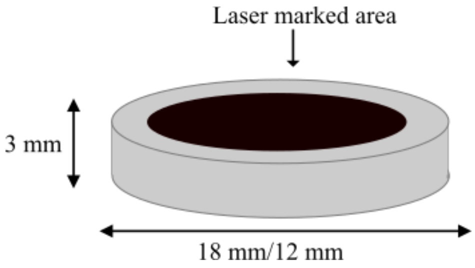

Figure 3.1: Sample geometry of steel discs with laser marked area on one side.

3.2.2. Methods

3.2.2.1. Laser Marking

Laser marking was applied onto one side of the disc-shaped samples under ambient conditions (Figure 3.1) using a pulsed nanosecond YAG fiber laser (Y.0200, FOBA, Germany), with a maximum average power of 20 W and a wavelength of 1064 nm. The equipment was operated with a focused laser beam and a nominal spot size of 30 µm. Average laser power (P) and scan speed (v) were varied, thereby varying the parameters that determine the peak power density Pp and the energy input Es, as described in equations (3.1) and (3.2). A pulse frequency of 200 kHz and pulse length of 200 ns were kept constant. Anti-parallel criss-cross pattern marking strategy was applied, as illustrated in Figure 3.2. The hatch spacing was 5 µm, giving a line overlap of 83 %. The laser marking strategy is representative of current methods utilized in the industry. The energy distribution of a fiber laser spot is approximately Gaussian, resulting in an inherent heterogeneity of the laser-marked surface. A large degree of line overlap contributes to more homogenous energy input to the surface, as each location is passed several times at different energy levels within the Gaussian energy distribution. Since the border of the laser marking displays heterogeneity, due to the lack of overlapping laser passings, it is excluded from microstructural analysis and electrochemical testing.

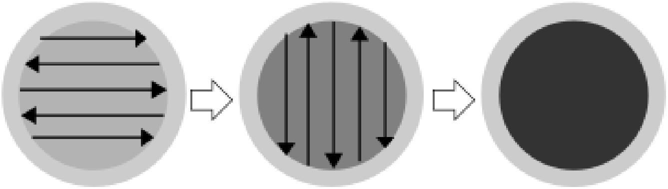

Figure 3.2: Laser marking strategy is anti-parallel lines with 90° rotation.

Four parameter sets (Table 3.2) were investigated to determine the effects on electrochemical behavior in relation to power density and energy input.

Table 3.2: Parameters utilized when laser marking samples for experiments.

Parameter set	P (W)	v (m/s)	P_p (W/m^2)	E_s (J/m^2)
#1	9	1.50	$3.1 \cdot 10^{11}$	$1.2 \cdot 10^{6}$
#2	5	0.80	$1.8 \cdot 10^{11}$	$1.3 \cdot 10^{6}$
#3	5	0.50	$1.8 \cdot 10^{11}$	$2.0 \cdot 10^{6}$
#4	5	0.25	$1.8 \cdot 10^{11}$	$4.0 \cdot 10^{6}$

3.2.2.2. Light optical microscopy and scanning electron microscopy (SEM)

Light optical microscopy was carried out with a Zeiss Axio Vert A1 microscope on polished and etched cross-sections of laser-marked samples. The cross-sections were embedded in Struers' Isofast epoxy resin, ground, and polished using standard metallographic preparation methods. For scanning electron microscopical investigations close to the surface, the samples were wrapped in aluminum foil to preserve the integrity of the oxide layer. The last steps included polishing with 1 µm diamond suspension, followed by polishing with a colloidal silica suspension. Etching was performed with Kalling's reagent to reveal microstructural features.

The topography was investigated with digital microscopy (Keyence VHX 6000) to document large portions of the laser-marked surfaces. A Zeiss Supra 35 scanning electron microscope (SEM) was used, applying acceleration voltages of 10–25 kV to investigate metallographic cross-sections and surface topography. The lower voltage was used for secondary and backscatter electron imaging, while the highest voltage was used for energy-dispersive X-ray spectroscopy (EDS). The working distance was between 12 and 13 mm for all modes of operation.

3.2.2.3. X-ray diffraction analysis

X-ray diffraction (XRD) analysis was utilized for phase identification. A Bruker discover D8 diffractometer equipped with a chromium tube, was used to analyze the base material and phases formed on laser irradiated surfaces. Diffractograms were recorded in the scattering angle range 30–110° 2ϴ with an increment of 0.04° and a counting time of 5 seconds per step. The wavelength of the Cr-Kα radiation was taken as 2.289 Å.

Two modes of operation were utilized: symmetrical scan and grazing incidence (GIXRD). In the symmetrical mode, the angle between the sample surface and X-ray source is identical to the angle between the detector and sample surface. In this measurement mode, the information depth increases from 1 µm for 20° 2ϴ to 5.5 µm for 150° 2ϴ. GIXRD maintains a constant incidence angle between the X-ray source and sample surface, and only the detector angle is varied. An incidence angle of 5° ensures an approximately constant shallow information depth of ~0.7 µm in the scattering angle range 20–150° 2ϴ. Data has been smoothed via the Savitzky-Golay method.

3.2.2.4. Electrochemical characterization

Potentiodynamic polarization tests were performed in a Gamry PTC 1 paint test cell with Gamry PT1 electrochemical masks covering the surface to expose a laser-marked area of 1 cm^2. The electrolyte consisted of 0.1 wt% NaCl in demineralized water. This relatively mild electrolyte was chosen to reveal differences between the two investigated conditions. A saturated calomel reference electrode and a graphite rod as the counter electrode (as supplied by Gamry) were used. All potentials are reported as standard hydrogen electrode (SHE) potentials, as obtained by the addition of 244 mV to potentials measured with the saturated calomel electrode.

The open current potential (OCP) was measured for 600 s just before polarization. Potentiodynamic polarization involved scanning from -100 to 500 mV relative to the measured OCP. A scan rate of 30 mV/min was utilized, and measurements were repeated three times on new samples. All experiments were performed at room temperature.

3.3. Results and Interpretation

3.3.1. Metallographic analysis

All samples showed a darkening of the surface after laser marking. Qualitatively, the highest contrast relative to the substrate is observed in samples treated with parameter set #4 followed by #3 and #1. #2 samples showed the least color saturation (Figure 3.3). Some difference is observed between laser parameter sets. Parameter sets #4 and #3, i.e., high Es, showed the darkest and most uniform laser marked surfaces. Specimen #2 exhibited an uneven, muddy appearance and features reminiscent of the steel production are still visible after laser marking. Specimen #1, i.e. high Pp, although dark, appears lighter than #3 and #4 on inspection from different angles.

Figure. 3.3. Appearance of laser marked samples for both investigated steels, for all four laser marking parameter sets

Surface images of both materials after laser marking with the four parameter sets are shown in Figure 3.4, to reveal differences in morphology and color. Apart from AISI 420Fmod marked with parameter set #2, the laser tracks are observed on the sample surfaces. Samples marked #1 with the highest power density, exhibited the most pronounced laser tracks. AISI 420Fmod suffers from abundant crater-like features. For AISI 420B fewer and smaller crater-like features are observed.

Brownish corrosion products appear to emerge from some craters on AISI 420Fmod #1 (see arrows). Specimen #2 has the lowest density of craters for 420Fmod but contains many areas without visible oxidation. These could potentially have developed into craters if sufficient energy had been applied. Qualitatively, specimen #3 has the highest density of craters. On 420B #2, the topography appears blue in certain areas, interpreted as colors caused by interference of light with a thin oxide layer. Increasing the energy input to the levels of #4 resulted in the darkest color and the largest crater diameter, while the laser track features are no longer visible.

An example of a cross-sectional analysis of etched laser-marked samples is shown in Figure 3.5. The hardness of AISI 420B and AISI 420Fmod is 554 ± 3 HV1 and 559 ± 4 HV1, respectively, as measured in the as-received condition, indicating a microstructure of tempered martensite. An apparent difference in bulk microstructure between AISI 420Fmod and 420B, is the appearance of stringers (≈50 μm long and 3–5 μm wide) elongated along the drawing direction in 420Fmod. These are interpreted as MnS inclusions. Although some MnS stringers were found in 420B, they are far more numerous in 420Fmod. At the top of the laser marked surface, a dark oxide layer is observed (Figure 3.5b), containing cracks perpendicular to the surface. The oxide layer on #3 is the thickest (≈2 μm) and most easily observable. The oxide layer thickness is < 1 μm for #1 and cannot be discerned with light optical microscopy for #2. Below the oxide layer, a heat-affected zone (HAZ) is identified. The top 2 μm appears to have a different etching response than the rest of the HAZ. This is interpreted as resulting from austenite stabilization.

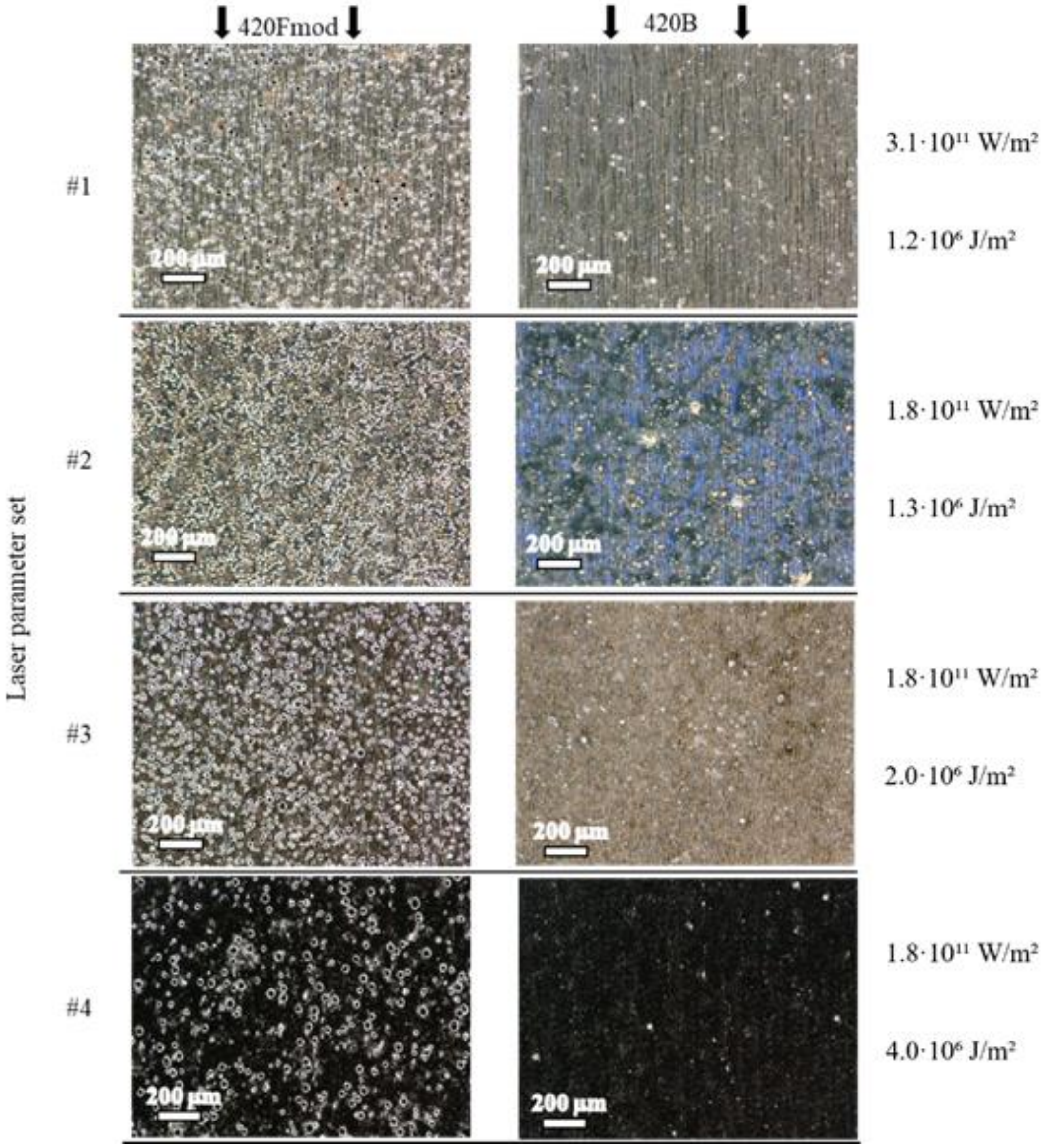

Figure 3.4. Birds-eye digital micrographs of representative areas of the laser marked surfaces of AISI 420Fmod and 420B for the four investigated laser parameter sets.

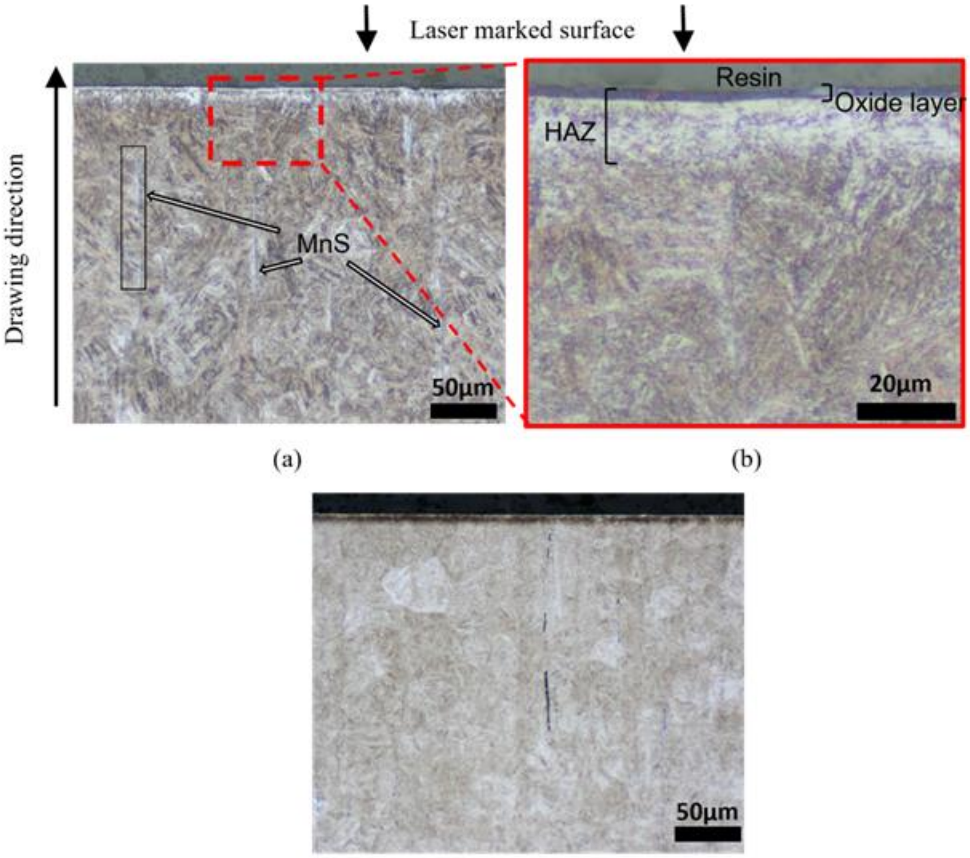

(a) (b)

(c)

Figure 3.5. Etched cross-section of AISI 420Fmod (a, b) and 420B (c) after laser marking with parameter set #3 at different resolutions.

Selected SEM micrographs of cross-sections and surface topography are given in Figure 3.6. Backscatter electron imaging of cross-sections shows an oxide layer that appears darker than the steel, because of a lower effective atomic number and, hence, a lower backscatter electron yield (Figure 3.6a). Additionally, Figure 3.6a shows a cross-section over one of the craters observed in Figure 3.4. The crater appears to be associated with the (former) presence of a MnS inclusion. EDS confirmed the abundant presence of sulfur and manganese at this location. EDS on the top of an unmarked and polished sample, revealed many locations with high manganese and sulfur intensity. The thickness of the oxide layer was estimated in SEM on samples wrapped in aluminum foil. Specimens #1 and #2 resulted in an oxide thickness up to ≈0.2 µm. The higher Es of specimens #3 and #4 resulted in a more uniform thickness of ≈0.4 µm and ≈0.7 µm, respectively. An example of an intact oxide layer is shown on Figure 3.6c.

The topography of the oxide developing during laser marking (Fig. 4.6b), clearly shows the direction of the laser tracks. The width of the tracks corresponds with the nominal hatch spacing of 5 µm. In-between the tracks, white spots are present, which are too small to be resolved with EDS for elemental analysis. The oxide layer contains many cracks originating from locations where laser tracks overlap. MnS craters appear to act as locations where cracks join or, rather, radiate from. Similar cracks were observed in all laser markings for both materials but were more numerous for specimen #3. In general, fewer cracks were found in the oxide layers on 420B, suggesting that the craters act as crack initiation sites.

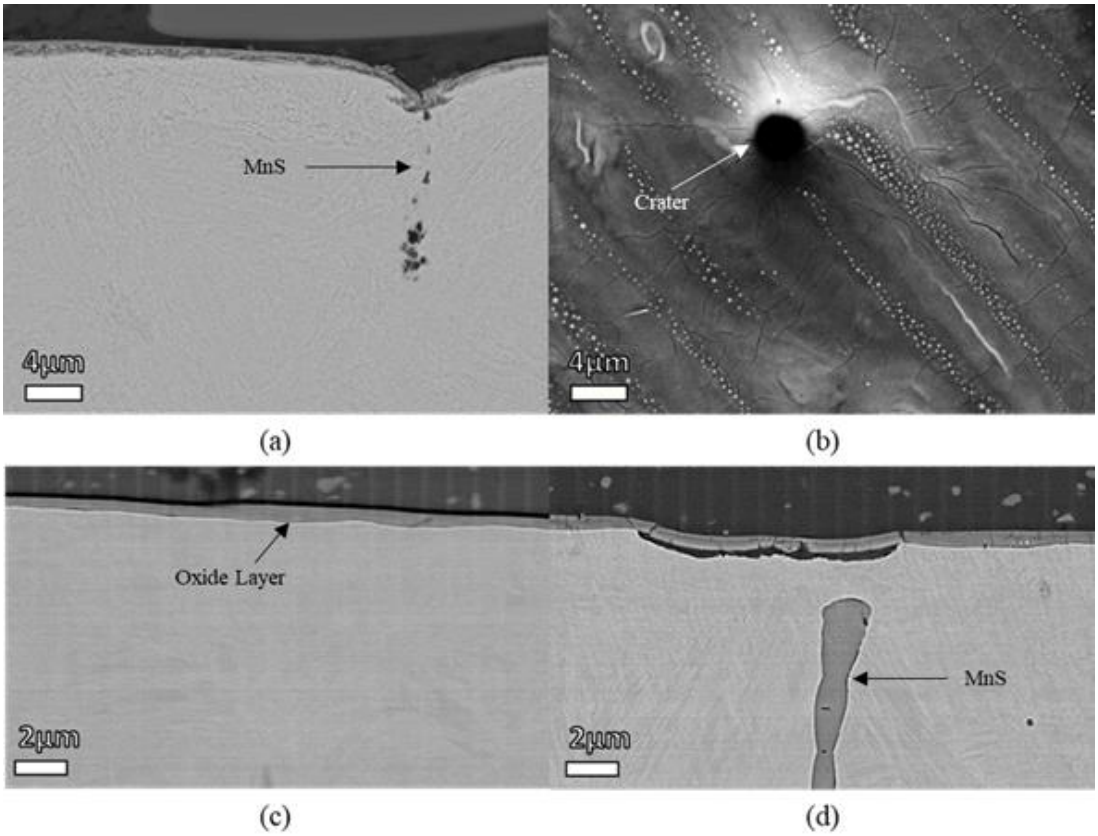

Figure 3.6. SEM images of 420Fmod (a) backscatter electron image of a cross-section and (b) secondary electron image of the laser marking viewed top down. A backscatter electron image of cross-section of a non-corroded area of laser marked 420Fmod with #4 (c) and a corroded area of the same sample (d)

Figure 3.6c shows laser-marked AISI 420Fmod at a location where the oxide layer appears intact. In Figure 3.6d another location on the same cross-section is presented, where the corrosive attack is observed. Apparently, the region below the oxide layer is partly dissolved and the oxide layer has sunken into the resulting cavity, thereby promoting crack formation in the oxide layer. The cracking may be aggravated by sample preparation; however, the dissolution of metal underneath is not. Below the corroded area, a MnS inclusion is present.

EDS analysis in cross-section confirmed enrichment of chromium in the oxide layer, while it is relatively poor in iron (Figure 3.7). Qualitatively,1 a slight trend is observed that the Cr content in the steel adjacent to the oxide layer is lower than in the bulk (see arrow). It is noted that the resolution of EDS (Figures. 3.7b–d) is not as good as in BSE imaging and, therefore, does not allow to distinguish all the features observed in Figure 3.7a (see also footnote [6]).

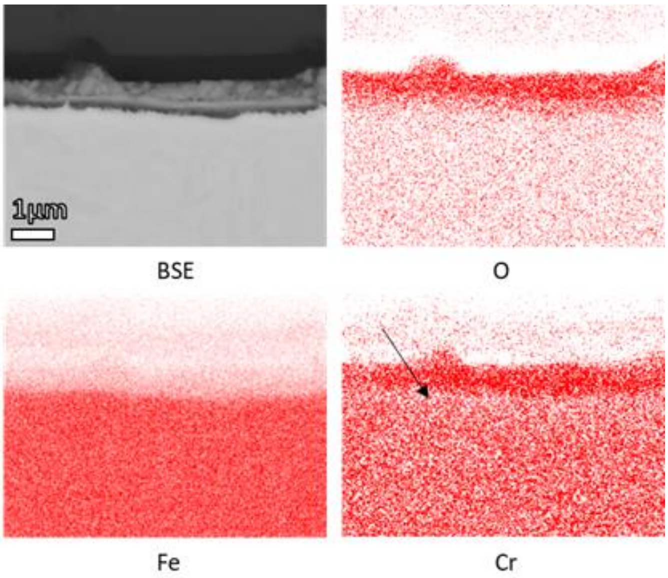

Figure 3.7. Backscatter image of oxide layer (BSE) and EDS maps of the cross-section of #3 laser marked 420Fmod, showing the distribution of Cr, O and Fe as red colors.

---

[6] It is noted that the features observed are too small to be analyzed (semi-)quantitatively with EDS, because the interaction volume from which the characteristic X-rays originate corresponds to a spatial resolution that is appreciably poorer than the size of the features themselves. Therefore, we suffice with a qualitative analysis only.

3.3.2. Phase analysis

Symmetrical XRD of unmarked samples revealed the presence of face-centered cubic (FCC) and body-centered cubic (BCC), denoted in Figure 3.8 as α and γ, respectively. BCC originates from (tempered) martensite, while FCC indicates the presence of retained austenite in the material. A relatively large amount of retained austenite is present in both alloys, as suggested by the relative intensity of austenite peaks; the fraction of (retained) austenite was not quantified. The key difference between the two materials is the abundant presence of manganese sulfide (MnS) in 420Fmod. Indeed, much lower intensities of MnS peaks are observed for 420B. Energy dispersive spectroscopy confirmed high concentrations of sulfur and manganese in the stringers observed in Figure 3.5. The lack of additional MnS peaks in Figure 3.8 and the clear directionality of the MnS stringers (see Figure 3.5a/c), suggests a strong crystallographic texture in this microstructural constituent. No diffraction evidence for the presence of carbides was observed, owing to the relatively low phase fraction of such carbide (< 5 %) and the relatively high background resulting from the chosen measurement conditions. Phase analysis with GIXRD revealed more details in the laser-marked surface region (Figure 3.9). Not all laser-marked surfaces showed diffraction peaks identifiable as oxide. The identifiable oxide peaks originate from FeCr2O4 spinel and/or Fe3O4 and are labeled as oxide in Figure 3.9. Obviously, the relative intensities of FCC and BCC peaks are affected by the laser treatment. A remarkable increase in austenite intensity is observed for all laser-treated surfaces as compared to the unmarked surfaces, indicating an increase in the amount of (retained) austenite. No apparent differences in austenite intensity were observed for the different laser marking conditions. Only one peak of the MnS phase is visible.

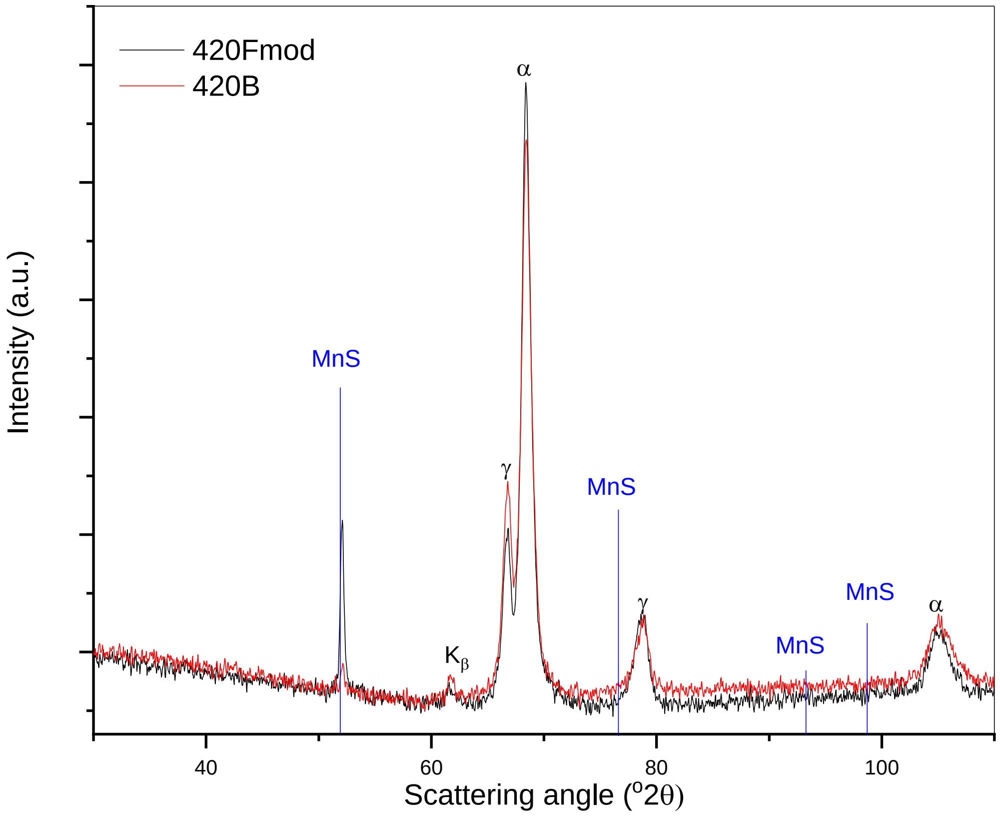

Figure 3.8: X-ray diffractogram of unmarked AISI 420Fmod and 420B (symmetrical scans).

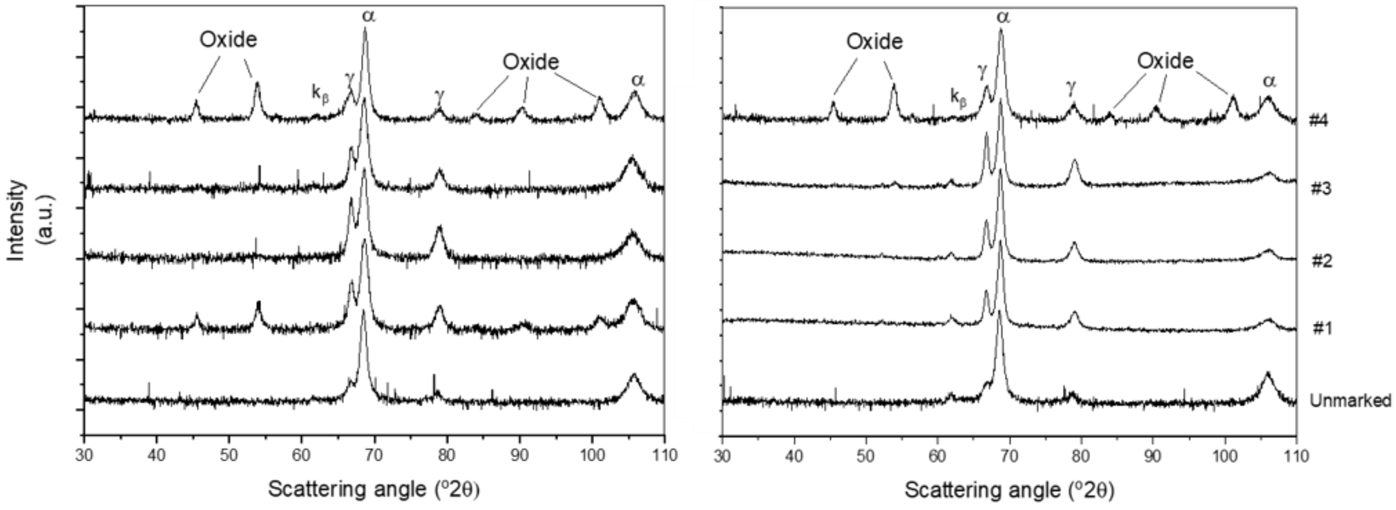

(a) 420Fmod

(b) 420B

Figure 3.9: GIXRD diffractograms of AISI 420Fmod and 420B before (bottom) and after laser marking with parameter sets #1-4 (increasing).

3.3.3. Electrochemical Analysis

Potentiodynamic polarization tests were performed to evaluate the electrochemical behavior of the laser marked specimens. Since the surface roughness can drastically change upon laser marking a polished sample surface, the unmarked (polished) samples are not directly compared, because they would establish an inappropriate reference. Instead, the results for the unmarked specimens are shown in Figure 3.10. The differences in electrochemical behavior between 420B and 420Fmod are interpreted as consistent with the higher Mo (and Ni) content in 420Fmod and the higher C content in 420B. The differences in composition lead to a higher corrosion potential, lower passive current density, and higher pitting potential for 420Fmod. The shape of the polarization curve of unmarked 420Fmod shows pseudo-passivation rather than active dissolution of the metal. This is also reflected by the PREN numbers [24] which are 16.3 and 12 for 420Fmod and 420B, respectively.[7] Evidently, the anticipated negative effect of MnS is effectively compensated for by the higher Mo (and lower C) content. Examples of polarization curves for marked laser specimens are collected in Figure 3.11 and the extracted electrochemical properties are listed in Table 3.3. The unmarked specimens in Figure 3.10 exhibit similar corrosion potentials as the laser-marked specimens #1 and #2 with lower energy inputs. As mentioned, the current densities should not be compared due to differences in corroding surface area.

---

[7] It is noted that PREN does not consider the influence of C in solid solution.

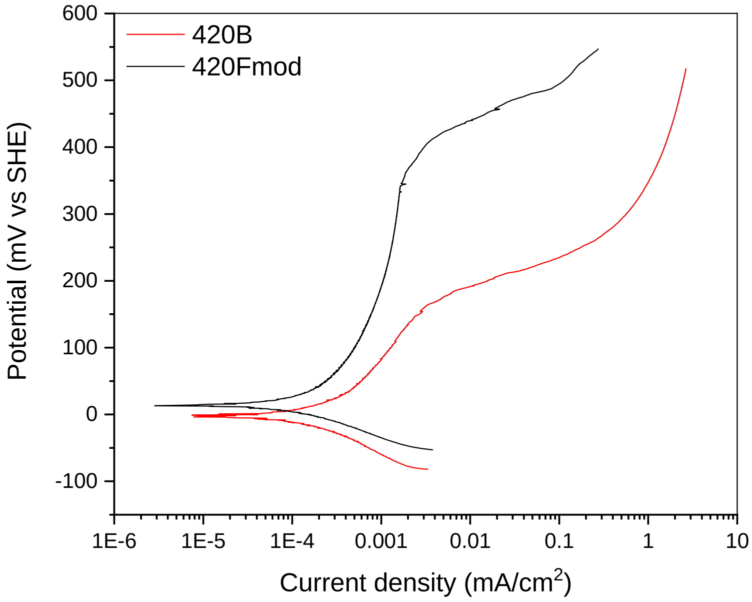

Figure 3.10: Potentiodynamic polarization curves of as received AISI 420Fmod and 420B ground surface without laser marking.

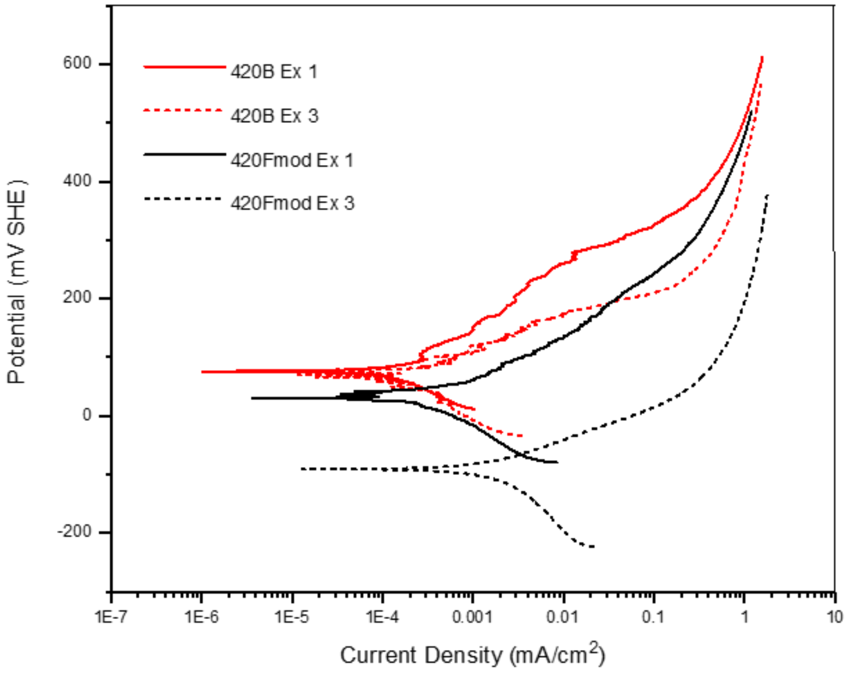

Figure 3.11: Potentiodynamic polarization curves of laser marked AISI 420Fmod (black) and 420B (red) with laser parameters #1 (solid) and #3 (dashed).

The data presented in Figure 3.11 shows that AISI 420Fmod exhibits limited passivity. Increasing the energy input from #1 to #3 reduces the corrosion potential by 145 mV (E_{corr}) and increases the corrosion current by approximately a decade (Table 3.3). No pitting potential can be determined in the polarization curves for 420Fmod; rather, this laser-marked steel manifests the characteristics of uniform corrosion. The corrosion current density increases approximately linearly with potential for almost three decades, indicating activation-controlled corrosion. This corrosion behavior enables the fitting of both cathodic and anodic Tafel slopes for assessment of the values reported in Table 3.3. The corrosion potential changes slightly on changing the laser marking parameters, whereas the passivity and pitting potential are reduced significantly for increased laser energy input. Figure 3.12 shows that a high energy input compromises the corrosion resistance, but also that it is material dependent. Generally, 420B performs better than 420Fmod and the corrosion potential is not as sensitive for an increase of the energy input from 100 to 200 J × cm^{-2}.

Table 3.3: Electrochemical values extracted via Tafel extrapolation from both anodic and cathodic Tafel curves. Values for unmarked samples are extracted by the cathodic Tafel curve and a horizontal line through the OCP. All values for laser marked specimens are averages of 3 measurements.

Laser Parameters	Material	E_{corr} (mV SHE)	i_{corr} (mA/cm^2)	β_c (mV/dec.)	β_a (mV/dec.)
#1	420F mod	32	$4.5 \cdot 10^{-4}$	-118	79
	420B	77	$1.6 \cdot 10^{-4}$	-99	68
#2	420F mod	36	$9.3 \cdot 10^{-4}$	-158	35
	420B	57	$1.4 \cdot 10^{4}$	-116	68
#3	420F mod	-113	$2.8 \cdot 10^{-3}$	-155	83
	420B	64	$1.6 \cdot 10^{-4}$	-100	51
#4	420F mod	-184	$6.9 \cdot 10^{-3}$	-200	80
	420B	-127	$4.2 \cdot 10^{3}$	-182	74
UM	420F mod	12	$1.9 \cdot 10^{-5}$	-57	-
	420B	-8	$1.1 \cdot 10^{-4}$	-70	-

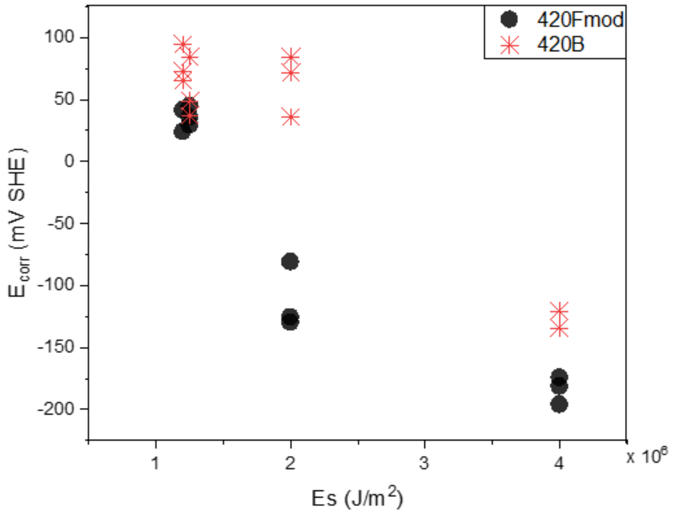

Figure 3.12: The measured corrosion potential vs the energy input of the laser marking.

3.4. Discussion

The present investigation identified two critical parameters that affect the corrosion resistance of martensitic stainless steels after laser-marking: the energy input of the laser and the chemical composition of the steel. Laser-markings with relatively high energy input were earlier reported to lead to the inferior corrosion resistance of austenitic stainless steels [10]. This was attributed to chromium depletion in the sub-surface region to form the chromium-containing oxide layer [9, 12]. A similar explanation may apply to the present martensitic stainless steels. As follows from Figure 3.12, the corrosion resistance is dramatically reduced, above a certain energy input during laser marking. Qualitative EDS of the oxide layer confirmed the presence of chromium-enrichment in the oxide layer, and an associated depletion of chromium in the underlying steel is faintly resolved with EDS. A steel with a relatively high chromium content is anticipated to perform best because it can tolerate more Cr-depletion before it loses its self-passivating performance at a threshold Cr-content in a solid solution of 10.5 wt% Cr. It should be noted that for lower energy inputs, the corrosion potential remains largely the same, which would be consistent with a remaining Cr content above the threshold value. AISI 420F mod and 420B have similar chemical compositions (see Table 3.1), apart from the substantial sulfur content, the presence of Mo, Ni, and the lower C content in 420Fmod steel. Even though in as-received condition 420Fmod shows better electrochemical performance than 420B (Figure 3.10 and Table 3.3), it performs poorer than 420B after laser marking for all conditions investigated, but particularly for the higher laser input. This difference in corrosion behavior should be discussed in relation to the observed microstructural changes in the near-surface regions of the steels after laser marking. Apart from the formation of an oxide layer under the consumption of Cr from the steel, the heat input is expected to lead to carbide dissolution. Upon repassing the laser beam, re-precipitation of Cr-based carbides (M23C6) would be expected. Considering the higher carbon content, this effect would be pronounced for 420B. Nevertheless, 420B shows the best electrochemical performance. Alternatively, a higher content of C in solid solution in austenite in 420B than in 420Fmod may be responsible for better electrochemical performance. In the respect, it is remarked that laser marking in air (with approximately 78 % N2) for surface oxidation may lead to local decarburization and nitrogen ingress. The presence of C and/or N in solid solution near the surface is interpreted as the cause for the stabilization of austenite in the heat-affected zone. The presence/absence of C/N in this region cannot be confirmed/excluded by EDS; instead, surface analytical investigation appears necessary. These will be the subject of future investigations.

The influence of the presence of MnS stringers on the electrochemical behavior after laser marking is discussed as follows. Comparing Figures 3.10 and 3.11, laser marking of 420Fmod results in a loss of the pseudo-passive behavior, even though the corrosion potential can be kept constant for relatively low heat input. Evidently, the interaction between the laser and protruding MnS results in the degradation of MnS. Access is then provided to the vulnerable material adjacent to MnS and underneath the oxide layer, which could have a higher content of sulfur or lower content of chromium than before laser marking [14–16]. A higher sulfur content would lower the activation energy for dissolution of metal, prevent re-passivation and promote corrosion. This would explain the difference between sulfur-containing and sulfur-free steels [20]. Access of the electrolyte to the sub-oxide region in 420Fmod is provided by the abundant craters and cracks that have formed in the oxide layer (cf. Figure 3.6b). It is likely that the craters on the surface of 420Fmod develop from thermal degradation of MnS by interaction with the laser. MnS should evaporate at temperatures > 1600 °C [21], which is certainly attainable with the investigated laser energies, depending on substrate absorptivity and heat capacity. After laser marking of 420Fmod, pit initiation is no longer required, as reflected by the absence of a pitting potential (cf. Figure 3.11), because essentially, the craters act as pits and still contain MnS at some distance from the surface. The presence of MnS inclusions in stainless steel affects the pitting potential adversely [22, 23]. It is suggested that the small white dots on top of the oxide layer in Figure 3.6b are redeposited metallic manganese. Upon entering through the craters and cracked oxide layer the electrolyte is expected to attack the shallow Cr-depleted zone. Accordingly, corrosion occurs sub-surface which can cause delamination of the oxide layers, accompanied by loss of contrast. In Figure 3.6d the result of corrosion attack is observed in the sub-surface with the oxide layer collapsing because of lack of support. This corroborates the hypothesis that corrosion takes place in a shallow Cr-depleted region below the oxide layer. Accordingly, the better corrosion resistance of 420B as compared to 420Fmod is explained by the smaller number of crater-like features, as a consequence of the lower sulfur and, thus, lower MnS content. Further improvement of the corrosion resistance after laser marking could be achieved by avoiding cracks in the oxide layer. It is inferred from Figure 3.12 that a thicker oxide layer leads to lower corrosion resistance. A thicker oxide layer implies more Cr-depletion in the underlying metal and promotes the occurrence of cracks. The origin of the cracks was not further investigated in this work, but it can be associated with the generation of tensile stresses in the oxide. Since the thermal expansion coefficient is smaller for oxide phases than for the metallic phases, a difference in thermal shrinkage does not cause tensile stresses in the oxide layer. A volume expansion in the region underneath the oxide layer could be martensite formation from austenite during cooling. Also, thermal gradients as imposed by local reheating on passing by an adjacent laser track could lead to the volume changes that lead to tensile cracking of the oxide layer. Hence, the hatch spacing is expected to play an important role. The origin and control of stresses during laser marking is the topic of future investigations.

The microstructural consequences of laser marking of martensitic stainless steel can be observed in the HAZ on Figure 3.5b and in the GIXRD phase analysis in Figure 3.9. The most obvious change is the formation of an oxide layer on top by a reaction between chromium from the substrate and oxygen from the atmosphere. Chromium is a strong oxide-forming element and the cation species in the oxide layer is primarily chromium, as shown by EDS analysis in Figure 3.7. During a laser pulse, tempered martensite in the HAZ is transformed to austenite; rapid cooling in-between pulses forms fresh martensite atop the original tempered martensite in the bulk. The content of retained austenite after laser marking is higher as evidenced by XRD in Figure 3.9. This could be observed as the featureless top part in the HAZ in Figure 3.5b. The top part of the HAZ has carbon from dissolved carbides and/or nitrogen dissolved from the ambient [19]. Promoting the ingress of nitrogen in the HAZ may compensate for the loss in corrosion resistance by Cr depletion because nitrogen has a large effect on the pitting resistance equivalent number (PREN) [24], provided that nitride formation is prevented. After laser marking the phase fraction of (retained) austenite decreases with depth until the retained austenite content of the unaffected steel is reached.

Summarizing, the successful application of UDI on stainless steel with oxidative laser marking requires optimization of material composition, oxide formation and laser parameters. An important factor in avoiding deterioration of the corrosion resistance after laser marking is selecting a steel free of manganese sulfides, as the abundant presence of such inclusions is equivalent to introducing pitting sites upon laser marking. Laser marking parameters should be chosen to achieve a compromise between low energy input and sufficient oxide layer thickness to obtain readable UDI. Moreover, a remedy for crack formation in the oxide layer has to be identified. Additionally, laser markings are preferably made on surfaces normal to the drawing/rolling direction, which is the direction of elongated MnS stringers. Laser marking on surfaces parallel to the drawing direction is anticipated to result in grooves instead of craters.

3.5. Conclusions

- The energy input during laser marking is a critical parameter; beyond a certain level, the inherent corrosion resistance of the stainless steel is adversely affected. If martensitic stainless steel has abundant MnS inclusions present as stringers, the critical energy input beyond which poor corrosion resistance is observed is significantly lower than for a MnS-lean steel quality of the similar composition.
- By interaction with the laser, MnS aligned normal to the marked surface will thermally degrade, leaving craters in the oxide layer. Such craters act as pits for corrosion, which is also reflected by uniform corrosion performance without identifiable pitting potential.
- The formation of a uniform protective oxide layer was not possible with the applied combination of laser marking parameters and martensitic stainless steels. Craters in the surface at the location of MnS inclusions and cracks in the oxide-layer provide routes for corrosion to degrade the Cr-depleted sub-oxide surface zone.

3.6. Acknowledgements

We are grateful to the head of engineering Henrik Andersen of Elos Medtech A/S, for most valuable support and for providing important industrial insight. Moreover, we are indebted to the workshop at Elos Medtech A/S for providing test specimens and access to industrial laser marking equipment.

3.7. References

[1] Regulation (EU) 2017/745 of the European Parliament and of the Council on Medical Devices, amending Directive 2001/83/EC, Regulation (EC) No 178/2002 and Regulation (EC) No 1223/2009 and repealing Council Directives 90/385/EEC and 93/42/EEC.

[2] The European Commision, Commision recommendation of 5 April 2013 on a common framework for a unique device identification system of medical devices in the Union. *Official Journal of the European Union .* (2013/172/EU).

[3] Wilson, Natalia, et al. “National Projections of Time, Cost and Failure in Implantable Device Identification: Consideration of Unique Device Identification Use.” Healthcare, vol. 3, no. 4, Elsevier B.V., 2015, pp. 196–201, doi:10.1016/j.hjdsi.2015.04.003.

[4] Gross, Thomas P., and Jay Crowley. “Unique Device Identification in the Service of Public Health.” New England Journal of Medicine, vol. 367, no. 17, Massachussetts Medical Society, 2012, pp. 1583–85, doi:10.1056/NEJMp1113608.

[5] Hack, Ruediger. “State-of-the-Art in Fiber Laser Marking.” Proceedings of Spie - the International Society for Optical Engineering, vol. 4974, 2003, pp. 202–08, doi:10.1117/12.484175.

[6] Lyubomir Lazov, Hristina Deneva, Pavels Narica. Laser Marking Methods, ch 1. *Environment Technology Resources.* 2015.

[7] Valette, S., et al. “Influence of Femtosecond Laser Marking on the Corrosion Resistance of Stainless Steels.” Applied Surface Science, vol. 252, no. 13, Elsevier, 2006, pp. 4696–701, doi:10.1016/j.apsusc.2005.07.161.

[8] Martin Kučera, Michal Švantner, Eva Smazalová. Influence of laser marking on stainless steel surface and corrosion resistance. *Lasers in Manufacturing Conference.* 2015.

[9] Lawrence, Samantha K., et al. “Environmental Resistance of Oxide Tags Fabricated on 304L Stainless Steel via Nanosecond Pulsed Laser Irradiation.” Surface and Coatings Technology, vol. 285, Elsevier, 2016, pp. 87–97, doi:10.1016/j.surfcoat.2015.11.021.

[10] Švantner, M., et al. “Thermal Effects of Laser Marking on Microstructure and Corrosion Properties of Stainless Steel.” Applied Optics, vol. 55, no. 34, OSA - The Optical Society, 2016, pp. D35–D45, doi:10.1364/AO.55.000D35.

[11] Pieretti, Eurico Felix, and Isolda Costa. “Surface Characterisation of ASTM F139 Stainless Steel Marked by Laser and Mechanical Techniques.” Electrochimica Acta, vol. 114, PERGAMON-ELSEVIER SCIENCE LTD, 2013, pp. 838–43, doi:10.1016/j.electacta.2013.05.101.

[12] Steyer, P., et al. “Surface Modification of Martensitic Stainless Steels by Laser Marking and Its Consequences Regarding Corrosion Resistance.” Surface Engineering, vol. 22, no. 3, TAYLOR & FRANCIS LTD, 2006, pp. 167–72, doi:10.1179/174329406X108861.

[13] Cai, D., et al. “Modelling the Evolution of MnS Inclusions and Macrosegregation during Solidification Using a Three-Phase Model.” Iop Conference Series: Materials Science and Engineering, vol. 861, no. 1, Institute of Physics Publishing, 2020, p. 012043, doi:10.1088/1757-899X/861/1/012043.

[14] Ryan, Mary P., et al. “Why Stainless Steel Corrodes.” Nature, vol. 415, no. 6873, NATURE PUBLISHING GROUP, 2002, pp. 770–74, doi:10.1038/415770a.

[15] Frankel, G. S. “Pitting Corrosion of Metals: A Review of the Critical Factors.” Journal of the Electrochemical Society, vol. 145, no. 6, Electrochemical Society Inc., 1998, pp. 2186–98, doi:10.1149/1.1838615.

[16] Reformatskaya, I. I., and L. I. Freiman. “Precipitation of Sulfide Inclusions in Steel Structure and Their Effect on Local Corrosion Processes.” Protection of Metals, vol. 37, no. 5, MAIK NAUKA/INTERPERIODICA/SPRINGER, 2001, pp. 459–64, doi:10.1023/A:1012370231337.

[17] Schmuki, P., et al. “The Composition of the Boundary Region of MnS Inclusions in Stainless Steel and Its Relevance in Triggering Pitting Corrosion.” Corrosion Science, vol. 47, no. 5, PERGAMON-ELSEVIER SCIENCE LTD, 2005, pp. 1239–50, doi:10.1016/j.corsci.2004.05.023.

[18] Hazra, J., et al. “Free Machining Steels—The Behavior of Type I MnS Inclusions in Machining.” Journal of Engineering for Industry, vol. 96, no. 4, 1974, pp. 1230–38, doi:10.1115/1.3438500.

[19] Berns, H. “Stainless Steels Suited for Solution Nitriding.” Materialwissenschaft Und Werkstofftechnik, vol. 33, no. 1, WILEY-V C H VERLAG GMBH, 2002, pp. 5–11, doi:10.1002/1521-4052(200201)33:1<5::AID-MAWE5>3.0.CO;2-V.

[20] P. Marcus, A. Teissier, J. Oudar, The influence of sulphur on the dissolution and the passivation of a nickel-iron alloy—I. electrochemical and radiotracer measurements, Corrosion Science, Volume 24, Issue 4, 1984, Pages 259-268, ISSN 0010-938X, https://doi.org/10.1016/0010-938X(84)90012-X.

[21] Valdez, M.E., Wang, Y. and Sridhar, S. (2004), In-Situ Observation of the Formation of MnS during Solidification of High Sulphur Steels. steel research international, 75: 247-256. https://doi.org/10.1002/srin.200405952

[22] Reformatskaya, I. I., and L. I. Freiman. “Precipitation of Sulfide Inclusions in Steel Structure and Their Effect on Local Corrosion Processes.” Protection of Metals, vol. 37, no. 5, MAIK NAUKA/INTERPERIODICA/SPRINGER, 2001, pp. 459–64, doi:10.1023/A:1012370231337.

[23] Meng, Q., et al. “Stainless-Steel Corrosion and MnS Inclusions.” Nature, vol. 424, no. 6947, Macmillan Magazines Ltd, 2003, pp. 389–90, doi:10.1038/424389b.

[24] R.A Perren, T.A Suter, P.J Uggowitzer, L Weber, R Magdowski, H Böhni, M.O Speidel, Corrosion resistance of super duplex stainless steels in chloride ion containing environments: investigations by means of a new microelectrochemical method: I. Precipitation-free states, Corrosion Science, Volume 43, Issue 4, 2001, Pages 707-726, ISSN 0010-938X, https://doi.org/10.1016/S0010-938X(00)00087-1.

4. Manuscript II: Effect of Manganese Sulfides and Nitriding on the Corrosion Resistance of Laser Marked Medical Martensitic Stainless Steel[8]

Nikolaj G. Henriksen – Elos Medtech, Denmark

Thomas L. Christiansen, Morten S. Jellesen, Marcel A. J. Somers – Technical University of Denmark, Department of Mechanical Engineering, Denmark

The medical device industry is required to apply unique device identification tags on multi-use equipment. In the industry, this is most commonly done via oxidative laser marking, which has been shown to decrease corrosion resistance of stainless steels locally in the laser marking. Two martensitic stainless steels, EN 1.4197 and 1.4028, commonly used in the medical industry, were subjected to high temperature solution nitriding, in an attempt to mitigate the loss of corrosion resistance associated with a subsequent laser marking. A nanosecond pulsed fiber laser was utilized to investigate different laser parameter sets on nitrided specimens. The key difference between the steels is that 1.4197 has been re-sulfurized to form MnS, while 1.4028 only contains MnS as impurities. An analysis of the microstructure and electrochemical properties was carried out to map the influence of nitrogen and different laser parameters. A positive effect of increased nitrogen content was not found, but instead nitriding resulted in a more severe laser oxidation. A large effect from the presence of abundant MnS and the laser energy input was identified.

Keywords: *Martensitic Stainless Steel – Manganese sulfide – Laser marking – Nanosecond pulsed laser – corrosion – Unique device identification – high temperature solution nitriding*

---

[8] Conference contribution: ESSC and DUPLEX 2022 - *11th European Stainless Steel Conference - Science and Market and 7th European Duplex Stainless Steel Conference and Exhibition. (2022). Essc and Duplex 2022 - 11th European Stainless Steel Conference* - Science and Market and 7th European Duplex Stainless Steel Conference and Exhibition. The format has been adapted to the format of this Ph.D. thesis.

4.1. Introduction: Laser Marking, Medical Device and Corrosion

In recent years the demands for unique device identification (UDI) markings have increased substantially, and all medical devices for multiple use are required to be marked with permanent UDI [1, 2]. UDI is applied for traceability and identification of equipment and, in extension, patient safety in case of a product recall [3]. In industry, the demands for a permanent and 'human readable' marking has been interpreted as a black laser marked UDI with high contrast to the substrate. These requirements combined with increased focus on testing corrosion properties have led to more issues with rust formation and UDI delamination on stainless steel products. The issues generally manifest as rusty stains or as a delamination of the black marking and thereby loss of contrast.

Laser marking of stainless steel can be realized in ablative or in oxidative mode. Ablative mode refers to a high power-density (in W/m^2) operation of the laser, so that the temperature locally reaches a level sufficient for evaporation. Accordingly, surface roughness contrast is achieved and generally the marking appears white. This mode of marking results in a negligible change in chemical composition of the exposed surface and thereby only a minor change in corrosion properties [4].

Oxidative mode operation of the laser provides black marking on a metallic substrate. As implied by the name, the power-density is adjusted to levels where ablation does not occur, but oxidation and possibly melting takes place [5]. The oxidative mode is by far the dominant method for laser marking of medical devices, and only oxidative mode laser marking is considered in this manuscript. Laser marking in air, as is predominantly applied, causes oxide forming elements from the substrate to react with atmospheric oxygen to form the black marking. It has been demonstrated that the corrosion resistance of the most commonly applied austenitic stainless steels EN 1.4301 and EN 1.4401 [6-9] as well as martensitic stainless steel EN 1.4028 [10], deteriorates by Cr-depletion underneath the oxide layer, as a result of providing and binding Cr to the oxide layer. In this work, it is investigated whether the negative effect of laser marking on the corrosion resistance could be mitigated by solution of nitrogen, which is known to improve corrosion resistance significantly [11], for instance regarding the pitting resistance equivalent number (PREN), which depends significantly on nitrogen content.

4.2. Materials and Methods

4.2.1. Materials

The materials investigated include two common martensitic stainless steels, that are widely utilized in medical device applications: EN 1.4197 and 1.4028 with the chemical compositions listed in Table 4.1. The main difference in chemical composition is the presence of sulfur and molybdenum in 1.4197. 1.4197 is a so-called free-machining steel, as it has been re-sulfurized to form sulfides (MnS). These sulfides act as a chip-breaking media, thereby enhancing machinability, surface finish and reducing tool wear [12]. Molybdenum is added to improve corrosion resistance and compensate for the negative effect from additional sulfur.

Both steels were supplied as drawn rods of 18mm and /12 mm for 1.4197 and 1.4028, respectively. Discs of 3mm thickness were cut from the rods. The surface was polished with 3µm diamond suspension as the last step prior thermochemical treatment. The discs were subjected to high temperature solution nitriding (HTSN) for 1 hour at 1080°C in 500 mbar N_2 gas, terminated by a gas quench in 6 bar nitrogen gas. Subsequently, the quenched specimens were tempered for 2 hours at 300°C in 1000mbar nitrogen.

Table 4.1**:** The chemical composition of the investigated steels. Carbon and sulfur were measured by infrared spectroscopy; heavier element contents were assessed with EDS.

CHEMICAL COMPOSITION								
Element (w%)	C	Si	Mn	S	Cr	Ni	Mo	Fe
EN 1.4197	0.21	0.4	1.5	0.27	12.7	0.8	1.1	Bal.
EN 1.4028	0.27	0.4	0.6	0.03	12.0	0.2	-	Bal.

4.2.2. Methods

4.2.2.1. Laser Marking

Laser marking was performed with a pulsed nanosecond YAG fiber laser (Y.0200, FOBA, Germany) on the nitrided and tempered discs, forming a black oxide over the entire sample surface. A criss-cross marking strategy at 90° offset angle was utilized, implying that the laser passed each location at the surface twice. Three sets of laser parameters were investigated (Table 4.2). The varied parameters include the average laser power (P), the laser scan speed, the power density (Pp) and the heat input (Es). The power density is calculated as:

$$Pp = \frac{E_p}{A \cdot t_p} \qquad [4.1]$$

where Ep is the energy of a single pulse, A is the area of the projected laser spot, and t_p is the pulse length. The heat input is calculated as:

$$E_s = \frac{P}{v \cdot l_s} \qquad [4.2]$$

where l_s is the hatch spacing.

Table 4.2: Laser parameters utilized for experiments.

Laser Parameters				
Parameter set	P (W)	v (m/s)	Pp (W/m^2)	Es (J/m^2)
#1	9	1.5	$3.1\cdot10^{11}$	$1.2\cdot10^{6}$
#2	5	0.8	$1.8\cdot10^{11}$	$1.3\cdot10^{6}$
#3	5	0.5	$1.8\cdot10^{11}$	$2.0\cdot10^{6}$

4.2.2.2. Microscopy

Light optical- and scanning electron microscopy were utilized. Light optical microscopy was performed using a Zeiss Axio Vert A1 microscope on epoxy embedded polished cross-sections. The embeddings were prepared with standard metallographic methods, finishing with 1µm diamond suspension polishing. The embeddings were then etched with Kalling's etchant, to reveal the microstructure.

Scanning electron microscopy (SEM) was performed with Zeiss Sigma microscope using an acceleration voltage of 20 kV. The SEM analysis included energy dispersive X-ray spectroscopy (EDS).

4.2.2.3. X-ray diffraction

X-ray diffraction (XRD) on a Bruker Discover D8 diffractometer was applied for qualitative phase analysis. The diffractometer was equipped with a Cr tube and diffractograms were recorded at scattering angles in the range 30-110º2ϴ. The wavelength of Chromium K_{α}-radiation was taken as 2.289 Å. The instrument was operated asymmetrically for grazing incidence X-ray diffraction (GIXRD) mode with an incidence angle of 5°.

4.2.2.4. Corrosion analysis

The corrosion analysis is reported as values achieved from Tafel extrapolation of electrochemical potentiodynamic polarization curves. Potentiodynamic polarization was performed in a Gamry PTC1 Paint Test Cell and Gamry PCT1 electrochemical masking tape, ensuring exposure of 1 cm^2 sample area. Only fully laser marked surfaces were investigated. Polarization occurred at 30 mV/min in a 0.1% NaCl electrolyte, using a saturated calomel reference electrode and an auxiliary graphite electrode. All potentials given refer to standard hydrogen potential (SHE). Before potentiodynamic polarization, open current potential was measured for 10 min and used to offset the polarization.

4.3. Results and Discussion

4.3.1. Light optical microscopy

Micrographs of nitrided and laser marked sample surfaces are given in Figure 4.1. Nitrided samples appeared significantly darker than non-nitrided specimen, despite identical laser marking parameters. As apparent from the difference between Figure 4.1a and b., there is an abundance of crater-like features on the 1.4197 (Figure 4.1a), while such features are not observed for the 1.4028 steel. It is likely that this is the result of interaction of the laser with MnS particles, forming craters by thermal degradation. MnS should evaporate at >1600°C, which is attainable with a pulsed nanosecond laser [13]. The darker laser markings of the nitrided samples are explained by a change in surface reflectivity after nitriding, as caused by the larger content of austenite at the surface, stabilized by the dissolution of nitrogen.

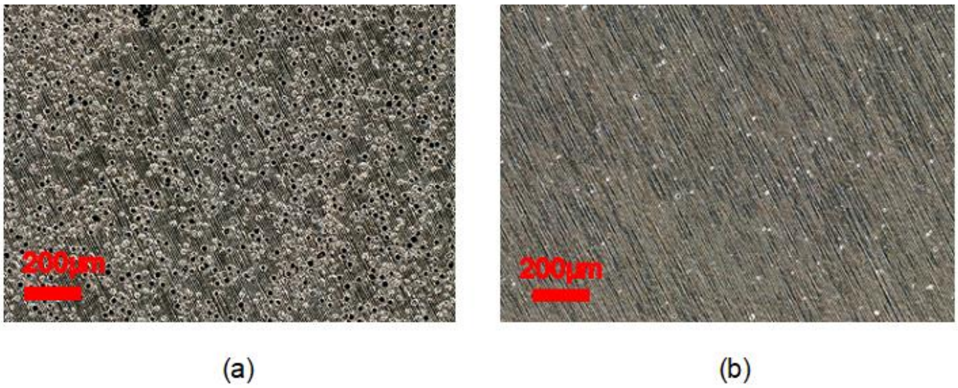

(a) (b)

Figure 4.1: LOM micrographs of laser marked surfaces of nitrided samples of (a) 1.4197 and (b) 1.4028.

Selected cross-sections of samples laser marked with parameter set #3 are shown in Figure 4.2, nitrided specimens of 1.4197 (a) and 1.4028 (b), while non-nitrided specimens are shown in (c) 1.4197 and (d) 1.4028. Some difference in microstructure is observed between 1.4197 and

1.4028(Figure 4.2 c/d), i.e., the presence of MnS stringers in 1.4197 (see arrows). The presence of sulfur and manganese was confirmed with EDS. The MnS stringer are a few microns wide and 30-50µm long; they are elongated parallel to the drawing direction. It is noted that the stringers protrude into the laser marked surface. Occasionally, MnS is observed in the 1.4028 steel. MnS should be considered an impurity, because it has a negative effect on the corrosion performance of stainless steel. The heat affected zone (HAZ) associated with laser marking is 4-6 µm deep for the non-nitrided samples, while it is 12-14 µm, twice as deep, for the laser-marked nitrided samples. For both 1.4197 and 1.4028 the amount of retained austenite has increased significantly after nitriding. This is attributed to the austenite-stabilizing effect of interstitially dissolved N, which causes a reduction in M_s. During laser processing, the material is heated to form austenite and then rapidly cooled to form fresh martensite. Nitriding the sample before laser marking increases the amount of retained austenite at the laser marked surface.

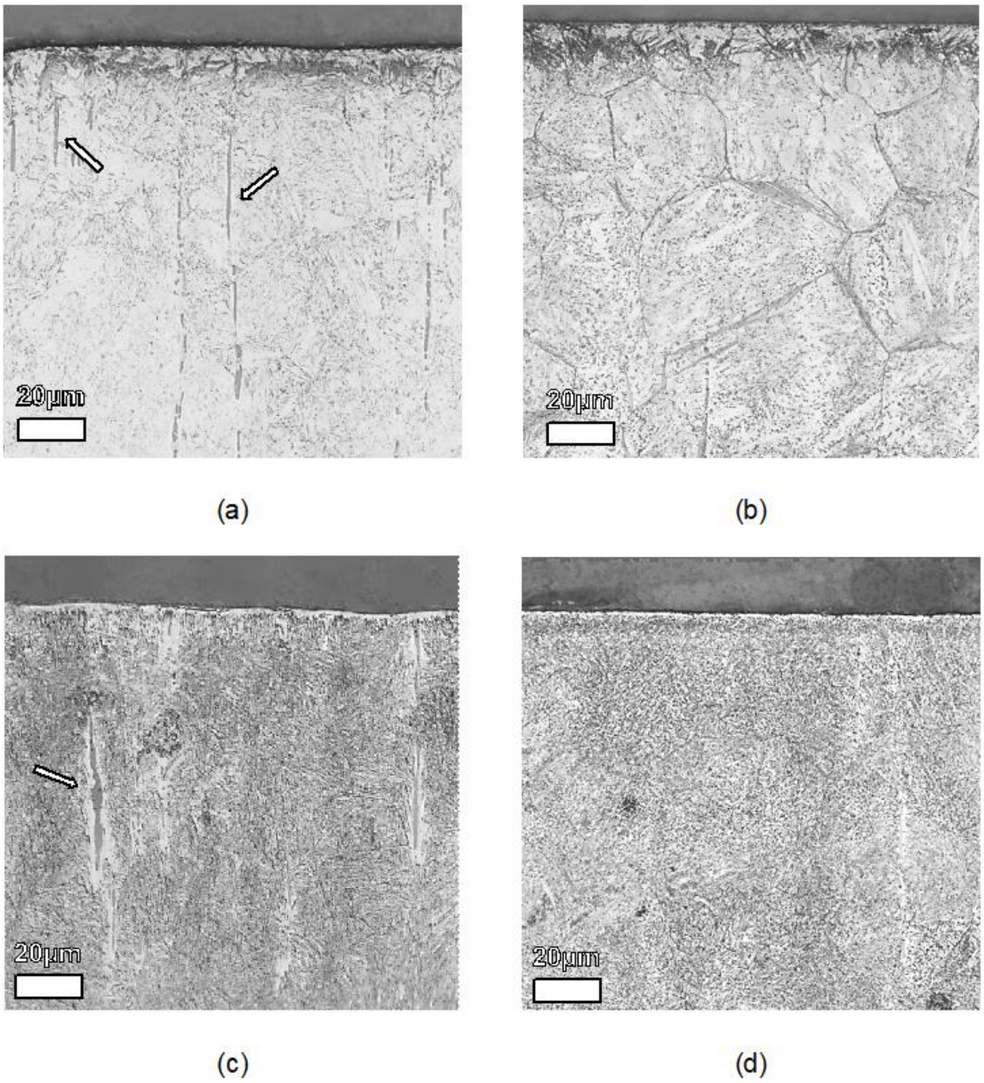

Figure 4.2: Etched cross sections of nitrided and laser marked 1.4197 (a), 1.4028 (b) and non-nitrided and laser marked 1.4197 (c) and 1.4028 (d).

4.3.2. Scanning electron microscopy and energy dispersive spectroscopy

SEM investigation of the nitrided surface (Figure 4.3) revealed that particles have formed on the surface of the samples. Two morphologies of particles are identified: triangular particles of 1-3μm protruding from the surface and shallower, less geometric particles. The triangular particles contain sulfur and manganese. These particles are likely the protruding MnS stringers developing facets during the prolonged high temperature treatment, while also extending further from the surface. The smaller particles are suggested to be surface (chromium) nitrides (see arrows on Figure 4.3). This could not be confirmed with EDS because the volume of such nitrides is much smaller than the relatively large interaction volume from which characteristic N K_α radiation originates.

Additionally, Figure 4.3 shows slip lines in the surface grains, resulting from the thermochemical treatment. During nitriding at 1080°C, all material would have been austenite. Undergoing quenching and cooling to room temperature, the bulk of the material will have transformed to martensite, while the surface remains largely austenitic due to the high concentration of FCC stabilizing nitrogen. This introduces a tensile stress state parallel to the surface from the difference in thermal expansion of austenite and martensite, and the volume expansion from the martensite transformation.

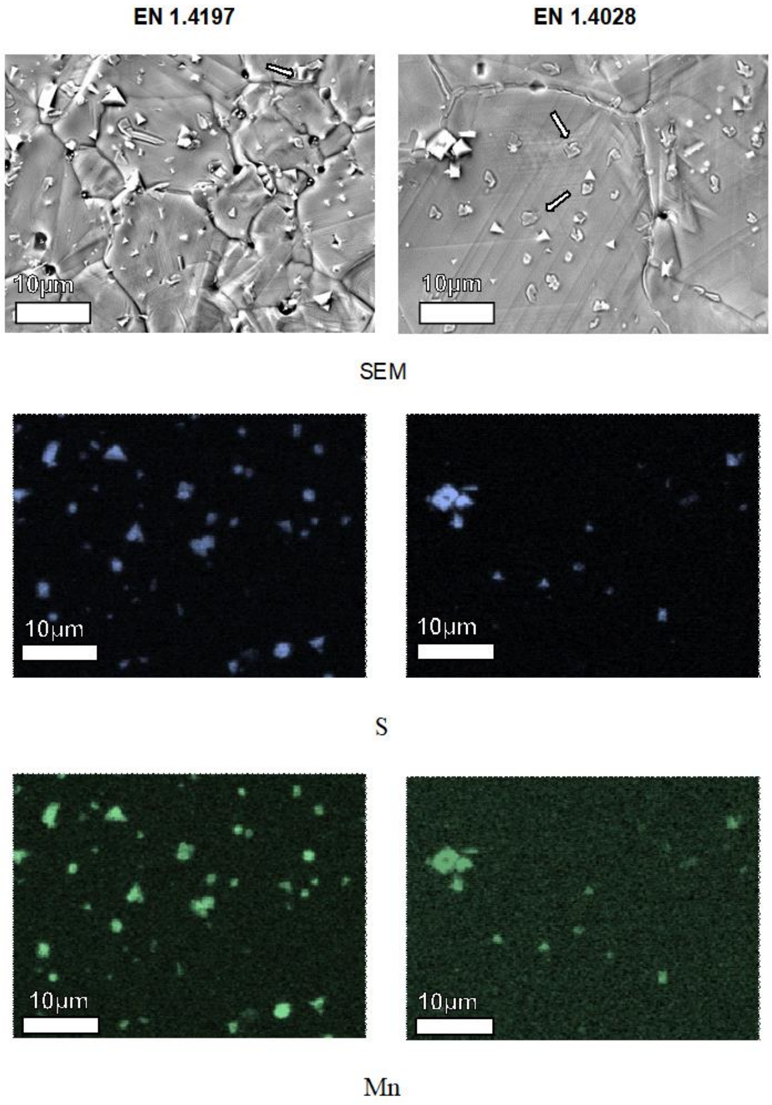

Figure 4.3: EDS maps of the unmarked surface of nitrided 1.4197 and 1.4028, showing the presence of sulfur- and manganese-containing particles on the surface.

4.3.3. X-ray Diffraction analysis

Examples of XRD phase analysis are provided in Figure 4.4 Comparison of the as-received and nitrided specimen, shows a significant increase in diffracted intensity of FCC austenite (γ-phase) as compared to martensite (α'-phase), consistent with austenite stabilization by interstitial nitrogen after high temperature solution nitriding. Only one peak can be related to MnS for the nitrided sample; mostly MnS remains undetected with grazing incidence XRD, probably because of the orientation of the MnS stringers and associated crystallographic texture, or that the phase fraction of MnS in the surface is simply low. After laser marking thermal degradation of MnS in the surface region hinders its detection.

The 200-martensite peak at ≈106°2Θ exhibits little change after laser marking a non-nitrided specimen. Nitriding of EN 1.4197 and quenching leads to a split of this peak into 200 and 002 because of tetragonality originating from the higher N content in the transforming austenite. Oxide peaks have a higher intensity for the laser-marked nitrided specimen than for the laser-marked non-nitrided specimen, consistent with the darker color of the nitrided specimens. The darker color and the higher oxide intensity are interpreted as a thicker oxide layer, meaning the nitriding of the martensitic stainless steel changes the subsequent (laser) oxidation. The slightly lower thermal conductivity of austenite could play a role, slowing the cooling and prolonging the oxidation. The presence of nitrogen could have an influence on oxidation kinetics or the laser absorption can have changed after nitriding.

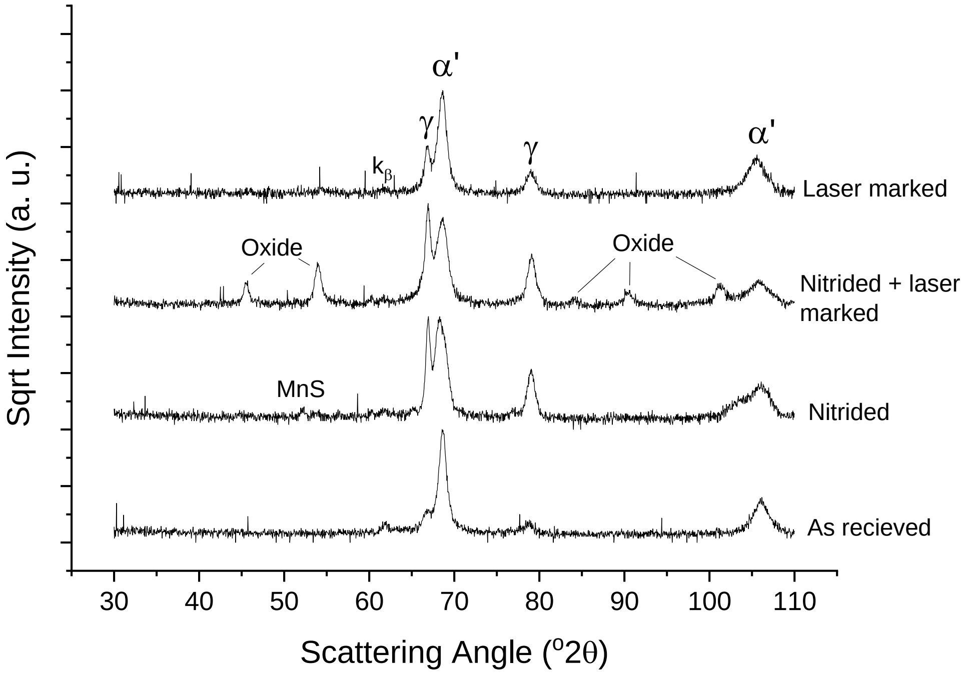

Figure 4.4**:** GIXRD of EN 1.4197 From the bottom, untreated surface, unmarked and nitrided, laser marked nitrided surface, and laser marked non-nitrided. Laser marked specimens were marked with parameter set #3.

4.3.4. Corrosion Analysis

Corrosion potentials determined by Tafel extrapolation of the polarization curves are shown in Figure 4.5 with dependence of laser heat input. Only values for the laser-marked specimens in nitrided and non-nitrided condition are given. Unmarked specimens are not included, because the surface roughness changes on laser marking, so unmarked specimens are not a valid reference. For the same reason the corrosion current density is not included, because the large unknown differences in corroding area can cause large variations in the calculated current densities, since there will be unknown differences between real and apparent surface area in exposure to electrolyte.

Evidently, 1.4197 has a consistently lower corrosion potential than sulfur free 1.4028, in agreement with deterioration of the corrosion resistance by the presence of MnS. The mechanisms suggested as responsible for poorer corrosion performance are local Cr-depletion around MnS inclusions during the manufacturing of the steel [14], or a sulfur crust from the corroding MnS [15]. The results in Figure 4.5 show that the negative effect of MnS cannot be mitigated by pre-nitriding the steel.

Rather, for lower laser heat inputs a trend is observed that the corrosion resistance is poorer. The data suggests some improvement at higher heat inputs, when Cr-depletion is severe, and the presence of nitrogen could compensate for this, because it has a large effect on the PREN number. For EN 1.4028 nitriding does not appear to affect the corrosion performance; the corrosion potential is not changing for the investigated range of heat input. It is anticipated that for higher heat input, the corrosion resistance must deteriorate due to more pronounced Cr-depletion in the subsurface.

Even if EN 1.4197 contains slightly more chromium as well as additional molybdenum, the presence of MnS renders the steel unsuitable for laser marking. This cannot be mitigated by increasing the amount of nitrogen to increase the corrosion potential. A sulfur free steel is strongly recommended if laser marking is essential, and the product should be used multiple times.

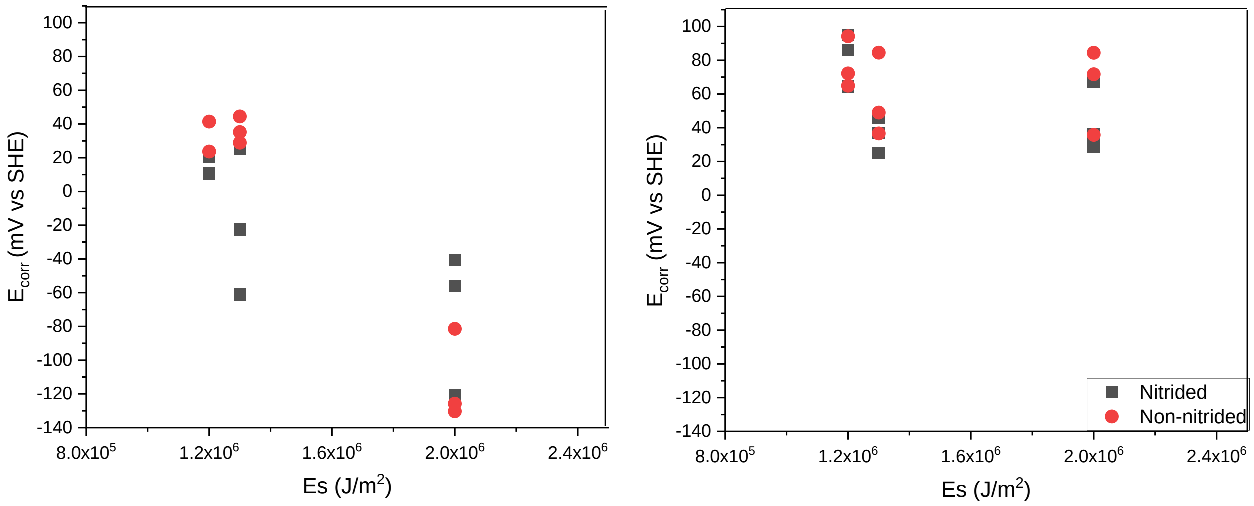

(a) (b)

Figure 4.5: Corrosion potential extracted by Tafel extrapolation of polarization curves in dependence of the laser heat input for (a) sulfur containing EN 1.4197 and (b) sulfur free EN 1.4028.

4.4. Conclusions

Based on the results and discussion of this manuscript, the following conclusions can be reached:

- Laser marking reduces corrosion resistance. When operating in the oxidative regime, it can be concluded that as the laser heat input (J/area) increases it compromises the corrosion resistance. There are indications that this deterioration is less pronounced in high nitrogen steels.

- High temperature solution nitriding does not inherently improve corrosion resistance. A higher content of nitrogen is expected to improve the corrosion resistance (higher PREN value), but other mechanisms as a potentially higher Cr-depletion as a consequence of different substrate-laser interaction of nitrided specimens, results in no improvement of corrosion resistance.
- The presence of MnS affects the corrosion resistance of the laser marked steels negatively, and the choice of a high-quality steel with low sulfur content has a higher effect on corrosion resistance than high temperature solution nitriding.

4.5. References

[1] Regulation (EU) 2017/745 of the European Parliament and of the Council on Medical Devices, amending Directive 2001/83/EC, Regulation (EC) No 178/2002 and Regulation (EC) No 1223/2009 and repealing Council Directives 90/385/EEC and 93/42/EEC.

[2] The European Commision, Commision recommendation of 5 April 2013 on a common framework for a unique device identification system of medical devices in the Union. Official Journal of the European Union . (2013/172/EU).

[3] P. Tracol, Materials vigilance and traceability, Orthopaedics & Traumatology: Surgery & Research, Volume 102, Issue 1, Supplement, 2016, Pages S95-S103, ISSN 1877-0568, https://doi.org/10.1016/j.otsr.2015.05.013.

[4] Steyer, P., et al. “Surface Modification of Martensitic Stainless Steels by Laser Marking and Its Consequences Regarding Corrosion Resistance.” Surface Engineering, vol. 22, no. 3, TAYLOR & FRANCIS LTD, 2006, pp. 167–72, doi:10.1179/174329406X108861

[5] Hack, Ruediger. “State-of-the-Art in Fiber Laser Marking.” Proceedings of Spie - the International Society for Optical Engineering, vol. 4974, 2003, pp. 202–08, doi:10.1117/12.484175.

[6] Martin Kučera, Michal Švantner, Eva Smazalová. Influence of laser marking on stainless steel surface and corrosion resistance. Lasers in Manufacturing Conference. 2015.

[7] Lawrence, Samantha K., et al. “Environmental Resistance of Oxide Tags Fabricated on 304L Stainless Steel via Nanosecond Pulsed Laser Irradiation.” Surface and Coatings Technology, vol. 285, Elsevier, 2016, pp. 87–97, doi:10.1016/j.surfcoat.2015.11.021.

[8] Švantner, M., et al. “Thermal Effects of Laser Marking on Microstructure and Corrosion Properties of Stainless Steel.” Applied Optics, vol. 55, no. 34, OSA - The Optical Society, 2016, pp. D35–D45, doi:10.1364/AO.55.000D35.

[9] Pieretti, Eurico Felix, and Isolda Costa. “Surface Characterisation of ASTM F139 Stainless Steel Marked by Laser and Mechanical Techniques.” Electrochimica Acta, vol. 114, PERGAMON-ELSEVIER SCIENCE LTD, 2013, pp. 838–43, doi:10.1016/j.electacta.2013.05.101.

[10] Steyer, P., et al. “Surface Modification of Martensitic Stainless Steels by Laser Marking and Its Consequences Regarding Corrosion Resistance.” Surface Engineering, vol. 22, no. 3, TAYLOR & FRANCIS LTD, 2006, pp. 167–72, doi:10.1179/174329406X108861.

[11] Hao Feng, Zhouhua Jiang, Huabing Li, Pengchong Lu, Shucai Zhang, Hongchun Zhu, Binbin Zhang, Tao Zhang, Dake Xu, Zhigang Chen, Influence of nitrogen on corrosion behaviour of high nitrogen martensitic stainless steels manufactured by pressurized metallurgy, Corrosion Science, Volume 144, 2018, Pages 288-300, ISSN 0010-938X, https://doi.org/10.1016/j.corsci.2018.09.002.

[12] Hazra, J., et al. “Free Machining Steels—The Behavior of Type I MnS Inclusions in Machining.” Journal of Engineering for Industry, vol. 96, no. 4, 1974, pp. 1230–38, doi:10.1115/1.3438500.

[13] Valdez, M.E., Wang, Y. and Sridhar, S. (2004), In-Situ Observation of the Formation of MnS during Solidification of High Sulphur Steels. steel research international, 75: 247-256. https://doi.org/10.1002/srin.200405952

[14] Reformatskaya, I. I., and L. I. Freiman. “Precipitation of Sulfide Inclusions in Steel Structure and Their Effect on Local Corrosion Processes.” Protection of Metals, vol.

37, no. 5, MAIK NAUKA/INTERPERIODICA/SPRINGER, 2001, pp. 459–64, doi:10.1023/A:1012370231337.

[15] Ryan, Mary P., et al. “Why Stainless Steel Corrodes.” Nature, vol. 415, no. 6873, NATURE PUBLISHING GROUP, 2002, pp. 770–74, doi:10.1038/415770a.

5. Supplementary Work: Effect of Citric Acid Passivation on Laser-Marked Stainless Steel

Chemical passivation has long been embraced as a standard method for enhancing the corrosion resistance of metallic medical devices for many years. Traditionally, nitric acid was utilized, but the industry has now embraced the safer and greener alternative of citric acid for passivation. The effect of chemical passivation on laser marked stainless steel has not been investigated in the scientific literature. It is unknown if the steel requires re-passivation or can be re-passivated at all with citric acid after the thermal process of oxidative laser marking. The effect of citric acid passivation on laser-marked stainless steel is investigated in this chapter.

5.1. Materials and Methods

5.1.1. Material

The samples in the form of discs were cut from a drawn rod of AISI 304L austenitic stainless steel with a diameter of 10 mm. The nominal composition is reported in Table 5.1. The discs were cut via lathe turning to 3 mm thickness without removal of the turned surface, thereby imitating the actual condition of manufactured components. Consequently, the surface area during electrochemical analyses and the degree of deformation are not precisely known.

Table 5.1: The nominal chemical composition of AISI 304L stainless steel.

Element	C	Si	Mn	P	S	N	Cr	Ni	Fe
wt.%	< 0.03	< 1.00	< 2.00	< 0.045	< 0.03	< 0.10	17.5-19.5	8-10.5	Bal.

5.1.2. Methods

5.1.2.1. Laser marking

Laser marking was performed with the Foba Y.0200 YAG pulsed nanosecond fiber laser with parameters chosen for oxidative laser marking. One parameter set with a high heat input at $2 \cdot 10^6$ J/m^2 and a power density of $1.8 \cdot 10^{11}$ W/m^2 was chosen as a slight exaggeration from currently applied industrial parameters.

5.1.2.2. Chemical Passivation

Citric acid passivation was performed at different stages of the manufacturing process in accordance with the ASTM A 967 standard for chemical passivation treatments for stainless steel parts. A citric acid content of 10 wt % was used at a temperature of 35 ± 2 °C for 20 min to conform with the subcategory of ‘Citric 3’ passivation, as it is a widely requested passivation process by Elos Medtech customers. Chemical passivation is applied on both the lathe-turned and laser-marked surface, to determine whether laser marking can benefit from chemical passivation. Specimen without laser marking and/or passivation were also included to act as reference specimen and determine the effect of passivation on the turned surface.

5.1.2.3. Corrosion Analysis

Samples were analyzed by electrochemical potentiodynamic polarization in the Gamry PTC1 cell, using a saturated calomel reference electrode. The specimens were first subjected to open current potential (OCP) measurements for 10 minutes, followed immediately by potentiodynamic polarization. The chamfering of the specimens was left exposed, as it is often the site of corrosion initiation on specimens which are not laser marked. Polarization was performed in a range of -100 to +500 mV offset to the measured OCP with a scan speed of 20 mV/min. Measured voltages have been recalculated and are reported with respect to the standard hydrogen electrode (SHE). The electrolyte was a 1 wt % sodium chloride solution, similar to the isotonic saltwater solution commonly used in dental practices for disinfection.

5.2. Results and Discussion

Figure 5.1 contains images of the samples before and after laser marking. Figure 5.1a shows the unmarked specimen, where the tracks from lathe turning are clearly visible. This is the state of the surface that would be laser marked and of products which are not laser marked. Figure 5.1b shows the sample after laser marking, where a dark layer has formed and the tracks from the lathe turning are only hardly visible. Laser marking with the utilized parameter set yields a satisfactory result, as enough contrast is generated to produce a readable marking.

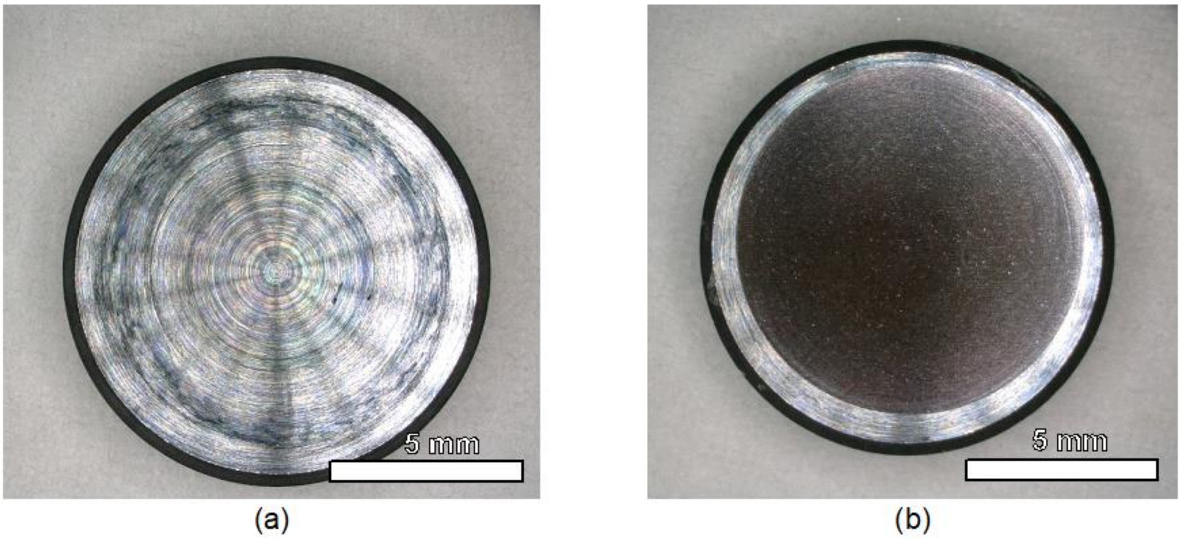

Figure 5.1: Images of the specimen (a) before laser marking with a turned surface and (b) after laser marking and the formation of dark oxide.

Electrochemical corrosion testing on the unmarked specimen resulted in preferential corrosion in the chamfering of the sample, as observed in Figure 5.2a. It is well-known that corrosion will be more likely to happen in areas with higher surface roughness and at edges, rendering the chamfering an obvious site for corrosion. On an unmarked specimen, corrosion will happen in areas with lower corrosion resistance as a result of the machining, which in the case of the investigated specimen, will be the chamfering and not the turning tracks. Some smaller pits are also visible in the center of the sample, but significant corrosion occurred only in the chamfering.

Chemical passivation resulted in significantly fewer pits forming, both in the large flat surface and in the chamfering. Some signs of corrosion could be observed, they were however less severe than for the non-passivated part. A positive effect from chemical passivation can be documented, as it appears to function as intended; by enhancing the already inherent corrosion resistance of stainless steel, removing pit initiation sites, and enabling the formation of a coherent passive film across the specimen.

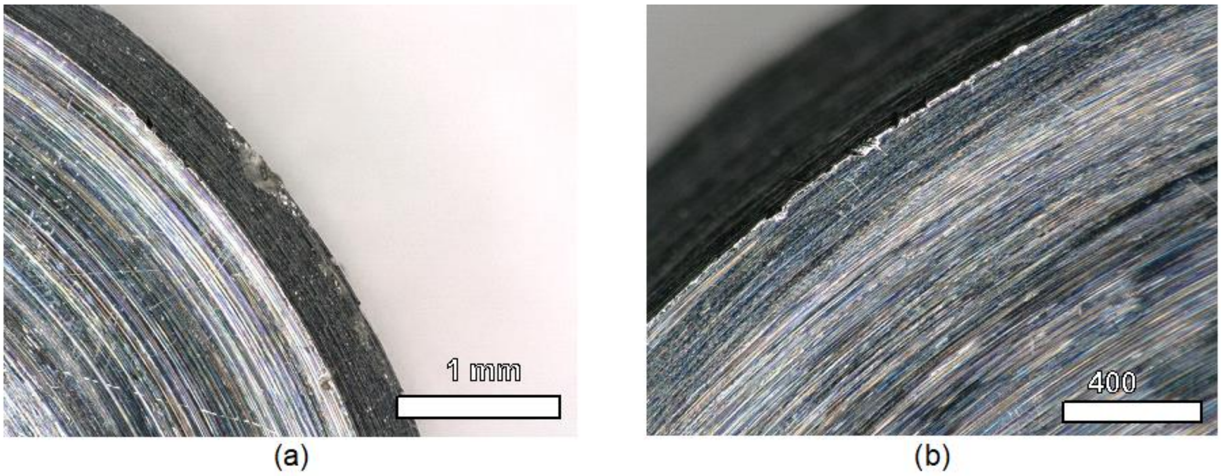

Figure 5.2: Images of material loss due to corrosion in (a) unmarked specimen with turned surface and (b) unmarked specimen which has been chemically passivated.

Laser marking the specimen leads to more visible corrosion, as can be observed in Figure 5.3a., where the oxide layer has delaminated at many locations. The delamination is concentrated in the middle of the sample and in the edges of the laser-marked area. If chromium depletion has occurred in the laser marked sub-surface and the electrolyte has access to it, galvanic coupling between the higher chromium base material and the lower chromium laser-marked sub-surface, can have been the cause for the preferential corrosion in the edges. It should be mentioned that after corrosion testing, the oxide layer could be rinsed or wiped off, as it had been reduced to flakes and particles. This indicates that the oxide itself is not corroding during testing, but rather the steel. As there has evidently been far greater corrosion in the laser marked sample, compared to the unmarked sample in Figure 5.2a, it appears that laser marking substantially increases the risk of corrosion and can be detrimental for the performance of the laser markings. Other repetitions of the same treatment showed similar delamination; however, the corrosion was not as limited to the middle and edge of the laser marking.

Figure 5.3b shows the specimen that was chemically passivated after laser marking. As compared to the non-passivated specimen in Figure 5.3a, it is obvious that chemical passivation after laser marking has a positive effect in that substantially less delamination has occurred. Instead, delamination appears to be limited to two areas of the specimen, where pitting occurred was present. One of the pits is indicated on Figure 5.3b. Corrosion has most likely developed underneath the oxide layer, spreading concentrically from the initiation sites. From the magnified area in Figure 5.3b, it is clear that a few larger pits are present, surrounded by shallow corrosion and delamination. Notably, a large pit is present at the edge of the laser marking and the chamfering. The repetitions of the laser-marked and passivated specimen showed corrosion to a similar (or lesser) degree as the specimen shown in Figure 5.3b. In previous research it was shown that laser marking can result in substantial crack formation and or pit formation by thermal degradation of MnS inclusions. Chemical passivation enables effective re-passivation of potential pit initiation sites, or sites for crevice/pitting corrosion, and thereby significantly increases the resistance to corrosion underneath the marking and prevents delamination.

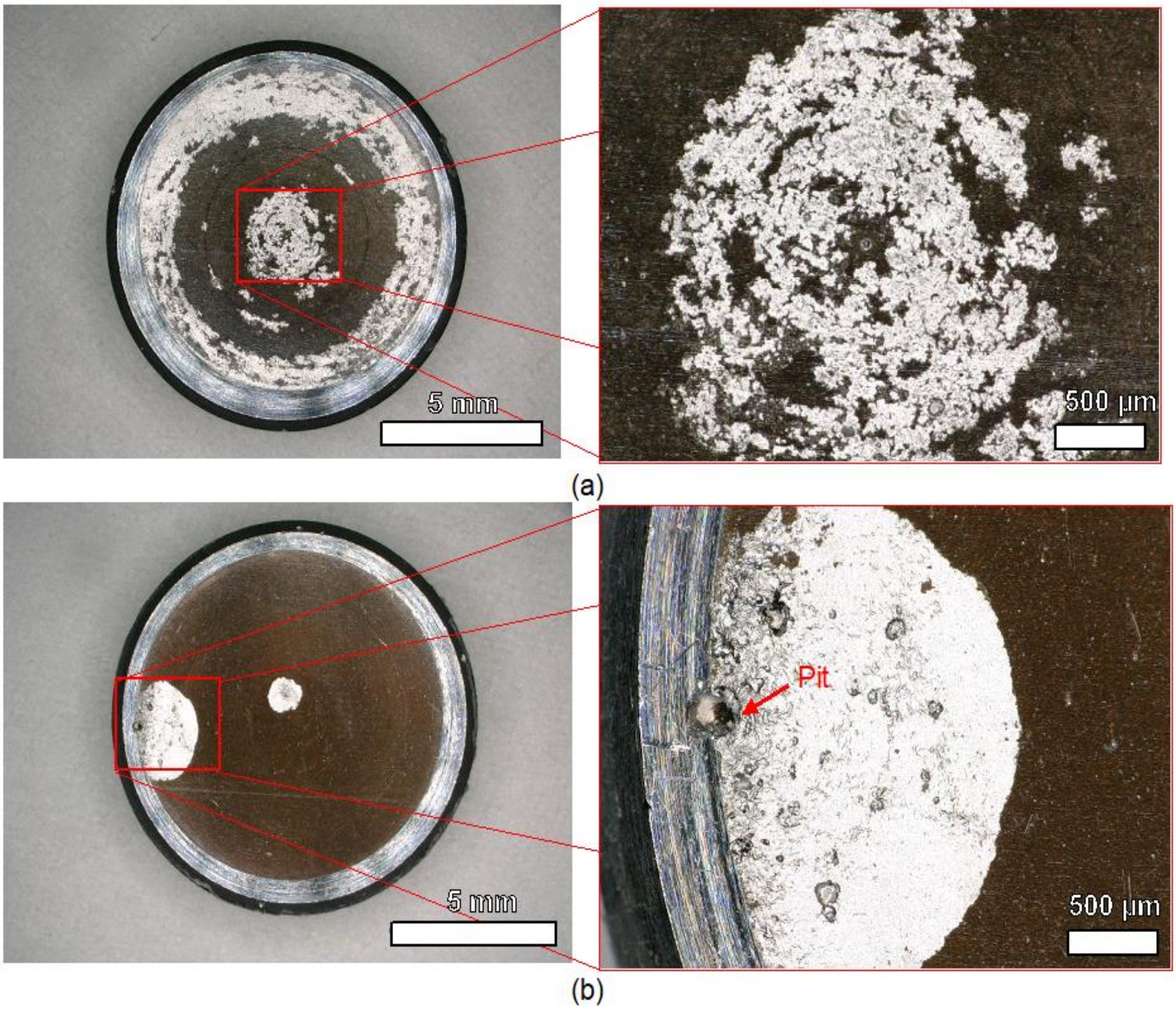

Figure 5.3: images of the laser marked specimen after corrosion testing (a) laser marked sample, (b) Laser marked followed by chemical passivation.

Potentiodynamic polarization curves for the unmarked specimen with and without chemical passivation are reported in Figure 5.4. The reference specimen with the lathe-turned surface, exhibits a corrosion potential at around 250 mV, followed by a passive regime from 260 to 450 mV where the pitting potential is reached. Substantial metastable pitting (reflected as spikes in the passive region) happens before the pitting potential is reached and the pits are unable to re-passivate. The turned specimen has a relatively rough surface and iron particles may be embedded into the material. Therefore, there may be pit initiation sites present on the surface, which will re-passivate after initial corrosion. Passivating the material yields a smoother polarization curve with little metastable pitting, only appearing as the actual pitting potential is approached. The passivated part has a similar pitting potential as the reference specimen, and the corrosion potential appears slightly lower after passivation. There is an overall positive effect of chemical passivation as was also observed upon visual inspection of the parts in Figure 5.2.

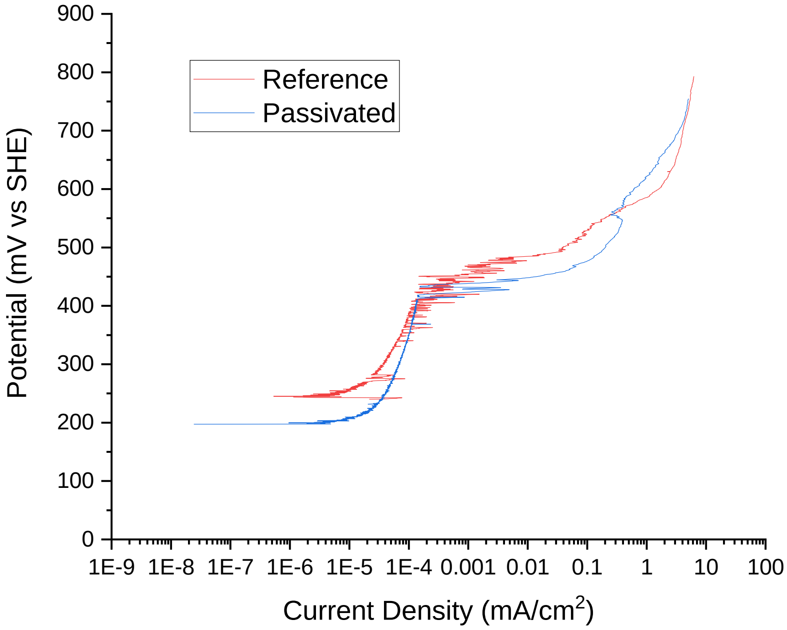

Figure 5.4: Potentiodynamic polarization curves for the reference specimen (red) and the passivated unmarked specimen (blue).

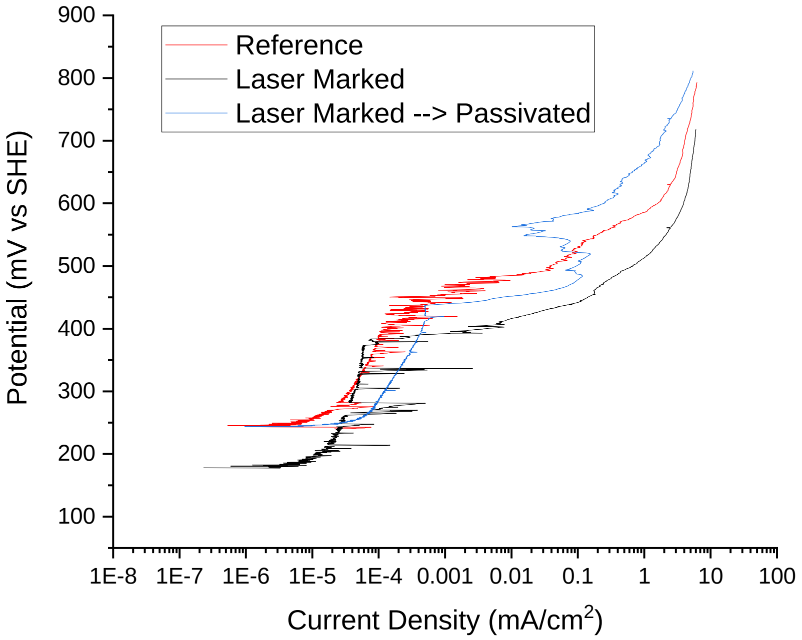

Figure 5.5: Potentiodynamic polarization curves of the reference specimen (red), laser marked specimen (black) and laser marked followed by chemical passivation (blue*).*

The effect on the potentiodynamic polarization of laser marking and passivation of laser markings can be seen on Figure 5.5. It is observed that laser marking lowers both the corrosion- and pitting potential by almost 100 mV. The laser marking is more susceptible to pitting than the chamfering and base material and this could be achieved by either chromium depletion or formation of crevices/pits on the surface. The subsurface is not likely to be protected by a passive film, so corrosion occurs underneath the oxide layer. It is noted that the investigated steel has a relatively high chromium content, so some passivity is retained. It is anticipated that a steel with lower initial chromium content is more severely attacked by corrosion after laser marking with the same laser parameters, because Cr-depletion by oxide formation will bring the steel locally in the active region. The polarization curve reflects the visual inspection in Figure 5.3 as it is obvious that substantial metastable pitting takes place, and more corrosion should have occurred during the experiment. Passivation of the laser-marked specimen yields a significantly different potentiodynamic polarization of the specimen. Several positive effects can be observed: The occurrence of metastable pitting is substantially reduced, the corrosion- and pitting potentials are equal to those of the unmarked specimen. It should be noted that interpreting the differences in current density should be performed with care, because the corroding area is unknown after laser marking. As corrosion takes place initially in pit initiation sites and/or cracks, and then continues below the oxide, the corroding area depends strongly on how much of the sub-surface has access to electrolyte. A comparison could be done between the unmarked specimen, even if there is an uncertainty to be found in the high surface roughness of the lathe-turned surface.

For application within the biomedical field, chemical passivation is strongly recommended, especially after a procedure such as laser marking, where corrosion resistance is compromised. Utilizing this process can potentially increase the corrosion resistance of the laser marked area to match that of the unmarked part. Laser marking without chemical passivation can cause full delamination of the marking, rendering the product unfit for application. As medical devices are subjected to harsh corrosive environments during sterilization/disinfection, such as autoclavation at >130 °C and isotonic saltwater, retaining corrosion resistance is of utmost importance. Care should be taken passivating steels with relatively low chromium content because citric acid solution could initiate corrosion in the base material and not only dissolve material at pit initiation sites.

5.3. Conclusions

The following conclusions can be drawn:

- There is a positive effect from chemical passivation of unmarked AISI 316L, because a significant reduction in metastable pitting, pit size and number of pits, can be achieved.
- Laser marking of AISI 316L promotes corrosion, causing delamination of the oxide layer. Pitting occurs at a lower applied potential than for material without laser marking.
- Chemical passivation of laser marked surfaces can improve the corrosion resistance to the level of the unmarked material.
- Obviously, chemical passivation of laser markings is recommended.

6. Manuscript III: Residual Stress Generation in Laser Marked Martenstic Stainless Steel and Dependence on Laser Parameters

Nikolaj G. Henriksen1), Thomas L. Christiansen 2), Laurent Barrallier 3) Sébastien Jegou3), Marcel A. J. Somers2)

1) Elos Medtech, Engvej 33, 3330 Gørløse, Denmark, nikolaj.henriksen@elosmedtech.com

2) Technical University of Denmark, Department of Civil and Mechanical Engineering, Produktionstorvet b. 425, 2800 Kgs. Lyngby, Denmark

3) Arts et Métiers, cours des Arts et Métiers 13617 Aix en Provence cedex 1 France

The effect of oxidative laser marking was investigated on martensitic stainless steel to determine the effect on the chemical composition and state of residual stress. Different hatch spacings resulting in laser markings with laser track overlaps of 83 %, 50 % and tracks with no overlap were investigated. An oxide layer was observed with scanning electron microscopy on the specimen with high track overlap and identified as either Fe_3O_4 or $FeCr_2O_4$ with X-ray diffraction (XRD). The oxide layer was confirmed to contain chromium iron and oxygen with Glow Discharge-Optical Emission Spectroscopy. Additionally, laser marking altered the chemical composition significantly, most notably causing chromium depletion underneath the oxide layer. Evidence of melting was observed several µm below the oxide layer. No detectable oxide layer was produced for larger hatch spacing. Adjusting the scan speed of the laser to increase the heat input, an oxide layer was formed in the central part of the laser tracks, while melting occurred in between the tracks without forming an oxide layer. This resulted in an oxide layer with a large variation in thickness. Residual stresses were investigated with XRD for a series of constant information depths forming a cumulative residual stress profile from 0.75 to 2 µm in the steel. It was found that laser marking with low hatch spacing resulted in high tensile stresses parallel to the surface in the very surface. The strain-free lattice parameter was lower close to the surface, which was attributed to the altered chemical composition, most notably the depletion of chromium. Specimens with no oxide layer also had a tensile stress state, albeit significantly lower. The specimen laser marked with large hatch spacing and low scan speed had a surface of highly heterogeneous stress states, reflected a high uncertainty in the measured stress values. The cumulative stress state was compressive at the very surface and changed to tensile with depth.

6.1. Introduction

6.1.1. Background and Motivation

In 2013 the European Union proposed a common framework for unique device identification (UDI) that has affected all products in medical applications [1]. The purpose of UDI is to warrant traceability and thereby reduce the risk of failures, which potentially could harm patients or cause a more critical course of illness. Many man hours are spent identifying the cause of failures in, for example, implants. Lack of traceability seriously prolongs such root cause analysis and inhibits proper action [2]. Presently, all medical device products for multiple uses are required to have UDI applied directly on the product, provided that the surface of the product can accommodate such a marking and the marking itself does not endanger the patient [3].

Laser marking has been embraced as the standard for medical device industry metallic products for multiple use [4], [5], because it offers a high degree of flexibility and customizability. Moreover, the common perception is that laser markings are permanent and thus warrant traceability [6]. Laser marking is subdivided in two distinct categories: ablative and oxidative. Ablative laser marking, also called laser engraving, generates contrast by material removal while scanning a laser with high power density (W/area). The laser is typically run at lower pulse frequency, to locally ablate and/or melt material [4]. The difference in surface roughness and height usually appears as white contrast on a metallic substrate. Oxidative laser marking generates contrast by locally growing an oxide layer and is the standard for laser marking of medical devices. In this manuscript, only oxidative laser marking is investigated.

The contrast and readability of UDI produced via oxidative laser marking comes from the growth of a black oxide layer on top. The power density (W/area) is chosen to reach a temperature that is high enough to accomplish a local chemical reaction with gaseous species from the atmosphere. Potentially this results in some degree of melting. The degree of oxidation for a chosen parameter set depends on the heat input (J/area). A higher heat input at a fixed power density enables the growth of a thicker oxide layer [4], [7]. In practice, this produces a darker oxide and higher contrast.

Residual stresses are present in most metallic components and products, and result from the manufacturing history. For steel, residual stresses are usually a consequence of mechanical, chemical or thermal processing, as deformation, chemical and temperature gradients lead to inhomogeneous volume changes, causing strains and associated stresses in a material. Lathe turning will, depending on the tool geometry and thermal effects, lead to compressive residual stresses in the surface of machined components with a steep gradient towards the interior [8]. The result of the thermal history on the state of residual stress depends strongly on the possible phase transformations; this is well-researched, especially in relation to welding [9]. Generally, compressive residual stresses are preferred in the surface-adjacent region of a component because it prolongs the fatigue life of a component, by postponing crack initiation and retarding crack growth. For this reason, specific treatments are routinely applied to introduce compressive stresses, such as rolling [10], shot peening [11], induction hardening and thermochemical treatments as carburizing and nitriding [12]. The source of the compressive residual stress in these treatments is a volume expansion near the surface by local plastic deformation, local phase transformation and/or local change in chemistry.

For stainless steels the residual stresses introduced by thermal processing (as laser treatment) depends on the type of steel. For (mono-phase) austenitic and ferritic stainless steels heating of the surface will lead to thermal expansion. As the yield stress is much lower at elevated temperature the thermal strain is accommodated plastically. Consequently, on cooling to room temperature, thermal shrink leads to tensile residual stresses. For martensitic stainless steels, the volume expansion associated with austenite-to-martensite transformation occurring under sufficiently fast cooling, counteracts the thermal stress, and adds a compressive residual stress component in the near-surface region [13].

Laser surface treatment is applied commercially for improvement of wear resistance of martensite-forming steels by increasing the hardness and introducing compressive residual stresses [14], [15]. It has been found that if the laser surface treatment is performed with a large degree of overlap of the laser tracks, the residual stress state can become tensile and reduce the wear resistance and fatigue life [16], [17].

Laser marking of UDIs is a surface treatment, which alters the microstructure and introduces residual stresses. Unfortunately, the industry and regulations have moved significantly faster than research on the effect of laser marking on component performance. The purpose of laser marking has been the generation of contrast, but several unintentional issues compromising component performance have been discovered in recent years. An example is the poorer corrosion resistance of laser-marked steel [18]. Previous work on the subject of laser-marked martensitic stainless steel has revealed abundant cracks in the oxide layer on laser marked UDI [19]. This was taken as a sign of residual stress generation in the heat affected zone (HAZ).

The purpose of the present investigation is to investigate the state of residual stress in medical grade martensitic stainless steel after laser marking and evaluating the potential impact on component performance. To this end, average lattice strains were determined over a series of depth ranges with grazing incidence X-ray diffraction. The hatch spacing and energy input of the laser tracks were varied to arrive at a recommendation for industrial application.

6.1.2. Determining Residual Stress

X-ray diffraction (XRD) has been performed routinely to determine residual stresses from lattice strains. The most widely applied method is the $\sin^2\psi$-method [20]. The method entails the measurement of Bragg-peaks at various polar ψ-angles, defined as the angle between the normal of the sample surface and the diffraction vector, i.e., the normal to the diffracting lattice planes. In practice, this is achieved by varying the inclination angle, χ, of the mounted specimen. For a symmetric diffraction geometry, the angles ψ and χ are identical.

Varying the inclination angle while keeping the incidence angle unchanged, as for a symmetric diffraction geometry, will result in a variation of the information depth with the ψ-angle. The information depth is defined as the diffracted power weighted depth, and corresponds to the depth range from which 63% of the diffracted intensity originates. This effect can be alleviated by an asymmetrical diffraction geometry, as grazing incidence, so the effective information depth is reduced. If stress (or composition) gradients are insignificant over the information depth, the symmetrical method is sufficient, but in the presence of steep stress, and particularly steep concentration gradients, it is insufficient [21]–[25]. Erbacher, et al. [26] further developed existing methods [27] to measure depth resolved residual stresses for a constant information depth for the data points in the $\sin^2\psi$ method.

For symmetrical XRD $\chi = \psi$ (see above), while the (effective) polar angle for asymmetrical XRD, such as grazing incidence, is:

$$\psi = \mathrm{acos}(\cos(\chi)\cdot\cos(\theta - \omega)) \qquad (6.1)$$

where 2θ is the Bragg angle and ω is the (grazing) incidence angle. The following equation can be used to ensure stress measurements at constant information depth:

$$\tau = \frac{Cos(\chi)(\sin(\omega)\sin(2\theta-\omega))}{\mu(\lambda)(\sin(\omega)+\sin(2\theta-\omega))} \qquad (6.2)$$

where τ is the information depth, μ is the linear absorption coefficient for wavelength λ in the, presumed homogeneous, matrix, χ is the inclination angle. By solving Equation (6.2), it should be possible to obtain combinations of χ and ω, for which the information depth is kept constant for a specific 2θ angle. Changing the incidence and tilt angle will also change the azimuth angle, φ, which translates into a change in the direction of the measured strain. The azimuth angle changes in the following way:

$$\tan(\Delta\varphi) = \frac{\tan(\theta - \omega)}{\sin(\chi)} \qquad (6.3)$$

On a laboratory scale, Erbacher's method for lattice strain determination within a constant information depth for a fixed wavelength comes with limitations for applicable effective $\sin^2\psi$ values (cf. Eqs. 1 and 2). For example, using a chromium anode, the range of tilt angles from 0-70° for an information depth of 2 μm in steel is not possible, because at high tilt angles (and high 2ϴ angles) the beam will not be able to reach an information depth of 2 μm. Thereby the range of available tilt angles may be reduced to 0-55°. This is illustrated in Figure 6.1, where the information depth and its dependence on effective $\sin^2\psi$ for different inclination angles has been calculated. Using synchrotron X-radiation larger information depths can be reached by a variation in wavelength and/or an energy dispersive method. Additionally, for small (grazing) incidence angles the accuracy in the determined d-spacing is relatively poor. Consequently, lattice strains determined for a relatively shallow information depth are associated with limited accuracy. For this reason, the shallowest information depth included in this investigation is 0.75 μm.

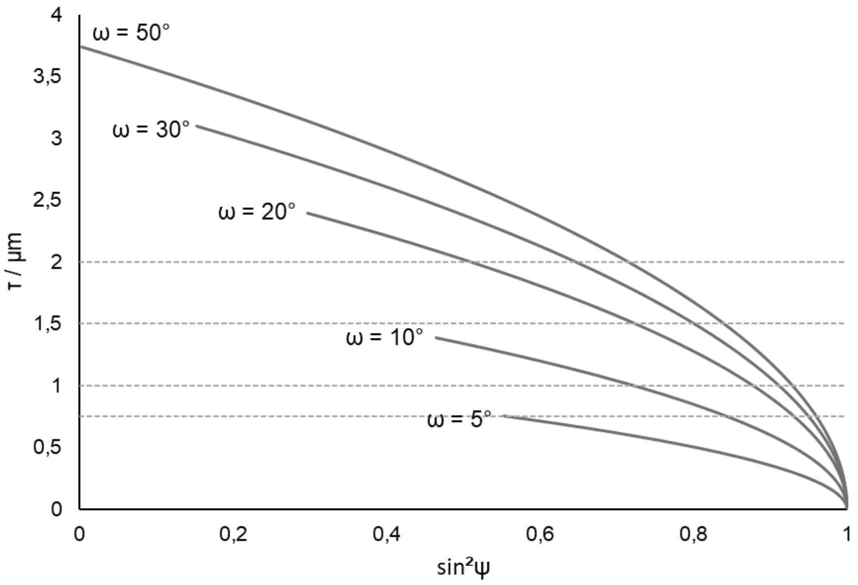

Figure 6.1: The dependence of information depth on the $\sin^2\psi$ for different incidence angles as well as the available $\sin^2\psi$ range in a stainless steel matrix.

6.2. Materials and Methods

6.2.1. Materials

Medical grade martensitic stainless steel EN 1.4028, described in ASTM F899 standard for surgical stainless steels [28], is utilized for this investigation. The nominal chemical composition is given in Table 6.1. For analysis of the morphology and appearance of the laser marked areas, as well as for X-Ray diffraction analysis lathe-turned discs were produced. The discs were produced to be 12 mm in diameter and 3 mm in thickness. Approximately 0.3 mm of the surface was removed by standard metallographic methods, with the last grinding step being grit # 4000 SiC abrasive paper.

Table 6.1: Nominal chemical composition of 1.4028 stainless steel as per ASTM F899.

Element **w%**	**C**	**Si**	**Mn**	**P**	**S**	**Cr**	**Ni**	**Fe**
1.4028 X30Cr13 AISI 420B	0.26- 0.35	Max. 1.00	Max. 1.00	Max. 0.04	Max. 0.03	12.00- 14.00	Max. 1.00	Bal.

A stress relieved specimen which was further polished with the last step being a 1 µm diamond suspension and subsequently heat treated in a vacuum for 6 hours at 650°C, was also included.

6.2.2. Methods

6.2.2.1. Laser Marking

A nanosecond pulsed yttrium Nd:YAG fiber laser, the FOBA Y.0200, was utilized for laser marking of all specimens. The equipment was operated at a wavelength of 1064 nm, a pulse length, t_p, of 200 ns, a pulse frequency, *f,* of 200 kHz and a laser spot size of diameter of 30 µm, used to approximate the spot area *A.* The power density (W/area), $P_p = \frac{\frac{P}{f}}{A \cdot t_p}$, was kept constant as the average power, *p,* of the laser was kept at 5 W. The power density is calculated to be $1.8 \cdot 10^{11}$ (W/m^2). In turn, the scan speed, *v,* and hatch spacing, l_s, were varied to alter the heat input (J/area) of the laser, which can be calculated as $E_s = \frac{P}{v \cdot l_s}$.

Table 6.2: A table containing the varied laser parameters investigated.

Parameter set	**Hatch spacing l_s (µm)**	**Scan speed v (mm/s)**	**Heat input E_s (J/m^2)**
#1	5	250	$4.0 \cdot 10^6$
#2	15	250	$1.3 \cdot 10^6$
#3	30	250	$6.7 \cdot 10^5$
#4	15	83	$4.0 \cdot 10^6$
#5	30	50	$3.3 \cdot 10^6$

The investigated laser parameters are reported in Table 6.2. A baseline parameter set #1 is chosen; this set is representative for parameters used in industry. A high degree of overlap of 83% is results from the small hatch spacing. In parameter set #2 the hatch spacing is 15 µm and overlap is reduced to 50%, while for set #3 overlap is eliminated by increasing the hatch spacing to the nominal laser spot size. Both parameter sets retain the scan speed, so the heat input decreases with increasing hatch spacing. In contrast parameter sets #4 and #5 increase the hatch spacing to 15 and 30 µm, but the scan speed is adjusted to retain the heat input of the baseline sample #1. Sample #5 cannot be adjusted to $E_s = 4.0 \cdot 10^6$ J/m^2, because the lowest scan speed of the equipment is 50 mm/s.

6.2.2.2. Microscopy

Surface morphology and cross-sectional analysis were performed with scanning electron microscopy (SEM). For this purpose, the Zeiss Sigma Field Emission SEM was utilized with a backscatter electron detector. The equipment was operated at 15 kV for imaging at working distances of 8-10 mm.

6.2.2.3. *X-ray Diffraction & Residual Stress Measurements*

X-ray diffraction and residual stress analysis were performed with the Bruker D8 Discover with a LynXeye detector. For stress measurements, Chromium was chosen as the anode and a vanadium filter was applied to suppress K_β; the wavelength of Cr K_α radiation was taken as 2.289 Å. For residual stress analysis the BCC 200 reflection of ferrite/martensite was investigated in the scattering angle range 103 - 115 °2ϴ; a step size of 0.1 °2ϴ and a counting time of 2 s were used. The BCC 200 peak was preferred over the generally recommended BCC 220 peak at higher Bragg angle, because high 2ϴ values limit the available ψ angles for the stress analysis (cf. Eq. (1)). In addition an azimuthal rotation of the specimen around the surface normal is applied to keep the φ direction within the plane of the specimen surface constant. This enables probing lattice strains for a range of information depths in a specific direction along the surface and thereby obtain insight in the variation of stress (and composition) in depth along and perpendicular to the laser tracks. The applied angles of incidence, inclination and azimuthal rotation for $\varphi=0$ and the effective ψ angles are provided in Table 6.3 for the constant information depths applied in this work, using Cr K_α radiation for BCC {200} in a 1.4028 stainless steel matrix.

Table 6.3: Incidence angle ω, tilt angle χ, effective tilt angle ψ and azimuthal angle Φ for (φ=0), as applied to obtain the given information depths. All numbers are in degrees.

τ µm																			
0.75				**1.0**				**1.25**				**1.5**				**2.0**			
ω	**χ**	**ψ**	**Φ**	**ω**	**χ**	**ψ**	**Φ**	**Ω**	**χ**	**ψ**	**Φ**	**ω**	**χ**	**ψ**	**Φ**	**ω**	**χ**	**ψ**	**Φ**
5.0	0	48.0	0	6.5	0	46.5	0	8.5	0	44.5	0	10.5	0	42.5	0	15.2	0	37.8	0
5.2	20	50.9	17	6.8	10	47.0	9	8.7	10	45.2	10	10.9	10	43.1	10	15.5	10	38.6	13
5.4	30	54.3	25	7.2	20	49.1	18	9.2	20	47.3	20	11.5	20	45.3	21	16.5	20	40.9	25
6.5	40	58.2	31	7.9	30	52.3	26	10.0	30	50.7	28	12.7	30	48.7	31	18.5	30	44.5	36
7.8	50	63.1	37	9.0	40	56.6	34	11.8	40	54.8	36	14.9	40	53.0	39	22	40	48.9	47
10.7	60	68.3	44	11.2	50	61.4	41	14.8	50	59.7	44	18.5	50	58.0	48	29	50	54.0	60
13.0	65	71.1	47	15.2	60	66.8	48	20.7	60	65.0	54	27.3	60	63.2	61	36.5	55	56.6	70
17.4	70	73.9	52	26.0	70	72.3	62	41.0	70	70.5	77	38.0	65	65.9	74	-	-	-	-

For the calculation of residual stresses from the measured strain the X-ray elastic constants for ferritic BCC {200} lattice planes were taken as $S_1^{200} = -1.9 \cdot 10^{-6} MPa^{-1}$ and $\frac{1}{2}S_2^{200} = 7.7 \cdot 10^{-6} MPa^{-1}$ [29]. All residual stress measurements were performed in the direction parallel (φ=0°) and perpendicular (φ=90°) to the laser tracks.[9]

Phase analysis was performed with a Bragg-Brentano beam geometry and a copper anode. The Cu k_α radiation wavelength is taken as 1.5418 Å. The specimens were measured in the range of 25-100 °2Ɵ, with a step size of 0.06 ° and a counting time of 2 s.

---

[9] Due to time constraints and the late addition of sample #4, residual stress measurements have not been performed on #4 and are instead planned as future work.

6.2.2.4. *GD-OES*

Glow discharge optical emission spectroscopy (GD-OES) was performed at Horiba France on the GD profiler 2 and repeated 5 times on the specimen laser marked with parameter #1. This specimen was chosen for measurement as it is laser marked with parameters closest to those applied in industry and was produced with the highest heat input. More alteration of the surface chemical composition to be measured via GDOES can be expected with high heat input. The parameters for GDOES are provided in Table 6.4. Before the measurements, the equipment was calibrated on a low alloy SRM 1766 steel.

Table 6.4: Parameter set utilized in GDOES measurements.

Pressure	720 Pa
Power	35 W
Module	6 V
Phase	5 V
Anode size	4 mm
Erosion rate	3.67 µm/min

6.3. Results and Interpretation

6.3.1. Characterization

Figure 6.2 shows backscatter electron micrographs of the investigated specimen, showing clear laser tracks for the various hatch spacings and morphologies. Figure 6.2a shows the baseline specimen with a track distance of 5 µm. A surface layer has formed, and cracks are abundant, as well as signs of possible melting. Increasing the hatch spacing to 15 and 30 µm (see samples #2 and #3 in Figure 6.2b and c, respectively) yields a relatively crack free surface. Structuring is visible in the tracks, hinting at austenitization followed by martensitic transformation upon cooling.

At a hatch spacing of 30 µm (sample #3 in Fig. 6.2c), the original surface is observed in-between the tracks. If a surface oxide is present, it is significantly thinner than for sample #1.

Reducing the scan speed to keep a high E_s on changing the hatch spacing, cracks are again abundant as well as flow patterns that indicate melting (samples #4 and #5 in Figure 6.2e and f, respectively). The darker elemental contrast of the central parts of the tracks hint at an uptake of interstitials from the ambient during laser marking. The cracks are most abundant at the central parts of the individual tracks, where the largest change in temperature is expected. Some cracks are present in between the tracks but to a much lesser extent.

Diffractograms of specimens #1-5 and the unmarked specimen are presented in Figure 6.3. The unmarked specimen shows a diffraction pattern characteristic for martensitic stainless steel, with high intensity α (BCC) peaks and some retained austenite marked as γ (FCC). The unidentified peak at 76 °2ϴ, can be explained from the presence of carbides or MnS, but is left unidentified as more peaks are necessary for a meaningful phase identification. After laser marking, oxide peaks are observed. The oxides were identified as $FeCr_2O_4$ or Fe_3O_4 spinel, which overlap significantly. Upon laser marking a significant increase in intensity of the γ-peaks is observed for all laser marked specimens, indicating an increase in the fraction of retained austenite. Oxide peaks are only identified for specimens #1, #4 and #5, which are laser marked with high heat input.

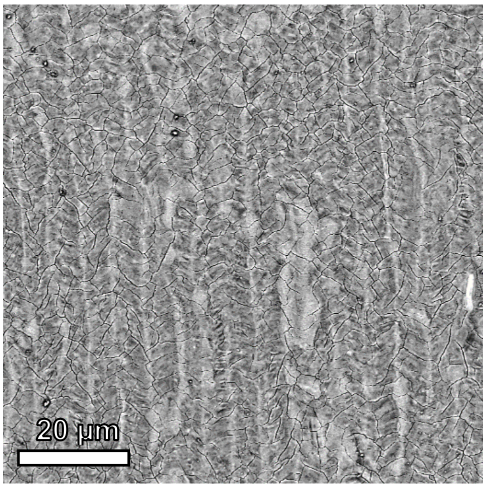

(a) #1

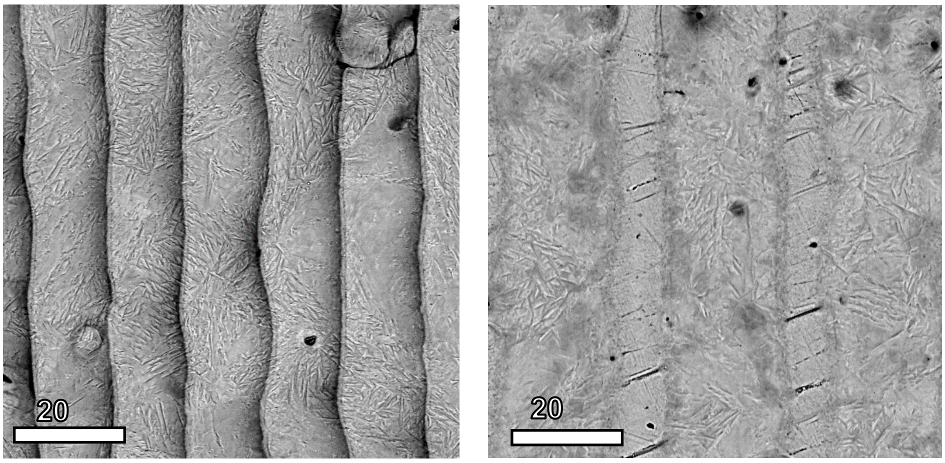

(b) #2 (c) #3

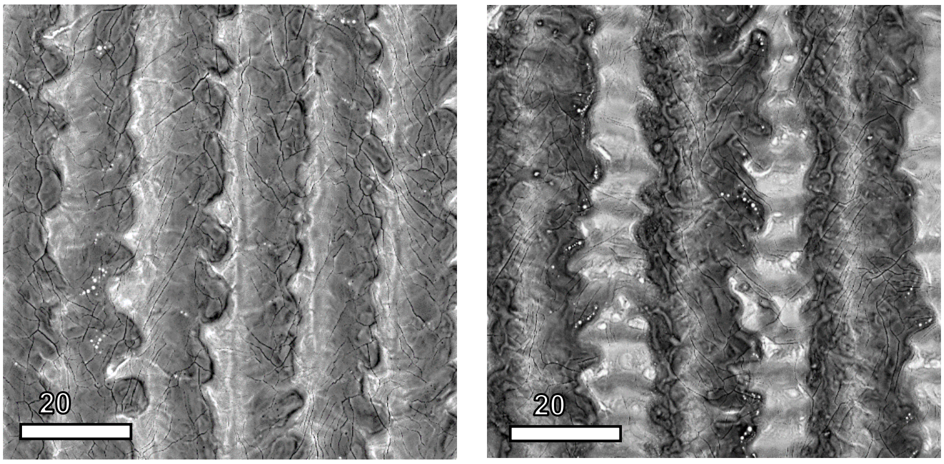

(e) #4 (f) #5

Figure 6.2: Backscatter electron images of the surface morphology of all laser marked samples, showing vertical laser tracks.

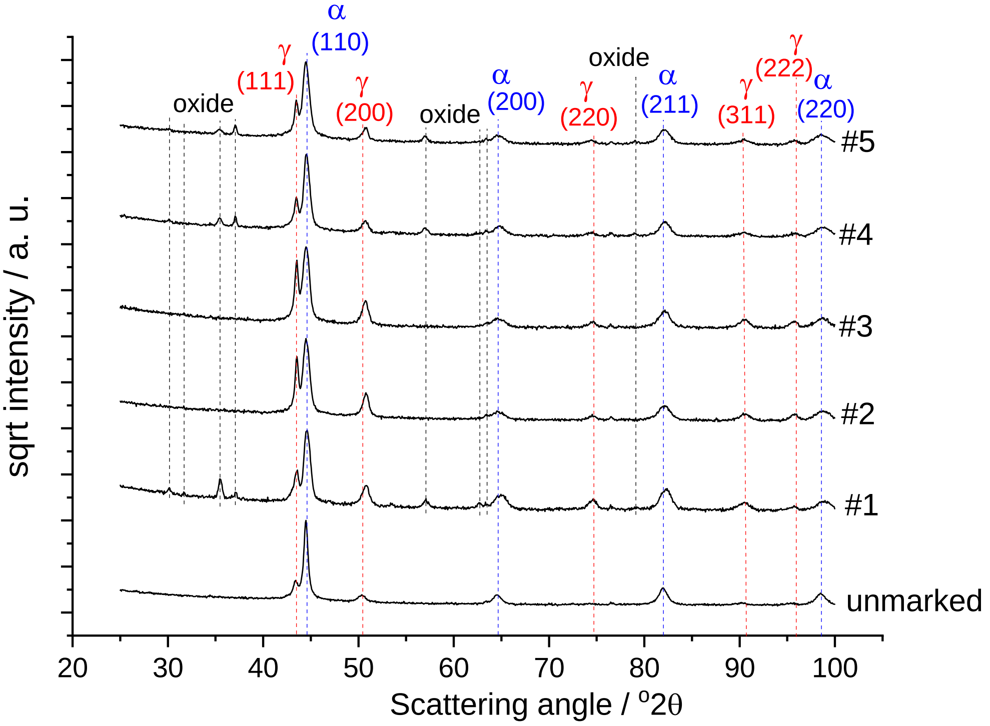

Figure 6.3: X-ray diffractogram of an unmarked reference sample and laser marked samples #1-5. Results are obtained using Cu k_{α} radiation and a Bragg-Brentano beam geometry.

Figure 6.4 shows micrographs of the baseline laser-marked specimen #1 and increased hatch spacing with adjusted heat input, samples #4 and #5. No oxide layer or HAZ could be observed in the specimen #2 and #3 with larger hatch spacing without adjusting the heat input. The baseline specimen with the lowest hatch spacing is shown in Figure 6.4a, where a uniform oxide layer has formed on the surface of the laser marked area. The thickness of the oxide layer is ≈ 0.3 µm with slight variations across the surface. A heat affected zone (HAZ) is identified that extends to a depth of about 1 µm; small dark spots are observed in the HAZ, which indicate oxides that may have formed in the melt. The cracks observed in Figure 6.2 are limited to the oxide layer and do not extend into the HAZ.

Changing the hatch spacing to 15 µm (Figure 6.4b) results in a less uniform oxide thickness ranging in thickness from 0.4 to 0.1 µm. Also, the depth of the HAZ varies slightly along the laser marked surface. These phenomena become more pronounced when the hatch spacing is further increased to 30 µm and the scan speed is decreased to the lowest value of 50 mm/s in Figure 6.4c. The oxide layer thickness varies widely and as indicated in Figure 6.2f, it is not present in-between the laser tracks. A similar behavior is observed in the HAZ: oxide particles in the HAZ are only observed underneath the oxide layer.

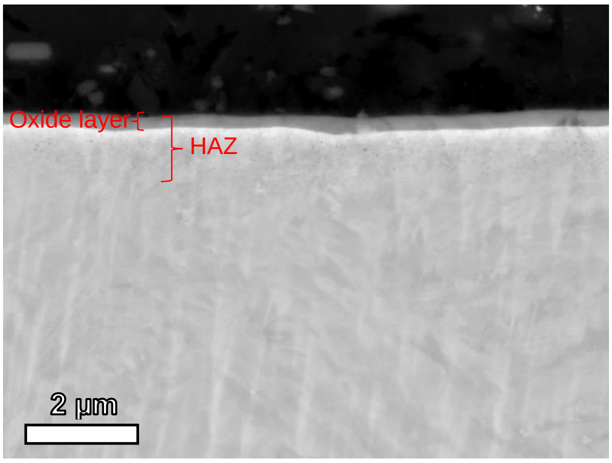

(a) #1

5 µm hatch

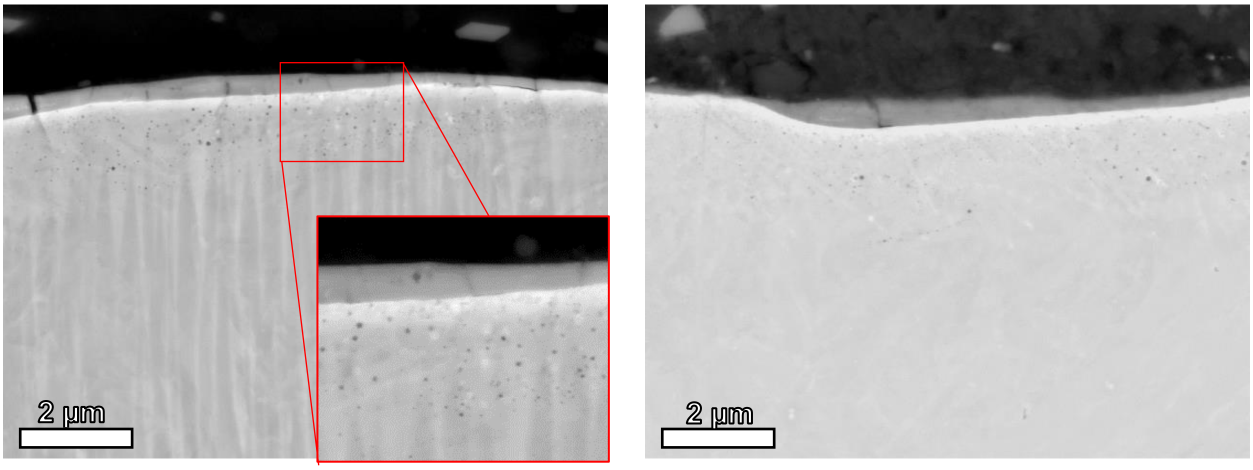

(b) #4

15 µm hatch

(c) #5

30 µm hatch

Figure 6.4: Backscatter electron micrographs of the cross section of samples #1, #4 and #5.

GDOES of the laser marked baseline sample #1 is shown in Figure 6.5 where at depths of >3 µm, the composition is similar to that of the nominal values. From the very surface to a depth of 0.2 µm, a large increase in oxygen content is measured. This corresponds well to the measured oxide thickness in Figure 6.4a, as well as the identification as Fe_3O_4/$FeCr_2O_4$ from the identification of a chromium enrichment and peaks in the iron content. It appears that the innermost oxide is chromium rich, while it is primarily iron based in the outer oxide. Chromium depletion is observed in the subsurface region, which is quite severe relative to the bulk level. Also, silicon and manganese depletion can be observed from 0.3 to 2 µm in the material, which gives rise to a higher silicon content and a slightly higher manganese content in the oxide layer (Figure 6.5a). This corresponds well with silicon’s high affinity for oxygen. For manganese, it is likely that some evaporation has occurred during laser marking.

Surprisingly, the uptake of nitrogen appears to be very limited, despite the fact that laser marking was performed in air (Figure 6.5b). In contrast, there is a substantial contribution of hydrogen (from moisture), which reaches a high concentration at the surface with a steady decline interrupted by a peak at 0.4 µm. A similar profile can be observed for carbon, which is also increased at the surface. Nickel maintains the nominal level throughout the steel, while it appears to be lower in the oxide layer. Oxygen extends deeper than just the oxide layer and may confirm the observation of tiny oxide inclusions in the part of the surface that was molten during laser marking (cf. Fig. 6.5a)

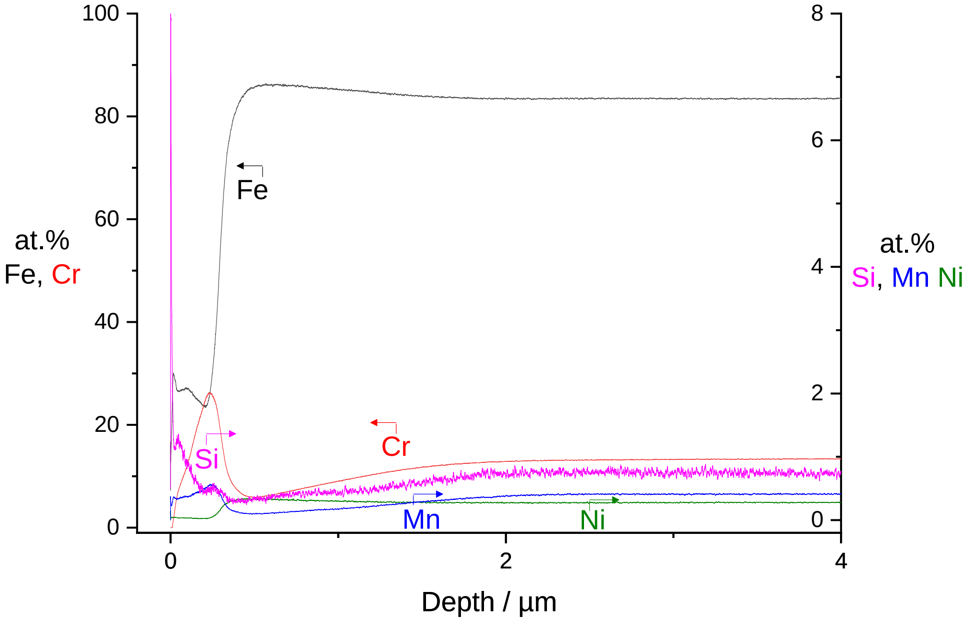

(a)

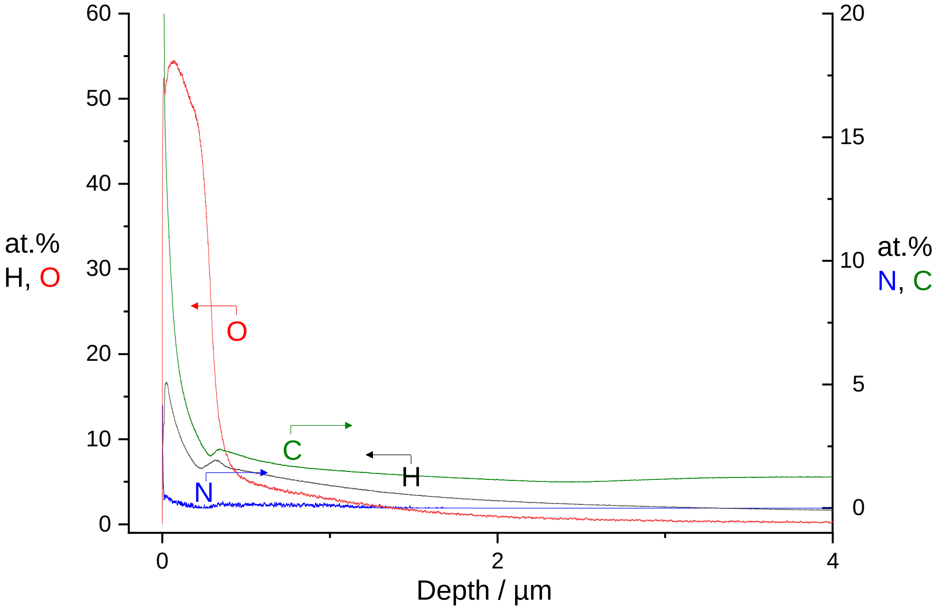

(b)

Figure 6.5: GD-OES depth distributions of a) substitutional elements and b) light elements.

6.3.2. Residual Stress Analysis

Firstly, d-spacings were evaluated in dependence of $\sin^2\psi$ in directions parallel (φ=0°) and perpendicular (φ=90°) to the laser tracks. Within experimental accuracy the straight lines through data for mutually perpendicular directions were equal. Therefore, for further analysis all d-spacings were included irrespective of the azimuth. Essentially, this implies that, within the volume probed with XRD, the stress state in the plane of the surface can be considered rotationally symmetric. No indications were observed for the presence of shear stress in the analyzed volumes. From the straight lines through d_ψ vs. $\sin^2\psi$ data for a fixed information depth, diffracted intensity weighted stress values within the surface plane ($\sigma_{//}$) and perpendicular to the surface (σ_{33}) were obtained, as well as the strain-free lattice spacing $d_{\varepsilon=0}$. The procedure to determine these values is provided in Appendix A. Data for laser marking parameter sets #1, #2, #3, #5 and for the stress annealed state are provided in Figure 6.6 and 6.7. It is noted that Figure 6.6 and 6.7 do not reflect the actual stress distribution in depth, but the presented stress and lattice spacing values represent an average over the volume, and hence depth range, from which the diffracted radiation originates[10]. In principle, the actual stress-depth profile could be obtained from inverse Laplace transformation of the presented profile in τ-space. An attempt to retrieve the actual stress profiles showed that the limited range of information depths in Figure 6.6 (from τ=0.75 to 2.0 µm) as compared to the actual depth range (starting at z=0, i.e. the interface with the oxide layer[2]) leads to an ill-defined mathematical evaluation as a consequence of extrapolation over a large depth range. For this reason, no actual stress-depth profiles are given.

For the stress-relieved specimen, the strain-free lattice spacing is independent of the information depth, as expected. The values for σ_{33} appear slightly positive, but the absolute values are maximally about 50 MPa, which could be considered to be about the accuracy of the measurement technique[11]. The resulting stress within the plane of the surface, $\sigma_{//}$, is about 200 MPa in compression.

---

[10] Note that the information depth is calculated assuming that iron starts at the surface. In fact, the contribution of iron starts underneath the oxide layer. Absorption of incoming and diffracted intensity in the oxide layer is neglected in the calculations of the information depth.

[11] For the applied step size, it is calculated that the error in the stress value corresponding to 1/5 of the step size is 69 MPa.

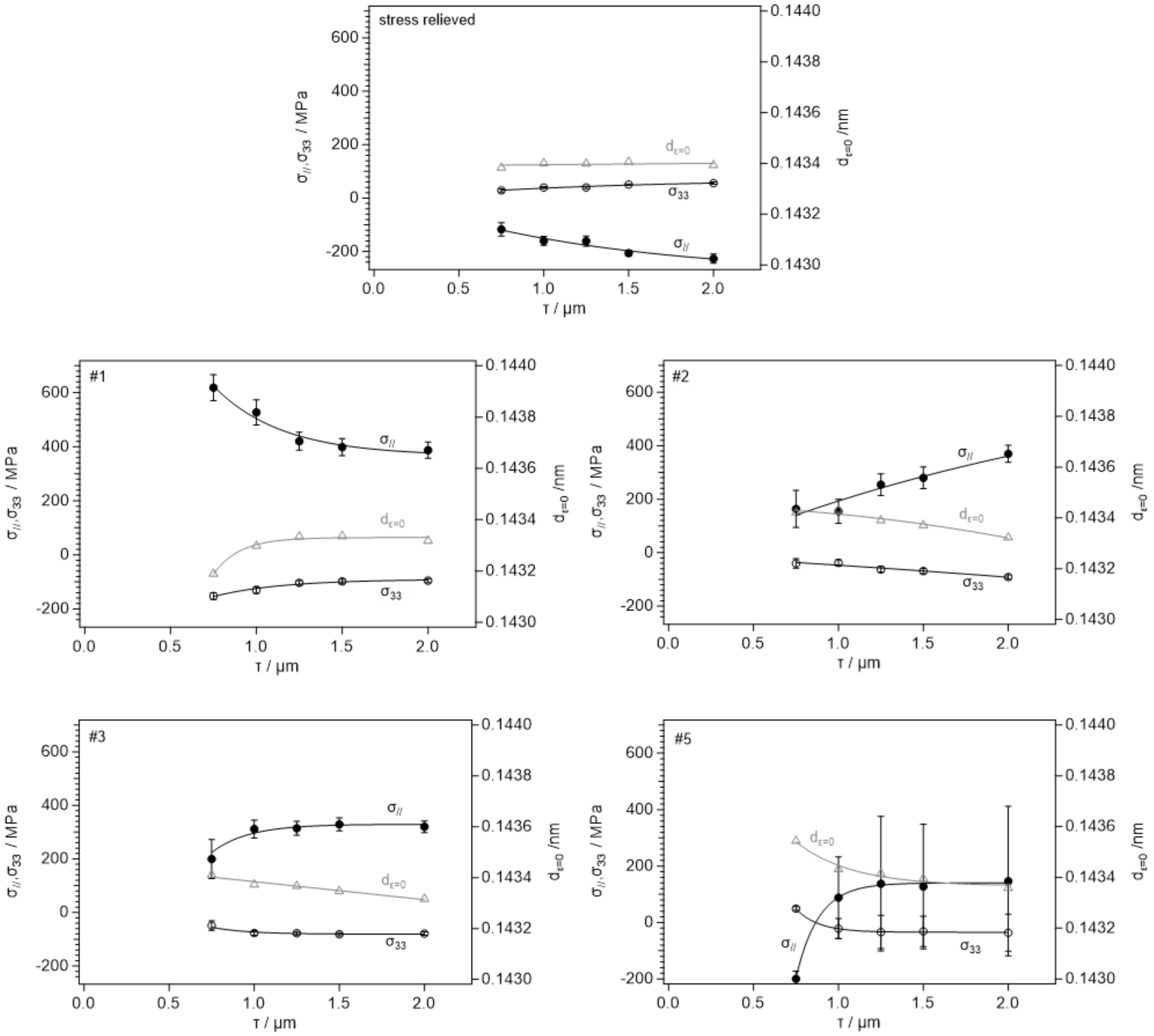

Figure 6.6: Residual stress (left axis) and strain free lattice parameter (right axis) in dependence of the information depth for different laser marking conditions and the stress relieved case prior to laser marking. Error bars for the stress values were obtained from the standard deviation in the slope of the straight line in d_ψ vs. $\sin^2\psi$ plots.

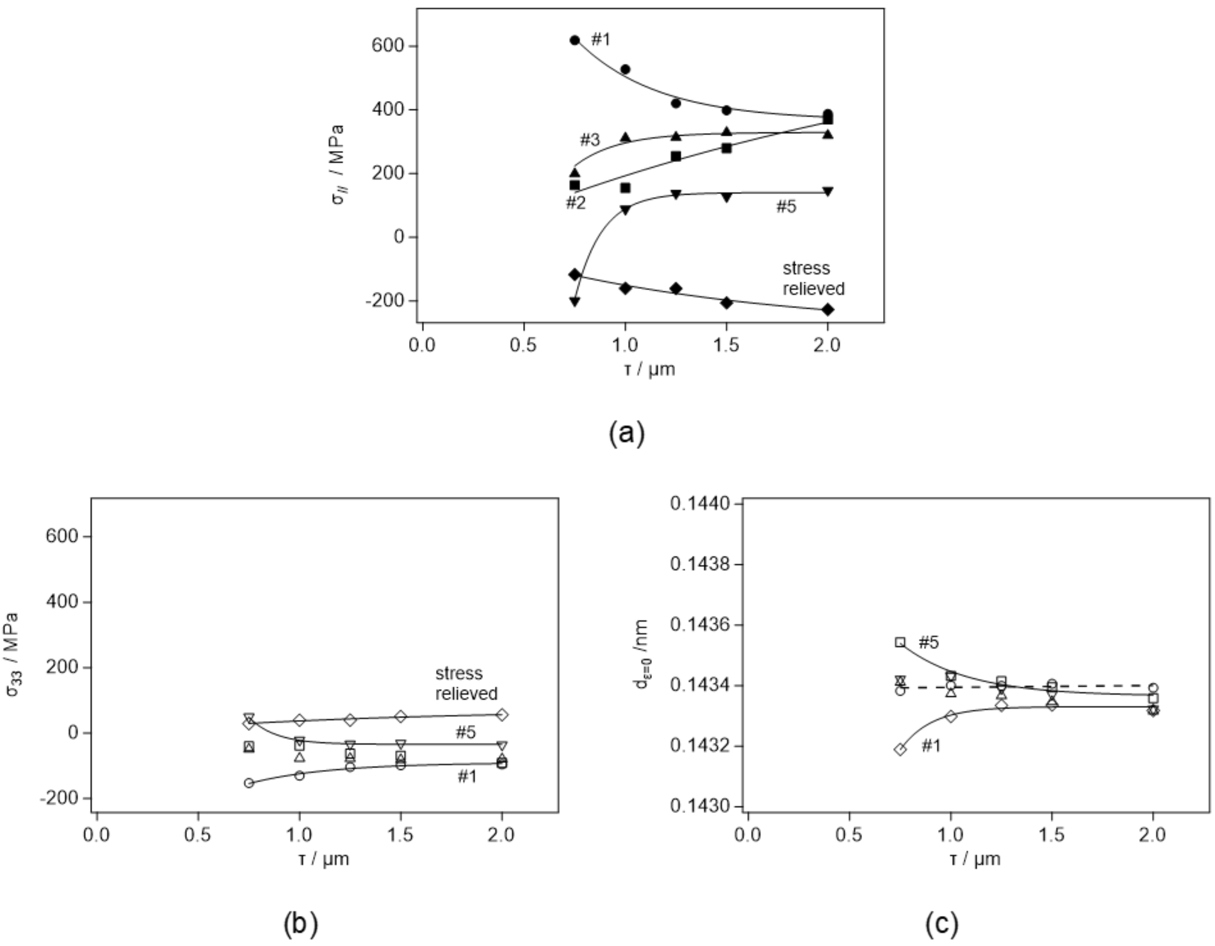

Figure 6.7: Comparison of residual stress (a,b) and strain-free lattice parameter (c) for the different specimens. The horizontal dashed line in (c) represents the strain-free lattice parameter in the stress relieved specimen. Open marker geometries in b. and c. are identical to the geometry of the filled markers in a.

Laser marking causes the stress state within the plane of the surface to change to tensile (Figure 6.6 and 6.7). This applies particularly if there is sufficient overlap of the laser tracks so that the surface is entirely covered with an oxide layer (#1). If no oxide layer is present the tensile stress values are lower (#2, #3). For laser marking with a large hatch spacing, such that no overlap of laser tracks occurs and where the oxide layer is not continuous (#5), relatively large errors are found in the determined stress values. For the laser marking conditions in #5, close to the surface, compressive stresses arise within the plane of the surface. This is related to the heterogeneity within the volume probed with X-ray diffraction. The parts of the steel surface in-between the oxide-covered tracks parts are not covered with oxide, so the diffracted intensity contribution of these regions dominates the total diffracted intensity for shallow information depths, i.e. where the compressive stress is observed. Deeper, tensile stresses are found, albeit lower in magnitude than for laser marking conditions #1-#3. This reduction in tensile stress is also attributed to the heterogeneity in the stress distribution: some regions experience compression, others tension. The residual stresses in #2 and #3 are in-between those for #1 and #5.

Overall, the values obtained for the diffracted intensity weighted stress value in the direction perpendicular to the surface are slightly compressive and appear most pronounced for laser marking set #1.

The strain-free lattice spacing for #1 appears to increase with information depth, while it declines with information depth for #5. For laser marking sets #2 and #3, the strain-free lattice parameter falls slightly with increasing information depth, but the values are very close to that of the strain-free direction (Figure 6.7c).

6.4. Discussion

The energy distribution in the laser spot approaches a Gaussian distribution, which causes relatively large deviations in oxide layer and HAZ thickness with increased hatch spacing, even if there technically is an overlap with the nominal spot size. It is also reflected in the color of the specimen. Sample #1 has the darkest color, #2 and #3 with larger hatch spacing, showed a light gray appearance. Adjusting the heat input by reducing the scan speed, darkened the color to some degree.

Phase analysis in Figure 6.3 shows a clear effect on the laser marked specimens, as several oxide peaks appear. The diffraction pattern is consistent with what has been obtained in previous research on the subject, namely the $FeCr_2O_4$ oxide [18]. The presence of Cr in the oxide layer is confirmed by the GD-OES results in Fig. 6.6, and further corroborated by chromium depletion in the sub-surface region for #1 in Fig. 6.6. Previous research shows a significant reduction in corrosion resistance after laser marking, which could be attributed to loss of passivity after chromium depletion. Alloying elements with a high affinity for oxygen and present in significant amounts will oxidize first, i.e., chromium (and silicon) [30]–[32]. This is again confirmed with GD-OES, as chromium oxide forms as the innermost oxide, while it appears to be mainly iron based in the outer oxide. There is no significant nitrogen enrichment in the surface, despite laser marking in atmospheric air. There is however an enrichment of both carbon and hydrogen in the surface. Carbon shows signs of a slight depletion from 1.3 to 3 µm which leads to an enrichment in the surface. There could also be an effect of forward sputtering that augments the carbon content in the HAZ. Hydrogen appears to have diffused quite deep into the steel. The only obvious source of hydrogen diffusion is moisture in the air because there was no control over the laser marking atmosphere, as is generally the case during industrial laser markings. Hydrogen could potentially be bound as hydroxides in the HAZ. The dispersed particles visible in the insert of Figure 6.4b are interpreted as (hydr)oxides and suggest that the material has been molten down to a depth of about 2 µm.

It is clear from Figure 6.2 that the hatch-spacing and scan speed have a large influence on the different morphologies in the laser marked surface. This is the result of a difference in dissolution of species from the atmosphere, different degrees of melting and remaining features from the grinding process. Sample #1 with the baseline heat input and hatch spacing, shows some sign of melting in the form of flow patterns, but also that a uniform oxide layer has formed on top. This is the consequence of a substantial overlap between individual tracks and many passes, gradually building the oxide layer. Also, the formation of oxides at the surface can decrease the amount of reflected energy [33], causing a relatively high laser energy absorption. Clearly, the repeated melting/solidification and heat treatment has led to chromium depletion below the oxide layer (Figure 6.5a). Considering this chromium depletion underneath the oxide layer for #1, and realizing that chromium atoms expand the bcc lattice, a decrease in strain-free lattice parameter towards the surface can be explained (Figure 6.6a and 6.7c). The decrease in strain-free lattice parameter should be accompanied by an increasing tensile stress parallel to the surface, as observed indeed. The occurrence of a tensile stress for an information depth of 2.0 µm, where the chromium content and associated strain-free lattice spacing have reached the bulk value (see Figure 6.5a and 6.6b), are mainly the result of thermal shrink. On surface-adjacent heating resulting in local melting, plastic accommodation of volume changes can occur to a relatively low temperature (after solidification). This plastic accommodation of volume changes will eventually lead to tensile strains and stresses within the plane of the surface after cooling of the surface adjacent part to room temperature. Fresh martensite formation from austenite introduces additional transformation stresses. Since martensite formation is associated with a volume expansion, it will counteract the tensile thermal stresses.

Increasing the hatch spacing as seen in Figure 6.2b/c has resulted in significantly less or no oxide formation. Apparently, the heat input was insufficient for substantial oxygen uptake. For #2 the laser tracks still overlap; for #3 the laser tracks are separated by surface regions where grinding marks are still visible. Therefore, it is concluded that surface melting has occurred within the laser tracks. Instead of oxide formation, the microstructural features reveal the formation of fresh martensite in the molten and solidified surface area for #2 and #3. The strain-free lattice parameter for #2 and #3 falls slightly with increasing information depth. Obviously, since no chromium-containing oxide layer has formed (Figure 6.3), no clear change in the sub-surface composition by chromium depletion can be expected. Possibly, the slight decrease is a result of the ingress of species from the atmosphere during laser treatment or a gradient in dissolved carbon associated with dissolution of carbides. For increasing information depth, both #2 and #3 show a trend of increasing tensile stress in the plane of the surface, while the stress in the direction perpendicular to the surface is slightly compressive and shows a trend to more negative stress values with increasing information depth. The tensile stresses parallel to the surface are interpreted as the result of thermal stresses during cooling and transformation during martensite formation upon laser marking. The total shrink and associated contraction depend on the maximum temperature reached by heat input from the laser. Analogously, the amount of fresh martensite formed depends on the amount of austenite that formed during heating and the amount of austenite that is retained.

Slowing down the scan speed to compensate for the loss of heat input, has resulted in a large degree of melting at the surface as is evident for samples #4 and #5 (Figure 6.2d/e) where flow patterns from the liquid are clearly distinguished at the surface. The elemental contrast is also very high in the laser tracks as compared to sample #2 and #3, indicating a higher content of light elements, consistent with the formation of an oxide layer (Figure 6.3) due to the higher heat input than for #2 and #3. For sample #5 with the largest hatch spacing and no overlap, evidence of melting is visible along the tracks, with martensite formation in between the oxide-covered tracks. The very heterogeneous microstructure in sample #5 has caused relatively large uncertainty in the determined stress values. In particular the error bars for $\sigma_{//}$ are very large for information depths beyond 1 µm; these error bars are larger than the systematic error in the current stress determination (approx. 70 MPa; see footnote 11). For a relatively shallow information depth, the total diffracted intensity for martensite comes mainly from martensite in-between the oxide-covered laser tracks (cf. Figure 6.2f). Apparently, this surface adjacent martensite experiences compression within the plane of the sample surface. This compression can be understood as follows. On laser marking, this part of the surface in-between the laser tracks are not experiencing the same heat input as the part that interacts directly with the laser beam, i.e. the heavily oxidized part. This leads to limited (or no) oxidation and the appearance of martensite directly at the surface. Most likely this part has been molten, but earlier solidification and faster cooling can occur than for the oxide-covered melt in the laser tracks. Consequently, martensite forms earlier in-between the laser tracks than under the oxide layer. The volume expansion during martensite formation underneath the oxide layer imposes compression onto the martensite that was formed earlier in-between the laser tracks. For deeper information depths, the diffracted intensity originates from a larger heterogeneous volume. Evidently, this leads to an, on average, slightly tensile stress within the plane of the surface.

The reduction in $d_{\varepsilon=0}$ with information depth for #5 is interpreted as follows. Underneath the oxide-covered laser tracks, chromium depletion is expected, as for #1. Nevertheless, for the shallowest information depth diffracted intensity from the steel in-between the laser tracks dominate. In this HAZ region carbides may have dissolved, leading to a higher content of carbon and chromium in austenite, and thus the resulting martensite (after cooling). Both chromium and carbon lead to an expansion of the bcc lattice.

6.5. Conclusions

The following conclusions can be reached based on the results of this investigation:

- Oxidative laser marking of stainless steel can significantly alter the residual stress state and chemical composition in the surface of martensitic stainless steel.
- The residual stress state is dependent on the laser parameters, most importantly on the heat input and the hatch spacing.
- Laser marking can lead to a state of high tensile stress in martensitic steel, due to the altering of the chemical composition in combination with thermal effects.
- Large stress gradients can be measured in the laser marked surface over shallow depths.

6.6. References

[1] European Union, “The European Commision, Commision recommendation of 5 April 2013 on a common framework for a unique device identification system of medical devices in the Union,” *Official Journal of the European Union*, Apr. 2015.

[2] N. Wilson, J. Broatch, M. Jehn, and C. Davis, “National projections of time, cost and failure in implantable device identification: Consideration of unique device identification use,” *Healthcare*, vol. 3, no. 4, pp. 196–201, Dec. 2015, doi: 10.1016/J.HJDSI.2015.04.003.

[3] European Union, *Regulation (EU) 2017/745 of the European Parliament and of the Council on Medical Devices, amending Directive 2001/83/EC*. 2017.

[4] L. Lazov, H. Deneva, and P. Narica, “Laser Marking Methods,” 2016.

[5] C. Neugebauer, S. Quaranta, S. Ehrenmann, C. Rest, and J. Sadowitz, “Latest advances in medical black marking: technology and techniques,” in *Laser-based Micro- and Nanoprocessing XIII*, U. Klotzbach, R. Kling, and A. Watanabe, Eds., SPIE, Mar. 2019, p. 3. doi: 10.1117/12.2508408.

[6] R. Hack, “State of the art in fiber laser making,” L. N. Durvasula, Ed., Jul. 2003, p. 202. doi: 10.1117/12.484175.

[7] M. Švantner, M. Kučera, E. Smazalová, Š. Houdková, and R. Čerstvý, “Thermal effects of laser marking on microstructure and corrosion properties of stainless steel,” *Appl Opt*, vol. 55, no. 34, p. D35, Dec. 2016, doi: 10.1364/AO.55.000D35.

[8] J. D. Thiele, S. N. Melkote, R. A. Peascoe, and T. R. Watkins, “Effect of Cutting-Edge Geometry and Workpiece Hardness on Surface Residual Stresses in Finish Hard Turning of AISI 52100 Steel,” *J Manuf Sci Eng*, vol. 122, no. 4, pp. 642–649, Nov. 2000, doi: 10.1115/1.1286369.

[9] D. Thibault, P. Bocher, and M. Thomas, “Residual stress and microstructure in welds of 13%Cr–4%Ni martensitic stainless steel,” *J Mater Process Technol*, vol. 209, no. 4, pp. 2195–2202, Feb. 2009, doi: 10.1016/j.jmatprotec.2008.05.005.

[10] S. Primee and P. Juijerm, “Modified Mechanical Surface Treatment for Optimized Fatigue Performance of Martensitic Stainless Steel AISI 420,” *Metals and Materials International*, vol. 27, no. 5, pp. 946–952, May 2021, doi: 10.1007/s12540-019-00517-7.

[11] R. Yang *et al.*, “Effect of shot peening on the residual stress and mechanical behaviour of low-temperature and high-temperature annealed martensitic gear steel 18CrNiMo7-6,” *IOP Conf Ser Mater Sci Eng*, vol. 219, p. 012046, Jul. 2017, doi: 10.1088/1757-899X/219/1/012046.

[12] S. Natarajan, “Thermochemical Surface Engineering of Steels,” *Surface Engineering*, vol. 31, no. 11, pp. 875–878, Nov. 2015, doi: 10.1080/02670844.2015.1119485.

[13] T. Ericsson, “Residual Stresses Produced by Quenching of Martensitic Steels,” in *Comprehensive Materials Processing*, Elsevier, 2014, pp. 271–298. doi: 10.1016/B978-0-08-096532-1.01209-7.

[14] D. I. Pantelis, E. Bouyiouri, N. Kouloumbi, P. Vassiliou, and A. Koutsomichalis, “Wear and corrosion resistance of laser surface hardened structural steel,” *Surf Coat Technol*, vol. 161, no. 2–3, pp. 125–134, Dec. 2002, doi: 10.1016/S0257-8972(02)00495-4.

[15] E. Liverani, A. H. A. Lutey, A. Ascari, A. Fortunato, and L. Tomesani, “A complete residual stress model for laser surface hardening of complex medium carbon steel components,” *Surf Coat Technol*, vol. 302, pp. 100–106, Sep. 2016, doi: 10.1016/j.surfcoat.2016.05.066.

[16] S. O. A. El-Helieby and G. W. Rowe, “Influences of surface roughness and residual stress on fatigue life of ground steel components,” *Metals Technology*, vol. 7, no. 1, pp. 221–225, Jan. 1980, doi: 10.1179/030716980803286450.

[17] B. A. Van Brussel and J. Th. M. De Hosson, “Residual stresses in the surface layer of laser-treated steels,” *Materials Science and Engineering: A*, vol. 161, no. 1, pp. 83–89, Mar. 1993, doi: 10.1016/0921-5093(93)90478-W.

[18] P. Steyer, S. Valette, B. Forest, J. P. Millet, C. Donnet, and E. Audouard, “Surface modification of martensitic stainless steels by laser marking and its consequences regarding corrosion resistance,” *Surface Engineering*, vol. 22, no. 3, pp. 167–172, Jun. 2006, doi: 10.1179/174329406X108861.

[19] N. G. Henriksen, O. Z. Andersen, M. S. Jellesen, T. L. Christiansen, and M. A. J. Somers, “Influence of Laser Marking on Microstructure and Corrosion Performance of Martensitic Stainless Steel Surfaces for Biomedical Applications,” *HTM Journal of Heat Treatment and Materials*, vol. 77, no. 3, pp. 177–196, Jun. 2022, doi: 10.1515/htm-2022-1010.

[20] E. Macherauch, “Das Sin^ 2ψ Verfahren von Rontgenographische Eigenspannungen,” *Z. angew. Phys*, vol. 13, pp. 305–312, 1961.

[21] A. Kämpfe, B. Eigenmann, and D. Löhe, “Comparative application of measuring techniques for X-ray analysis of grinding residual stresses in Al2O3 and AlN,” *Zeitschrift Fuer Metallkunde/materials Research and Advanced Techniques*, vol. 91, no. 11, pp. 967–975, 2000.

[22] D. F. Arias, A. Gómez, R. M. Souza, and J. M. Vélez, “Residual stress gradient of Cr and CrN thin films,” *Mater Chem Phys*, vol. 204, pp. 269–276, Jan. 2018, doi: 10.1016/j.matchemphys.2017.10.053.

[23] T. Christiansen and M. A. J. Somers, “Avoiding ghost stress on reconstruction of stress- and composition-depth profiles from destructive X-ray diffraction depth profiling,” *Materials Science and Engineering: A*, vol. 424, no. 1–2, pp. 181–189, May 2006, doi: 10.1016/j.msea.2006.03.007.

[24] T. L. Christiansen, T. S. Hummelshøj, and M. A. J. Somers, “Expanded austenite, crystallography and residual stress,” *Surface Engineering*, vol. 26, no. 4, pp. 242–247, May 2010, doi: 10.1179/026708410X12506870724316.

[25] M. A. J. Somers and E. J. Mittemeijer, “The rise and fall of stress in thin layers; the γ’-Fe4N1-x layer as a model,” *Journal of Materials Engineering*, vol. 12, no. 2, pp. 111–120, Jun. 1990, doi: 10.1007/BF02834064.

[26] T. Erbacher, A. Wanner, T. Beck, and O. Vöhringer, “X-ray diffraction at constant penetration depth – a viable approach for characterizing steep residual stress gradients,” *J Appl Crystallogr*, vol. 41, no. 2, pp. 377–385, Apr. 2008, doi: 10.1107/S0021889807066836.

[27] T. Dümmer *et al.*, “Depth-resolved X-ray analysis of residual stresses in graded PVD coatings of Ti(C,N),” *Zeitschrift Fuer Metallkunde/materials Research and Advanced Techniques*, vol. 90, no. 10, pp. 780–787, 1999.

[28] ASTM International, “ASTM F899-20 Standard Specification for Wrought Stainless Steels for Surgical Instruments.” 2020.

[29] M. Villa, F. Niessen, and M. A. J. Somers, “In Situ Investigation of the Evolution of Lattice Strain and Stresses in Austenite and Martensite During Quenching and Tempering of Steel,” *Metallurgical and Materials Transactions A*, vol. 49, no. 1, pp. 28–40, Jan. 2018, doi: 10.1007/s11661-017-4387-0.

[30] T. Zheng and J. T. Han, “High Temperature Oxidation Behavior of SUS310S Austenitic Stainless Steel,” *Adv Mat Res*, vol. 941–944, pp. 212–215, Jun. 2014, doi: 10.4028/www.scientific.net/AMR.941-944.212.

[31] S. Chandra-ambhorn, S. Hayashi, L. Latu-Romain, and P. Wongpromrat, “CHAPTER 4 High Temperature Oxidation of Stainless Steels,” *Solid State Phenomena*, vol. 300, pp. 81–106, Feb. 2020, doi: 10.4028/www.scientific.net/SSP.300.81.

[32] R. K. Wild, “HIGH TEMPERATURE OXIDATION OF AUSTENITIC STAINLESS STEEL IN LOW OXYGEN PRESSURE,” *Corros Sci*, vol. 17, no. 2, pp. 87–104, 1977.

[33] M. Seo and M. Lee, “Vivid structural colors produced on stainless steel,” *Acta Mater*, vol. 159, pp. 1–7, Oct. 2018, doi: 10.1016/j.actamat.2018.08.011.

[34] *Structural and Residual Stress Analysis by Nondestructive Methods*. Elsevier, 1997. doi: 10.1016/B978-0-444-82476-9.X5000-2.

6.7. Appendix

This appendix details how residual stresses and lattice parameters have been calculated following the $\sin^2\psi$-method. The utilized equations are based on the solutions provided by Hauk [34]. For a rotationally symmetric triaxial stress state it follows that $\sigma_1 = \sigma_2 = \sigma_{//}$ and that $\sigma_{33} \neq 0$. The strain can then be expressed as:

$$\frac{d_\psi - d_0}{d_0} = \frac{1}{2} S_2 \left[\left(\sigma_{//} - \sigma_{33} \right) \sin^2 \psi + \sigma_{33} \right] + S_1 \left(2\sigma_{//} - \sigma_{33} \right) \text{ (6.4)}$$

The σ independent direction can be calculated as $\sin^2 \psi_{\sigma_{//}=0} = -\frac{2S_1}{½S_2}$ [34], and equation (6.4) can be rewritten as:

$$d_{\psi_{\sigma_{//}=0}} = d_0 (3S_1 \sigma_{33} + 1) \qquad (6.5)$$

Solving equation (6.4) instead for the σ_3-independent direction, which can be found as $\sin^2 \psi_{\sigma_{33}=0} = \frac{½S_2 + S_1}{½S_2}$ yields the following equation:

$$d_{\psi_{\sigma_{33}=0}} = d_0 \left(\sigma_{//} \left(2S_1 + \frac{1}{2} S_2 \right) + 1 \right) \qquad (6.6)$$

It is known that the linear dependence of the lattice parameter on the $\sin^2\psi$ has a slope of $\frac{1}{2} S_2 d_0 \left(\sigma_{//} - \sigma_{33} \right)$. Taking the slope from the linear fits on d vs $\sin^2\psi$ plots as M, a third equation is obtained:

$$M = \frac{1}{2} S_2 d_0 \left(\sigma_{//} - \sigma_{33} \right) \qquad (6.7)$$

Values for d_ψ can be obtained by extrapolation or interpolation of the linear dependence of d on $\sin^2\psi$ and the directions for which the equations are derived; these directions depend only on the X-ray elastic constants (see above). Hence, three unknown variables are left: $\sigma_{//}, \sigma_{33}$ and d_0. These are then calculated by solving the system of linear equations (6.5-6.7).

7. Manuscript IV: Impact of Laser Marking on Microstructure and Fatigue Life of Medical Grade Titanium[12]

Nikolaj G. Henriksen1), Konstantinos Poulios2), Marcel A. J. Somers3), Thomas L. Christiansen3)

1) Elos Medtech, Engvej 33, 3330 Gørløse, Denmark, nikolaj.henriksen@elosmedtech.com

2) Technical University of Denmark, Department of Civil and Mechanical Engineering, Nils Koppels allé b. 404, 2800 Kgs. Lyngby, Denmark

3) Technical University of Denmark, Department of Civil and Mechanical Engineering, Produktionstorvet b. 425, 2800 Kgs. Lyngby, Denmark

Medical devices are required to feature a unique device identification marking to enable traceability. These identification tags are extensively applied directly onto metallic devices. Universally, the technology utilized to apply such markings is laser marking, where the device is heated locally in atmospheric air to form a dark oxide layer and generate contrast. Despite the wide application, the consequences of laser marking on materials performance are largely unknown. In this study, the effect of laser marking on the most common titanium alloys in the medical industry, i.e., commercially pure titanium and Ti6Al4V, is investigated. The morphology and composition of the generated oxide layer were investigated, along with a characterization of the heat affected zone. Additionally, the effect on fatigue strength is investigated in relation to the application of laser-marked titanium in a dental implant. Morphologically the laser-marked titanium surfaces exhibited signs of melting on the very surface and the generation of an abundance of cracks which

---

[12] Published work: Henriksen, N. G., Poulios, K., Somers, M. A. J., & Christiansen, T. L. (2023). Impact of laser marking on microstructure and fatigue life of medical grade titanium. Materials Science and Engineering a, 873, 145020. https://doi.org/10.1016/j.msea.2023.145020. The format has been adapted to the format of this Ph.D. thesis.

formed upon cooling. Scanning electron microscopy shows that these cracks are perpendicular to the surface and reach deep into the HAZ. Evidence of substantial oxygen ingress was demonstrated: various titanium-based oxides were identified via X-ray diffraction, as well as oxygen stabilized α-phase. The fatigue analysis showed a severe reduction in endurance limit for all investigated parameters and materials of up to 80%. This was attributed the notch effect resulting from crack formation during laser marking. The fractured surfaces were investigated and showed a clear crack propagation from the entire laser-marked surface.

Keywords: *Characterization, Fatigue, Titanium alloys, Laser methods, Biomaterials, Electron Microscopy*

7.1. Introduction

Titanium alloys are used extensively for dental and orthopedic implants, due to their inherently good corrosion resistance and osseointegration. Mainly two classes of titanium alloys are used for the purpose: commercially pure (CP) titanium and Ti6Al4V [1]. CP titanium has for decades been the material of choice for dental implants [2], while Ti6Al4V is more common in orthopedic implants. In orthopedics, also more specialized titanium alloys are applied, mainly β-alloys due to an attainable elastic modulus very close to that of bone. Implants manufactured from titanium are generally considered safe, but implant failures are reported. The most common failures are of biological or mechanical origin [3]. A biological failure would be a lack of osseointegration when the bone does not grow around the implant. Mechanical failure is related to the implant itself. The most common cause of mechanical failures of dental implants are fractures initiated at screw threads [3]. Cyclic loading of dental implants during chewing or of orthopedic implants during walking implies that fatigue performance is important. Hence, the fatigue performance - and thus the applied alternating load - determines if the implant may eventually suffer from fatigue failure. Fatigue crack initiation usually occurs at the surface of components, so the surface quality of titanium is of paramount importance. Stress concentrations as porosity or sharp edges should therefore be avoided. Also, surface treatments, for example to improve osseointegration can affect the fatigue crack initiation susceptibility adversely [4].

Traceability is of key importance in the medical device as it can save money, time, and lives. It is anticipated that surgeons waste valuable time on identifying failed surgical equipment, because no proper traceability system is in place [5]. In 2013, a common framework for traceability was proposed in the European Union in the form of unique device identification markings (UDI) [6]. Such markings are required to be applied directly onto the device, or, if direct product marking is not feasible, on the lowest level of packaging [7]. According to the mentioned regulations, implants can have markings on the product, which should be readable in-vivo after implantation without surgery. Clearly, UDI and traceability have important advantages in the medical world, but regulations have moved faster than research on the subject and the impact of UDI on device performance remains largely unexplored.

Traceability is required for medical implants in the EU and USA. Although direct product marking is not required for implantable devices, it is not forbidden either and has been applied extensively. Traceability marks should be permanent and easily readable, which has resulted in laser marking as the industry standard and the only real option for tagging UDIs onto medical device and implants. Laser marking technology distinguishes between two main modes of operation: ablative and oxidative mode. Ablative mode utilizes high power density to locally evaporate material (laser engraving). Oxidative mode is associated with lower current density and locally increases the temperature resulting in a reaction between the device and gaseous species in the atmosphere, yielding a dark surface layer [8,9]. The primary purpose of laser marking directly on an implant, is to enable identification of the implant after it is removed from its packaging [7] and enable identification in case of failure. Furthermore, companies are required to rapidly detect any medical device malfunction by adhering to the concept of materials vigilance. This basically entails speedy detection of materials failure. The traceability that laser-marked UDI provides is pivotal for materials vigilance [10].

Laser marking of medical implants introduces surface defects/alterations that potentially act as local stress raisers that may impair fatigue life. Ablative laser marking (laser engraving) has been used to provide traceability to hip-implants by the engraving of a serial number. This has been shown to be a preferred crack initiation site in titanium, presumably due to the stress concentration of what is effectively a notch [11, 12]. In addition, dissolution of appreciable amounts of oxygen has been identified in the surface-near region after engraving, which potentially contributes to embrittlement. Laser engraving and the generation of a heat affected zone (HAZ) has experimentally been shown to result in significant build-up of tensile residual stresses and to jeopardize the fatigue strength as compared to unmarked specimens. The dangers of ablative laser marking are obvious: it will introduce surface defects/alterations such as local changes in microstructure and thus effectively reduce the fatigue life by (inadvertently) introducing a “notch effect”. This effect is of particular importance for titanium alloys [13]. In order to avoid ablative laser marking and associated stress concentrations, oxidative laser marking would be preferred. Moreover, oxidative laser marking leads to black marking on the metallic substrate; a preferred feature. If performed properly, no material is removed, but only diffusion of species from the atmosphere into the alloy and the formation of a black oxide layer. In a short study, it was found that oxidative laser marking of CP titanium introduces residual stresses [14]. Depending on the applied laser parameters, the stress state can range from tensile to compressive. Although compressive residual stresses are generally anticipated to contribute to improved fatigue performance, laser marking negatively impacts the fatigue strength, regardless of residual stress state [14].

In the present study, an in-depth investigation of the impact of oxidative laser marking on the fatigue strength of CP titanium and titanium grade 5 (Ti6Al4V) is presented. The purpose of the investigation is to evaluate the impact of laser marking on fatigue strength and understand the mechanisms for crack initiation and propagation in relation to implant applications. The ramifications of applying laser marking on medical titanium products are discussed.

7.2. Materials and Methods

7.2.1. Materials

Two medical grade titanium alloys were included in this study: grade 5 (Ti6Al4V) and CP Ti grade 4. The key difference is the significantly higher strength of Ti6Al4V obtained from the alloying elements and the microstructure consisting of both the hexagonal close packed (HCP) α-phase and body centered cubic (BCC) β-phase. CP titanium consists essentially of α-phase titanium but depending on the impurity (particularly Fe) content β-phase can be present, too; the grade classification refers to the amount of oxygen and impurities (mainly Fe). Both materials were applied in annealed and stress relieved condition.

Table 7.1: Chemical composition as reported by the supplier given in wt%.

Alloy	C	N	O	Fe	Al	V	Ti
Ti6Al4V	0.01	0.01	0.10	0.14	6.01	3.84	Bal.
CP4-Ti	0.01	0.01	0.34	0.07	-	-	Bal.

Table 7.2: Relevant mechanical properties as measured and reported by the supplier.

Alloy	Tensile strength (MPa)	Yield strength (MPa)	Elongation %
Ti6Al4V	1135-1179	887-907	14.9-15.6
CP4-Ti	769-805	627-669	19.8-24.8

Both materials were supplied by Zapp in the form of drawn rods; the chemical compositions of the provided materials' certificates are listed in Table 7.1, while relevant mechanical properties are listed in Table 7.2 as reported by the supplier. Two sample geometries were manufactured by lathe turning. Fatigue specimens were manufactured in a "chess pawnlike" geometry, as illustrated in

Figure 7.1. Discs were cut from the rods by lathe turning for analysis of the laser marks. Laser marks were applied after grinding of the surface to remove features from the lathe turning. Grinding was performed by standard metallographic methods using successively finer SiC abrasive grinding paper with grit # 4000 in the final grinding step. Laser marking was performed covering almost the entire area of the ground surface.

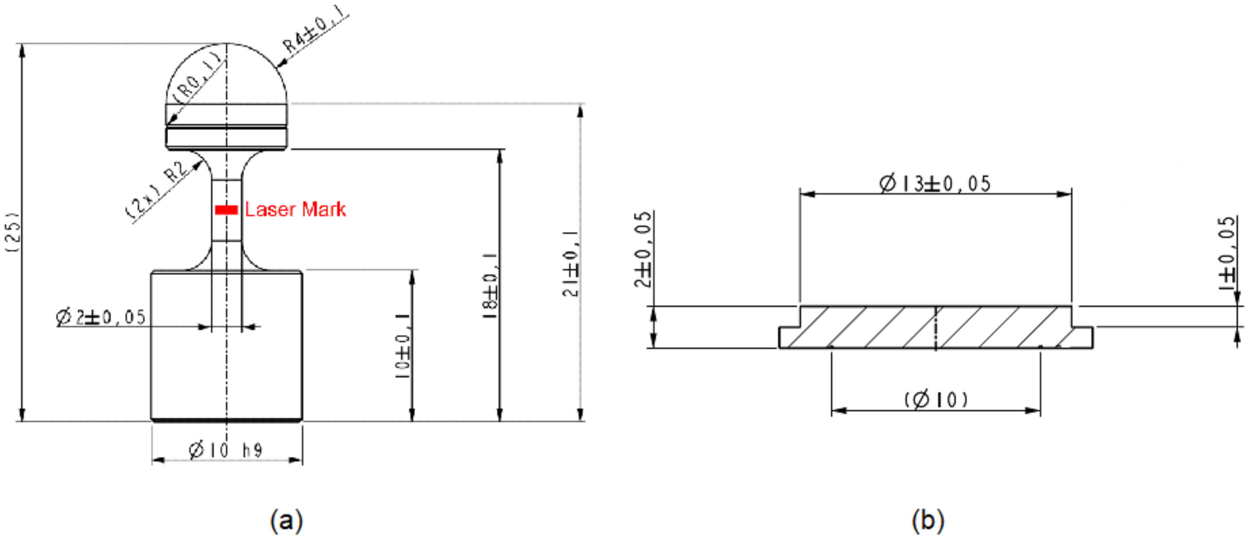

(a) (b)

Figure 7.1. Technical drawings of (a) specimens manufactured for fatigue testing and (b) discs cut for metallographic characterization. All dimensions are in mm.

7.2.2. Methods

7.2.2.1. Laser Marking

Laser markings were applied using the FOBA Y.0200 pulsed nanosecond YAG fiber laser. Constant and relevant laser parameters are listed in Table 7.3. The average power, scan speed, and pulse length were varied. From these laser settings the heat input (J/area) and power density (W/area) could be calculated [15]. The heat input is calculated as:

$$E_s = \frac{P}{v \cdot l_s} \qquad (7.1)$$

where P is the average power, v is the scan speed and l_s is the hatch spacing. The power density is calculated from the energy of a single pulse, which depends on the average power P, the pulse frequency f, the approximate laser spot area A, and the pulse length tp:

$$P_p = \frac{\left(\frac{P}{f}\right)}{A \cdot t_p} \tag{7.2}$$

Four parameter sets were investigated as listed in Table 7.4. The parameters were chosen within a range that will represent plausible industrial parameters to form black markings. Oxide layers are expected to form for all parameters and significant melting may occur for parameter sets with higher heat input.

Table 7.3: Laser parameters common among all investigated parameter sets.

Wavelength (nm)	Laser spot diameter (µm)	Pulse frequency (kHz)	Hatch spacing (µm)
1064	30	200	10

Table 7.4: Laser parameter sets applied in the study.

Parameter set	Average power P (W)	Pulse length tp (ns)	Scan speed v (mm/s)	Power density P_p (W/m^2)	Heat input E_s (J/m^2)
#1	6	100	70	$4.2 \cdot 10^{11}$	$8.6 \cdot 10^{6}$
#2	6	200	70	$2.1 \cdot 10^{11}$	$8.6 \cdot 10^{6}$
#3	12	200	70	$4.2 \cdot 10^{11}$	$1.7 \cdot 10^{7}$
#4	6	200	35	$2.1 \cdot 10^{11}$	$1.7 \cdot 10^{7}$

7.2.2.2. Scanning electron microscopy

The topography and microstructure of cross sections of the disc specimens were investigated by scanning electron microscopy (SEM). A Zeiss Sigma Field Emission SEM was utilized at acceleration voltages of 10–20 kV with the lower range used for secondary electron imaging and the higher range for backscatter electron imaging. The working distance was in the range 8–13 mm. For the cross-sectional analysis, the specimens were cut and embedded in Struers' Isofast epoxy resin. The embeddings were subsequently prepared by standard metallographic methods, with the last steps involving a colloidal silica suspension.

7.2.2.3. X-ray diffraction

X-ray diffraction (XRD) was utilized for phase analysis with the purpose of identifying the phases that formed on the sample surface during laser marking. The diffractometer used was a Bruker D8 Discover, equipped with a Cu anode (wavelength 0.15418 nm) and operated with Bragg-Brentano beam geometry. The scattering angle was varied in the range 20–65 ◦2Θ using a step size of 0.04◦ and a count time of 2 s per step.

7.2.2.4. Fatigue Analysis

Fatigue testing was performed with a Dyna-mess Dyna5dent-14801 according to ISO 14801 [16] standard for fatigue testing of dental implants. Fatigue testing simulates chewing, the worst-case scenario for a dental implant. The most severe testing is assumed to apply if the implant is inclined at a 30° angle with respect to the compressive force from chewing; the number of load cycles corresponds to the lifetime of the implant. The tests were stopped at $5 \cdot 10^6$ cycles if the specimen had not failed. The specimens were loaded with a harmonic force between 20 N and various maximum values to achieve different load amplitudes in the range from 40 N to 260 N. This corresponds to load ratios R of 0.33 to 0.07. The individual tests were performed at a constant maximum load and thereby constant load ratio. The maximum load was only varied in-between tests to construct S–N curves in accordance with ISO 14801. The loads were chosen to identify the endurance limit for a comparison between parameter sets and a reference specimen. The frequency was kept constant at 15 Hz. Temperature was monitored by a thermocouple next to the specimen to ensure that it was within the range 25–30 ◦C. ISO 14801 specifies two possible environments for fatigue testing of dental implants: 20 ± 10 ◦C in air at a frequency of 15 Hz, or 37

± 2 ◦C in saline solution at a frequency of 2 Hz. For this investigation, the former test method was preferred because of the higher allowed frequency. The rotational positioning of the specimen with respect to the laser mark position relative to the applied force was again chosen in order to ensure simulation of the worst-case scenario, where the laser-marked area would experience the highest tensile stresses. As the axial position of the piston is only limited by the specimen, the equipment will register a failure/fracture when the piston's axial displacement exceeds a preset value without reaching the nominal force.

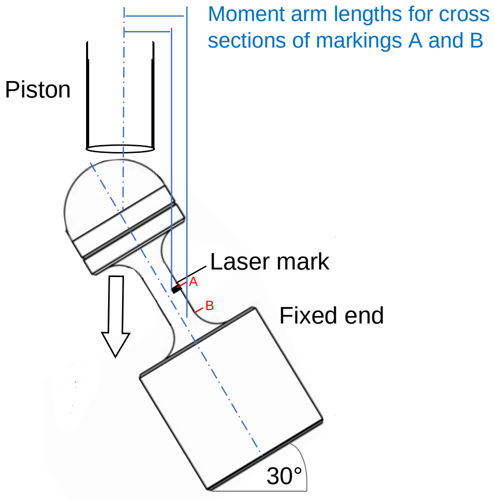

Figure 7.2: An illustration of the fatigue testing setup, showing the angled positioning of the specimen relative to the applied force.

Results of the fatigue tests are reported as cycles to failure at different stress amplitudes. The stress amplitudes were calculated as the difference between minimum and maximum bending stress:

$$\Delta\sigma = \Delta F\left(\frac{L\,r}{I} - \frac{\cos\alpha}{A}\right) \qquad (3)$$

Where 'ΔF' is the difference between minimum and maximum applied force in the individual test, 'r' is the radius of the shaft, 'I' is the moment of inertia for a cylinder I = π 4r4, 'A' is the cross-sectional area of the shaft, and ‘α’ is the tilt angle of the specimen. ‘L’ is the moment arm length indicated in Figure 7.2.

7.3. Results and Interpretation

7.3.1. Surface topography and microstructure after laser marking

All parameter sets for laser marking resulted in the formation of a black surface, with some degree of variation, see Figure 7.3 showing examples for Ti6Al4V. Parameter sets #1, 2 and 4 were almost glossy with #1 having the darkest coloration. #3 was also dark, but the surface appeared matte.

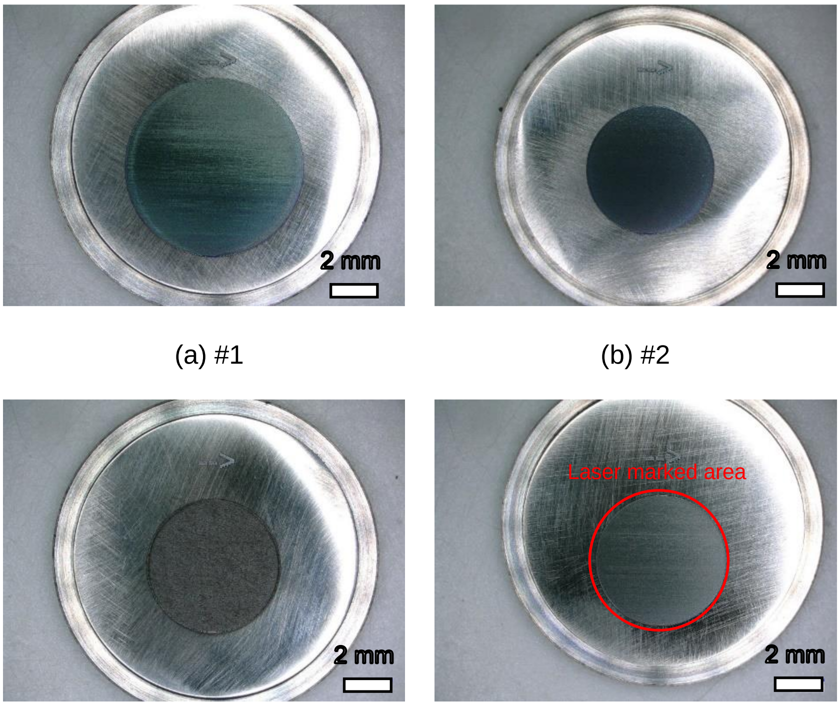

(a) #1 (b) #2

(c) #3 (d) #4

Figure 7.3. Digital microscopy images of laser-marked Ti6Al4V discs laser-marked with parameters #1 (a), #2 (b), #3 (c) and #4 (d)

In Figure 7.4 SEM micrographs of the laser-marked surfaces are presented, showing areas with several laser tracks. The laser track distance is indicated and is consistent with the nominal value of 10 µm (cf. above). Using a laser spot size of approximately 30 µm, results in 33% overlap of laser tracks, hence all areas have experienced 3 passes by the laser. Some variation in surface level is observed for the specimen that was laser-marked with parameter set #1 (Figure 7.4a.), most evident at the edges of each laser track. The same features can be observed for #2 and 4 (Figure 7.4b/d.), albeit to a lesser extent, while #4 has circular outcroppings in addition to the variation between laser tracks. On Figure 7.4d. parameter set #3 shows a significantly different morphology from the other parameter sets, as the surface appears to have been subjected to high temperatures causing melting and, possibly, ablation (note the larger scalebar). This structuring explains the matte appearance of the sample surface. Additionally, #3 differs from the other parameter sets in terms of cracks, as it has a significantly different crack pattern exhibiting a larger crack width and larger separation of cracks. In samples #1, #2 and #4, the pattern of the cracks remains largely the same, while #4 may have a slightly larger crack separation. #3 has a crack separation of 30–60 μm while the other samples have just 5–15 μm. The crack width for #3 is also several microns, while it is sub-micron for the other samples.

The laser-marked surfaces of the Ti6Al4V are shown in the following Figure 7.5 for all laser parameters. The morphologies in dependence of laser parameters are similar to their CP-Ti counterparts. Slight differences can be observed between CP-Ti in Figure 7.4 and Ti6Al4V in Figure 7.5. Ti6Al4V #3 has the same morphology as CP-Ti for the same laser parameters, because severe surface melting is responsible for the morphology. On #4 the same features are visible; however, the tracks are not as pronounced on Ti6Al4V, and the protrusions are larger. Slight differences in the structures inside the laser track can be observed, but a more significant difference is the distance between cracks between the two materials. Ti6Al4V generates cracks with almost twice the separation distance as compared to CP-Ti. CP-Ti has a crack distance of 5–10 μm while Ti6Al4V reaches almost 20 μm.

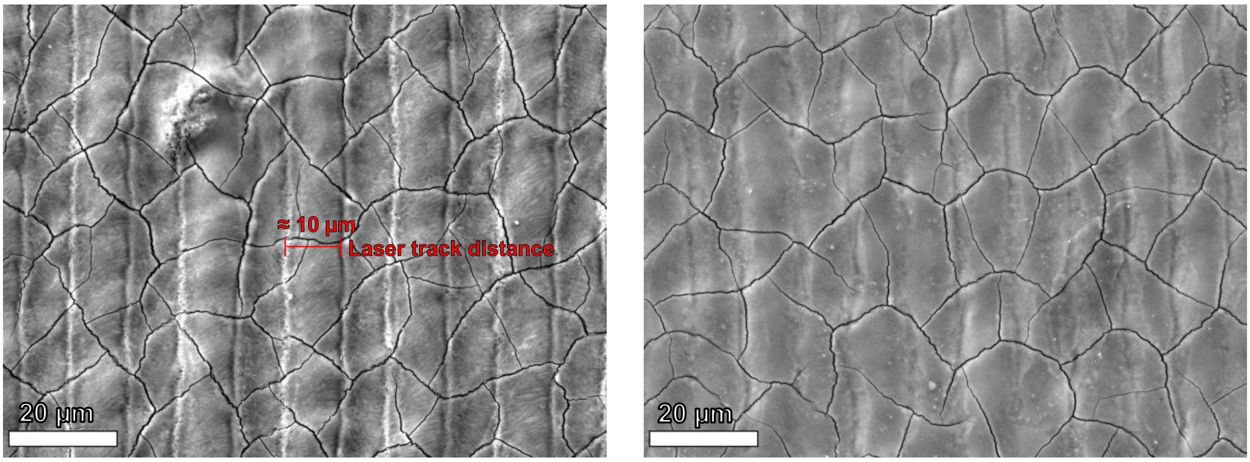

(a)

#1 Pp high – Es low

(b)

#2 Pp low – Es low

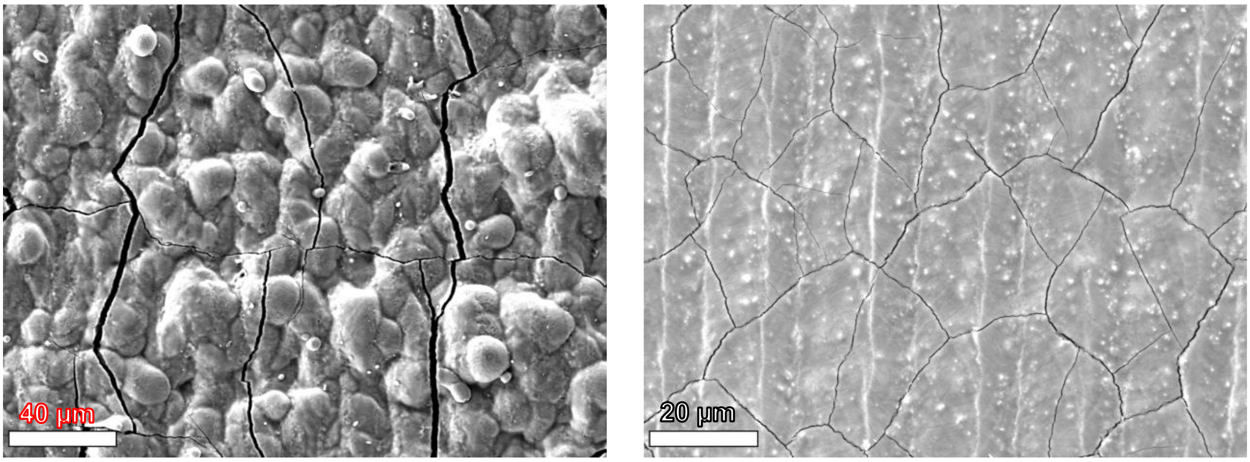

(c)

#3 Pp high – Es high

(d)

#4 Pp low – Es high

Figure 7.4. Top-down secondary electron imaging of laser-marked CP-Ti. Note different scale bar in (c).

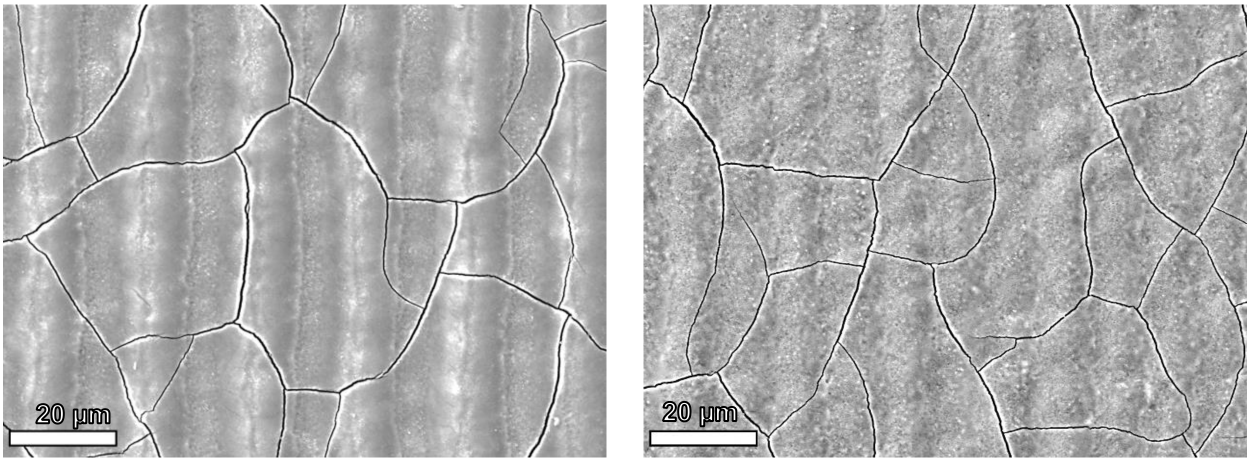

(a) (b)

#1 Pp high – Es low #2 Pp low – Es low

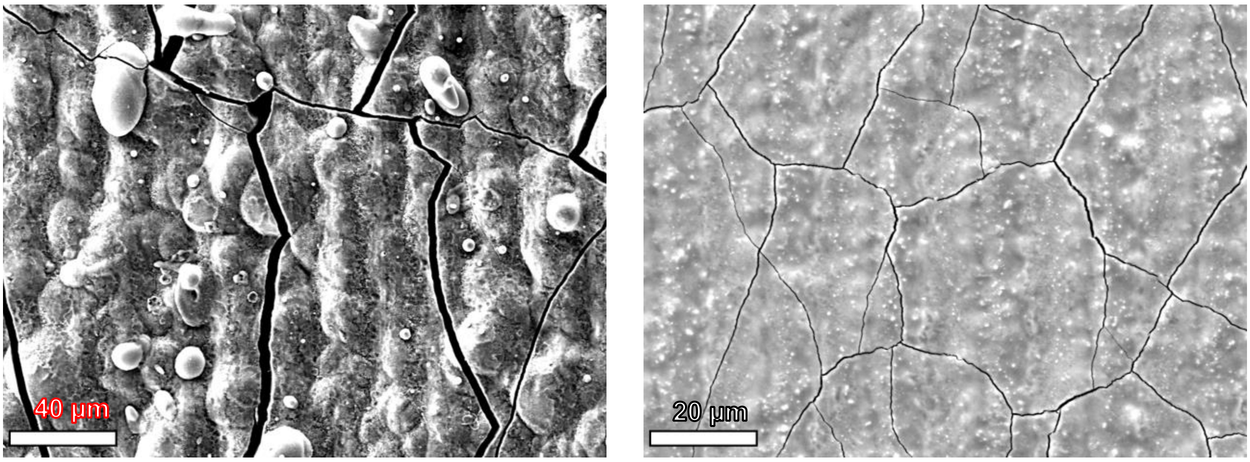

(c) (d)

#3 Pp high – Es high #4 Pp low – Es high

Figure 7.5. Top-down secondary electron micrographs of laser-marked Ti6Al4V. Note different scalebar in (c).

The cross-sections presented in Figures 7.6 and 7.7 show clear HAZ's with distinct microstructures and vertical cracks. The cracks observed in the surfaces shown in Figures 7.4 and 7.5 extend into the material and are not limited to a surface oxide layer. Especially for #3, the high degree of melting caused a rough surface, which can also be observed in the cross section. The dark coloring of the laser-marked surfaces, as previously shown in Figure 7.3, is in the cross sections located in the zone nearest to the surface, which contains very small grains.

From the cross-sections of the CP-Ti laser-marked specimens in (Figure 7.6), it is clear that the cracks are not restricted to the surface oxide layer, but penetrate deeper into the material, regardless of the laser parameters. The crack length is approximately 2 µm for parameters #1–2, while #4 has a slightly longer crack length of ≈4 µm. Parameter set #3, shown in Figure 7.6c., differs dramatically from the others as the cracks reach lengths of up to 40 µm, i.e., more than 10 times the maximum crack length of the other parameter sets. Condition #3 also exhibits an uneven surface, as expected from the apparently high surface roughness observed in Figure 7.4c. The HAZ is almost equal to the crack length of 40 µm for #3. The HAZ of #1 is comparatively small, reaching only 4 µm in depth. #2 has the shallowest HAZ of 1–2 µm, while #4 has a HAZ of 5–6 µm, slightly larger than that of #1.

The HAZ for parameter sets #1, #2 and #4 can be divided into three microstructurally distinct regions before the bulk is reached, as presented in Figure 7.6d. for backscatter electron imaging. Closest to the surface, very fine grains are observed; this is interpreted as direct α-phase solidification from a liquid phase. It is likely that oxygen was dissolved into the melt, enabling direct solidification as nano-sized α-grains. Underneath, a layer of a few microns consisting of grains is identified, which is interpreted as oxygen (and/or nitrogen) stabilized α-Ti. Sandwiched in-between the α-Ti layer and the bulk material a layer of martensite is observed, indicating that this part has been β-Ti during laser treatment, which transformed martensitically to α′ -Ti on cooling. Cracks appear to extend into oxide and α-Ti layers and only occasionally into martensite.

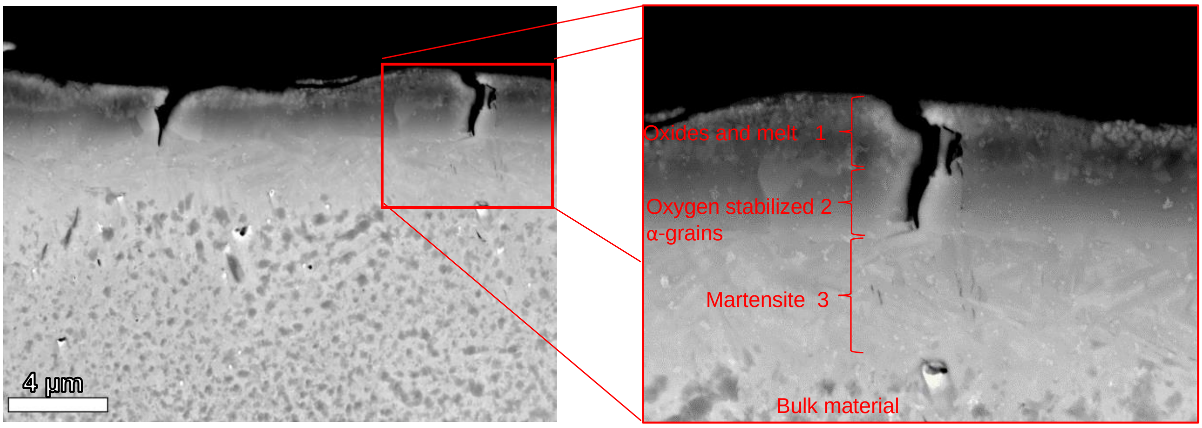

(a)
#1 Pp high – Es low

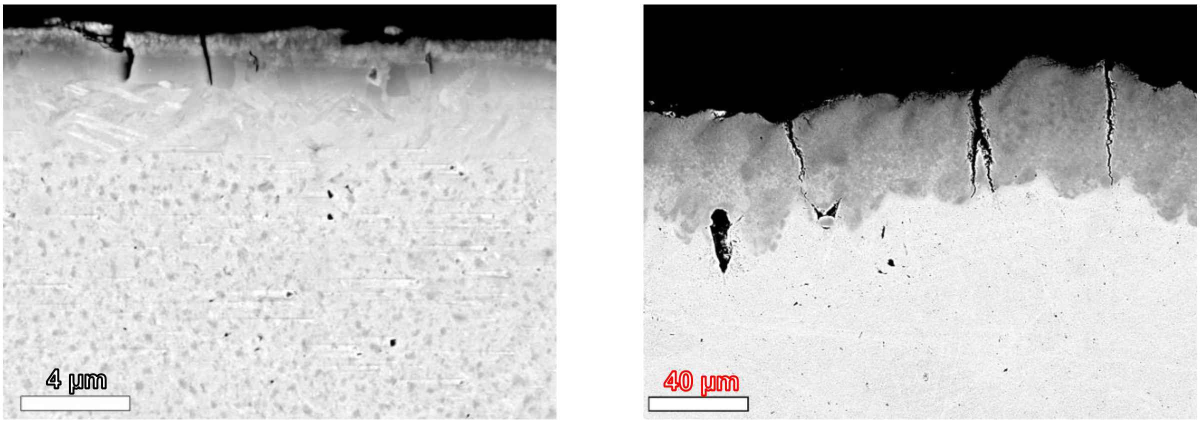

(b)
#2 Pp low – Es low

(c)
#3 Pp high – Es high

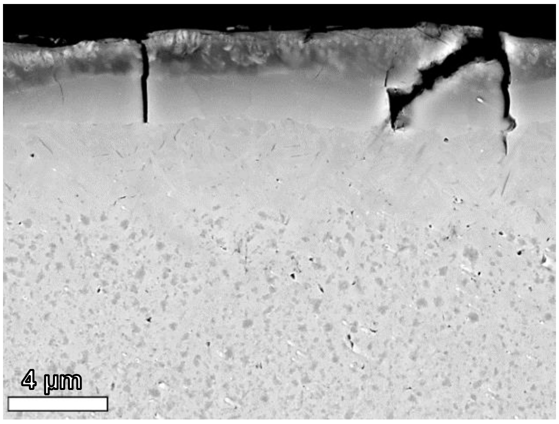

(d)
#4 Pp low – Es high

Figure 7.6. Backscatter electron micrographs of cross-sections of laser-marked CP-Ti marked with (a) #1, (b) #2, (c) #3 and (d) #4. Note different scalebar on (c)

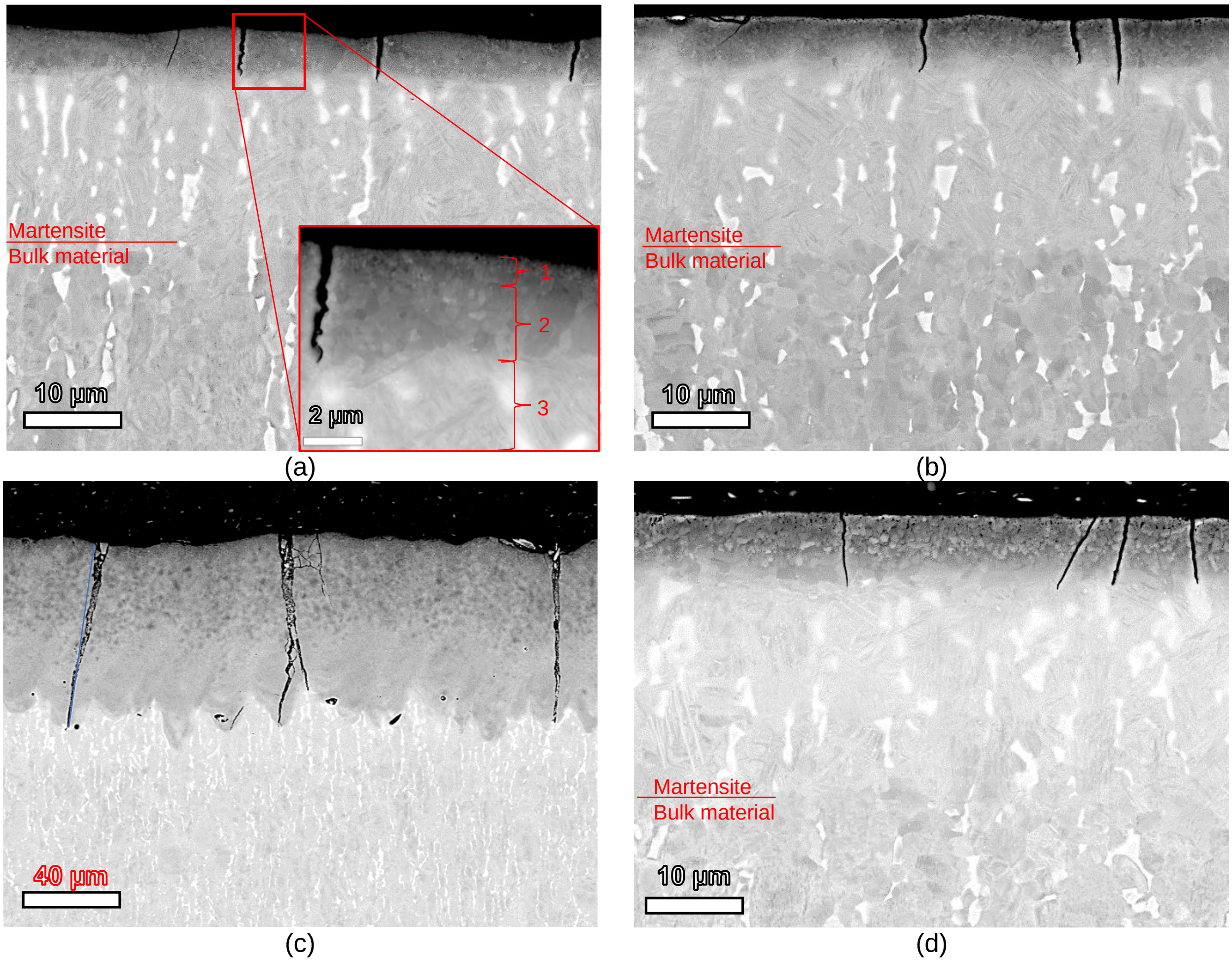

Figure 7.7. Backscatter electron micrographs of cross sections of laser-marked Ti6Al4V marked with (a) #1, (b) #2, (c) #3 and (d) #4. Note different scalebar in (c).

As compared to CP Ti, some differences are observed after laser marking the α/β microstructure of Ti6Al4V (Figure 7.7). The bulk structure contains a minor fraction of β-phase in-between the α-grains. The β-phase regions range from 0.5 µm to 2 µm in size and are elongated in the drawing direction perpendicular to the surface. The β-phase appears bright in the backscatter electron images, due to the higher content of heavier alloying elements (in this case V). All laser marking parameters resulted in visible HAZ's deeper than that of the CP-Ti, as martensite can be observed to have formed 20 µm deep in the material. In Ti6Al4V, the region closest to the surface consists of nano-sized grains (see insert in Figure 7.7a). It would be the result of an oxygen-rich melt solidifying, as seen in CP-Ti. The depth of this zone indicates significantly more melting in Ti6Al4V, and no zone of the larger oxygen stabilized α-grains can be observed. This zone is followed by a deep zone where martensite coexists with V-stabilized β-Ti. Martensite formed from V-lean β-Ti during rapid cooling. For specimen #3, the HAZ is much deeper, but the same features are visible.

Performing phase analysis using XRD of the laser-marked CP-titanium yields the diffractograms presented in Figure 7.8; a reference sample is shown along with the laser-marked specimens. The reference sample contains peaks of hexagonal close packed (HCP) α-titanium and a single peak of (BCC) β-titanium can be resolved. The α-phase is still detectable in the laser-marked specimens, but the peaks are shifted and asymmetric, which is especially evident for the α-peak at ≈62°2ϴ, with a visible shoulder on the laser-marked peaks. The peak appears to have shifted to lower °2ϴ, indicating an expansion of the lattice. Double peaks can be observed for the α-phase at 52 °2ϴ. Peak shift, in this case to a smaller scattering angle, is the consequence of a larger lattice spacing in the measurement direction and is a consequence of either residual stresses and/or dissolution of interstitials. Abundant cracks indicate that relaxation of stresses in the direction parallel to the surface has occurred (at least partly). The presence of oxides indicates dissolution of oxygen, which indeed leads to an increase in particularly the ‘c’ lattice parameter of α-Ti [17]. The asymmetry of certain peaks could indicate a gradient in residual stress or in interstitial content along the measurement direction. As a consequence of stress relaxation in the plane of the surface, 3D stress distributions develop in the islands separated by cracks. In principle asymmetry may arise from such stress (strain) distributions. Nevertheless, the presence of oxygen gradients in the analyzed volume is held responsible for the asymmetry, because changes in composition have generally a larger effect on the peak shift than stress/strain inhomogeneities. The formation of double peaks and the largest shift for peaks related to the ‘c’ lattice parameter corroborate this interpretation, because the c lattice parameter is most sensitive for the dissolution of interstitials [17].

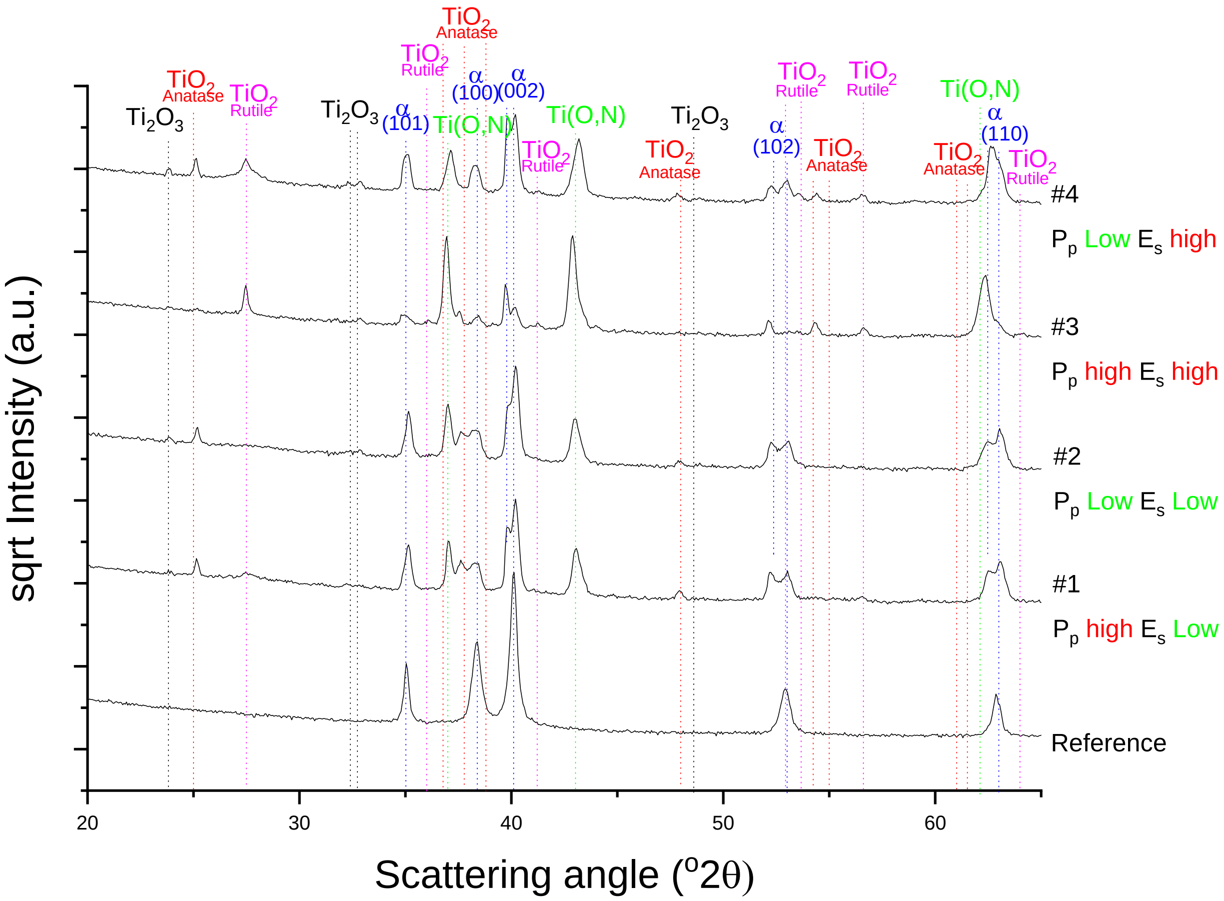

Figure 7.8: Diffractogram of a reference sample of CP-Ti and laser marked surfaces.

Several new phases were identified after laser marking. Clearly, several oxides are present: Ti_2O_3, TiO_2 in the form of both rutile (tetragonal) and anatase (BCC), as well as rock-salt type “TiO”; it is noted that TiO is isomorphous with TiN and that these compounds are considered fully intersoluble. Accordingly, the identified TiO peaks could just as well be a mixed compound, i.e. Ti(O,N). The Ti(O,N) peaks vary in position for different laser parameters and are slightly asymmetric. Specimen #3, which is assumed to have reached the highest temperatures for the longest duration, exhibits a significant deviation in Ti(O,N) peak position from the remaining laser parameter sets. The amounts of TiO and TiN that have formed can vary for the different heat treatments. Especially the Ti(O,N) peak of #4 is located at a position different from the other parameter sets.

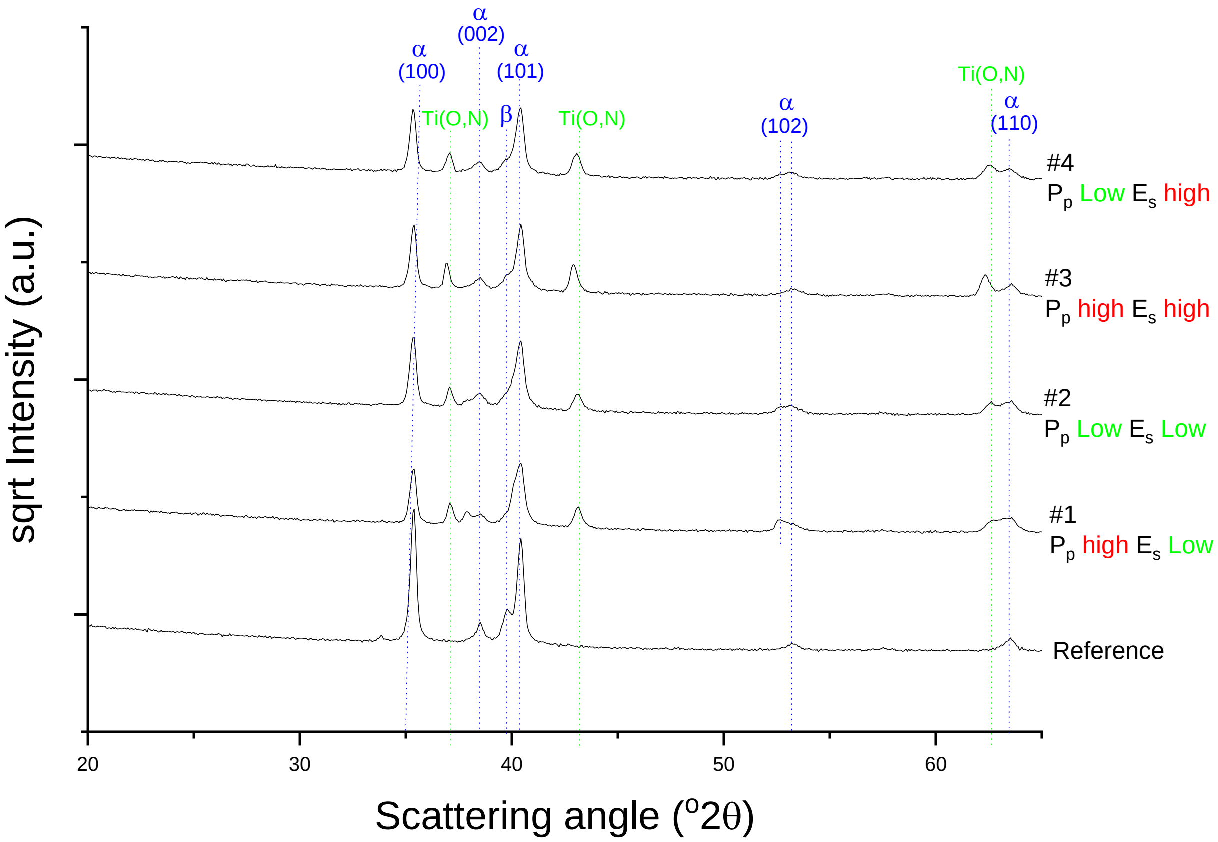

Figure 7.9: Diffractogram of laser marked Ti6Al4V with parameters #1-4 as well as a reference sample.

The diffractograms for laser-marked Ti6Al4V in Figure 7.9 show that only Ti(O,N) can be identified, but with a relatively high intensity. Significant shifts of the α-phase (002) and (102) peaks in Figures 7.8 and 7.9 are observed, because their peak positions are most sensitive for the c lattice parameter of hcp Ti and interstitially dissolved O and/or N affects the c lattice parameter much more pronouncedly than the a lattice parameter [17]. A broadening of the peaks could be a consequence of the formation of nano-sized grains as observed in Figure 7.7 or a variation in chemical composition within the diffracting volume. The diffractogram in Figure 7.9 contains an artefact peak at 33 ◦2Θ, produced by the step in the sample geometry, as illustrated in Figure 7.1b.

7.3.2. Fatigue and fracture analysis

Figure 7.10 a and b show two S–N diagrams summarizing all fatigue testing results for CP-Ti and Ti6Al4V, respectively[13]. For both materials, the obtained data follow in general the characteristic form of S–N curves for metals, irrespective of the presence or the type of laser markings. The applied load is presented as the stress amplitude because the effective arm length is different for laser-marked specimens as compared to the reference specimen. Laser-marked specimen fracture at the laser mark (see point A on Figure 7.2), yielding a horizontal arm length of 3.5 mm, while the unmarked specimens fracture in the neck (see point B on Figure 7.2) at a horizontal arm length of 4.5 mm. In the high cycle fatigue range the allowable stress amplitude decreases linearly with the logarithm of the number of cycles. Below a certain fatigue endurance threshold, virtually infinite lifetime is observed for tests stopped after a maximum of $5 \cdot 10^6$ cycles (filled markers in the diagrams). The absence of a plateau in the low cycle regime indicates that none of the tests were performed above the yield strength, which would lead to low cycle fatigue.

CP-Ti specimens without laser markings are included in Figure 7.10a as a baseline case and exhibit an endurance limit of approximately 750 MPa in bending moment. The surface quality of these specimens is as manufactured by lathe turning. A dramatic reduction in fatigue strength is observed for all laser-marked specimens in comparison with the baseline, regardless of the specific laser parameters. Parameter sets #1, #2 and #4 exhibit similar fatigue performance, with approximately the same slope in the high cycle fatigue region and an endurance limit characterized by a stress amplitude of about 330 MPa. This is a reduction in fatigue limit by more than 50% as compared to the baseline. The performance of parameter set #3 is significantly worse than the

---

[13] Endurance limits of the reference specimen were identified to be at higher stress amplitudes than the tensile yield strength given by the supplier and measured in uniaxial tensile testing. The yield strength as determined in a bending test is anticipated to be higher, as part of the component is in compression. Values reported by other authors obtained from CP-Ti testing via ISO 1801, are consistent with the current values after recalculation for their loads, diameters and arm lengths [37]–[39].

other three laser parameter sets, resulting in an “endurance limit” of only 100 MPa, i.e., a reduction of the fatigue limit of about 85%.

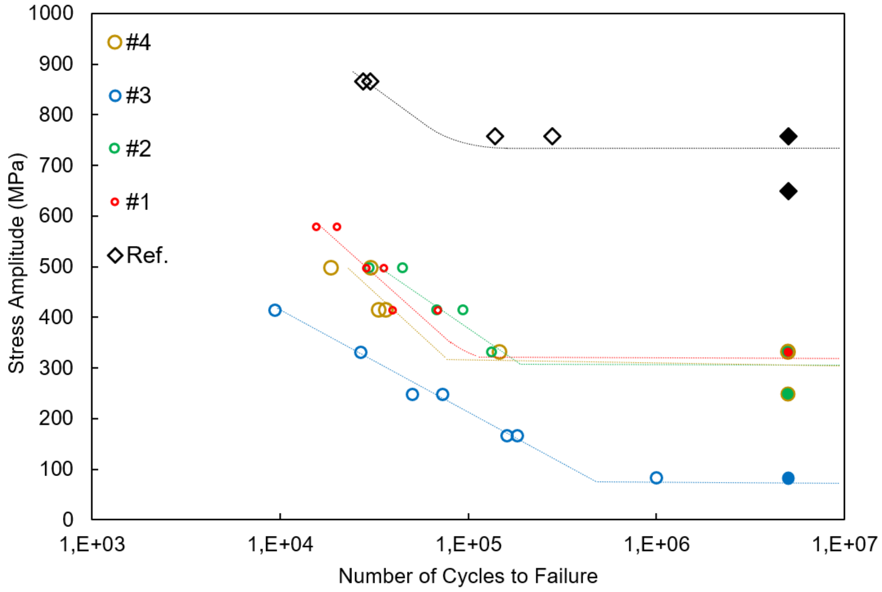

(a)

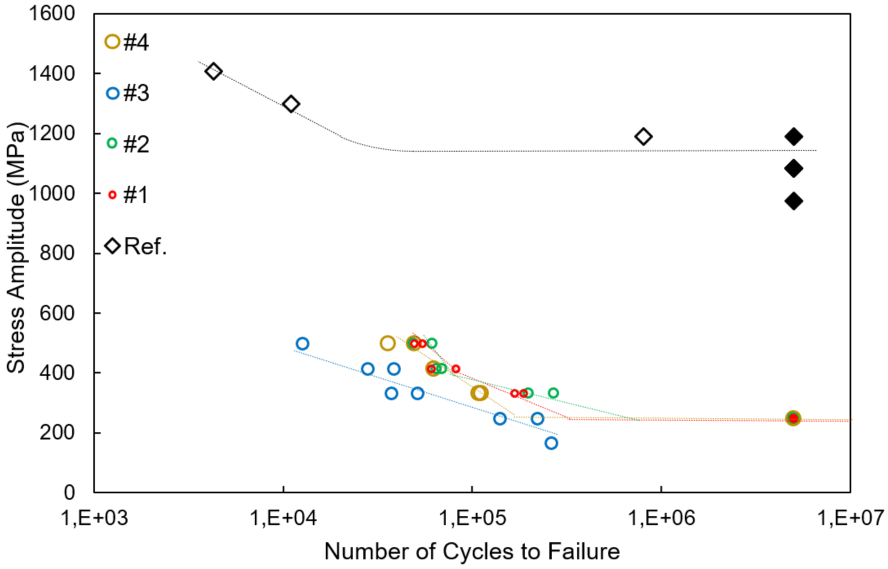

(b)

Figure 7.10. S–N data of fatigue tested (a) CP-titanium and (b) Ti6Al4V specimens, tested with different laser marking parameter sets (#1–4) and without laser marking (Ref.). Lines are given to guide the eye.

For Ti6Al4V, the detrimental effect of laser marking on fatigue performance is even stronger than for CP-Ti. The endurance limit of the unmarked baseline specimens at about 1150 MPa stress amplitude, significantly higher than the CP-Ti baseline. As before, parameter sets #1, #2 and #4 lead to similar fatigue performance, which is significantly deteriorated compared to the baseline for Ti6Al4. For the parameter set #3, the reduction in endurance limit is even more dramatic than for sets #1, #2 and #4, as was the case also for CP-Ti. Parameter sets #1, #2 and #4 exhibit an endurance limit of just 250 MPa, lower than the corresponding parameter sets in CP-Ti. This is a reduction of 80% relative to the untreated alloy. Ti6Al4V specimens treated with parameter set #3 exhibit an endurance limit similar to that of the corresponding CP-Ti specimens.

Selected fractography images of fractured specimens are shown in Figures 7.11–7.14. The surface shown in Figure 7.11 corresponds to the baseline CP-Ti specimen fractured at a stress amplitude of 860 MPa. The fracture pattern extending at the top of the cross section indicates the crack initiation site. The steady crack propagation area extends from the top downward over approximately one third of the cross section. Higher magnification images of this region show striations that are typical for stage II fatigue crack propagation [18]. The lower two thirds of the cross section correspond to accelerated (stage III) crack propagation towards the final fracture. For CP-Ti the final stage of crack propagation occurs along grain boundaries. This is different from the results for Ti6Al4V, discussed later, where ductile fracture is observed in the final stage, with formation of the characteristic dimples seen in the corresponding region in Figure 7.15 [18].

Different fatigue behavior is observed in the laser-marked sample, with an example of laser-marked CP-Ti shown in Figure 7.12. No clear crack initiation site can be identified. Rather, the crack appears to have propagated from the entire laser-marked surface. Propagation lines do not emerge from a single point, but from the surface area instead. Closer inspection of the laser-marked area reveals the HAZ closest to the surface then followed by a crack propagation zone. At higher magnification in the stage II propagation zone, striations are observed, but are significantly smaller than for the baseline CP-Ti owing to the lower load levels for fatigue testing. The fracture surface for parameter set #3 is shown in Figure 7.13. The stage II propagation zone is much larger, covering more than half of the cross section, because the overall load level during this fatigue test is very low, as the specimen fractured at a stress amplitude of just 170 MPa, cf. Figure 7.10.

The crack initiation sites on the fracture surfaces are compared in Figure 7.14 for all laser parameters. It is clear that #3 has a much deeper case of brittle material and that the fracture in this HAZ is approaching a brittle fracture. In most specimens, the HAZ is clearly visible in the fractured surfaces. Some areas, especially for CP-Ti #1, the HAZ is not visible as a consequence of deformation of the fracture surface. Upon further inspection, such areas are visible on most specimens, but only close to the surface. An explanation can be in the nature of the test and the many cycles where crack propagation close to the surface is slow. The two surfaces may have touched each other repeatedly, resulting in this kind of deformation.

Ti6Al4V behaves slightly different than CP-Ti and the fracture surface has a different morphology. Ti6Al4V has smaller grains, which results in a finer morphology. Striations are visible at higher magnifications but are smaller than the corresponding specimen manufactured in CP-Ti for all laser parameters and fatigue analysis loads. An example of a fractured surface of parameter set #3 and a stress amplitude of 400 MPa, is shown in Figure 7.15. Ti6Al4V has a significantly higher strength than CP-Ti (Table 7.2), which resists crack propagation, leading to more finely spaced striations. The HAZ shows signs of brittleness, as cracks remain in the zone. The crack has propagated primarily through the α-phase.

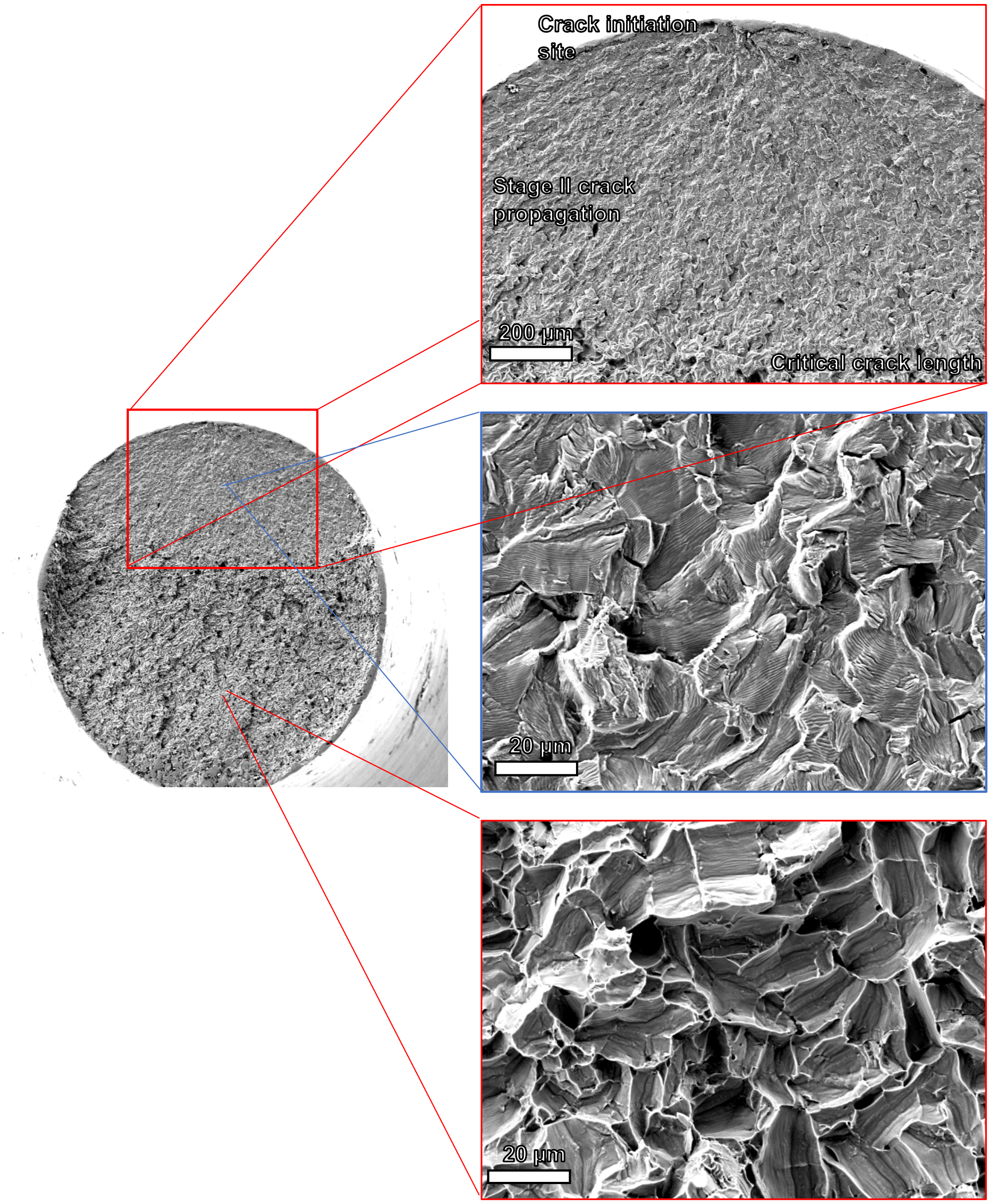

Figure 7.11: Secondary electron images of a fractured fatigue specimen, tested at 850 MPa manufactured in CP-Ti and without laser marking. The left side shows an overview image of the fractured surface, and the right side shows magnified areas in the crack initiation-, crack propagation- and fast fracture zones.

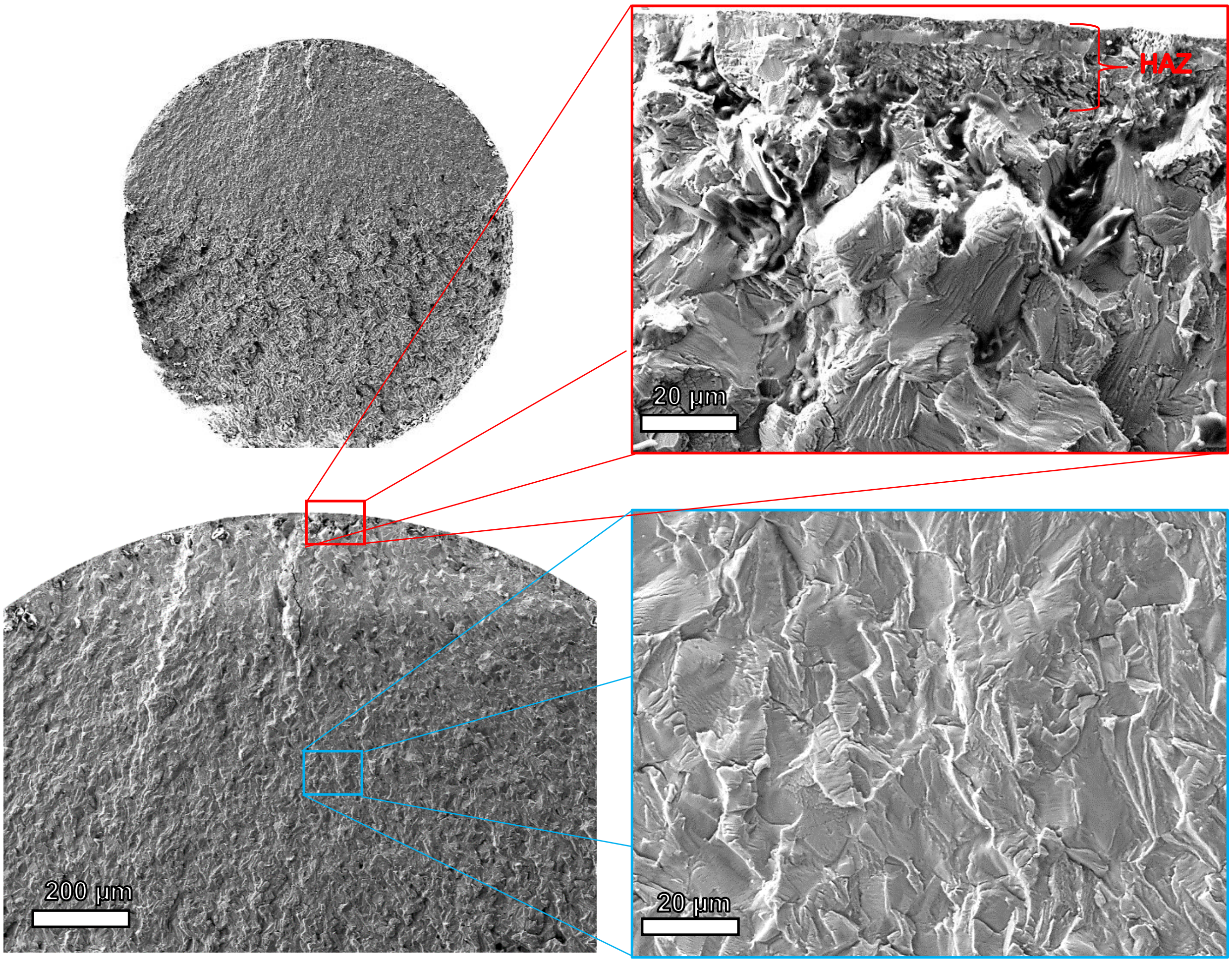

Figure 7.12: SEM micrographs of fractured CP-Ti after laser marking with parameter set #4 and fatigue testing at 420 MPa

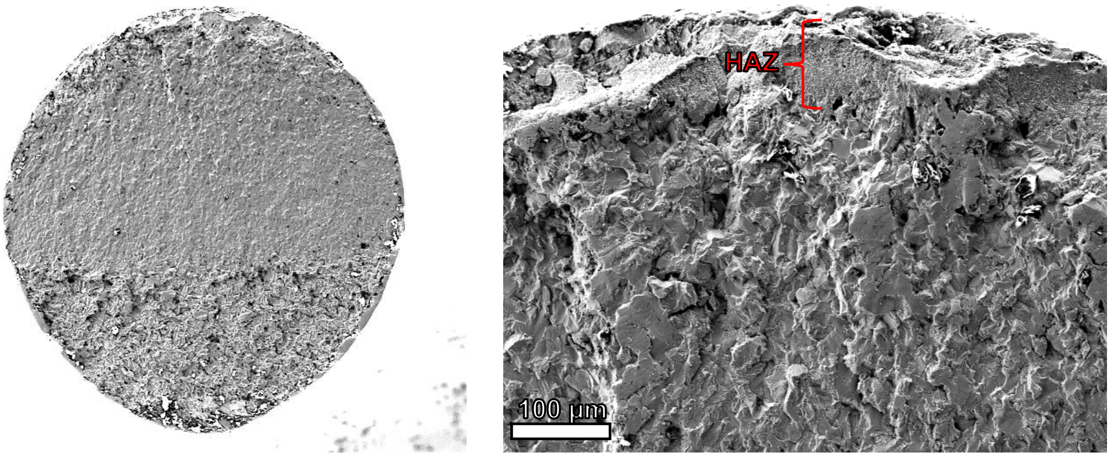

Figure 7.13: Overview image of CP-Ti laser marked with parameter set #3 after fatigue testing and a magnified image of the crack initiation at the laser mark. Images are captured via secondary electron detector.

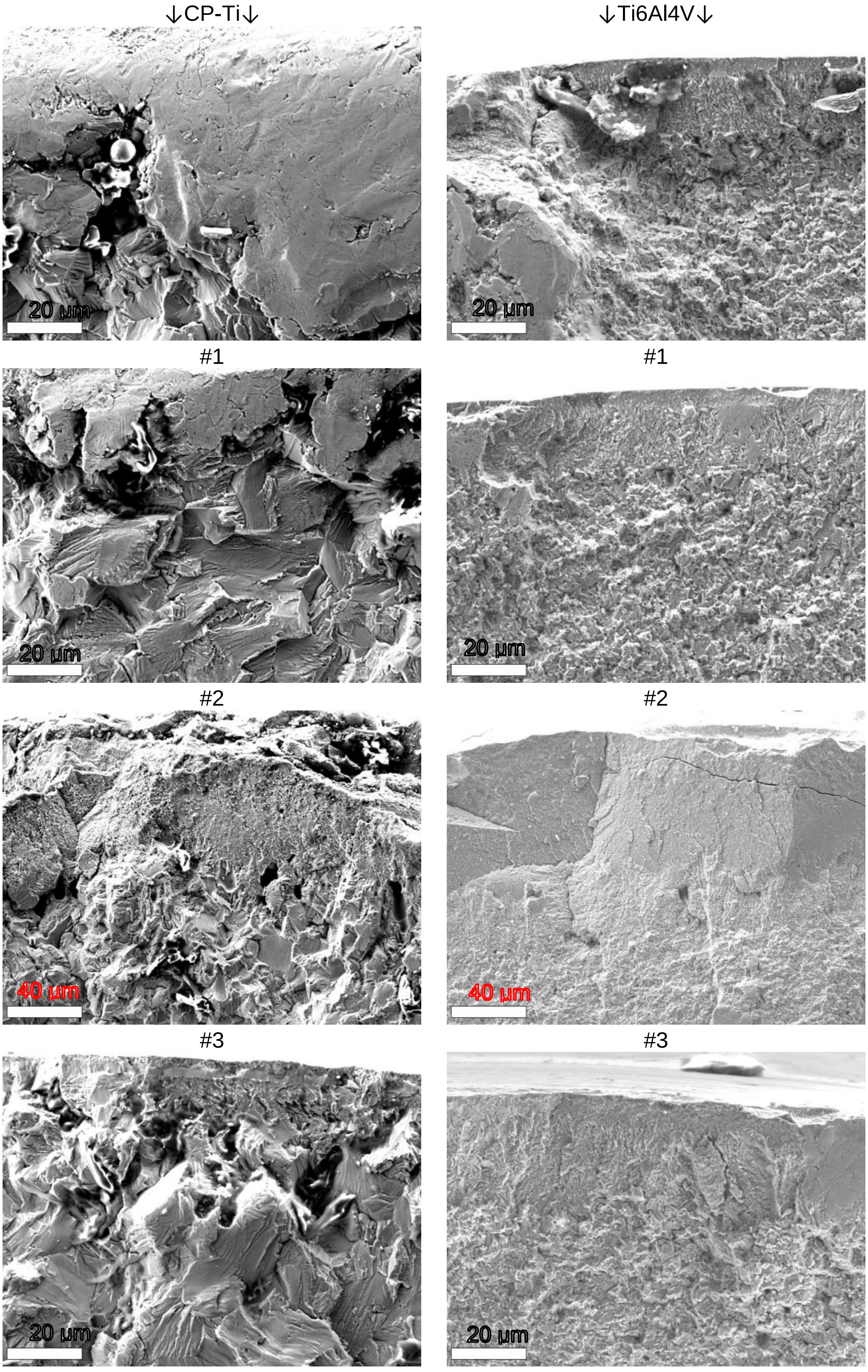

Figure 7.14: SEM secondary electron micrographs of the crack initiation sites of fractured fatigue specimens for all parameters for CP-Ti (left) and Ti6Al4V (right).

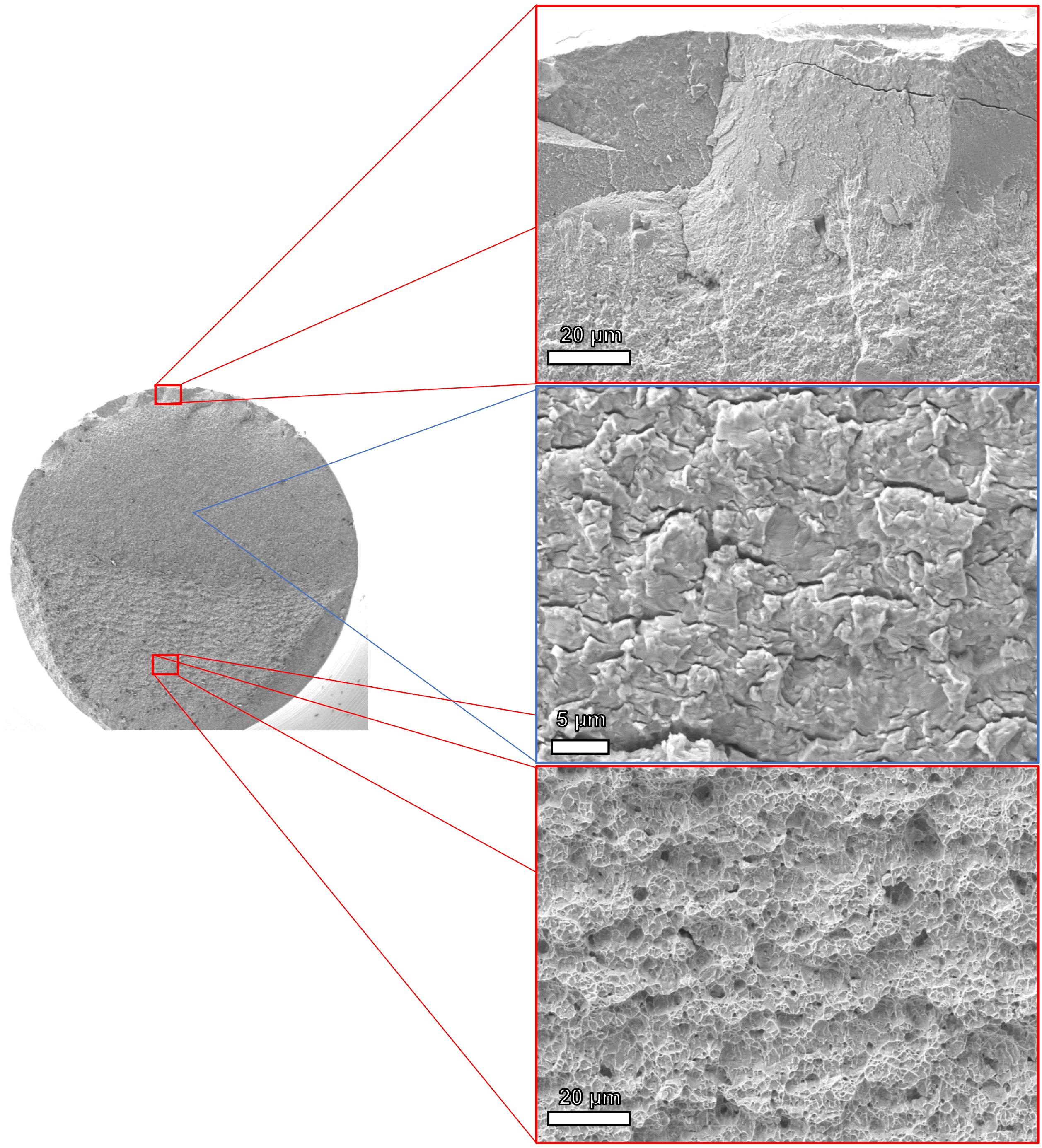

Figure 7.15: Secondary Electron Micrographs of the fractured surface of a Ti6Al4V specimen, laser marked with parameter set #3 and tested at 400 MPa.

7.4. Discussion

All laser-marking parameters produced black markings capable of producing a text/tag readable without aid. This means that all parameters, in principle could fulfill the requirements for formation of UDI on medical devices [7]. It is however also clear that cracks form in the surface zone upon laser marking as is evident from Figure 7.4, and that the cracks penetrate a considerable distance into the HAZ as observed in Figure 7.6 and 7.7. These cracks formed during the cooling of the laser tracks. Other investigations have shown that high residual stresses can form indeed during laser marking of titanium alloys [14]. It should be noted that no apparent correlation was observed between the crack networks and the laser tracks. Several mechanisms contribute to residual stresses in the top layer. Since only the surface is heated during laser marking while the bulk stays cold, thermal shrink on cooling as well as volume changes associated with phase transformations as liquid→solid and β→α are the obvious sources of residual stresses during cooling [14]. The origin of tensile residual stresses and crack initiation will be identified below.

Considering the cross sections of the laser-marked specimen on Figures 7.6 and 7.7, it is observed that the cracks reach below the oxide layer. For all laser parameters but #3, the cracks terminate at, or near, the transition from α-Ti to martensite in the HAZ. The cracks are perpendicular to the laser-marked surface, which indicates that they originate from tensile stresses imposed by the volume underneath the oxide and α-Ti zones (cf. Figures 7.6 and 7.7). The observation that cracks end near the martensitic zone in the HAZ strongly suggests that crack initiation has occurred as a consequence of a volume expansion associated with the β→α transition [19–22].[14]

---

[14] For pure titanium the transition from BCC β-Ti to HCP α-Ti is accompanied by a volume decrease from 18.25 10^{-30} m^3 per Ti atom to 17.70 10^{-30} m^3 per Ti atom [40], because the latter is more densely packed. The presence of (unintentional) alloying elements in the lattice may change this volume reduction into a volume expansion. For example, the presence of O in HCP α-Ti will cause a larger volume expansion (expressed per Ti atom) in BCC β-Ti than in HCP α-Ti. Hence, the presence of O in β-Ti can lead to a volume expansion on martensitic transformation.

The development of the HAZ can be discussed as follows. The depth range of the HAZ is taken as the transition from a martensitic structure to the initial microstructure of the alloy. The transition from martensite to initial microstructure corresponds to a temperature where β-Ti was stable during laser marking, i.e., the β-transus, which corresponds to 882 ◦C for pure titanium. Since titanium has an extremely high affinity for oxygen, atmospheric air is a highly oxidizing environment at elevated temperatures. Above β-transus, ingress of oxygen occurs rapidly by diffusion into β-phase. However, the solubility of oxygen in β-phase is limited, such that ingress of oxygen promotes the formation of α-Ti, which has a much higher capacity for oxygen [23,24]. Accordingly, at high temperature, for parameter sets #1, #2 and #4 the HAZ consists of a sequence of melt at the surface, an oxygen stabilized layer of α-Ti and a layer of β-Ti. The melt will have a high content of oxygen and solidifies directly as α-grains, as the oxygen suppresses the β-transformation, explaining the small grain size. Oxide particles can have precipitated along with the α-Ti or been generated during subsequent cooling [25]. The dissolution of oxygen in α-Ti leads to a volume expansion, which is corroborated by the peak shift/split of metallic α-Ti peaks in Figure 7.8. Thermodynamically, a series of oxides including TiO and Magnéli oxides (TinO2n-1) would be expected in-between O-rich α-Ti and TiO2 [25]. Short oxidation times in the microsecond regime may have prevented the nucleation of all expected oxides, because only TiO and Ti_2O_3 were found occasionally. The titanium-based oxides identified with XRD are consistent with those expected [26,27], apart from the relatively low abundance in Ti6Al4V of the most stable oxide TiO_2. Titanium is known to become harder by solution strengthening and more brittle by dissolution of oxygen [28,29]. This is anticipated to have played a role in crack initiation upon martensitic transformation of oxygen lean β-Ti into α-Ti.

For Ti6Al4V the HAZs are similar to those for CP-Ti. However, the martensitic transformation extends appreciably deeper for Ti6Al4V than for CP-Ti. A variety of mechanisms can be responsible for this difference in HAZ. The thermal conductivity of Ti6Al4V is lower than for CP-Ti, giving a larger accumulation of heat in the surface, since the bulk is a less effective heat sink. The interaction with the laser can vary between the two materials, as the absorption is dependent on temperature and formation of oxides. When another phase, such as oxides, form on the surface, the laser absorption would naturally change [30]. Evidently, the abundance of oxides is different on the CP Ti and Ti6Al4V surfaces (Figures 7.8 and 7.9). Hence, under the influence of the temperature gradient β-Ti has developed much deeper into Ti6Al4V than in CP-Ti, which, on cooling, has led to a thicker zone where martensite has formed. The V-rich β-phase in the original microstructure is clearly identified in the microstructure in Figure 7.7 as the bright areas. This original β-phase did not transform during laser treatment, only the surrounding α-matrix transformed to β-phase and subsequently transformed to martensite. The much thicker martensite zone in the HAZ in Ti6Al4V than in CP Ti, and the dual phase nature of the original (and transformed) microstructure of Ti6Al4V will cause a different distribution of the transformation stresses. Also, the different compositions of the transforming β-phase and forming martensite in the two alloys will affect the volume change during the transformation. These circumstances may provide an explanation for the difference in crack density at the surface as observed in Figures 7.4 and 7.5 for corresponding laser parameter sets.

E. Györgi et al. found a network of microcracks after laser processing which they believed to be a consequence of consecutive remelting of the surface [31]. This could contribute on a large scale in the present experiments for parameter set #3, where the cracks are both wider and more widely spaced. It is clear from the surface morphology of #3, that a large degree of melting did occur during laser marking and that the cracks extend deeper into the material. Hence, they are wider at the surface. No clear indications of martensite formation were observed for parameter set #3. Instead, the initiation of cracks is entirely attributed to tensile stresses caused by thermal shrink of the solidified zone, which contains a large abundance of oxides.

There are other potential issues regarding laser-marked titanium as implants, since a myriad of titanium oxides can form on the surface. The passive film of TiO_2, characteristic for titanium alloys, is responsible for the bio-inert properties which makes titanium alloys such an attractive biomaterial. However, this film also retards the initial osteointegration [32]. When a significantly thicker oxide layer is produced via laser marking, it could potentially inhibit osteointegration indefinitely. There is also the issue of toxicity, and as the surface of titanium is conventionally TiO_2, the toxicity of the other oxides has not been investigated yet. But TiO_2 has been researched extensively in biological systems and doubt has recently been raised regarding the biocompatibility with much discrepancy between studies [33]. TiO_2 in the form of nanoparticles has been shown to accumulate and potentially cause cell death and affect the nervous system [34,35]. Laser markings should be investigated to rule out the formation of oxide particles, which could be absorbed into the body. The large cracks generated in the laser markings could potentially be a factor negatively affecting the cleaning procedure and bacterial growth on implants. It has been shown that porous titanium implants, although they improve osteointegration, may be more susceptible to bacterial growth [36].

The effect of laser marking on fatigue strength of the two most common titanium alloys is obvious from the S–N curves in Figure 7.10. Oxidative laser marking dramatically jeopardizes the fatigue performance at stress levels far below the endurance limit of unmarked alloys. Evidently, the presence of surface cracks reaching several microns into the alloys to the depth where the martensite zone in the HAZ begins, bypasses the crack initiation stage during fatigue testing. Often, crack initiation establishes 80–90% of the fatigue life. The deeper cracks and HAZ in laser-marked Ti6Al4V explains the more dramatic deterioration in fatigue performance for this alloy as compared to CP Ti. The consistently poor fatigue performance for laser marking parameter set #3 is attributed to the significantly deeper initial cracks. It should be mentioned that there was no compensation for the curved surface of the fatigue specimen during laser marking, and that the laser was focused on the highest point on the curve. This translates into slight variation of laser spot size which would affect the power density as described by equation (7.2). Some degree of variation in the degree of melting and oxidation can therefore be expected along the laser mark, however the black color was present in the whole mark, and the HAZ was visible along the entire laser-marked edge.

For industrial applications, precautions should be taken regarding laser-marked UDI on medical implants and devices which experience cyclic stress. Due to the significant reduction in fatigue strength, UDIs should not be applied at locations where the component is subjected to cyclic loading. Instead, laser marking should be placed at locations where the applied load is far below design load. In particular, laser markings should be avoided on implants or tools. For torque wrenches for implant surgeries, UDIs should be avoided on the shaft and, instead, be applied on the end of the shaft. The implications of UDI on implants are likely more critical; UDI should not be applied onto dental implants, as opposed to the growing demands and regulations. If UDIs are demanded despite the associated surface deterioration, the parameters should be selected such that surface melting is minimized. Particularly, the anticipated origin of crack initiation, the martensitic β→α transformation, should be avoided, by choosing a suitable alloy. In this respect CP-Ti is less vulnerable than the widely applied Ti6Al4V. Preferably, an alloy is used that either does not suffer from martensite formation, as for example a (near) stable β-titanium alloy, or an α-titanium alloy where the martensitic transformation is associated with imposing compressive stress in the top part of the HAZ.

7.5. Conclusions

The following conclusions can be drawn based on the results of this investigation.

- Laser marking by conventional methods to form UDI, will result in crack formation on the surface of the two most common titanium alloys for medical purposes: CP-Ti and Ti6Al4.
- The application of UDI by oxidative laser marking on titanium alloys will significantly reduce the fatigue strength. UDI should be avoided on critical locations where alternating loads are applied.

- The oxidation and crack formation, and thereby the reduction of fatigue strength, can to some degree be affected by the laser parameters. More laser energy and more melting are likely to result in deeper cracks and thereby a more dramatic reduction in fatigue strength.
- CP-Ti performs better after laser marking than the Ti6Al4 regarding fatigue strength relative to the baseline, depending on the laser parameters as the HAZ and cracks are generally deeper for Ti6Al4V.
- Several distinct microstructures and oxides form during laser marking. Crack initiation in the HAZ reaches to the transition from oxygen-enriched α-Ti to prior β-Ti, that has transformed to martensite during cooling.

7.6. References

[1] J. W. Nicholson, “Titanium Alloys for Dental Implants: A Review,” *Prosthesis*, vol. 2, no. 2, pp. 100–116, Jun. 2020, doi: 10.3390/prosthesis2020011.

[2] M. McCracken, “Dental Implant Materials: Commercially Pure Titanium and Titanium Alloys,” *Journal of Prosthodontics*, vol. 8, no. 1, pp. 40–43, Mar. 1999, doi: 10.1111/j.1532-849X.1999.tb00006.x.

[3] K. Shemtov-Yona and D. Rittel, “An Overview of the Mechanical Integrity of Dental Implants,” *Biomed Res Int*, vol. 2015, pp. 1–11, 2015, doi: 10.1155/2015/547384.

[4] L. Pazos, P. Corengia, and H. Svoboda, “Effect of surface treatments on the fatigue life of titanium for biomedical applications,” *J Mech Behav Biomed Mater*, vol. 3, no. 6, pp. 416–424, Aug. 2010, doi: 10.1016/j.jmbbm.2010.03.006.

[5] N. Wilson, J. Broatch, M. Jehn, and C. Davis, “National projections of time, cost and failure in implantable device identification: Consideration of unique device identification use,” *Healthcare*, vol. 3, no. 4, pp. 196–201, Dec. 2015, doi: 10.1016/J.HJDSI.2015.04.003.

[6] European Union, “The European Commision, Commision recommendation of 5 April 2013 on a common framework for a unique device identification system of medical devices in the Union,” *Official Journal of the European Union*, Apr. 2015.

[7] European Union, *Regulation (EU) 2017/745 of the European Parliament and of the Council on Medical Devices, amending Directive 2001/83/EC*. 2017.

[8] C. Neugebauer, S. Quaranta, S. Ehrenmann, C. Rest, and J. Sadowitz, “Latest advances in medical black marking: technology and techniques,” in *Laser-based Micro- and Nanoprocessing XIII*, Mar. 2019, p. 3. doi: 10.1117/12.2508408.

[9] L. Lazov, H. Deneva, and P. Narica, “Laser Marking Methods,” 2016.

[10] P. Tracol, “Materials vigilance and traceability,” *Orthopaedics & Traumatology: Surgery & Research*, vol. 102, no. 1, pp. S95–S103, Feb. 2016, doi: 10.1016/j.otsr.2015.05.013.

[11] B. Jang, A. Kanawati, D. Brazil, and W. Bruce, “Laser etching causing fatigue fracture at the neck–shoulder junction of an uncemented femoral stem: A case report,” *J Orthop*, vol. 10, no. 2, pp. 95–98, Jun. 2013, doi: 10.1016/j.jor.2013.04.007.

[12] D. Kluess *et al.*, “Laser engravings as reason for mechanical failure of titanium-alloyed total hip stems,” *Arch Orthop Trauma Surg*, vol. 135, no. 7, pp. 1027–1031, Jul. 2015, doi: 10.1007/s00402-015-2225-7.

[13] C. Kühn and E. Kerscher, “Consequences of Micro-Milled and Laser Structured Surfaces of CP-Titanium on Tension-Compression Fatigue Behaviour,” *Materials Science Forum*, vol. 765, pp. 653–657, Jul. 2013, doi: 10.4028/www.scientific.net/MSF.765.653.

[14] A. Shivaram, E. Baker, M. Ewing, and S. Nambu, “Effects of Laser Marking on Fatigue Strength of Titanium Alloys,” *Mater Perform Charact*, vol. 8, no. 6, p. 20180124, Jun. 2019, doi: 10.1520/MPC20180124.

[15] M. Švantner, M. Kučera, E. Smazalová, Š. Houdková, and R. Čerstvý, “Thermal effects of laser marking on microstructure and corrosion properties of stainless steel,” *Appl Opt*, vol. 55, no. 34, p. D35, Dec. 2016, doi: 10.1364/AO.55.000D35.

[16] DIN EN ISO, “Dentistry - Implants - Dynamic loading test for endosseous dental implants (ISO 14801:2016),” 2016.

[17] F. B. Kværndrup, Ö. C. Kücükyildiz, G. Winther, M. A. J. Somers, and T. L. Christiansen, “Extreme hardening of titanium with colossal interstitial contents of nitrogen and oxygen,” *Materials Science and Engineering: A*, vol. 813, p. 141033, May 2021, doi: 10.1016/j.msea.2021.141033.

[18] T. L. Anderson, *Fracture Mechanics*. CRC Press, 2017. doi: 10.1201/9781315370293.

[19] Y. Fei, X. N. Wang, G. Q. Shang, J. Li, L. W. Zhu, and Z. S. Zhu, “Influence of Cooling Rate on Phase Transformation of a α+β Titanium Alloy,” *Materials Science Forum*, vol. 849, pp. 327–331, Mar. 2016, doi: 10.4028/www.scientific.net/MSF.849.327.

[20] C. Ding, X. Li, H.-Y. Zhu, F.-W. Chen, F. Li, and H. Chang, “Microstructure evolution and phase transformation kinetics of low cost Ti-35421 titanium alloy during continuous heating,” *Journal of Materials Research and Technology*, vol. 14, pp. 620–630, Sep. 2021, doi: 10.1016/j.jmrt.2021.06.071.

[21] H. Yu, W. Li, H. Zou, S. Li, T. Zhai, and L. Liu, “Study on Non-Isothermal Transformation of Ti-6Al-4V in Solution Heating Stage,” *Metals (Basel)*, vol. 9, no. 9, p. 968, Sep. 2019, doi: 10.3390/met9090968.

[22] X. Li *et al.*, “Phase transformation and microstructure evolution of Ti6Al4V-0.55Fe alloy with different initial microstructure during continuous heating,” *Journal of Materials Research and Technology*, vol. 18, pp. 1704–1716, May 2022, doi: 10.1016/j.jmrt.2022.03.093.

[23] C. J. Rosa, “Oxygen diffusion in alpha and beta titanium in the temperature range of 932° to 1142°C,” *Metallurgical and Materials Transactions B*, vol. 1, no. 9, pp. 2517–2522, Sep. 1970, doi: 10.1007/BF03038377.

[24] M. SONG, S. HAN, D. MIN, G. CHOI, and J. PARK, “Diffusion of oxygen in β-titanium,” *Scr Mater*, vol. 59, no. 6, pp. 623–626, Sep. 2008, doi: 10.1016/j.scriptamat.2008.05.037.

[25] H. Okamoto, “O-Ti (Oxygen-Titanium),” *J Phase Equilibria Diffus*, vol. 32, no. 5, pp. 473–474, Oct. 2011, doi: 10.1007/s11669-011-9935-5.

[26] W. Guo *et al.*, “Effect of laser shock processing on oxidation resistance of laser additive manufactured Ti6Al4V titanium alloy,” *Corros Sci*, vol. 170, p. 108655, Jul. 2020, doi: 10.1016/j.corsci.2020.108655.

[27] J. Dai, J. Zhu, C. Chen, and F. Weng, “High temperature oxidation behavior and research status of modifications on improving high temperature oxidation resistance of titanium alloys and titanium aluminides: A review,” *J Alloys Compd*, vol. 685, pp. 784–798, Nov. 2016, doi: 10.1016/j.jallcom.2016.06.212.

[28] Y. B. XU and Z. S. XU, “Interstitial segregation and embrittlement in Ti-6Al-4V alloy,” *JOURNAL OF MATERIALS SCIENCE* , vol. 25, pp. 3976–3981, 1990.

[29] C. Dupressoire, M. Descoins, A. vande Put, D. Mangelinck, P. Emile, and D. Monceau, “The nitrogen effect on the oxidation behaviour of Ti6242S titanium-based alloy: contribution of atom probe tomography,” *MATEC Web of Conferences*, vol. 321, p. 06005, Oct. 2020, doi: 10.1051/matecconf/202032106005.

[30] M. Seo and M. Lee, “Vivid structural colors produced on stainless steel,” *Acta Mater*, vol. 159, pp. 1–7, Oct. 2018, doi: 10.1016/j.actamat.2018.08.011.

[31] E. György, A. Pérez del Pino, P. Serra, and J. L. Morenza, “Structure formation on titanium during oxidation induced by cumulative pulsed Nd:YAG laser irradiation,” *Appl Phys A Mater Sci Process*, vol. 78, no. 5, pp. 765–770, Mar. 2004, doi: 10.1007/s00339-002-2054-8.

[32] N. Jiang *et al.*, “Exploring the mechanism behind improved osteointegration of phosphorylated titanium implants with hierarchically structured topography,” *Colloids Surf B Biointerfaces*, vol. 184, p. 110520, Dec. 2019, doi: 10.1016/j.colsurfb.2019.110520.

[33] A. D. Racovita, “Titanium Dioxide: Structure, Impact, and Toxicity,” *Int J Environ Res Public Health*, vol. 19, no. 9, p. 5681, May 2022, doi: 10.3390/ijerph19095681.

[34] M. Czajka, K. Sawicki, K. Sikorska, S. Popek, M. Kruszewski, and L. Kapka-Skrzypczak, “Toxicity of titanium dioxide nanoparticles in central nervous system,” *Toxicology in Vitro*, vol. 29, no. 5, pp. 1042–1052, Aug. 2015, doi: 10.1016/j.tiv.2015.04.004.

[35] M. T. Hamed *et al.*, “Novel Synthesis of Titanium Oxide Nanoparticles: Biological Activity and Acute Toxicity Study,” *Bioinorg Chem Appl*, vol. 2021, pp. 1–14, Aug. 2021, doi: 10.1155/2021/8171786.

[36] C. Domínguez-Trujillo *et al.*, “Bacterial behavior on coated porous titanium substrates for biomedical applications,” *Surf Coat Technol*, vol. 357, pp. 896–902, Jan. 2019, doi: 10.1016/j.surfcoat.2018.10.098.

[37] Y. Duan, J. A. Gonzalez, P. A. Kulkarni, W. W. Nagy, and J. A. Griggs, “Fatigue lifetime prediction of a reduced-diameter dental implant system: Numerical and experimental study,” *Dental Materials*, vol. 34, no. 9, pp. 1299–1309, Sep. 2018, doi: 10.1016/j.dental.2018.06.002.

[38] P. Pérez León, J. F. Bartolomé, C. Lombardía, and G. Pradíes, “Mechanical fatigue behaviour of different lengths screw-retained restorations connected to two designs prosthetic connection level,” *J Oral Rehabil*, p. joor.12809, May 2019, doi: 10.1111/joor.12809.

[39] P. Sevilla, C. Sandino, M. Arciniegas, J. Martínez-Gomis, M. Peraire, and F. J. Gil, “Evaluating mechanical properties and degradation of YTZP dental implants,” *Materials Science and Engineering: C*, vol. 30, no. 1, pp. 14–19, Jan. 2010, doi: 10.1016/j.msec.2009.08.002.

[40] A. San-Martin and F. D. Manchester, “The H−Ti (Hydrogen-Titanium) system,” *Bulletin of Alloy Phase Diagrams*, vol. 8, no. 1, pp. 30–42, Feb. 1987, doi: 10.1007/BF02868888.

8. Industrial Laser Marking Guidelines

8.1. Stainless Steel

The result of laser marking on stainless steel has been found to be particularly influenced by both parameters and choice of material. Failed markings are found in the form of corrosion, resulting in either rusty stains or a delamination of the oxide layer, and consequently parameters and material should be decided upon as to maximize the corrosion resistance. Additionally, chemical passivation can be utilized to increase the corrosion/pitting resistance after laser marking.

The choice of steel should be based on the knowledge on how the chemical composition and microstructure can affect the corrosion resistance. High content of passivating elements, such as chromium and molybdenum are preferred, as a high content of these elements may counteract the loss of passivity following chromium depletion upon oxidative laser marking. To avoid severe loss of passivity, stainless steel grade with low chromium content (11-14 wt.%) should be avoided, if possible, especially if a strong black color is required. Otherwise, manufacturers might have to settle with a grey appearance instead of black. Other alloying elements were also found to affect the performance of oxidative laser marking, such as the presence of MnS. As it was found that thermal degradation of MnS was a source of preliminary pits in the laser marking, manufacturers might wish to compromise the enhanced machineability from MnS to gain corrosion resistance.

Even if nitrogen in solution has a positive effect on the PREN, it was found that it did not increase the corrosion resistance of laser marked stainless steel. As the color of nitrided specimen was also significantly darker, it is hypothesized that the nitrided surface affects the laser marking process itself, either by increasing the absorption of laser energy or by increasing the diffusion of oxygen. Therefore nitriding, which is a conventional method of increasing corrosion resistance, should not be applied without performing a parameter study on the laser marking process.

A common method of increasing the corrosion resistance of stainless steel is by applying chemsical passivation to the finished product. This process is traditionally performed in nitric acid, but there is consensus in scientific literature that citric acid passivation can be utilized to the same effect on the most common stainless steels. Therefore, it is recommended that citric acid passivation is performed rather than nitric acid passivation, as nitric acid is more dangerous to handle and can cause injuries. Citric acid is on the other hand a common additive in food products and is safe to handle.

The effect of chemical passivation on laser marked stainless steel is generally positive and can prevent pit initiation which will develop to cause delamination of the oxide layer and thereby render the product unfit for application. The laser marking must be re-passivated as it is otherwise in significant risk of corrosion. Laser markings will still be locations for corrosion, but to a much lesser degree.

It has been found that the laser parameters affect the corrosion resistance and color strength significantly. The color strength is dependent on the heat input and thereby the oxide layer thickness and so a paradox is presented. High heat input will result in low corrosion resistance, thereby producing markings with high color strength and corrosion resistance has proven difficult via oxidative laser marking. Experiments should be performed on each material to determine a good compromise between heat input and color strength. If a higher color strength is preferred, a material with higher chromium content is required.

There was little effect on the corrosion resistance from the power density, but literature suggests that good corrosion resistance can be achieved via ablative laser marking. Ablative laser marking is commonly achieved with a high power density and low pulse frequency, to generate contrast by evaporation and melting of material. A summary of the laser marking guidelines regarding corrosion resistance of stainless steel, is presented in Figure 10.1. The corrosion resistance has been found to decrease slightly with increasing heat input, until a certain threshold is reached, and the corrosion resistance drops rapidly. It is thought that with certain heat inputs, the sub-surface loses its ability to passivate. Eventually the corrosion resistance of a low-chromium steel is achieved. More research would be necessary to determine the exact shape of the curve, and Figure 10.1 is merely intended to be a guideline and rule of thumb.

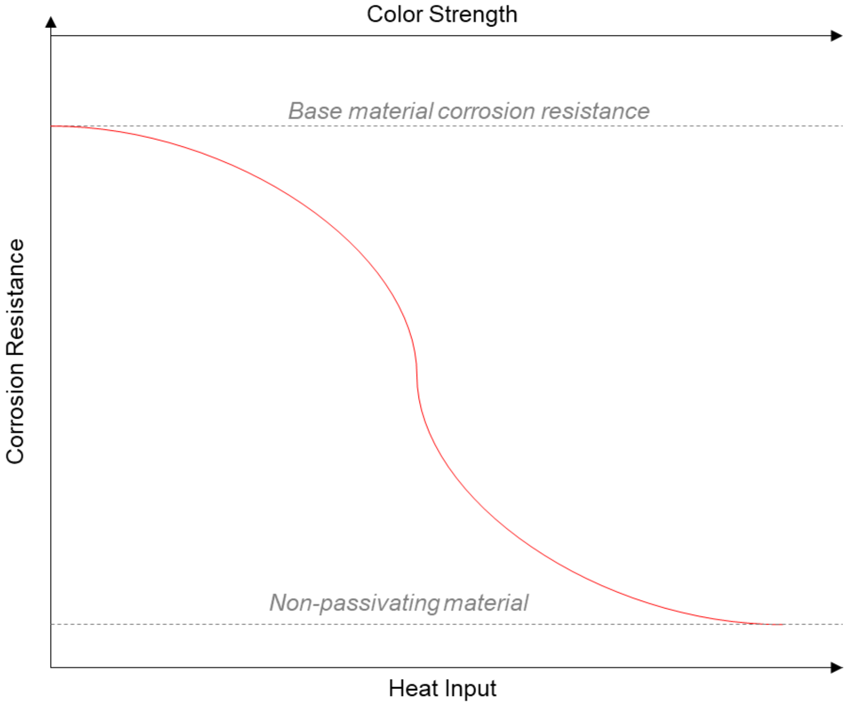

Figure 10.1 An illustration of how the heat input during oxidative laser marking is thought to influence the corrosion resistance of stainless steel.

8.2. Titanium Alloys

Laser marking of titanium alloys was not found to impact corrosion resistance significantly, as there is no chromium depletion to be responsible for reduced corrosion resistance. The issue of laser marking titanium is the generation of cracks of significant depth into the material, acting as notches and completely bypassing the crack initiation during cycling loading.

In present work, only commercially pure titanium and Ti6Al4V have been investigated, and the crack formation was detrimental to both materials. Crack initiation is up to 95 % of the fatigue life of metallic components, and this stage is essentially skipped upon laser marking. Ti6Al4V has a higher percentwise decrease in fatigue strength as all investigated parameter sets reduced fatigue life by almost 80 %. CP-Ti performed slightly better with some dependence on laser parameters. The reduction in fatigue strength appeared to be largely independent of laser parameters on Ti6Al4V, while on CP-Ti a dependence on the crack length could be observed. The largest crack length was achieved by applying high power density and heat input during laser marking, causing a large degree of melting.

The effect on less common titanium alloys is unknown and the impact on fatigue strength should be investigated before application. This includes the so-called β-alloys, where the introduction of oxygen can alter the transformations occurring during laser marking. When laser marking titanium, the degree of melting should be minimized, and the fatigue strength should be tested in loading conditions similar to that in application. Most importantly, Ti6Al4V which is significantly stronger than CP-Ti in the unmarked condition, does not perform better after laser marking. The unprecedented reduction in fatigue strength could be detrimental to the product. Therefore, the location of the laser mark may be of higher importance than the parameters, given that the degree of melting is controlled.

If laser markings must be applied to titanium alloys, it should be located in a position where the marking does not experience cyclic loading. If applied on an implant, a fracture could endanger patient health.

9. Summary and Conclusions

This thesis addresses the issues and challenges of laser-marking in the medical device industry, to ensure application without failure of the laser-marking. Two types of materials are investigated: Titanium alloys and stainless steel, as they are by far the most utilized metallic materials in the medical device industry. The results are presented in the form of 4 manuscripts and a supplementary section, each containing detailed conclusion and discussions. This section presents the overall results and most important conclusions divided into two categories: Laser-marking of stainless steel and laser-marking of titanium.

9.1. Laser Marking of Stainless Steel

A black oxide could be reliably formed on both martensitic and austenitic stainless steels and the color strength was determined to depend largely on the laser heat input. A reduction of the corrosion potential was measured for all laser parameters when laser-marking in the oxidative regime. Severe corrosion would lead to a delamination of the black oxide. This was attributed to chromium depletion in the material below the oxide layer. A chromium depletion in the first few µm below the oxide was measured via GDOES, and a chromium containing oxide layer was identified with EDS. The corrosion potential was drastically reduced at high laser heat inputs to the point where the substrate had likely lost its ability to form a passive layer. The oxide layer exhibited significant crack formation, but the cracks were limited to the oxide layer and did not penetrate into the material. High tensile residual stresses were measured in the sub-surface on martensitic stainless steel, following laser-marking. This is thought to be a consequence of the altered chemical composition and phase changes.

The presence of MnS inclusions had a negative impact on the ability to retain corrosion resistance after laser-marking. Abundant MnS would result in crater-like features across the laser-marked surface, as a consequence of the degradation of rod-like inclusions during laser interaction. Access of the electrolyte to the chromium depleted and high sulfur subsurface would be the result, drastically reducing the corrosion resistance relative to similar steels with a low content of MnS. It was attempted to mitigate the deterioration of the corrosion resistance by increasing the nitrogen content before laser marking, as nitrogen is known to have a positive influence on the PREN. However, an increased color strength and reduced corrosion resistance of the laser-marking on nitrided specimen relative to non-nitrided samples, showed that nitriding alters other properties related to the laser-marking process. A higher content of retained austenite or formation of nitride compounds on the surface is hypothesized to have changed the laser absorption, thereby increasing the effective laser heat input. Citric acid passivation is a more promising method of retaining corrosion resistance, at least on stainless steels with higher chromium content. It was shown that citric acid passivation significantly reduced the metastable pitting and increased the pitting potential to values similar to those of the reference material.

9.2. Laser Marking of Titanium

Laser-marking on titanium alloys altered the surface morphology and microstructure significantly. Most notably, large vertical cracks developed, penetrating deep into the substrate. The crack length depended to some degree on the laser parameters. Combining high power density and high heat input, a large amount of material was melted and the crack length increased significantly. There were signs of melting in all samples and indications of an increased content of oxygen in the outer part of the HAZ. The melted part of the HAZ solidified directly as nano-sized grains of α-Ti, by-passing β-formation from the melt. This observation suggests a high content of α-stabilizing oxygen. Oxygen-stabilized α-Ti was also found deeper in the HAZ, where the material did not melt. The cracks were limited to the oxygen-stabilized α-Ti and did not extend into the deepest part of the HAZ, which consisted of martensite originating from the β→α transformation. The resulting vertical cracks indicate that tensile stress resulted in the surface-adjacent region by a volume expansion associated with β→α transformation underneath.

Laser-marking decreased the fatigue strength of the titanium alloys dramatically. The cracks introduced during laser marking prior to loading of the specimen implies that crack initiation, which is by far the longest stage, was essentially skipped. It was observed that the cracks propagated from the entirety of the laser marked surface and did not have a single point of initiation. The reduction in fatigue life depended for CP-Ti on the crack length, with the highest reduction observed in specimen with the deepest cracks. This was also observed for T6Al4V, albeit to a lesser extent. No oxide layer was observed with microscopy on laser marked titanium, but the presence of oxides was confirmed XRD. These results indicate that the oxides were present in the melt as particles, rather than as a continuous layer on top of the melt.

Appendix: Simulation of Laser Marking on Stainless Steel

As nanosecond laser marking takes place on small timescales with rapid cooling and heating, the thermal history of a laser-marked surface can be quite complicated. It is important to understand how the material was heated and cooled, to understand the mechanism behind changes in microstructure, residual stress state and general performance of the material. Numerical simulation is a useful tool to understand complicated phenomena in detail. The situation of laser marking is complicated indeed, with a large degree of overlap both in the laser tracks and of the pulse spots as high pulse frequencies are common.

The numerical model was developed during a special course supervised by Mohamad Bayat and Jesper Hattel, titled “Modelling of the laser-marking post-process”. The presented results have previously been handed in as a report for the special course but in a different format. The contents are reproduced for completeness and illustration. The contents cannot be evaluated as a part of the thesis, because they have been evaluated earlier as a 5 ECTS special course.

9.3. Symbols

Symbols	Definition
P	Average power of the laser, W
f	Pulse frequency, Hz
v	Laser scan speed, m/s
t_p	Pulse length, s
E_p	Energy of a single pulse, J
A	Laser spot size, m^2
l_s	Hatch spacing, m
P_p	Peak power density, W/m^2
E_s	Energy input, J/m^2

η	Laser energy absorptance of a material
r	Radius of the gaussian laser spot, m
q_{laser}	Gaussian laser heat source, W/m^2
ρ_s	Density of solid, kg/m^3
ρ_l	Density of liquid, kg/m^3
C_{ps}	Specific heat capacity of solid, J/(kg·K)
C_{pl}	Specific heat capacity of liquid, J/(kg·K)
T	Temperature, K
k	Thermal conductivity, W/(m·k)
Q	Total transferred energy
q_{air}	Convection to ambient air, W/m^2
h	Convection heat transfer coefficient, $W/(m^2 \cdot K)$
T_{amb}	Ambient temperature, K
q_{rad}	Heat transfer to ambient by radiation, W/m^2
σ	Boltzmann constant, $5.67 \cdot 10^{-8}$ Wm^2K^4
ε	Surface emissivity
w	Phase fraction of liquid
ΔH_{fus}	Latent heat of fusion, J/kg
α	Thermal diffusivity, m^2/s

9.4. Materials and Methods

9.4.1. Numerical Modelling

The modelling of the nanosecond laser marking method was performed as a FEM using COMSOL Multiphysics 5.4, with the purpose of simulating and validating the thermal field and melt pools during laser marking. Due to time constraints, a simplified laser marking process was investigated, where only a single track was simulated. In reality, laser-marking involves many tracks and overlap of these. For the purpose of numerical modelling, the following assumptions have been made:

- The laser energy, q_{laser} (W/m^2) distribution can be described as a Gaussian distribution with the equation $q_{laser} = \frac{2\left(\frac{P}{ft_p}\right)\eta}{\pi r^2} \cdot e^{-2\frac{(x-x_0)^2+(y-y_0)^2}{r^2}}$.
- It is assumed that the Marangoni effect and liquid flow can be ignored.
- Evaporation is assumed negligible.
- The material properties are assumed to be uniform in the entire specimen.
- The laser marked surface is assumed to be perfectly flat.

As laser marking generates a shallow HAZ, the geometry for the model can be small. A finely meshed box of 0.62 x 0.15 x 0.05 mm is utilized for the laser marking simulation. This small box is placed within a larger geometry with a much coarser mesh which can act as a heat sink, as would be the case for laser-marking in industry. The geometries are illustrated in Figure 3.1 and are mirrored in the plane marked as 3 during simulation. As the laser spot energy distribution is assumed to be symmetrical, it is possible to simulate half of the laser marked part and mirror the results. A single laser track is simulated, moving from point 1 to point 2 illustrated on Figure 3.1. The geometries are meshed with tetrahedral elements. Furthermore, plane 4 is to be the only surface with ambience heat transfer, all other surfaces are considered adiabatic.

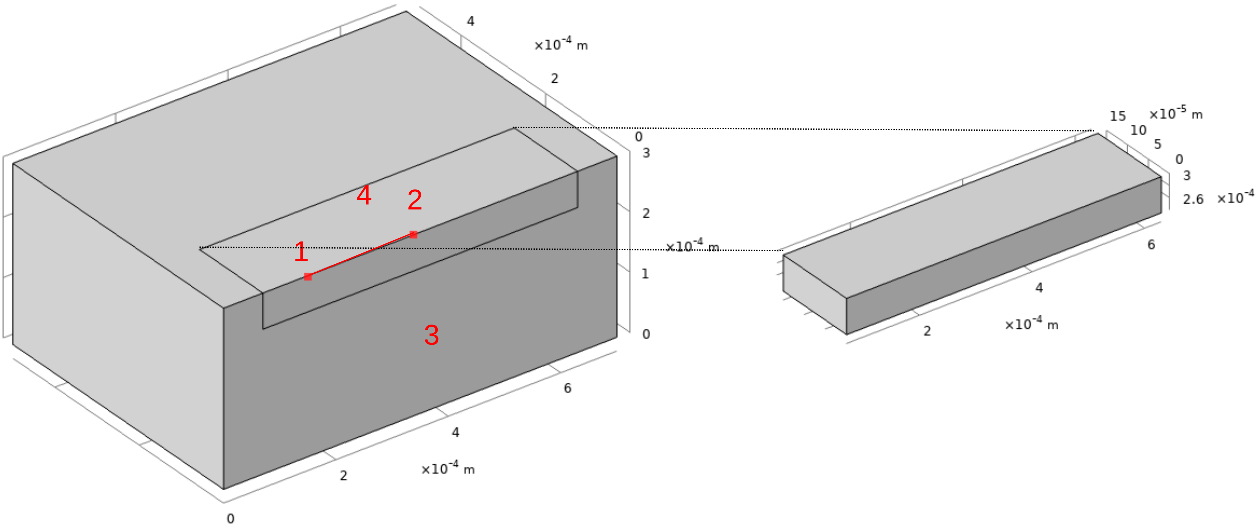

Figure 3.1: The geometries used for numerical modelling of pulsed nanosecond laser marking.

The heat transfer from plane 4 is assumed to be happening by radiation and convection with air. Radiation is calculated as:

$$q_{rad} = \epsilon\sigma\left(T_{amb}^4 - T^4\right)$$

Surface emissivity is taken as 0.4, which is a common value for stainless steel. Convection from plane 4 is calculated as:

$$q_c = h(T_{amb} - T)$$

The convection heat transfer coefficient is assumed to be 19.2 W/(m^2·K), a common value for convection between metallic surfaces and air. An ambient temperature of 293 K is assumed. Stainless steel is a phase changing material and the physical properties change with phase transformation. AISI 304 is assumed to have only two phases during laser marking, which are a solid austenite phase and liquid phase. Therefore, the physical properties will depend on the phase fraction of each:

$$\rho = (1 - w)\rho_s + w\rho_l$$

$$k = (1 - w)k_s + wk_l$$

$$C_p = \frac{1}{\rho}\Big((1-w)\rho_s C_{ps} + w\rho_l C_{pl}\Big) + \Delta H_{fus}\frac{\delta\alpha}{\delta T}$$

Furthermore, the latent heat of fusion, ΔH_{fus}, is absorbed or released depending on the phase transformation. It will be released during the transformation of liquid to solid, while the same amount of extra energy is required for the opposite transformation. The general equation for the temperature field is calculated as:

$$\rho C_p\left(\frac{\partial T}{\partial t}\right) + \rho C_p u \nabla T = \nabla(-k\nabla T)Q'''$$

It describes the change in temperature with time, as heat is transferred via conduction and convection, however as flow was assumed to be negligible, the heat transfer is dominated by conduction.

9.4.2. Material

For both the numerical modelling and the verification of the model, the stainless steel AISI 304L is utilized. The nominal chemical composition can be found in Table 3.1. As AISI 304L is a very common material, the physical constants are well-known [1–3]. It is assumed to be fully austenite when solid. The utilized physical constants are listed in Table 3.2.

Table 3.1: The nominal chemical composition of AISI 304L.

Element	C	Mn	P	S	Si	Cr	Ni
W%	<0.07	<2.00	<0.05	<0.03	<1.00	17-19	8-11

Table 3.2: Physical constants utilized for numerical modelling of laser marking on AISI 304L.

	Solid	Liquid
Density, kg/m^3	7200	6900
Specific heat capacity, J/(kg·K)	712	837
Latent heat of fusion, J/kg	$-2.74\cdot10^5$	-

Thermal conductivity, W/(m·K)	19.2	209.2
Viscosity, kg/(m·s)	1	$6 \cdot 10^{-2}$
Solidus temperature, K	-	1697
Liquidus temperature, K	1727	-

9.4.1. Experimental

For experimental validation of the numerical model, the FOBA Y.002 Nd:YAG nanosecond pulsed fiber laser was used to produce laser-markings on AISI 304L discs. The purpose was to validate the model by comparing melt pool size and shape between the model and experimental samples. The discs were cut from a drawn rod via lathe turning, where the surface was subsequently ground with SiC abrasive paper, the final grinding step being with coarseness # 4000P. The discs were of Ø 7 mm and a thickness of 2 mm. The laser tracks were applied parallel to each other and the hatch spacing was set to 35 µm. As the nominal laser spot size is 30 µm, this should ensure a limited track overlap. For cross-sectional analysis of the melt pools, the laser marked discs were cut perpendicular to the laser tracks.

As Conventional laser parameters for oxidative laser marking did not produce melt pools which were easily detectable with light optical microscopy, the melt pool verification was performed with somewhat exaggerated laser parameters. Conventional marking speeds are in the range of 500-3000 mm/s and the average power is 4-10 W. For this investigation, the marking speed was reduced to 100 mm/s and the average power increased to 14 W. This yields a substantial increase in both power density and heat input, as the heat generated from each pulse is increased and there is a high overlap for each laser spot. An overview of the laser parameters can be found in Table 3.3.

Table 3.3: Parameters utilized during laser marking and numerical simulation of laser marking.

Marking scan speed	100 mm/s
Average power	14 W

Hatch spacing	35 µm
Frequency	200 kHz
Pulse length	200 ns

9.5. Results and Discussion

To simulate the laser pulses, the Gaussian heat distribution of the laser is multiplied with a square wavefunction, w, as to imitate the laser turning on and off. The wavefunction should repeat for each total pulse cycle of the laser, for which the time can be calculated as the inverse of the pulse frequency:

$$\frac{1}{f} = \frac{1}{2 \cdot 10^5 \left(\frac{1}{s}\right)} = 5 \cdot 10^{-6} s$$

However, the laser will only be active for 200 ns of the pulse cycle time, which amounts to 4 %. The wavefunction can then be constructed and will have an active duty-cycle of 0.04 and occur at an angular frequency of $\frac{2\pi}{5 \cdot 10^{-6} s}$. The amplitude can be set to 0.5. The following equation will describe the laser as a pulsing moving heat source:

$$q_{laser} = (w+1)\left(\frac{2\left(\frac{P}{f t_p}\right)\eta}{\pi r^2} \cdot e^{\left(-2\frac{(x-x0)^2+(y-y0)^2}{r^2}\right)}\right)$$

A mesh dependency study was performed on the model, as to determine how many elements are required to simulate the laser process. The model was investigated on two parameters: maximum temperature and liquid phase fraction. The mesh dependency was investigated with 100,000, 300,000 and 600,000 elements.

From Figure 3.2a, it is clear that the coarser meshes of 100,000 and 300,000 elements are insufficient to simulate the laser marking process. This is because there are no clear temperature spikes, as would be the case during pulsed laser-marking. Instead the coarser meshes are relatively stable around 1800 K. 600,000 elements are enough to resolve part of temperature spikes up to 3500 K, but it must be noted that a finer mesh and sampling interval could be beneficial to capture the thermal effects of the laser pulses. On Figure 3.2b it can be seen that coarser meshes exaggerate the melt pool size after steady state has been reached. The finest mesh exhibits the lowest melt pool size and the least variation in size. The time resolution of the model appears to be too low to really capture the effect of the laser pulses, whereas the effect is instead seen as incomplete spikes in the melt pool size and maximum temperature.

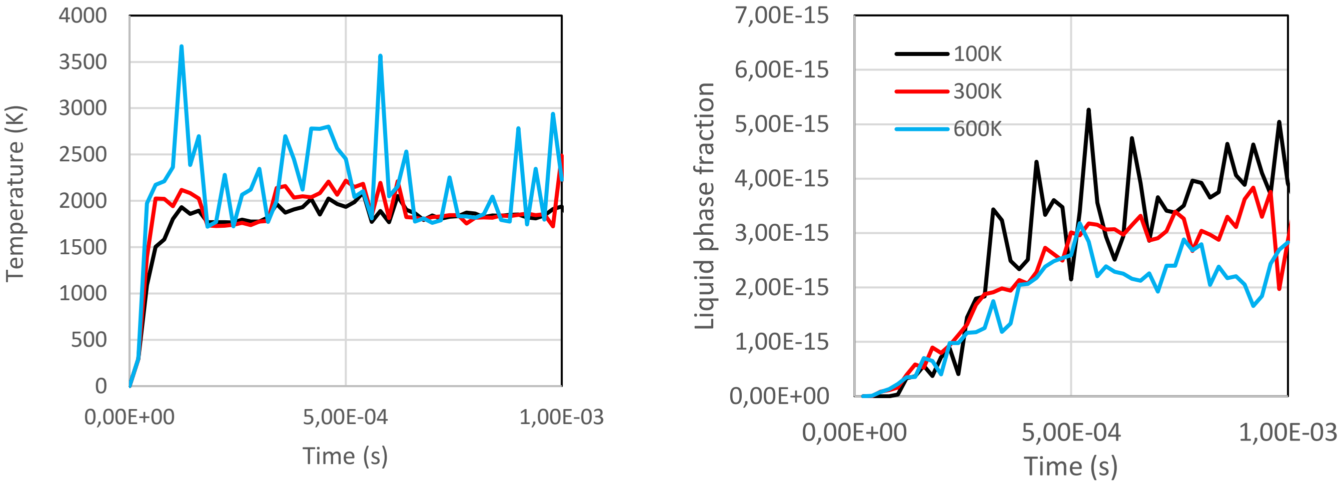

(a) (b)

Figure 3.2: The maximum temperature (a) and the fraction of liquid phase (b) at different mesh sizes during a simulated laser marking.

Some parameters are relatively uncertain during laser marking and can vary substantially [4]. The laser spot size for example can vary significantly and even change during operation as the equipment heats. The absorption of the laser is also an uncertainty as it depends on the material, but also on how the surface develops during processing. Oxides on the surface could for example have a different laser absorption than the base material. Therefore, the model is run with varying laser absorptions and laser spot sizes, to first and foremost validate the model with the correct parameters against experiments. Additionally, these simulations can be used in combination with the experimental data to determine if a steady state is reached within the simulated timeframe.

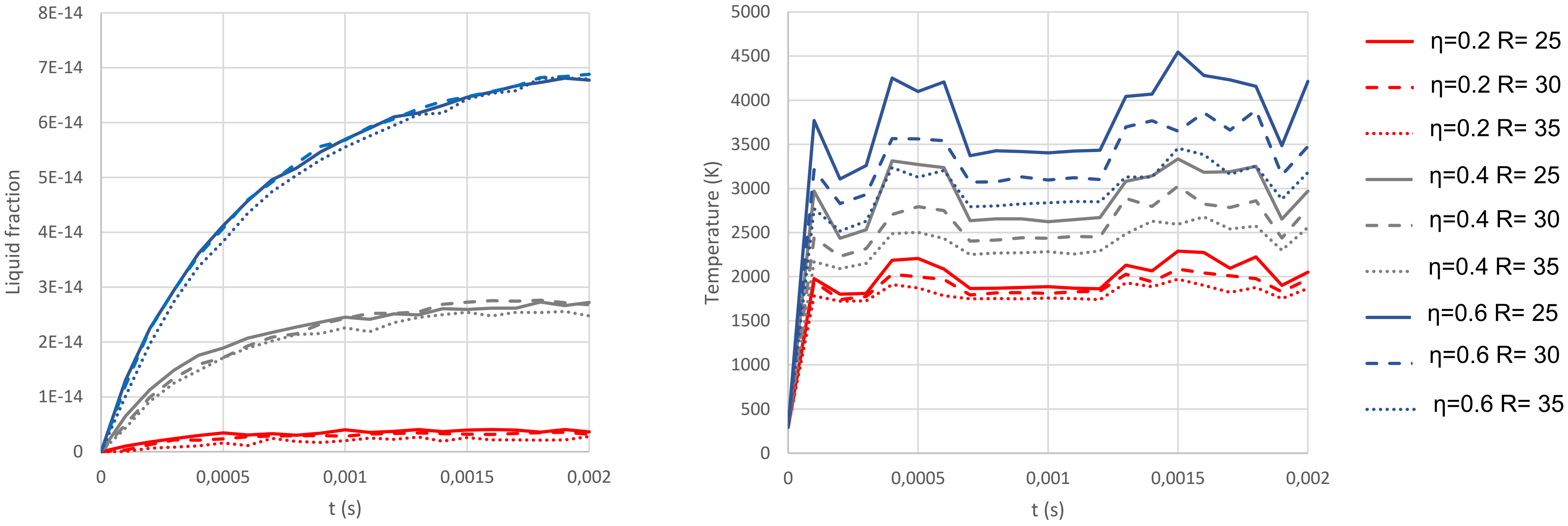

(a) (b)

Figure 3.3: Simulated (a) fraction of liquid phase as a function of time and (b) the maximum temperature. Simulations are performed at different absorption coefficients and laser spot sizes.

Figure 3.3 shows how the phase fraction of liquid metal and the maximum temperature develops during simulation of 20 ms, with different laser absorptions and laser spot sizes. On Figure 3.3a, it is obvious that the determining factor for liquid phase fraction and thereby melt pool size is the laser absorption, as a higher absorption can drastically change the amount of liquid present during laser marking. A steady state in liquid phase fraction is reached quite early for low absorptions of 0.2 and 0.4, while for the highest absorption of 0.6, steady state is not reached during the simulated timeframe. There is no significant effect from the laser spot radius. The maximum temperature shown on Figure 3.3b is also largely dependent on the laser absorption, but the laser spot radius has a significant effect as well. It is seen that the maximum temperature is approached after the first laser pulse and does not appear to increase with time. It should be noted that the sampling interval of the simulation is not small enough to distinguish the temperature development during a single laser pulse. Therefore, there can be maximum temperature development from pulse to pulse.

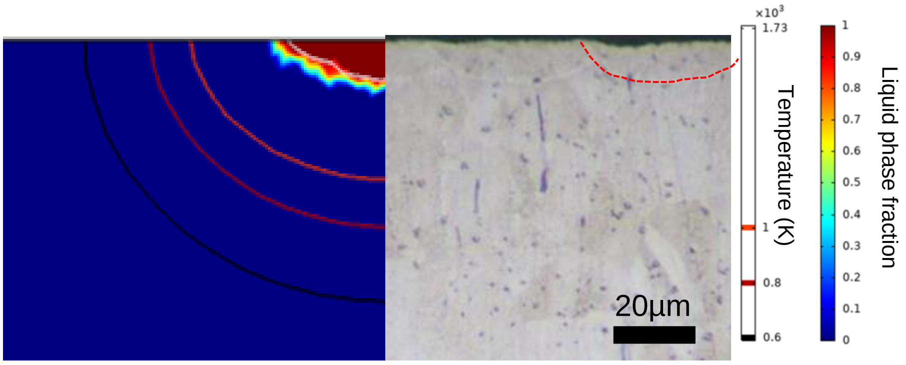

Figure 3.4: Simulated cross-section of the melt pool during laser marking, compared to a micrograph of the cross-section of a laser marked sample of AISI 304L. A red line has been added to one visible melt pool to guide the reader.

A cross-section of the simulated melt pool is shown in Figure 3.4 up against the melt pool in a laser marked sample of AISI 304L. The simulated melt pool is performed with the parameters η = 0.2 and R = 30 µm, is captured in the middle of the last simulated laser pulse and is a good fit with the experimental melt pool geometry and size. With these parameters validated we can confirm from Figure 3.3 that steady state is reached within the simulated timeframe. It also confirms that the assumptions taken in the model are correct. If the Marangoni effect was not negligible and shear flows were present, a wider melt pool and different melt pool morphology should have been observed. Assuming higher temperatures than what is simulated in Figure 3.3, it is possible that evaporation of material can have happened but is appears that the volume of evaporated material would then be low enough that the model can still be validated.

The melt pool itself is relatively shallow of just 5 µm in maximum depth, but there is a significant volume of material at an increased temperature. Temperatures of > 1000°C are reached almost 40 µm into the material, meaning that a relatively deep HAZ can form. It is furthermore discovered that the cooling rate is significantly higher from the bottom of the heated zone than from the surface. This is attributed to the bulk of the part acting as a heat sink, whereas conduction within the material is much faster than convection to the ambient air.

The validated model is run with a smaller sampling interval to resolve the temperature development during single pulses. It is clear from the temperature that a constant melt pool is present. Very high temperatures are reached at the end of each laser pulse, but cooling also takes place extremely fast. The material which was melted during laser marking should solidify with small grains given the fast cooling.

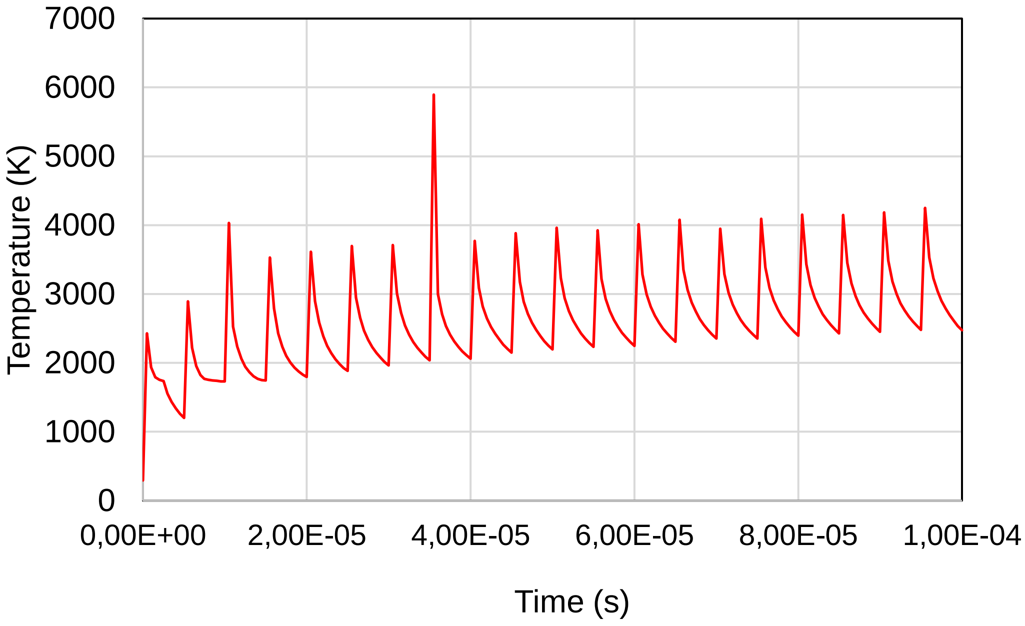

Figure 3.5: The maximum temperature in the workpiece during laser marking, as simulated with the validated model.

9.6. Conclusions

The validation and formulation of a finite element model of the pulsed nanosecond laser marking process allowed the following conclusions to be met:

- The accuracy of the model is sufficient to simulate the thermal field of laser marked steel to a degree where validation is possible.
- Although there is a possibility that flow and evaporation takes place in the melt pool, these effects appear to be negligible as was assumed when constructing the model.
- It can be concluded that a steady state was reached in the model, and as the experimental specimen was cut in the middle, after a sufficient length of laser track, the model was validated at a steady state.
- Deviation from the reality can be expected as a coarser mesh was chosen out of necessity, meaning that the melt pool size is likely slightly exaggerated.

9.7. References

[1] Zhou J, Tsai HL, Lehnhoff TF. Investigation of transport phenomena and defect formation in pulsed laser keyhole welding of zinc-coated steels. J Phys D Appl Phys. 2006 Dec 21;39(24):5338–55.

[2] Ki H, Mazumder J, Mohanty PS. Modeling of laser keyhole welding: Part I. mathematical modeling, numerical methodology, role of recoil pressure, multiple reflections, and free surface evolution. Metallurgical and Materials Transactions A. 2002 Jun;33(6):1817–30.

[3]. Zhou J, Tsai HL, Wang PC. Transport Phenomena and Keyhole Dynamics during Pulsed Laser Welding. J Heat Transfer. 2006 Jul 1;128(7):680–90.

[4]. Criales LE, Arısoy YM, Özel T. Sensitivity analysis of material and process parameters in finite element modeling of selective laser melting of Inconel 625. The International Journal of Advanced Manufacturing Technology. 2016 Oct 29;86(9–12):2653–66.

Department of Civil and Mechanical Engineering

Section of Materials and Surface engineering
Nils Koppels Allé
2800 Kongens Lyngby

www.construct.dtu.dk

978-87-7475-756-6